Molecular and Surface Catecholato Complexes of Titanium(IV)

Dissertation

der Mathematisch-Naturwissenschaftlichen Fakultät

der Eberhard Karls Universität Tübingen

zur Erlangung des Grades eines

Doktors der Naturwissenschaften

(Dr. rer. nat.)

vorgelegt von

Dipl.-Chem. Andrea Sonström

aus Templin

Tübingen

2023

Gedruckt mit der Genehmigung der Mathematisch-Naturwissenschaftlichen Fakultät der Eberhard Karls Universität Tübingen.

Tag der mündlichen Qualifikation: 28.07.2023

Dekan:	Prof. Dr. Thilo Stehle
1. Berichterstatter:	Prof. Dr. Reiner Anwander
2. Berichterstatter:	Prof. Dr. Hermann A. Mayer

Molecular and Surface Catecholato Complexes

of

Titanium (IV)

Andrea Sonström

Tübingen, 2023

Für meine Großeltern

“Nichts motiviert so
wie der innere Antrieb,
etwas verstehen zu wollen.“

(Martin Korte, Hirnforscher an der TU Braunschweig)

Preface

The following PhD thesis consists of some selected insights into the possibilities of influencing the bandgap of titania, surface chemistry strategies and special emphasis on catecholato (surface) complexes, a summary of the main results, and two scientific papers. The work has been carried out at the Institut für Anorganische Chemie of the Eberhard Karls Universität Tübingen, Germany, over the period August 2014 to January 2019 under the supervision of Prof. Dr. Reiner Anwander.

Parts of this thesis have been presented at the International Symposium “Nanoporous Materials VIII” in Ottawa, Canada in 2017 as poster contribution.

Acknowledgements

First of all, I want to thank my supervisor Prof. Dr. Reiner Anwander for welcoming me into his group and for the interesting research topic for this thesis. His outstanding scientific mentoring significantly contributed to the outcome of this thesis. I am grateful for the opportunity to conduct the research in cooperation with ams Sensors Germany GmbH, to their financial support, the possibility to contribute to the European Project SAFESENS® to develop an optimized fire detector and would like to thank Dr. Stefan Raible, Dr. Ulf Struckmeier, Akbar "Ali" Mazaheri, Eva Lang, Wolfram Simmendinger, Simone Scheurer, Dr. Heiko Ulmer, Dr. Alex Harscher, Sandro Berg and Manuel Maurer.

Special thanks are due to PD Dr. M. Benedetta Casu for introducing me into the techniques of XPS and UPS, for the "all-time-support" and for many inspiring discussions.

Thanks go to Dr. Cäcilia Maichle-Mössmer, Dr. Daniel Werner, Dr. Christoph Schädle, Dr. David Schneider, Dr. Regine Herbst-Irmer and Elke Niquet for the crystal structure analyses and several useful advices in this area, to Wolfgang Bock for the elemental analysis measurements, to Dr. Klaus Eichele and Kristina Heß for their support and the solid-state NMR spectroscopy measurements, to Barbara Boldrini and Prof. Dr. Karsten Rebner from Reutlingen University for the possibility to perform solid-state UV/vis measurements of my samples and for their support, to Dr. Peter Grüninger, Prof. Dr. Udo Weimar, Dr. Nicolae Barsan, Dr. Alexander Haensch, Andre Sackmann, Dr. Inci Boehme, Elke Nadler, the groups of Prof. Dr. Andreas Schnepf, Prof. Dr. Thomas Chassé, Prof. Dr. Hans-Jürgen Meyer and Prof. Dr. Hermann A. Mayer for their support and the possibility to use their analytical devices.

Furthermore, I thank Prof. Dr. Karl W. Törnroos, Prof. Dr. Warren E. Piers, Prof. Dr. Philip Mountford and Dr. Thomas Grösser for numerous interesting and inspiring discussions.

I also would like to thank the current and former coworkers "in and around" the Anwander-Group, Holli, Dan, Cili, Nicole D., Christoph St., Lorenz, Lars J., Damir, Uwe, Andreas B., Verena, Martin, Dominic, Jochen F., Felix K, Yucang, Leilei, Nicole M., Doro, Tatiana, Renita, Benni, Ning, Felix T., Sonja, Dennis, Georgios, Markus, Eric, Theresa, Tassilo, Lars H., Simon, Jochen G., Elke Niquet, Tobias Wolf, Nadja Wettering, Sabine Ehrlich, Jenny Steinhilber, Heinz-Jürgen Kolb, and PD Dr. Peter Sirsch for the kind reception, many inspiring discussions and a great time together!

My thanks also go to all my lab course and Bachelor students Marc Rebhan, Lena Merten, Matthias Kotsch and Franziska Kern – it was a great pleasure to have you on board!

I thank my dear friends Rita & Oli, Tommy, Holli & Lena, Julia & Sven, Fafa, Janine, Ana & Jonas, Jessi & Matze, Jessi H., Miri & Fabi, Henni, Alice & Tobi, Marc S. and Miri & Lennart for their friendship, for their support and for the great and funny moments together!

Last, but not least, I want to thank my family – especially my parents and grandparents – for their love and support, for giving me the opportunity for studying and for always being all ears.

Contents

Abbreviations

@	at ("X@Y" = X is immobilized at Y)
Ar	aryl
a_S, BET	specific surface area (by BET method calculations from nitrogen physisorption data)
BE	Binding Energy
BET	Brunauer-Emmett-Teller
BINOL	binolato
BJH	Barrett-Joyner-Halenda
*t*Bu	*tert*-Butyl
CAT	catecholato
CL	core level(s)
CN	coordination number
CP	Cross polarization
C_6D_6	benzene-d_6
DB	3,4-dihydroxyl benzoic acid
DHN	2,3-dihydroxy naphthaleno
$\delta_{M\text{-}OH,\ surf.}$	amount of accessible surface hydroxyls related to 1g of metal oxide material
Do	Donor ligand
$d_{P,\ ads}$	pore diameter (taken from the adsorption branch of the physisorption curve in the BJH region)
DRIFTS	Diffuse Reflectance Infrared Fourier Transform Spectroscopy
EA	Elemental Analysis; Electron Affinity
EDC	1-Ethyl-3-[3-(dimethyl amino)propyl]carbodiimide (with NHS ester chemistry: conjugation method for protein and nucleic acid functionalization)
e.g.	for example, from lat. *exempli gratia*

E_{kin}	Kinetic energy
E_F	Fermi energy
EISA	evaporation induced self-assembly
eqiv	equivalent
ESI	Electronic Supporting Information
et al.	and others, from lat. *et alia*
Et	Ethyl
DFT	density functional theory
Hb	haemoglobin
H_2BINOL	2,2′-Dihydroxy-1,1′-binaphthyl
HIB	hole injection barrier
HL	protonated ligand
HMBC	Heteronuclear Multiple Bond Correlation
HOES	highest occupied electronic state(s)
HOMO	highest occupied molecular orbital (=HOES of a single molecular orbital)
HSQC	Heteronuclear Single Quantum Coherence
in vivo	in a living organism, from lat.
IP	Ionization Potential
*i*Pr	*iso*-Propyl
IR	InfraRed
KIT	Korean Institute of Science and Technology
lat.	latin
Ln	Rare-earth metal (Sc, Y, La - Lu)
LUES	lowest unoccupied electronic state(s)
LUMO	lowest unoccupied molecular orbital (=LUES of a single molecular orbital)

M	Metal
MAS	Magic Angle Spinning
MCM	Mobil composition of matter
Me	Methyl
$M(NR_2)_x$	metal alkylamide
$M[N(SiR_3)_2]_x$	metal silylamide
$M(OR)_x$	metal alkoxide
MR_x	metal alkyl
m-TiO_2	mesoporous titanium dioxide
NHS	*N*-hydroxy succinimide
NMe_2	dimethyl amido
NMR	Nuclear Magnetic Resonance spectroscopy
n-SC	n-semiconductor
OAr	aryl oxide
OCH_2tBu	neopentanolato
O*n*Bu	*n*-Butoxy
O*t*Bu	*tert*-Butoxy
OEt	Ethoxy
pK_a	logarithmic value of Brønsted acid dissociation constant K_a
PEG	polyethylene glycol
PEO	polyethylene oxide
φ	workfunction, greek letter small Phi
PMS	periodic mesoporous silica
PPG	polypropylene glycol
PPO	polypropylene oxide
PXRD	Powder X-Ray Diffraction

SBA	Santa Barbara amorphous
SECO	Secondary Electron Cut-Off
$Si(OR)_x$	silyl alkoxide / alkoxy silane
solv	solvent
SOMC	surface organometallic chemistry
SS UV/vis	Solid State UV/vis spectroscopy
TEOS	tetraethyl orthosilicate
thf	tetrahydrofuran
TPD	Temperature Programmed Desorption
UPS	Ultraviolet Photoelectron Spectroscopy
UV	ultraviolet
$V_{P, des}$	pore volume (taken from the desorption branch of the physisorption curve in the BJH region)
via	by way/means of, through, from lat.
vide supra	see above, from lat.
VR	Valence region
XPS	X-ray Photoelectron Spectroscopy

Summary

Surface functionalized titanium dioxides (TiO_2) are among the most studied hybrid materials for photocatalytic reactions and their potential application in the field of biomedicine, *e.g.* for light-induced targeted drug delivery, was pointed out. Catechols are prominent organic dyes, which generate different surface species on TiO_2, dependent on the latter´s surface curvature and the surface loading.

In order to investigate the surface species, which has previously been detected, only on very small nanoparticles, heteroleptic Ti(IV) catecholate complexes were synthesized, aiming at a monomeric Ti(IV) catecholate complex, whose basic actor ligands would readily react with the surface hydroxyls of the substrate, and whose catecholato binding mode (chelating) is predefined and retained upon the grafting reaction.

In a first approach $Ti(NMe_2)_4$ was reacted with five differently substituted catechols, giving oxo-bridged dimers (except for $[Ti(CAT\textit{t}Bu\text{-}3,6)(NMe_2)_2]_2$, where one nitrogen atom was involved in the bridging, too). A ligand scrambling test with the largest and the smallest catecholate complexes indicated the presence of monomeric species in solution. Therefore, the sterically most demanding dimer $[Ti(DHN)(NMe_2)_2]_2$ was further investigated according to two grafting routes – the sequential approach gave the same dominant surface species as the convergent approach, but in both cases more than one species was present at the surface.

To prevent dimerization, the complexes with none and with the highest degree of catecholato-oxygen shielding by *tert*-butyl groups at the benzene ring – $[Ti(CAT)(NMe_2)_2]_2$ and $[Ti(CAT\textit{t}Bu\text{-}3,6)(NMe_2)_2]_2$ – were reacted with neopentanol to exchange the small amido groups with bulkier actor ligands. In both cases $HNMe_2$ stayed coordinated at the Ti(IV) centers to ensure an octahedral geometry. But only for the bulkier catecholato ligand a monomeric complex, $[Ti(CAT\textit{t}Bu\text{-}3,6)(OCH_2\textit{t}Bu)_2(HNMe_2)_2]$, was obtained. This was further used for the grafting onto KIT-6 for characterization of the surface species and onto m-TiO_2 for optical and electronic investigations. Only the convergent approach gave exclusively the desired bidentate chelating surface species $[Ti(CAT\textit{t}Bu\text{-}3,6)(OCH_2\textit{t}Bu)_2(HNMe_2)_2]$@[KIT-6], which was compared to an aqueous route species $H_2CAT\textit{t}Bu\text{-}3,6$@$Ti(OH)_x$@[KIT-6] on the same support. The energy levels of the hybrid m-TiO_2 from the aqueous route mirrored the well-known type-II excitation mechanism, which is accompanied by a slight increase of energy levels and a reduced bandgap, compared to virgin m-TiO_2. The novel hybrid-m-TiO_2 from the convergent approach displayed decreased energy levels compared to virgin m-TiO_2, and an even smaller bandgap than the aqueous approach material.

Zusammenfassung

Oberflächenfunktionalisierte Titanoxide (TiO_2) gehören zu den am besten untersuchten Hybridmaterialien für photokatalytische Reaktionen und auf ihre potenzielle Anwendung im Bereich der Biomedizin, z.B. für lichtinduzierte Medikamentenfreisetzung im Zielorgan, wurde hingewiesen. Catechole (1,2-Dihydroxybenzole) sind bekannte organische Sensibilatoren, wobei das Entstehen verschiedener Oberflächenspezies, in Abhängigkeit der Oberflächenkrümmung und -beladung des TiO_2-Trägers, betrachtet wird.

Um auch diejenige Oberflächenspezies auf einem Bulkmaterial untersuchen zu können, welche zuvor lediglich auf sehr kleinen Nanopartikeln gefunden wurde, wurden heteroleptische Ti(IV)-Catecholatkomplexe hergestellt, deren basische Co-Liganden gut mit den Oberflächenhydroxylgruppen des Substrats reagieren würden, und deren Bindungsmodus (chelatisierend) vordefiniert und nach der Graftingreaktion erhalten bleibt.

In einem ersten Ansatz wurde $Ti(NMe_2)_4$ mit fünf Catecholen unterschiedlichen sterischen Anspruchs umgesetzt. Hierbei ergaben sich oxo-verbrückte Dimere (abgesehen von $[Ti(CAT\textit{t}Bu\text{-}3,6)(NMe_2)_2]_2$, wo auch ein Stickstoffatom an der Verbrückung beteiligt ist). Ein Ligandenaustausch zwischen dem größten und dem kleinsten Catecholatkomplex deutete auf das Vorhandensein monomerer Spezies in Lösung hin. Deshalb wurde das sterisch anspruchsvollste Dimer $[Ti(DHN)(NMe_2)_2]_2$ gemäß zweier Graftingrouten untersucht, wobei der sequenzielle Ansatz dieselbe dominante Oberflächenspezies ergab wie der konvergente Ansatz, aber in beiden Fällen war mehr als nur eine Spezies auf der Oberfläche vorhanden.

Um einer Dimerisierung vorzubeugen, wurden die Komplexe mit keiner und mit der höchsten Abschirmung der Catecholatosauerstoffatome durch *tert*-Butylgruppen am Benzolring – $[Ti(CAT)(NMe_2)_2]_2$ and $[Ti(CAT\textit{t}Bu\text{-}3,6)(NMe_2)_2]_2$ – mit Neopentanol umgesetzt, um die kleinen Amidogruppen durch etwas größere Liganden auszutauschen. In beiden Fällen blieben $HNMe_2$- Moleküle an den Ti(IV)-Zentren in dem Ausmaß koordiniert, dass eine oktaedrische Geometrie entstand. Lediglich für den Catecholatkomplex mit der höchsten *tert*-Butylgruppenabschirmung der Catecholatosauerstoffe konnte ein monomerer Komplex $[Ti(CAT\textit{t}Bu\text{-}3,6)(OCH_2\textit{t}Bu)_2(HNMe_2)_2]$ erhalten werden. Dieser wurde für die Immobilisierung weiterverwendet, einerseits auf KIT-6 zur Charakterisierung, und andererseits auf TiO_2 zur Untersuchung der optischen und elektronischen Eigenschaften. Nur die konvergente Syntheseroute ergab ausschließlich die gewünschte, bidentat-chelatisierende Oberflächenspezies $[Ti(CAT\textit{t}Bu\text{-}3,6)(OCH_2\textit{t}Bu)_2(HNMe_2)_2]$@[KIT-6], welche mit der Spezies

aus der wässrigen Syntheseroute und identischem Trägermaterial H_2CAT*t*Bu-3,6@Ti(OH)$_x$@[KIT-6] verglichen wurde. Die Energieniveaus des m-TiO_2-Hybridmaterials aus der wässrigen Route spiegelten den bekannten Typ-II-Anregungsmechanismus wieder, was sich in der Anhebung der Energieniveaus und einer kleineren Bandlücke, im Vergleich zum reinen m-TiO_2, äußert. Das neue m-TiO_2-Hybridmaterial aus der konvergenten Route zeigte hingegen abgesenkte Energieniveaus im Vergleich zum reinen m-TiO_2, sowie eine noch etwas kleinere Bandlücke als das Hybridmaterial aus dem wässrigen Syntheseansatz.

Publications

Publications incorporated into this thesis

Paper I Titanium(IV) Catecholate-Grafted Mesoporous Silica KIT-6: Probing Sequential and Convergent Immobilization Approaches.
A. Sonström, D. Schneider, C. Maichle-Mössmer, R. Anwander
Eur. J. Inorg. Chem. ***2019,*** *2019 (5), 682-692.*

Paper II Titanium(IV) Surface Complexes Bearing Chelating Catecholato Ligands for Enhanced Band-Gap Reduction.
A. Sonström, B. Boldrini, D. Werner, C. Maichle-Mössmer, K. Rebner, M. B. Casu, R. Anwander.
Inorg. Chem. **2023,** *62* (2), 715-729.

Publications with collaboration partners

Paper III Intercorrelation of Electronic, Structural, and Morphological Properties in Nanorods of 2,3,9,10-Tetrafluoropentacene.
S.-A. Savu*, A. Sonström*, R. Bula, H. F. Bettinger, T. Chassé, M. B. Casu
ACS Appl. Mater. Interfaces **2015**, *7* (35), 19774-19780.

Paper IV Highly active Sm_2O_3-Ni xerogel catalysts for CO_2 methanation
J. Ilsemann*, A. Sonström*, T. M. Gesing, R. Anwander, M. Bäumer
ChemCatChem **2019,** *11* (6), 1732-1741.

*These authors contributed equally to the work.

Personal Contribution

Paper I: Titanium(IV) Catecholate-Grafted Mesoporous Silica KIT-6: Probing Sequential and Convergent Immobilization Approaches.

All reactions and analyses, which are described therein, were planned and conducted by myself, except for those, which are listed below. The writing of the publication was done by myself and revised by PD Dr. Cäcilia Maichle-Mössmer and Prof. Dr. Reiner Anwander.

Elemental Analyses were done by Wolfgang Bock (*EA*: C,H,N) and by "Mikroanalytisches Labor Pascher" in Remagen, Germany (*ICP-OES*: Ti). ^{13}C MAS NMR experiments were performed by Dr. Klaus Eichele and Kristina Heß. Single crystal X-ray diffraction experiments and structure solutions were performed by PD Dr. Cäcilia Maichle-Mössmer, Dr. David Schneider, Dr. Daniel Werner and Elke Niquet. The synthesis and characterization of the KIT-6 material **M1b** was done by Lena Merten during her work for her Bachelor thesis, which has been supervised by myself.

Paper II: Titanium(IV) Surface Complexes Bearing Chelating Catecholato Ligands for Enhanced Band-Gap Reduction.

All reactions and analyses, which are described therein, were planned and conducted by myself, except for those, which are listed below. The writing of the publication was done by myself and revised by:

First part on KIT-6: Dr. Daniel Werner, PD Dr. Cäcilia Maichle-Mössmer and Prof. Dr. Reiner Anwander

Second part on m-TiO_2: PD Dr. Maria Benedetta Casu and Prof. Dr. Reiner Anwander

Elemental Analyses were done by Wolfgang Bock (*EA*: C,H,N) and by "Mikroanalytisches Labor Pascher" in Remagen, Germany (*ICP-OES*: Ti). ^{13}C MAS NMR experiments were performed by Dr. Klaus Eichele and Kristina Heß. Single crystal X-ray diffraction experiments and structure solutions were performed by PD Dr. Cäcilia Maichle-Mössmer, Dr. Daniel Werner

and Dr. Regine Herbst-Irmer. Dr. Peter Grüninger supported me during the XPS and UPS measurements. Barbara Boldrini performed the Solid-state UV/vis measurements together with me.

Objective of the Thesis

The aim of the thesis was the investigation and elucidation of a bidentate chelating surface-catecholate complex at mesoporous titanium dioxide *via* the surface organometallic chemistry (*SOMC*) approach and its comparison with the surface species, which is obtained at mesoporous titanium dioxide *via* the established aqueous synthesis route.

Part A mentions possibilities to influence the bandgap of titania with focus on surface functionalization. Potential applications, perspectives, and drawbacks are outlined from recent literature with special emphasis on DFT calculations concerning different surface species when using catechols as organic dyes to tune the bandgap of titania materials. The sequential and convergent grafting strategies are described in detail in order to introduce the reader into the field of SOMC. Further, the advantages to utilize Periodic Mesoporous Silicas (*PMS*) for the characterization of obtained surface species, and the transfer of their syntheses towards porous titania are described.

Part B contains the summary of the main results from the papers I and II.

Part C contains the bibliography.

Part D contains copies of the papers I and II, including the respective electronic supporting information.

A

Introduction

1. Surface functionalization of titania

In nature, titanium oxides (*titanias*) occur within minerals like ilmenite ($FeTiO_3$), perovskite ($CaTiO_3$) or titanite ($CaTiO[SiO_4]$), but most abundantly as titanium(IV) dioxide.[1] There are four prominent modifications of titanium (IV) dioxide, which are displayed in Figure 1: a) rutile, b) anatase, c) brookite and d) riesite.[2] Anatase is very stable under ambient conditions,[3] but transforms – like brookite – into rutile at high temperatures, before reaching a melting point.[1] The melting point of rutile is ~1843 °C.[1] As brookite is quite rare[1] and has not been straightforward to synthesize, it is of little industrial importance until today.[3-4] Riesite was discovered only in the year 2015 and has been presented in a recent publication as high-pressure polymorph of TiO_2.[2]

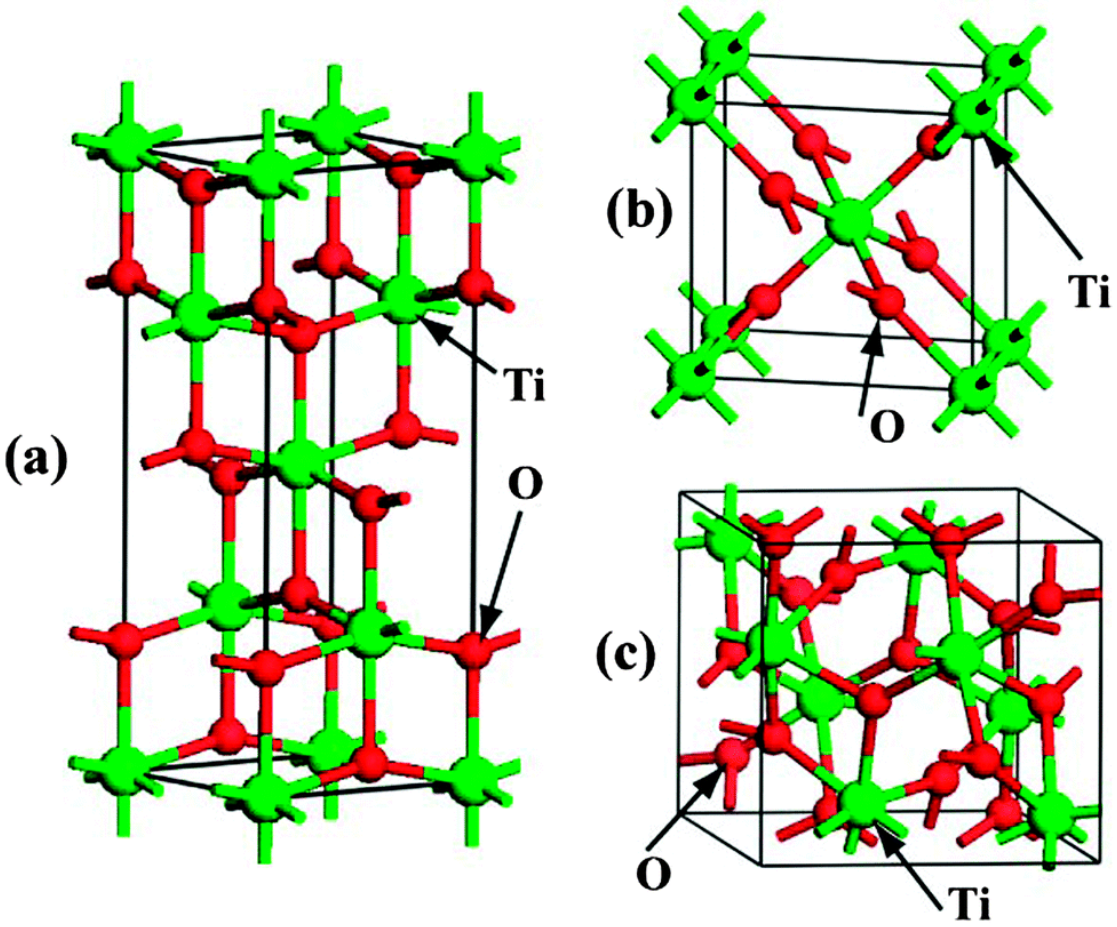

Figure 1: Structures of (a) anatase, (b) rutile and (c) brookite. Titanium atoms are represented by green spheres, and oxygen atoms are represented by red spheres. (Extracted from Fig.1 by *Zhang et al.*)[5]

Anatase, rutile and mixtures of the two can be found in several products of our everyday life, such as paint, plastics, powders, sun-blocking lotions and as coverage of sweets, salami and drugs.[1] Most applications of titania are based on its strong absorption of UV radiation, which originates from the quite huge bandgap: 3.0 eV for rutile and 3.2 eV for anatase.[5] Rutile, therefore has the higher UV absorption capacity and is often used within the applications, mentioned above, to serve as degradation protectant.[3] Anatase on the other hand, has the higher photocatalytic activity compared to rutile,[5] and is therefore of special interest for further applications, such as photocatalytic water splitting[4] or solar cells,[6] sensing,[7-10] and – due to its biocompatibility – also in biomedicine.[11-16] In these fields a fine-tuning of the chemical and (opto-) electronic properties of the TiO_2 is often required. Therefore, influencing the bandgap of titania has been of interest within the scientific community for many years – and quite a few methods have been found, depending on the individual goals of the researchers. Prominent examples are doping,[3] mixed metal oxide syntheses[9] and surface functionalization.[16]

As TiO_2 forms coordinative bonds with amino and carboxyl groups of biomolecules,[17] enzyme-functionalized titania surfaces can be used to modulate certain processes within the human cells: The advantage of immobilized over native enzymes is their reusability as catalysts and the non-contamination of the surrounding biological tissue by potentially wandering soluble enzymes.[18] But not only "pollution" of the tissue is to be avoided – undesired side reactions can become an even greater problem: Immobilized enzymes or other ligands, which can be used for light-induced targeted drug-delivery itself or by carrying a releasable drug on their backbone, often tend to experience ligand-leaching within *in vivo experiments*, which can lead to apoptosis.[11-12, 14] Cell death can be desired in the case of fighting cancer cells, but usually the drug shall only distort the metabolism of the cancer cells and shall not react with healthy cells. Therefore, the apoptosis, which is meant here, is not caused by the released drug, but by leaching of the full ligand-backbone. This is known to happen due to a surface ligand-exchange reaction with another enzyme/protein or biomolecule within the cells, which has a higher affinity towards the titania surface, or due to the reaction of the dye itself with cell proteins.[15] Both can severely interfere with the metabolism of healthy cells and originate from weak ligand-to-substrate interactions.[15]

Creating a ligand backbone with stable bonding towards the titania surface therefore appears to be an interesting target. The ligand backbone needs to fulfill prerequisites, such as covalent immobilization, the ability to be functionalized with enzymes or drugs and interaction with

Scheme 1: Illustration of the subsequent immobilization of 3,4-dihydroxyl benzoic acid (DB) and haemoglobin (Hb) at Degussa P25 TiO_2 nanoparticles and the light-induced release of the surface species. 1-Ethyl-3-(-3-dimethylaminopropyl) carbodiimide hydrochloride (*EDC*) forms an ester with *N*-hydroxy succinimide (*NHS*), which builds a conjugate with Hb. (According to Fig.1 by *Luo et al.*)[16]

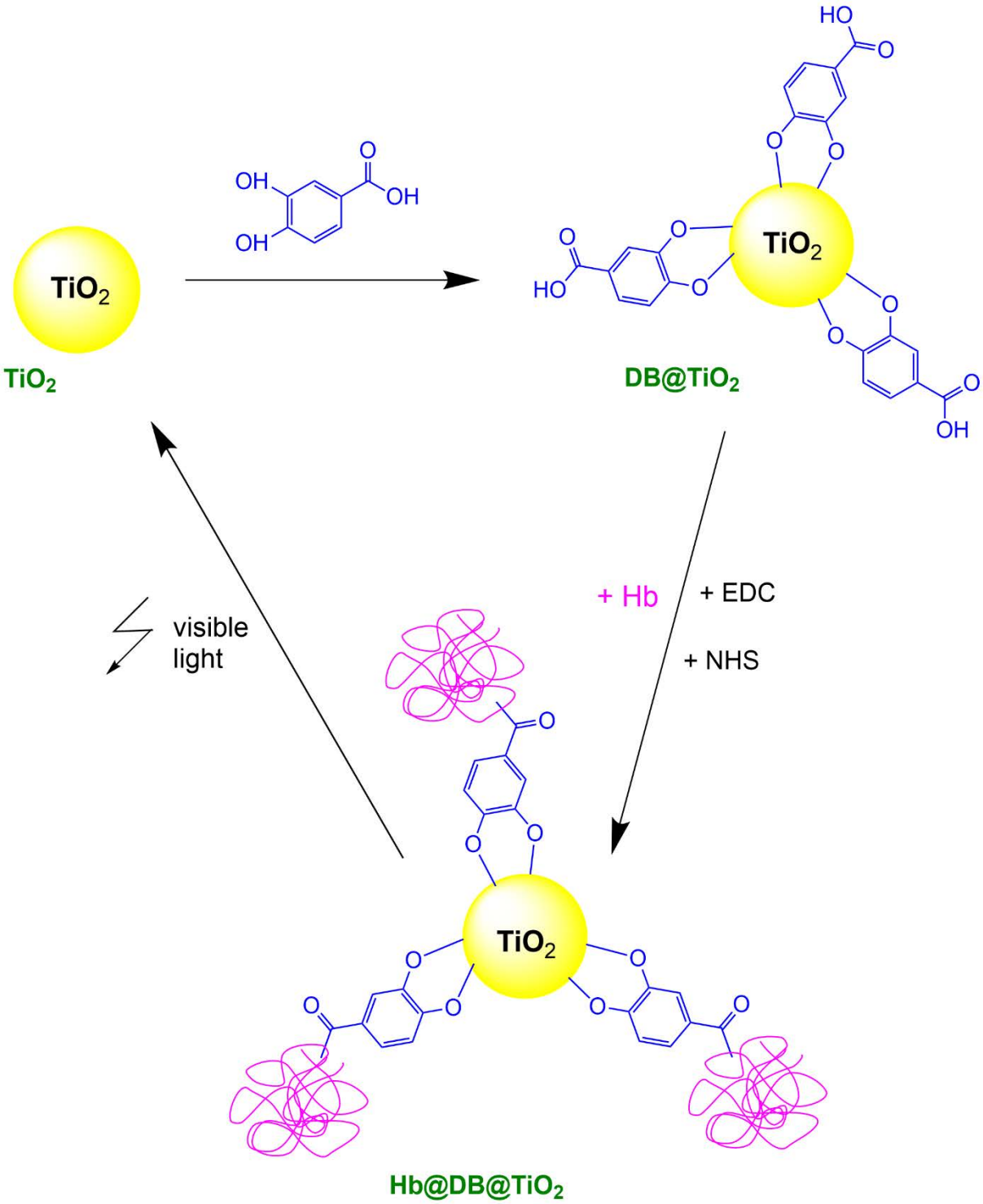

the bandgap of TiO_2 to enable light-induced reactions or release of the attached drugs or enzymes. *Luo et al.* discussed materials, which were synthesized for this kind of applications and pointed out that the high energy of the UV radiation, which was necessary to induce the release of the biomolecules, can also destroy them.[16] Therefore, they immobilized 3,4-dihydroxyl benzoic acid, which served as carrier backbone for the biomolecule to be released, at the surface of TiO_2 nanoparticles, which is shown in Scheme 1. The 3,4-dihydroxyl benzoic acid itself is known as organic dye to reduce the photoexcitation energy of the system due to its catecholate binding mode towards the titania surface.

2. Catecholates at titania surfaces

Catechols (vicinal acenediolates) are known as efficient complexation agents for free metal ions[19] as well as for oxide surfaces, whereas catecholato complexes with TiO_2 surfaces actually are the hot-spot of numerous investigations for optical and electronic applications,[20] (see references 21-23, 25, 26, 28, 42, 52, 69, 78, 84, 160-163 within ref. 20).

A significant red shift of the optical absorption is observed after surface modification of TiO_2 nanoparticles (compared to the bare titania nanoparticles), what is ascribed to the diminished band gap due to surface charge-transfer complex formation by *Dugandzic et al.*[21] The HOMO (S_0) of the catechol is located within the bandgap of TiO_2. Therefore, the excitation of electrons from there by light energy (hν) leads to a charge transfer into the conduction band of titania, as displayed in Scheme 2:[22]

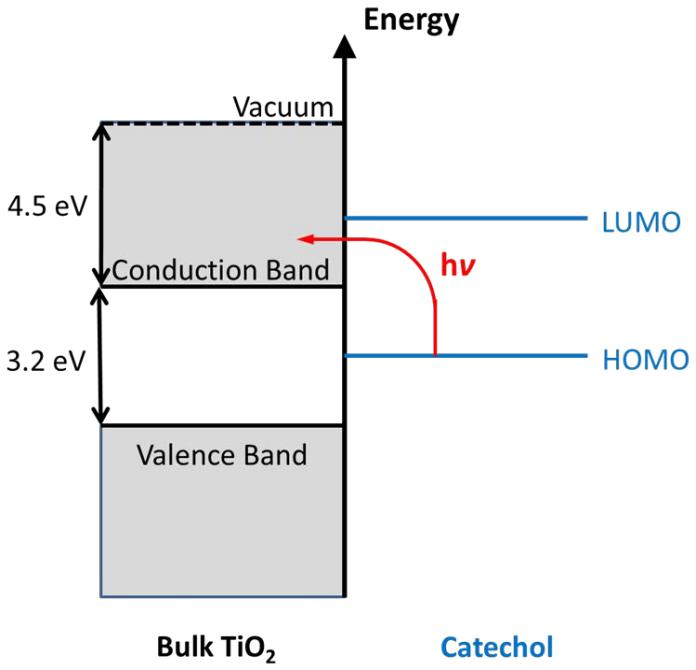

Scheme 2: Energy diagram of the catechol-TiO_2 interface.(According to Fig.1 by *Duncan and Prezhdo*)[22].

DFT calculations of respective molecular complexes suggest an energy decrease of the corresponding HOMO-LUMO transition (and thus, of the band gap) for the surface complexes as well as for the molecular metal-catecholate complexes:[20] The influence of the metal ion on the catecholato ligands was found to be negligible, because the complexation results in neutral species with much smaller charging effects (in contrast to deprotonation) to the catechol

orbitals. The HOMO is described to be mainly located at the organic ligand and the LUMO is mentioned to belong to the conduction band of titania (n-SC), which is lower in energy than the LUMO of the organic ligand itself, what explains the origin of the charge-transfer formation.

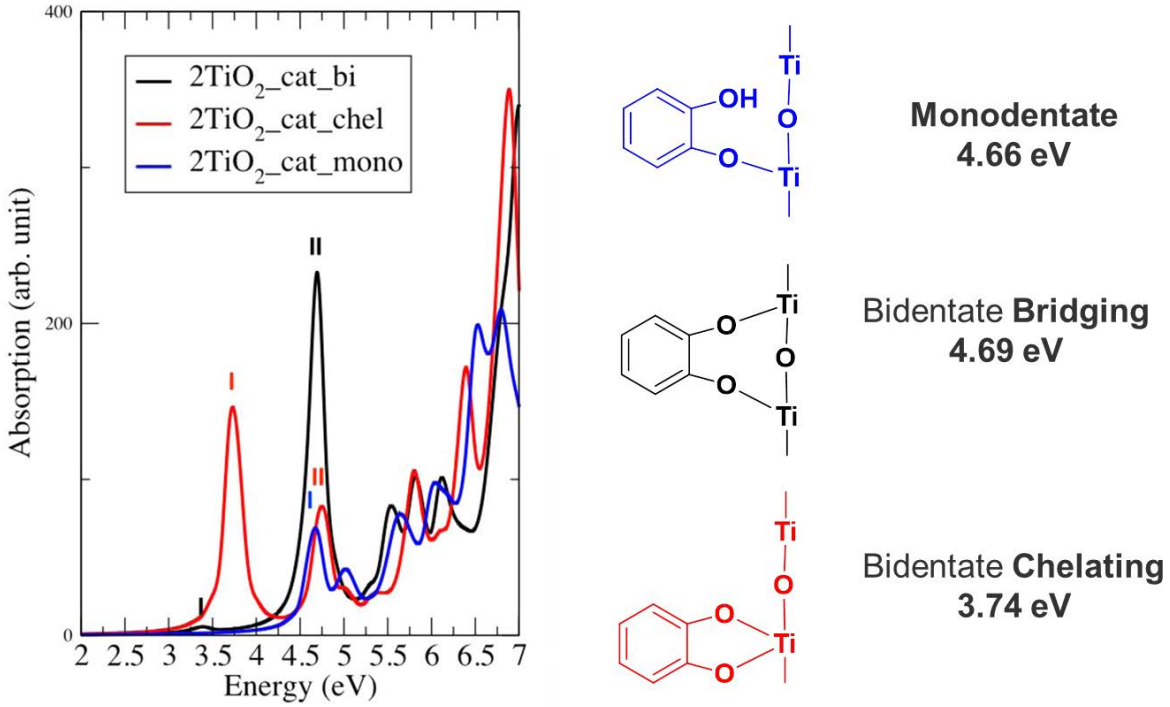

Figure 2: Optical absorption spectra of the three different surface species, shown on the right together with their respective excitation energy. (Leftside spectra according to Fig.4 by *Luppi et al*)[23].

This charge-transfer formation has also been observed by *Luo et al*, due to immobilization of 3,4-dihydroxyl benzoic acid (a catechol with carboxyl group) on titania nanoparticles, mentioned in the previous section. They obtained the so-called bidentate bridging surface structure – one of three binding modes for catechols on titania surfaces, which are shown in Figure 2. Bidentate bridging (black structure in Figure 2) means, that one catecholate molecule is bound to two surface titanium atoms *via* its two oxygen atoms. The other two binding modes are called bidentate chelating (red structure in Figure 2) and monodentate (blue structure in Figure 2). For the latter two one catechol molecule is bound to only one surface titanium atom respectively, whereas both catechol-oxygen atoms are bound to titanium in the chelating case, but only one catechol-oxygen atom in the monodentate case.[23] *Luppi et al* performed time-dependent DFT calculations to predict absorption spectra for these three surface species:[23]

Though they claim the bidentate bridging mode to be the most stable one, their calculated spectra for the bidentate chelating surface structure exhibit lower energy bands than those for the bidentate bridging and the monodentate structures, (Figure 2).

Coming from calculations to reality, the type of catecholate binding mode at titania surfaces was found to be dependent on the particle size and on the surface loading, as illustrated in Figure 3: The surface-Ti atoms of very small titania nanoparticles (< 4.5 nm) are quite "exposed" due to the huge surface curvature of such small particles. Therefore, they only exhibit a coordination number of five (square pyramidal geometry), which is energetically less stable than a coordination number of six (octahedral geometry), prevailing within bigger particles or bulk TiO_2.[24-25] Thus, it does not seem surprising, that the bidentate chelating binding mode is found at small titania nanoparticles (< 4.5 nm), as chelating ligands, like catecholates, are known to stabilize metal centers with unsaturated geometry.[19, 23-26] This originates from coordination chemistry: The stability of a metal complex depends on thermodynamic factors (such as size and oxidation state of the metal center, as well as size, polarizability and amount of the ligands) and kinetic factors (such as spatial and electronic shielding of the metal cation by its ligands). Whether a ligand coordination or a ligand exchange reaction on a metal center is energetically possible at all can be estimated by means of thermodynamics, whereas the rate and the final probability of the reaction is determined by kinetics. A simple rationalization of kinetic and energetic factors is given in the following: If the metal center is assumed to be a basketball, which is thrown in the direction of the two-armed person A and the one-armed person B (who are both considered to be ligands, bidentate and monodentate, respectively), standing next to each other, the following appears logical: It will become difficult for person B to catch the ball with only one arm (energetically disadvantaged). This can become easier when person A is helping with one of his arms, but depends on the probability of nearly simultaneous, precise actions of both persons (kinetically disadvantaged). The energetically and kinetically most stable situation is achieved by person A when using both of his arms to catch the basketball. This effect is known as chelate effect of metal complexes with multidentate ligands (ligands with more than one arm) like catechol.

For titania materials with less surface curvature the bidentate bridging binding mode of catecholates was found at lower surface coverage, whereas the monodentate one is dominant at higher surface loading.[23-26]

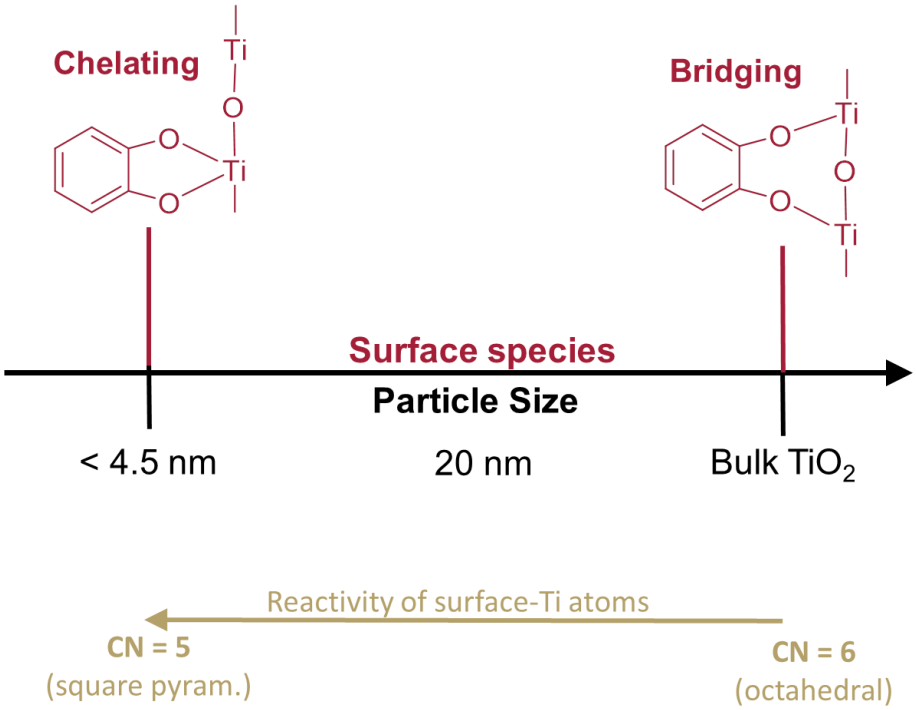

Figure 3: Illustration of factors to be considered for obtaining chelating or bridging surface species.

The synthesis of the bidentate chelating surface species on a bulk material, providing the possibility to study its influence on the bandgap of titania (on the same type of support material, which would usually carry the bidentate bridging or the monodentate surface species) would deliver a crucial missing piece in the investigation of these complexes. The obtained experimental data would enable a real comparison of the different surface species concerning their electronic influence on titania and might open the pathway to novel stable enediol species to be tuned for biomedical applications.

Regarding the challenge to create a bidentate chelating catecholate species on a bulk TiO_2, where the surface-titanium atoms already have a coordination number of six, the common aqueous synthesis routes needed to be replaced by strategies, which allow a more concise control of the desired ligand binding mode.

3. Sequential and convergent grafting strategies

One of the most prominent tools for post-synthesis functionalization of oxides (like titania and silica) is known as surface organometallic chemistry (SOMC) approach.[27-31] It often consists of two synthesis steps (if the desired surface species has not already been obtained within the first step), which can be varied in their order:

1) *Sequential approach*[29] – primary grafting of a reactive, homoleptic organometallic complex onto an oxidic material may be followed by a secondary ligand exchange.[32]
2) *Convergent approach* – a reactive, heteroleptic organometallic complex is synthesized and grafted onto the oxide surface of choice afterwards.

Scheme 3: Illustration of the sequential and convergent grafting strategies.

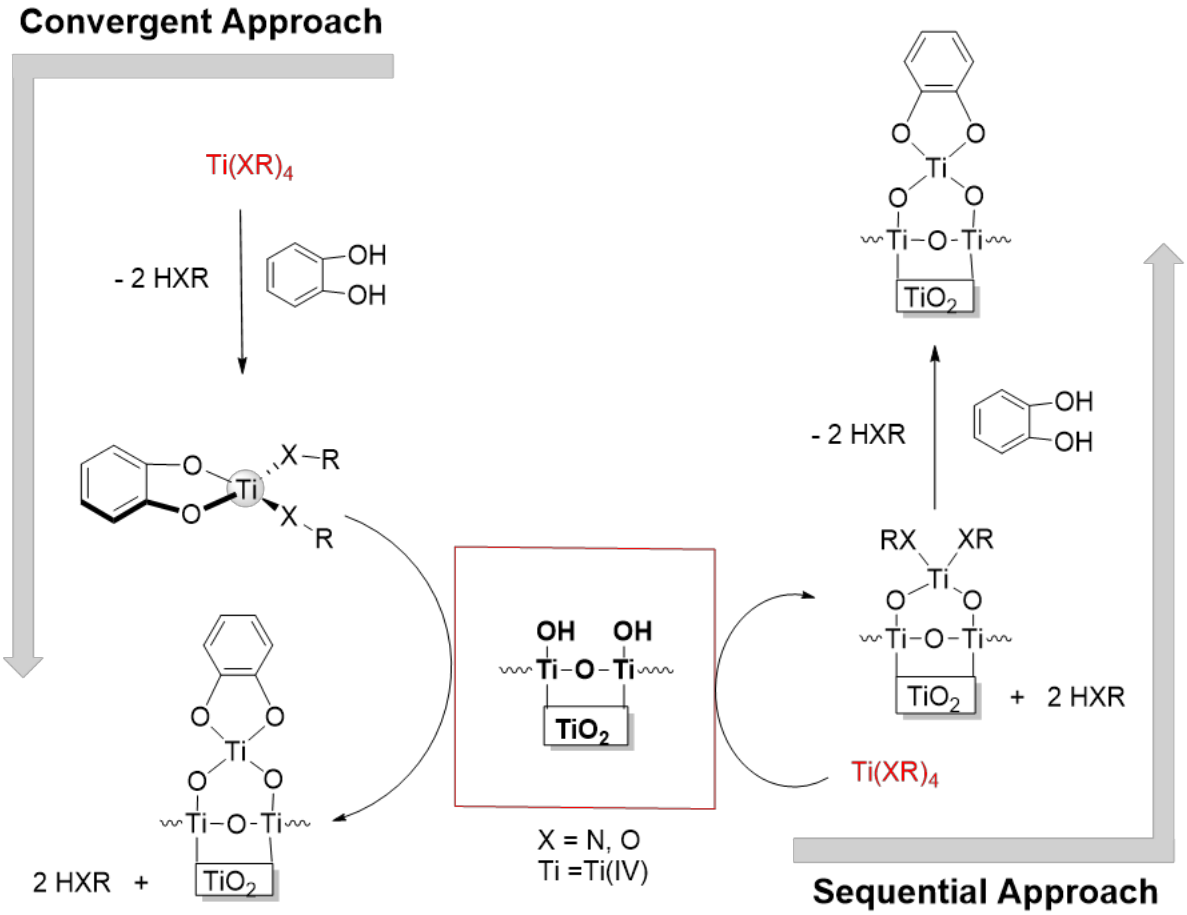

Depending on the desired final product, the one or the other strategy is to be favored. In heterogeneous catalysis the need for more than one surface species is imaginable, as subsequent catalysis steps could be conducted at the same support. To create a surface functionalized material of that type the sequential approach offers the possibility of subsequent or simultaneous ligand exchanges with multiple ligands.[27]

On the other hand, the convergent approach seems more convenient for the generation of surface species with complex geometries, as the organometallic precursor can be tailor-made in advance and grafted onto the oxidic substrate under preservation of its geometric constraints afterwards.[29, 31, 33]

Transferring this principle, displayed in Scheme 3, towards the synthesis of a bidentate chelating catecholate species on bulk TiO_2, a titanium precursor complex with ligands, which are reactive towards the catechol and towards the Ti–OH groups of the titania substrate, is required. Surface hydroxyls of titania have a pK_a of 7.8[34] and are therefore even more acidic than the phenolic OH groups of catechol (pK_{a1}(catechol) = 9.2 and pK_{a2}(catechol) = 13.0).[35]

Therefore, a titanium precursor complex with more basic ligands needs to be considered. Titanium alkoxides appear to be an option at first sight, as some alcohols are comparatively basic (e.g. pK_a(*t*BuOH) = 18),[36] but in general the pK_a of alcohols can vary between 5 and 20.[27]

Scheme 4: Overview on the basicity of metal-bonded ligands – expressed by the pK_a value of the protonated ligands (According to Scheme 2 by *R. Anwander 2001*).[27]

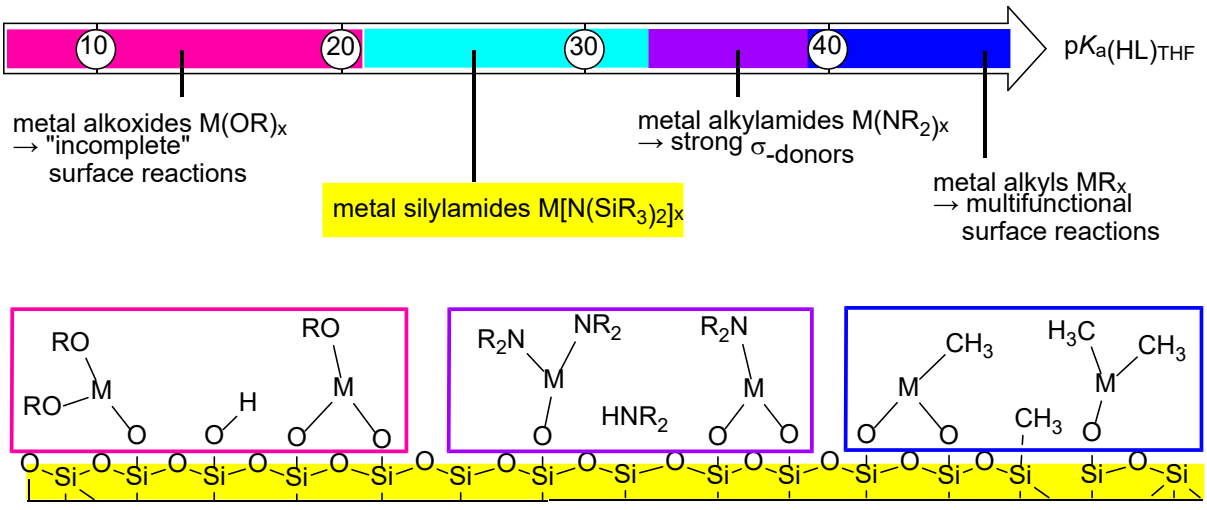

The homoleptic titanium alkoxide complexes moreover could contain some more challenges: Some of them are already dimers or even oligomers in solution (e.g. Ti(O*n*Bu)$_4$ and Ti(OEt)$_4$),[37]whereas monomeric precursors are favored to create a monomeric heteroleptic titanium-catecholate complex for the convergent approach displayed in Scheme 3. Ti(O*i*Pr)$_4$, which is monomeric,[37] has been utilized within grafting reactions on MCM-48 (*note:* this material is defined in the next subchapter "Periodic Mesoporous Silica") as an example, which resulted in good yields of bipodally anchored surface species, but was accompanied by a huge amount of surface-coordinated isopropanol, which was released upon protonolysis reactions of the Ti(O*i*Pr)$_4$ with the support hydroxyls.[38] Alcohols tend to interact with other substrate hydroxyls and therefore block potential grafting sites for other precursor complexes. The consequence is incomplete surface functionalization with the precursor and alcohol residues on the surface.[27, 38]

Regarding the molecular chemistry of Ti(O*i*Pr)$_4$, subsequent addition of equimolar amounts of (*S*)-2,2′-dihydroxy-1,1′-binaphthyl ((*S*)-H$_2$BINOL) and catechol (H$_2$CAT) gave the corresponding heteroleptic titanium(IV) complex bearing both ligands, which implies for a comparable reactivity of the proligands.[39] Notably, with (*R*)-H$_2$BINOL a heteroleptic amido titanium(IV) complex was obtained by using Ti(NMe$_2$)$_4$ as a precursor, and successful grafting reactions were performed on the silica material MCM-41 by applying the sequential approach described above (see: Scheme 3).[40] Silica surface hydroxyls have a pK_a of ~7.1,[41] which is close to the pK_a of Ti–OH at titania surfaces, and metal-alkyl amides are even far more basic than metal alkoxides.[27] These are generally good prerequisites for the transfer of the corresponding reactions from H$_2$BINOL to catechol.

Especially Ti(NMe$_2$)$_4$ appears as a suitable precursor, because gaseous dimethylamine (HNMe$_2$) is released upon protonolysis reactions, as shown in equation 1:

$$Ti(NMe_2)_4 + Ar(OH) \longrightarrow (ArO)Ti(NMe_2)_3 + HNMe_2\uparrow \quad (Ar = aryl) \qquad (eq.1)$$

Further on, using porous silica supports for the exploration of the surface chemistry of the titanium(IV) complexes appears to be a favorable option – especially regarding the characterization of the resulting surface species: As an example, surface titanium content determination *via* elemental analysis (*EA*) on a bulk TiO$_2$ seems little promising compared to the determination on a bulk SiO$_2$.

4. Periodic mesoporous silica

Periodic mesoporous silicas (*PMSs*) have become of great scientific interest during the past 20 years. These special silicas with ordered pore architecture, tunable pore size and high surface area offer the opportunity to obtain newly-synthesized hybrid materials or to use the pores as a nanoreactor for the preparation of heterogeneous catalysts.[27]

Porous materials can be classified into three categories, microporous materials (pore size is smaller than 2 nm), mesoporous materials (pore size ranges from 2 to 50 nm) and macroporous materials (pore size is larger than 50 nm). For PMSs, two well-known examples are MCM-41 and MCM-48. MCM-41 has a one-dimensional hexagonal mesopore structure with

P6mm symmetry, and MCM-48 has a three-dimensional cubic mesopore structure with *Ia-3d* symmetry, as illustrated in Figure 4. Both materials show a channel-like pore configuration and pore walls composed of amorphous silica. In general, MCM-41 and MCM-48 were synthesized using long chain alkylammonium salts as surfactants and tetraethyl orthosilicate (TEOS) as silicon source under basic conditions. In this case, the obtained MCM-41 and MCM-48 materials do not possess any micropore structure.[27]

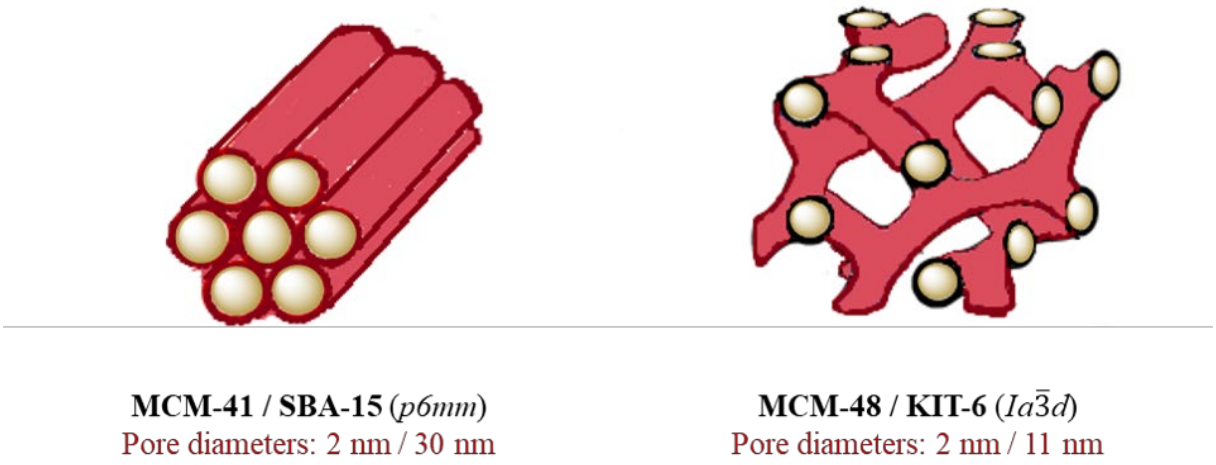

Figure 4: Topologies of MCM-41 and MCM-48, as well as their large-pore types SBA-15 and KIT-6. (From Fig.3 by *Liang and Anwander*)[32]

Original MCM-41 materials normally exhibit pore diameters of less than 4 nm,[42] which greatly restricts their applications, such as the separation of biomacromolecules and transport of bulkier

reaction substrates to the catalytic sites within the pores to perform heterogeneous catalytic reactions.

Amphiphilic block copolymers were first used as templates or surfactants for the fabrication of MCM-41-like materials under acidic conditions.[43-44] This development greatly enhanced the pore size of the obtained MCM-41-like materials up to 12 nm[42] called SBA-15.[44] Incorporation of hydrophobic molecules such as hexane into the micelles built by the block copolymers enabled an expansion of the pore size of the synthesized SBA-15 materials up to 17 nm, whereas such materials were abbreviated as SBA-15LP (LP = large pores).[42, 45] In addition, the supplementary use of hydrotropic molecules such as *n*-butanol can effectively expand the micelles that were built by the block copolymers. By using such micelles as a template and TEOS as silicon precursor under acidic conditions, the pore-size controlled MCM-48-like mesoporous materials can be obtained, which show high thermal and hydrothermal stability due to increasing thickness of pore walls compared to previously reported MCM-48 materials with pore diameters of less than 4 nm and thin pore walls.[46] These large-pore MCM-48-like materials were called KIT-6. Both SBA-15 and KIT-6 contained micropores[27] whose walls connect the mesopore channels and stabilize their structures.[46 47]

Within the sol-gel process in general, the precursor(s) and relative reactants are dissolved in a solvent respectively to form a clear solution. These solutions are mixed and stirred well, whereupon colloidal particles in solution form, which is called “sol”. Due to further hydrolysis of the precursor and condensation of the hydrolyzed species within the sol, gelation starts. Consequently, a solid network develops, whose pores are filled with liquid and/or micelles and/or surfactant templates. After an ageing process of a specific time, some sol-particles still remain distributed within the liquid, and some attach to the present gel-matrix to form a stable structure. During the ageing process, rearrangements within the gel-matrix are occurring. Finally, a solid product is collected by removing solvent and possible side products as well as reactant residues. These processes are finished either *via* several solvent exchanges, off-pipetting of the solvent residues after the last exchange, ambient or supercritical drying and subsequent calcination (monolithic materials)[48] or by filtration, ambient drying and successive calcination (powdery materials). [49 50 51]

To gain porous silica materials through the sol-gel route, alkoxysilanes ($Si(OR)_4$) such as tetraethoxy silane (or tetraethyl orthosilicate (TEOS); $Si(OEt)_4$) are mostly used as silica

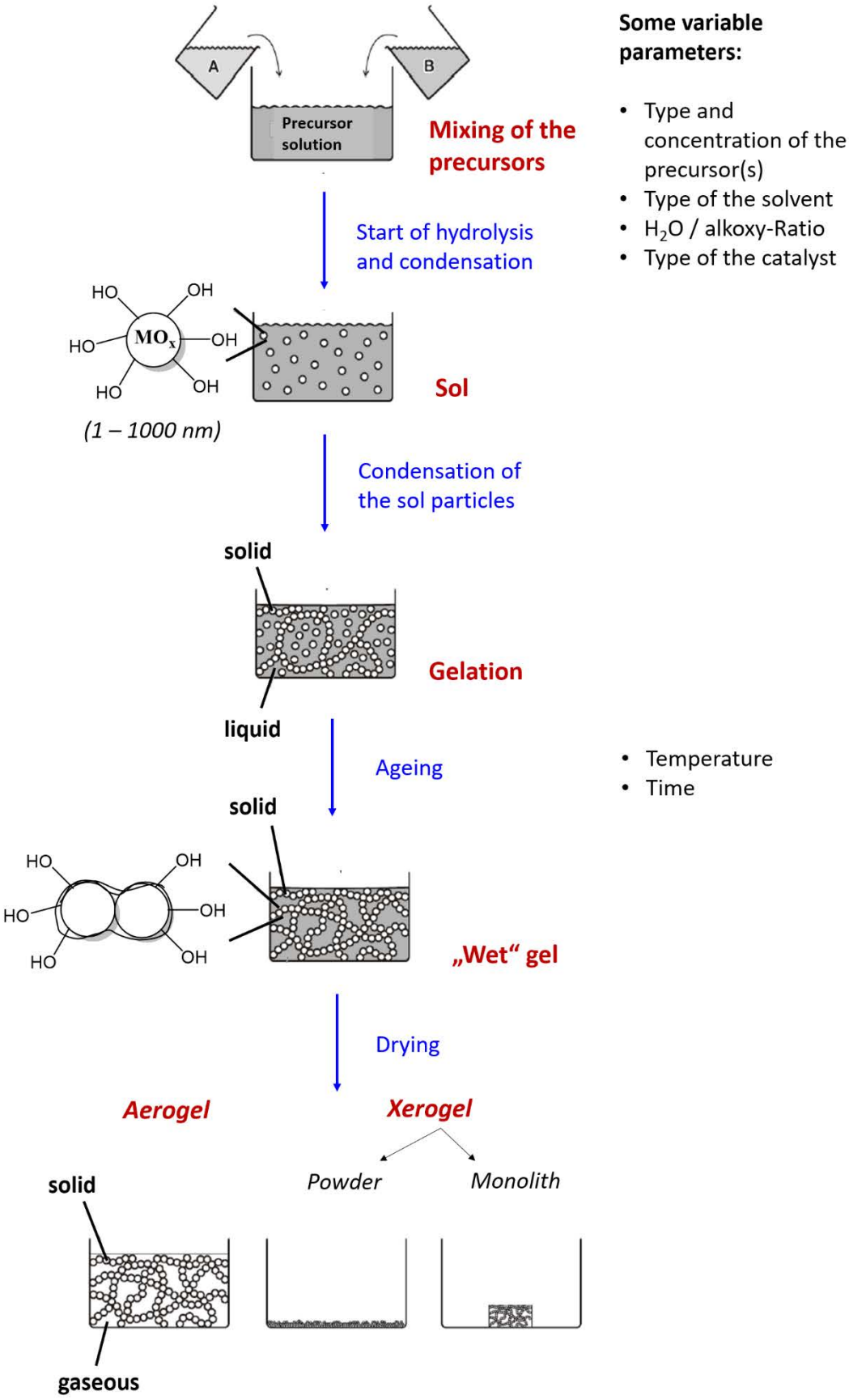

Figure 5: The sol-gel process. (According to Fig.4, p.27 by *Hüsing and Schubert*) [51]

precursors nowadays. The fabrication process, including hydrolysis of TEOS and further condensation of the hydrolyzed silicon species, in aqueous solution is shown in Figure 5. [51]

Alkoxysilanes ($Si(OR)_4$) are the least reactive alkoxy species (compared to several metal alkoxides) in hydrolysis reaction, so that a(n acidic or a basic) catalyst is needed. As the hydrolysis and condensation reactions of tetraalkoxy silanes are most dependent on the pH-value, the choice between a basic or an acidic catalyst has to be taken carefully.[51]

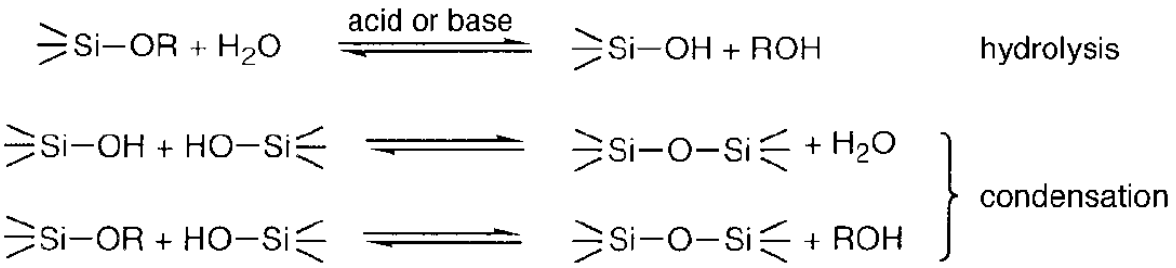

Figure 6: Gelation- process reactions. (According to Scheme 1, p.28 by *Hüsing and Schubert*) [51]

Under basic conditions, particle-like materials with comparatively large pores are achieved, as condensation is faster than hydrolysis (Eden-growth), but this growth is spoiled by Si-OR-groups, which hinder an even condensation cluster.[51] This may be a disadvantageous precondition when intending materials with ordered pore structure.

Under acidic conditions, hydrolysis is faster than condensation and hence polymer-like materials with smaller pores are obtained. Furthermore, diffusion processes are impaired by small pores (so that it is difficult to evaporate solvents and other reaction residues after the synthesis),[51] as well as collapsing or at least severe shrinkage of the gel network during drying or/and calcination (due to large capillary forces) is quite probable.[50] *Hench and West* recommended that the addition of surfactants might control the drying process by decreasing the liquid surface energy and thus might avoid the shrinkage or collapse of the gel network of these materials.[50] *Kresge et al.* further proposed the application of surfactant liquid crystal structures as organic templates for the developing silica gel,[52] whose pore-structure determining influence could be proven by *Beck et al*.[53] Both also suggested, that quaternary ammonium salt surfactants with increasing alkyl chain length as well as auxiliary organic molecules (the latter solubilized inside surfactant micelles) cause an increase in micelle size and thus in the pore

diameter of the resulting mesoporous silica materials.[51 53] This solved the problem of earlier synthesized silica materials which only had relatively small pores, which normally arose from sol gel syntheses under acidic conditions in the past. But *Beck et al.* also found that the increased pore diameter is accompanied by an increasing network instability in the case of ammonium salt surfactants with long alkyl chains, as the pore wall thickness decreases proportionally to the increase of pore diameter with the chain length.[53] Consequently, the addition of auxiliary organic molecules to the prevailing surfactant micelles seems to be the best way to obtain larger pores and a comparably stable silica network.

There are many cationic (e.g. ammonium salts), neutral (e.g. alkyl amides) and anionic (e.g. sodium sulfate alkyls) surfactants, which build isolated micelles, such as in the cases mentioned before. Undesirably, their application frequently leads to isolated particles,[53] which have to stick together to form a gel network during the ageing process. This results in the formation of disordered or amorphous networks in numerous cases.[42] Amphiphilic triblock-copolymers such as Pluronic P123 (PEG_{20}-$PPG_{70}PEG_{20}$; PEG = polyethylene glycol; PPG = polypropylene glycol) have shown, in contrast to the above mentioned surfactants, to be able to further stabilize the pore architecture by templating micropores[42] and thick pore walls.[46]

Accordingly, TEOS will be used as silica precursor and Pluronic P123 as templating surfactant for the preparation of periodic mesoporous silica for the exploration of the surface organotitanium chemistry.[46] A related synthesis approach will be transferred to the final porous titania support to be utilized for the investigation of the optical and electronic influence of the titanium(IV) surface complexes on the titania material.

5. Mesoporous titania

The development of suitable titania supports for (photo-)catalytic and biomedical applications struggles with very similar challenges as known from silica supports for immobilized molecular catalysts: Conventional titanium(IV) oxides display very low specific surface areas (< 10 m^2 g^{-1}), which give low surface loadings with catalytically active species and therefore low conversion efficiency.[54] The catalytic performance was found to be dependent on porosity, domain crystallinity and the size of the particles, pores and crystallites, as these parameters determine the surface area, accessibility of active sites and influence the semiconductor properties of TiO_2.[55-56]

Porous materials exhibit higher surface areas than non-porous analogues, but disordered pore architectures may hamper diffusion of reactants and products by blockage of smaller pores, or by the formation of different (potentially bulkier) surface species, which can be built in dependence of the surface curvature of the support material (see *e.g.*: catecholate binding modes on titania surfaces in chapter 2).

Therefore, inspired by MCM-41 syntheses, *Antonelli and Ying* reported on the synthesis of the first mesoporous TiO_2 (*m-TiO₂*) material with ordered (hexagonal) pore structure:[57] Whereas the pore structure is preserved upon calcination in air at 350 °C for 4 hours, the tetradecylphosphate, which serves as micelle-forming surfactant, is not completely removable at that temperature. The average pore size of 3.5 nm is smaller than for MCM-41 (5 nm)[42] and even smaller than for MCM-48 (4 nm)[46] materials.

Since then, the pore size of mesoporous titanias could be increased by using either hard templating methods (*e.g.* SBA-15 nanocasts) or by the application of swelling agents (like *n*-butanol) in soft templating methods[58] as known from PMS materials in the previous chapter, but the network of the m-TiO_2 materials easily collapses upon heating at high temperatures. The post-synthesis high-temperature treatment (between 400 and 800 °C, depending on the desired modification of TiO_2) is of great importance from two perspectives: The surfactant residues from the synthesis are removed and crystalline frameworks (anatase or rutile) can be obtained, as crystalline phases display less surface defects and better photocatalytic performance than amorphous materials.[58] The rising crystallinity with increasing calcination temperature is unfortunately accompanied by smaller pores compared to amorphous m-TiO_2.[58-59]

To obtain thermally more stable titanias with ordered pore structure, several post-synthesis treatments were discussed: functionalization with silica,[60] Ti(IV)-chelation[61-63] and supplementary charge introduction onto the micelle surfaces.[62-64] The study of *Tian et al*[64] demonstrated, that phase stability could be achieved for ammonia treated samples over a range of 300 K: anatase to rutile conversion occurred already at 600 °C for untreated titanias, whereas it was shifted to 900 °C for titania samples with ammonia treatment before calcination.

Most of the approaches to obtain ordered m-TiO_2 materials, mentioned herein so far, utilized surfactants with long alkyl chains and ionic head groups (like *e.g.* ammonium halides or sodium phosphates). What finally led to stable large-pore PMS materials was also transferred onto the synthesis of ordered mesoporous metal oxides like ordered m-TiO_2: *Yang et al.* propose a general mechanism, where

1) complexation of hydrolyzed metal centers by hydrophilic chains (like polyethylene glycol (*PEG*)) of block copolymers (like Pluronic P123 (PEG_{20}-$PPG_{70}PEG_{20}$, whereby PPG = polypropylene glycol) *via* weak coordinative interactions and
2) the self-assembly of the block copolymers into micelles
3) are followed by densification of the respective metal oxide network, due to progressive hydrolysis and condensation of the precursor molecules along the surfactant chains.[65]

Transition metals like titanium are more electrophilic than silicon and can have several stable coordination states, which is why they are more easily affected by nucleophilic reactions (hydrolysis, oxo-bridging, alcohol abstraction, *etc.*).[66] Therefore, compared to silica precursors, the hydrolysis and condensation rates of metal oxide precursors like alkoxides are very fast.[67] Especially in aqueous solution (as water is also a nucleophile), this mostly results in the rapid formation of particle-like colloids, which are prone to precipitation.[65] Whether precipitation or gelation occurs, depends on processing factors (pH-gradients, mixing speed, temperature, *etc.*) and on condensation kinetics: When dimerization is slow (if needed, it can be sped up by base addition), gelation occurs. When dimerization is fast instead, precipitation occurs.[66] Thus, the kinetics of condensation determines the original structure and alignment of the amorphous metal oxide.[67] It was found, that in non-aqueous media, the primary processes are ligand-exchange reactions followed by condensation reactions, which are very slow.[68] To have neither

too fast nor too slow reactions, utilizing catalytic amounts of acid in water, seemed promising: The *Blin*-group[59] combined the Liquid-Templating EISA approach with P123[65] (and catalytic amounts of $HCl_{(aq)}$) with the post-synthesis ammonia treatment[64] and obtained stable mesoporous anatase with hexagonally ordered pores of 6.4 nm in size (for calcination at 450 °C or 550 °C).

B

Summary of the Main Results

1. Mesoporous titania and silica

For the exploration of the surface organotitanium chemistry of the Ti(IV) catecholate complexes (which are discussed in detail in the next subchapter) the mesoporous silica KIT-6 was chosen as support material. KIT-6 is a large-pore silica analogue to MCM-48, which was previously used successfully for the surface organometallic chemistry (*SOMC*) of $Ti(NMe_2)_4$.[38] The KIT-6 syntheses were performed on the basis of a well-established route (see Table 1 and Paper I).[46] The obtained materials (M1a and M1b) were characterized *via* Powder X-Ray Diffraction (*PXRD*) and Nitrogen Physisorption (*N_2 Physisorption*): The pore structure of the mesopores with cubic symmetry ($d_{p,\,ads}$ = 8.5 nm and 7.7 nm) and with interconnecting micropores, which are characteristic for KIT-6 materials, could be confirmed by the diffraction patterns, and type IV isotherms (H1 hysteresis loops) *via* Brunauer-Emmett-Teller (*BET*)[69] and Barrett-Joyner-Halenda (*BJH*)[70] calculations. Diffuse reflectance infrared Fourier-transformed (*DRIFT*) spectroscopy of the high surface area silicas ($a_{s,\,BET}$ = 620 m^2/g and 622 m^2/g) after surface silylation with $HN(SiHMe_2)_2$ indicated full consumption of accessible SiOH groups with silyl. The amount of these accessible silanol groups at the KIT-6 surface was calculated (δ_{SiOH} = 2.08 mmol/g and 1.84 mmol/g) *via* a published procedure.[71]

Beyond the facts, mentioned in the last subchapter of the introduction, the synthesis approach of the Blin-group[59] to obtain ordered mesoporous titania was also interesting, because of the similarity concerning type and amount of the main precursors, to the ones used within the first steps of the mesoporous silica syntheses:

Table 1: Molar ratios of the main components used for the syntheses of KIT-6 and m-TiO_2

KIT-6[46]	TEOS	P123	HCl	H_2O	*n*-butanol	
n [mmol/g]	1	0.017	1.83	195	1.31	
m-TiO_2[59]	$Ti(OiPr)_4$	P123	HCl	ethanol		
n [mmol/g]	1	0.016	2.68	40.9		

The synthesis of *Zimny et al.*[59] was adjusted and adapted to the available laboratory equipment, *i.e.* we did not use gaseous ammonia in the last synthesis step, but worked in an aqueous ammonia solution (see Paper II). The obtained m-TiO_2 was characterized analogously to the silica materials above. The reflexes from the small-angle PXRD patterns were not sharp enough for a distinct calculation of the pore structure, but the type IV isotherms with H1 hysteresis loops, obtained from the N_2 physisorption measurements, were indicative for mesopores with

even and narrow pore shape as well as comparatively narrow pore size distributions, which together implies for a relatively ordered pore architecture.[72] The average mesopore diameter is in the same range as for KIT-6, but the specific BET surface area and accordingly the number of accessible surface-OH groups are much smaller compared to the silica materials (see Paper II). For comparison, Table 2 gives an overview on the relevant characterization data:

Table 2: Nitrogen physisorption data of the synthesized porous silica and titania materials

	$a_{S,\ BET}$ [m^2/g]	$V_{P,\ des}$ [cm^3/g]	$d_{P,\ ads}$ [nm]	$\delta_{M\text{-}OH,\ surf.}$ [mmol/g]
KIT-6 No.1 (**M1a**)	620	1.19	8.5	2.08
KIT-6 No.2 (**M1b**)	622	1.24	7.7	1.84
m-TiO_2	93	0.189	7.0	0.762

2. Molecular heteroleptic titanium(IV) catecholate chemistry

2.1. Dimeric heteroleptic titanium(IV) amide complexes (Paper I)

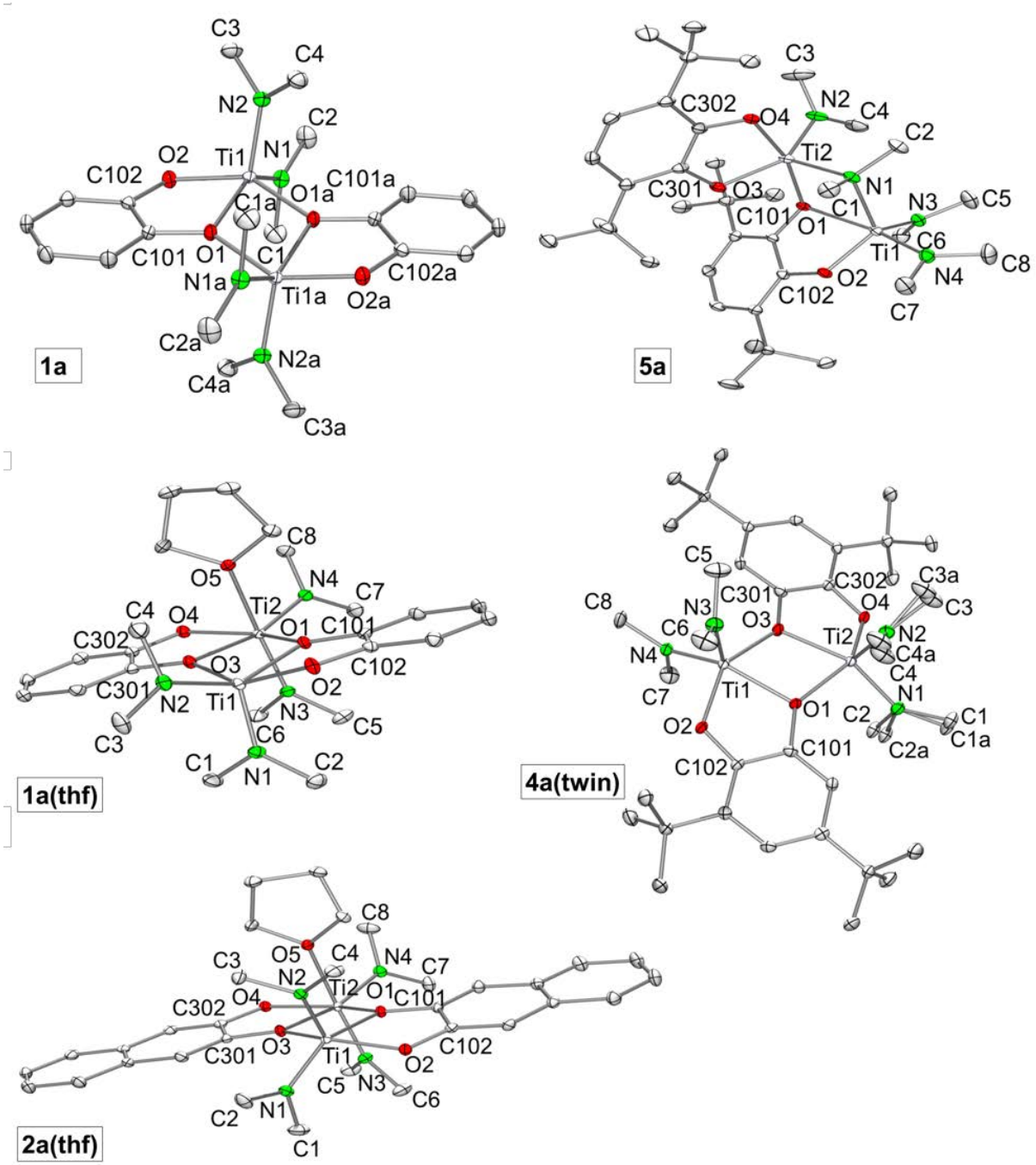

Figure 1: Crystal structures of **1a**, **1a(thf)**, **2a(thf)**, **4a(twin)**, and **5a** with atomic displacement parameters set at the 50% level. Hydrogen atoms are omitted for clarity.

Tetrakis(dimethylamido) titanium(IV), [$Ti(NMe_2)_4$], was reacted with several proligands, *i.e.* catechols with different spatial demands [pyrocatechol (**1**), 2,3-dihydroxynaphthalene (**2**), 4-*tert*-butylcatechol (**3**), 3,5-di-*tert*-butylcatechol (**4**), and 3,6-di-*tert*-butylcatechol (**5**)].

The pK_a values for the corresponding acids of metal bonded amides, such as $HNMe_2$ for $Ti(NMe_2)_4$, are in the range between 32 and 40.[27] Therefore, they are far more basic than catechols (pK_{a1}(catechol) = 9.2 and pK_{a2} (catechol) = 13.0).[35] This huge acidity difference between $HNMe_2$ and catechols creates the driving force of the reactions mentioned above, where the protonolysis of the basic NMe_2 ligands is promoted and gaseous dimethylamine ($HNMe_2$) is released:

$$Ti(NMe_2)_4 + Ar(OH) \longrightarrow (ArO)Ti(NMe_2)_3 + HNMe_2 \quad (Ar = aryl) \qquad (eq.1)$$

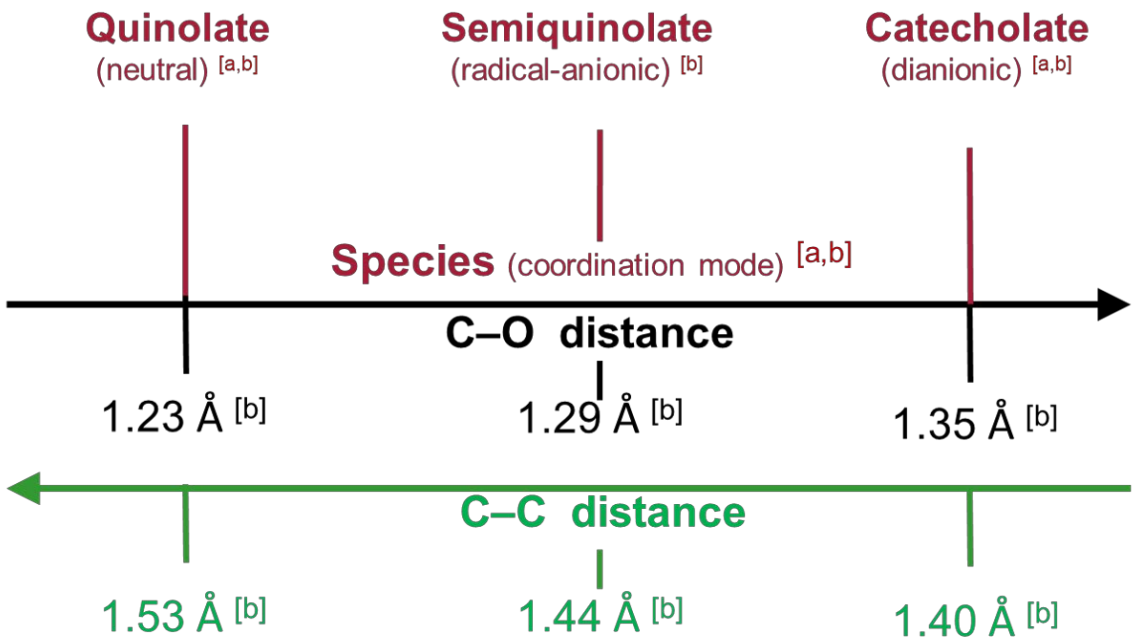

[a] *Chem. Sci.*, 2015, **127**, 527-535. [b] *Coord. Chem. Rev.*, 1981, **38**, 45-87.

Figure 2: Illustration of different coordination modes of catechol ligands with metal centers in dependence of the C–O and C–C distances. (Information for this illustration was taken from ref. a [73] and b [74]).

The obtained heteroleptic catecholato titanium(IV) complexes $[Ti(CAT)(NMe_2)_2]_2$ (**1a**), $[Ti(DHN)(NMe_2)_2]_2$ (**2a**), $[Ti(CAT\textit{t}Bu\text{-}4)(NMe_2)_2]_2$ (**3a**), $[Ti(CAT\textit{t}Bu\text{-}3,5)(NMe_2)_2]_2$ (**4a**) and $[Ti(CAT\textit{t}Bu\text{-}3,6)(NMe_2)_2]_2$ (**5a**) are dimers in the solid state, as proven by crystal structure analyses (Figure 1), except for the complex **3a**, where no crystals have been obtained.

When proligands with vicinal hydroxyl groups, like catechols, are reacted with metal complexes, three different coordination modes of the catechol with the metal center can be observed, as illustrated in Figure 2. These three modes can be determined from the C–O distances and the C–C distance of the ring-carbon atoms, which are bound to the oxygen atoms. From the C–O distances of the complexes discussed in Tables 3 and 4 are ≥ 1.35 Å, and the corresponding C–C distances are around 1.40 Å. Therefore, it can be concluded, that the dianionic coordination mode is present in all of these complexes.

The dimers **1a** and **4a** are bridged *via* their catecholato-oxygen atoms, creating 5-coordinated Ti(IV) centers respectively. The Ti–O distances are longer for the bridged than for the nonbridged oxygens (see Tables 3 and 4), but increasing spatial demand from **1a** to **4a** did not prevent dimerization. Crystallization from THF/*n*-pentane created the adduct complexes **1a(thf)** and **2a(thf)**, with one 6-coordinated and one 5-coordinated Ti(IV) each. The Ti–N distances of the 6-coordinated titanium center are longer than those of the 5-coordinated titanium center (see Table 3), but again dimerization could not be avoided.

Table 3: Selected interatomic distances [Å] of **1a**, **1a(thf)**, **2a(thf)**, **4a** and **5a** (a detailed description of the crystal structures and their measurements can be found in **Paper I**)

	1a	**1a(thf)**	**2a(thf)**	**4a**	**5a**
Ti---Ti	3.361(1)	3.358(2)	-	3.341(1)	3.191(1)
ArC–O	1.362(2)	1.357(2)	1.354(2)	1.368(2)	1.362(2)
OC–CO	1.407(2)	1.402(3), 1.415(3)	1.431(2), 1.437(2)	1.400(3), 1.407(3)	1.410(1)
Ti–N	1.874(1)	1.898(2)	1.897(2)	1.876(2)	1.895(2) [2.124(1)][a]
Ti–O[b]	1.936(1) – 2.000(1)	1.917(1) – 2.179(2)	1.926(1) – 2.178(1)	1.901(2) – 2.119(2)	1.901(1) – 2.011(1)

[a] Ti–N (bridging), [b] Ti–O (catecholato).

Examples of homoleptic Al(III), Co(III), and Ga(III) complexes were found in the literature, where catechols with bulky substituents adjacent to both oxygen atoms enabled the formation of the desired monomers.[75] Therefore, 3,6-di-*tert*-butylcatechol (**5**) was chosen as a bulky proligand for the reaction with $Ti(NMe_2)_4$. However, the reaction did not produce a monomer, but a dimer (**5a**), which is bridged *via* one catecholato-oxygen atom and one nitrogen atom.

Table 4: Selected interatomic distances [Å] of **1a**, **1b**, **5a**, **5b** and **5c** (a detailed description of the crystal structures and their measurements can be found in **Papers I** and **II**)

	1a	**1b**	**5a**	**5b**	**5c**
Ti---Ti	3.361(1)	3.364(1)	3.191(1)	-	-
ArC–O	1.362(2)	1.348(3), 1.365(3)	1.362(2)	1.357(5)	1.347(5), 1.360(5)
OC–CO	1.407(2)	1.409(4)	1.410(1)	1.409(9)	1.400(5)
Ti–N	1.874(1)	2.317(2)	1.895(2)	2.205(15), 2.224(3)	2.227(3), 2.229(3)
Ti–O[a]	1.936(1) – 2.000(1)	1.906(2) – 2.108(2)	1.901(1) – 2.011(1)	1.915(3)	1.936(3), 1.937(3)
Ti–O[b]	-	1.767(2), 1.843(2)	-	1.840(3)	1.886(3), 1.886(3)

[a] Ti–O(catecholato). [b] Ti–O(neopentoxy/siloxy).

Thus, shielding the catecholato-oxygen atoms was not sufficient. An isopropoxy *meso*-BINOLATO Ti(IV) complex Ti[BINOL($SiMe_2$*t*Bu)-3,3´][O*i*Pr]$_2$, where the BINOLATO ligand was bearing bulky silyl groups adjacent to its two oxygen atoms, was reported to be monomeric.[76] *Prima facie*, this suggested to utilize Ti(IV) isopropoxide $Ti(OiPr)_4$ instead of $Ti(NMe_2)_4$ in the reaction with 3,6-di-*tert*-butylcatechol (**5**). The catecholato chemistry of Ti(IV) isopropoxide on the other hand was reported to be very similar to the results herein,

shown above for the proligands **1**-**4** with $Ti(NMe_2)_4$,[77-79] what rather suggested a similar result with proligand **5**, too.

2.2. Monomeric Ti(IV) catecholates *via* 2nd ligand exchange with neopentanol (Paper II)

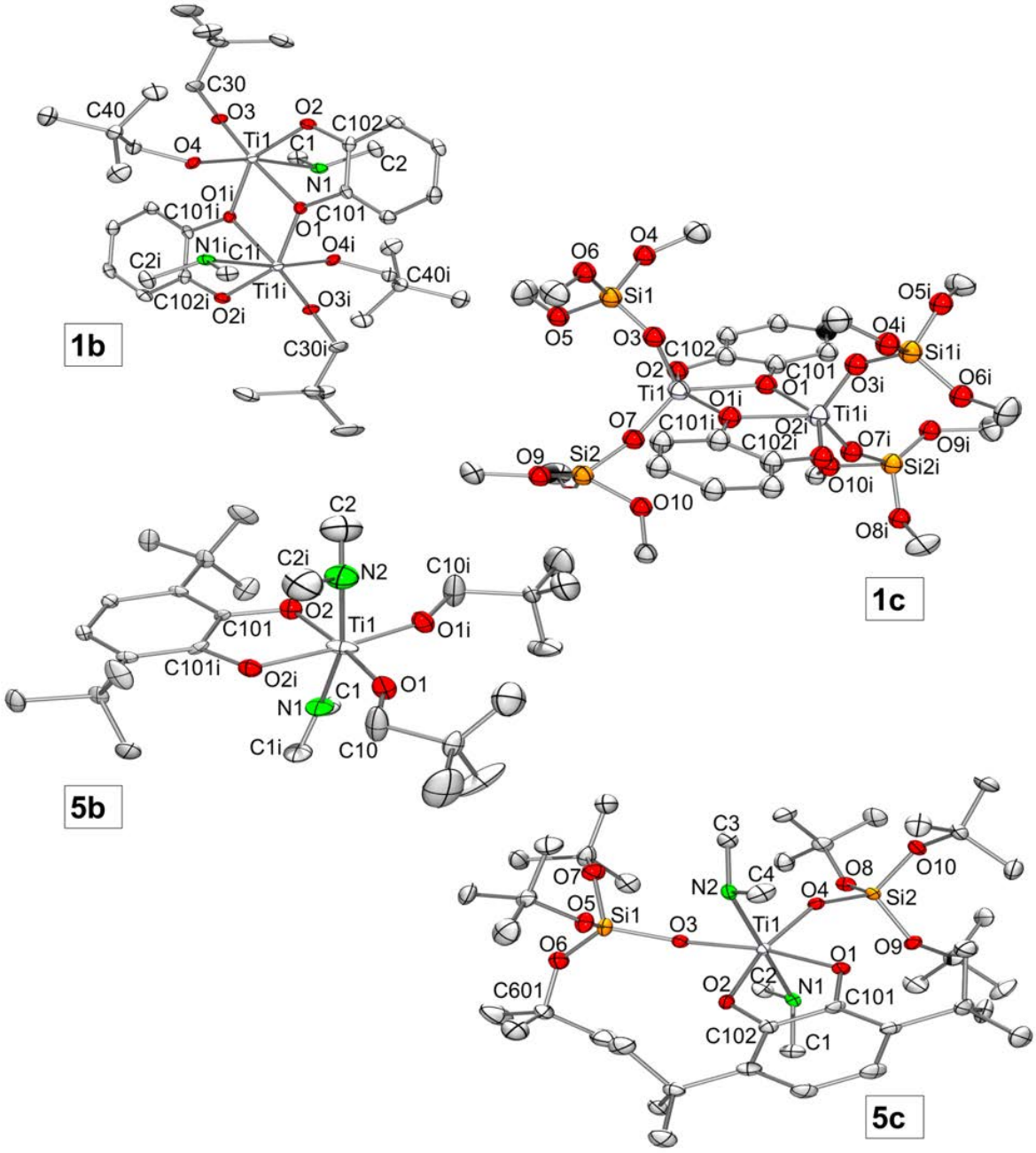

Figure 3: Crystal structures of complexes **1b**, **1c**, **5b**, and **5c** with atomic displacement parameters set at the 50% level. Hydrogen atoms and the *tert*-butyl methyl groups in **1c** are omitted for clarity.

Consequently, neopentoxy, which is a slightly bulkier alkoxy ligand than isopropoxy, was chosen as a co-ligand. $[Ti(CAT)(NMe_2)_2]_2$ (**1a**) and $[Ti(CAT\textit{t}Bu\text{-}3,6)(NMe_2)_2]_2$ (**5a**) were treated with two equivalents of neopentanol. From complex **1a**, another dimer $[Ti(CAT)(OCH_2\textit{t}Bu)_2(HNMe_2)]_2$ (**1b**) was obtained, again bridged *via* its catecholato-oxygen atoms (see Figure 3). Interestingly, both Ti(IV) centers of dimer **1b** were 6-coordinated, still carrying one of their two former NMe_2 groups each. The Ti–N distances are, however, longer here than for amido ligands (see Table 3). The corresponding DRIFTS spectra revealed a N–H vibration at 3199 cm^{-1} indicating the coordination of amines ($HNMe_2$). Furthermore, the ^1H NMR spectrum of **1b** displays a broad resonance at 2.28 ppm, which can be attributed to the methyl protons of dimethylamine (see **Paper II** and Figure S2 in the corresponding ESI). From amide complex **5a** the monomeric complex $[Ti(CAT\textit{t}Bu\text{-}3,6)(OCH_2\textit{t}Bu)_2(HNMe_2)_2]$ (**5b**) was obtained. Complex **5b** has a 6-coordinated Ti(IV), because both former amido groups stayed coordinated as amines upon the protonolysis reaction. This is proven by elongated Ti–N distances (see Figure 3 and Table 3), and a N–H vibration at 3294 cm^{-1} in the DRIFTS spectrum of complex **5b**. The corresponding ^1H NMR spectrum of **5b** further displays a broad resonance at 2.11 ppm, which can be attributed to the methyl protons of dimethylamine (see **Paper II** and Figure S4 in the corresponding ESI). The amine coordination in both heteroleptic neopentoxide complexes **1b** and **5b** was even more unexpected, because the homoleptic Ti(IV) neopentoxide complex $Ti(OCH_2\textit{t}Bu)_4$ (**6**), which was derived from $Ti(NMe_2)_4$ with neopentanol, did not display coordinated amine. This accounts for a stabilizing effect of the latter on heteroleptic Ti(IV) catecholate complexes.

2.3. Molecular models of grafted complexes *via* ligand exchange with tris(*tert*-butoxy)silanol (Paper II)

To obtain insights into possible surface structures upon grafting onto KIT-6, amide complexes **1a** and **5a** were reacted with tris(*tert*-butoxy)silanol, to yield the complexes $[Ti(CAT)(OSi(O\textit{t}Bu)_3)_2(HNMe_2)_2]_2$ (**1c**) and $[Ti(CAT\textit{t}Bu\text{-}3,6)(OSi(O\textit{t}Bu)_3)_2(HNMe_2)_2]$ (**5c**). Neopentoxide complex **5b** was also reacted with the silanol in order to simulate its grafting reaction onto KIT-6 giving complex **5c** in nearly quantitative yield, as well. Whereas complex **1c** is a dimer like its precursors, complex **5c** is a monomer (see Figure 3 and Table 3), what suggested, that the nuclearity of **1b** and **5b** would probably stay intact upon grafting.

2.4. Ligand scrambling test

The ligand scrambling reaction observed in an ^{1}H NMR experiment of a mixture of complexes **1a** and **2a** in C_6D_6 implies for the (at least temporary) presence of monomers in solution, (**Paper I** and Figure S24 in the corresponding ESI). Therefore, grafting of a (in solid state) dimeric, heteroleptic amide complex, besides the monomeric neopentoxide complex, appeared promising, as well.

3. Surface Chemistry

3.1. Dimeric heteroleptic amide @KIT-6 (Paper I)

Except for the 3,6-di-*tert*-butylcatecholate complex, all the dimeric heteroleptic amide complexes display the same structure motif. If the backbone of the catechol(s) is aimed to be functionalized with releasable drugs / medication, which have a quite huge space demand, it appeared to be the best choice to perform the grafting reactions with the amide complex which is carrying the largest catecholate ligand to investigate potential pore-blocking behavior.

Thus, sequential and convergent grafting strategies were performed as shown in Scheme 1. In the first step of the sequential route tetrakis(dimethylamido) titanium(IV) [$Ti(NMe_2)_4$] has been immobilized onto KIT-6 (**M1a**) giving $Ti(NMe_2)_4$@[KIT-6] (**MS1**), which was followed by a ligand exchange with 2,3-dihydroxynaphthalene (H_2DHN) to yield H_2DHN@$Ti(NMe_2)_4$@[KIT-6] (**MS2**) in the second step. For the convergent approach the dimeric heteroleptic complex [Ti(CAT*t*Bu-3,6)$(NMe_2)_2]_2$ (**5a**) has been directly immobilized onto KIT-6 (**M1b**) to obtain [Ti(CAT*t*Bu-3,6)$(NMe_2)_2]_2$@[KIT-6] (**MC1**).

The pore volume subsequently decreased from KIT-6 (**M1a**) over **MS1** to **MS2,** and from KIT-6 (**M1b**) to **MC1,** respectively, whereby the type IV isotherms with H1 hysteresis loops were retained, indicating absence of pore blocking. Further on, the pore volume of **MS2** and **MC1** are nearly identical, which implies a similar spatial demand of the obtained surface species in both approaches, (see Figure 4). The DRIFTS spectra of **MS2** and **MC1** display the disappearance of SiO–H vibrations at 3745 cm^{-1}, and the occurrence of Ti–O–C vibrations (especially the vibration at 741 cm^{-1}) is indicating a successful ligand exchange reaction in the case of **MS2**, and a successful grafting reaction of complex **2a** in the case of **MC1**.

The ^{13}C MAS NMR spectra of **MS2** and **MC1** display an upfield shift of their β-C signal (from 110 ppm to 105 ppm each) and a downfield shift of the α-C signals (from 148 ppm to 160 ppm (**MS2**) and 157 ppm (**MC1**)) compared to the signal in the ^{13}C NMR spectrum of 2,3-dihydroxynaphthalene in thf-d_8, (see Figure 5). These findings account for a chelating catecholato binding to the Ti(IV) center,[80] but also indicate different surface species for **MS2** and **MC1**.

Scheme 5: Overview of the two grafting strategies (sequential and convergent) and possible surface species in the products of the sequential (**MS1** and **MS2**) and the convergent (**MC1**) routes.

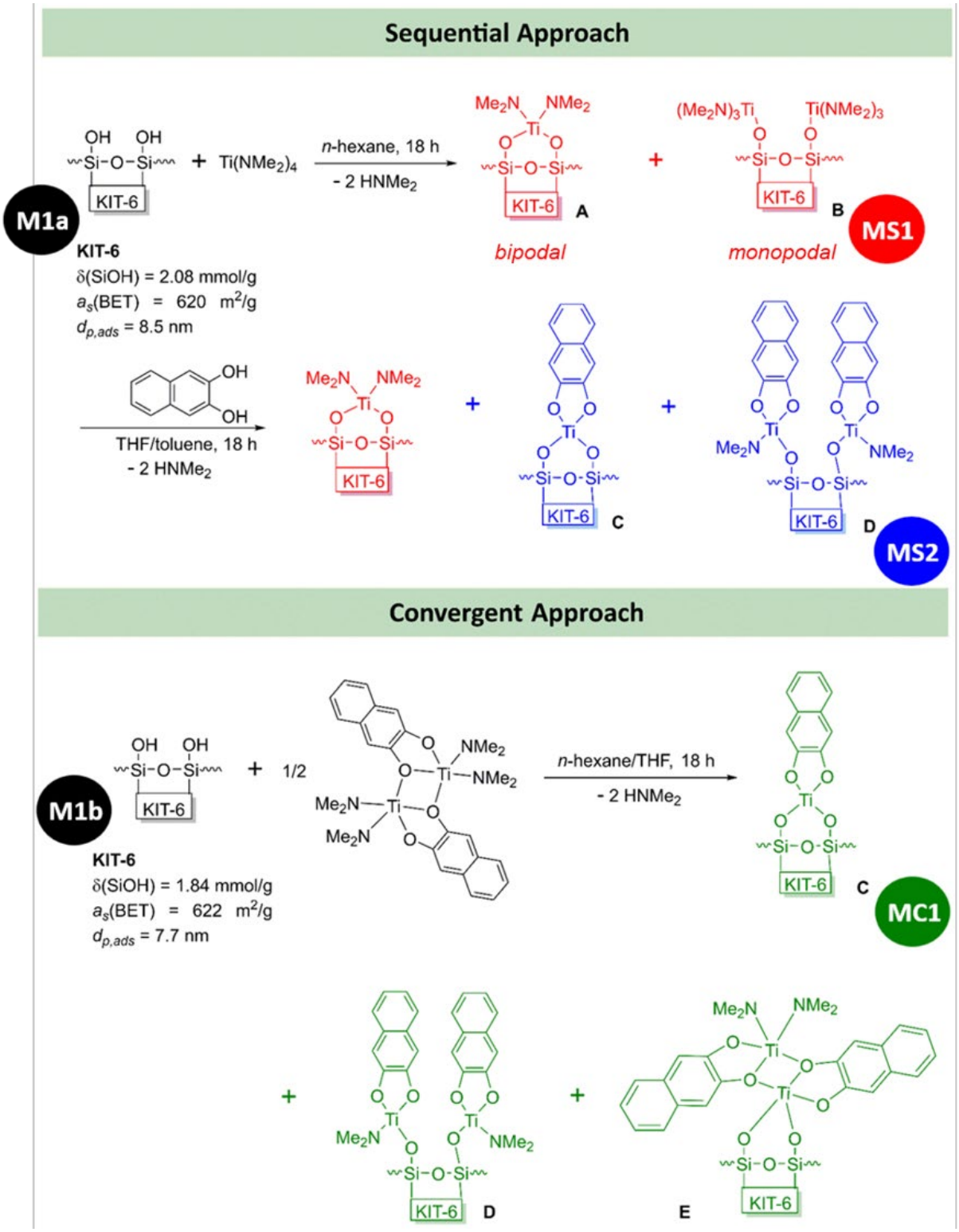

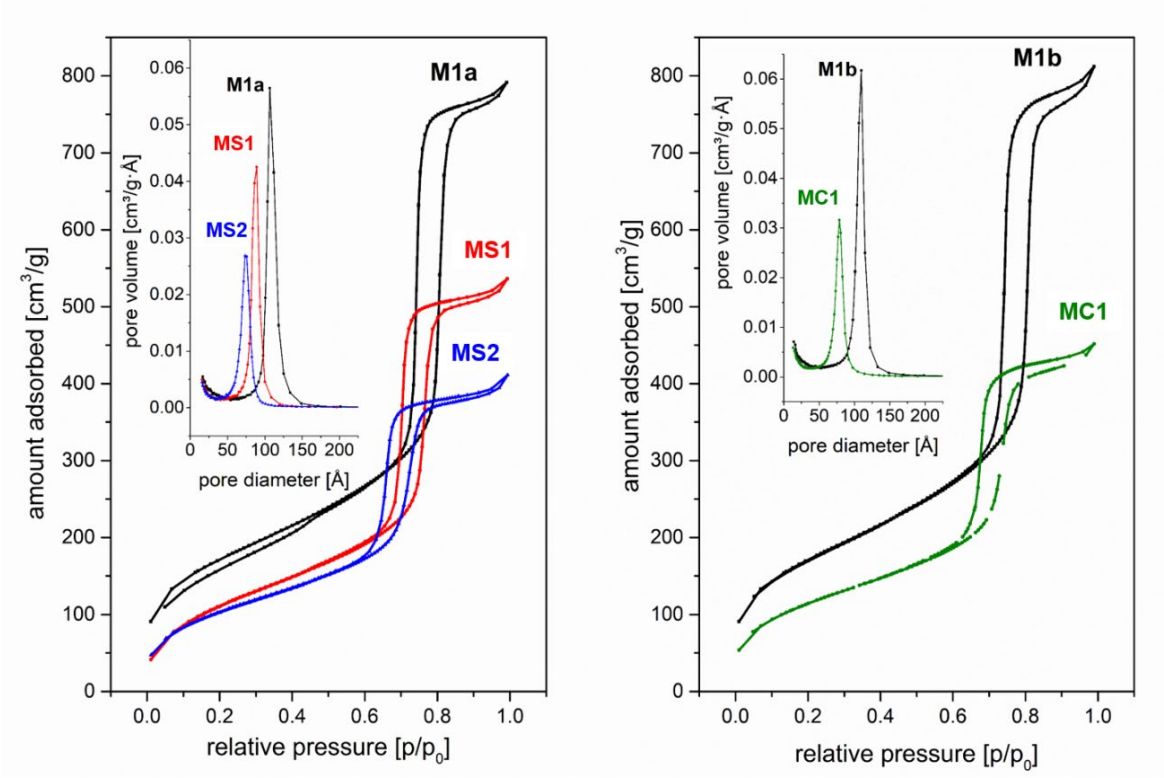

Figure 4: Nitrogen adsorption/desorption isotherms at 77.4 K and the corresponding BJH pore size distributions *(insets),* derived from the respective isotherm adsorption branch, of the sequential route materials **M1a**, **MS1** and **MS2** *(left)*, and of the convergent route materials **M1b** and **MC1** *(right)*.

The elemental analyses revealed nitrogen contents of 2.01 wt% for **MS2** and 2.21 wt% for **MC1**, what may imply for (partially) monopodally grafted surface species or coordinated $HNMe_2$, and for **MS1**-residues (**A**, Scheme 1) in material **MS2**, and for grafting of a complete **2a**-dimer with two free amido groups (**E**, Scheme 1) in material **MC1**. The highfield region of the ^{13}C NMR spectrum of the precursor $Ti(NMe_2)_4$ in C_6D_6 displays one NMe_2 carbon signal at 44 ppm (see Figure S19, ESI **Paper I**). In the corresponding region of the ^{13}C MAS NMR spectrum of **MS1** two signals are visible – the signal at 43 ppm is ascribed to the amido-carbon atoms of a monopodally anchored $[(\equiv SiO)Ti(NMe_2)_3]$ species, whereas the signal at 36 ppm is ascribed to the amido-carbon atoms of a bipodally anchored $[(\equiv SiO)_2Ti(NMe_2)_2]$ species (see Figure S16, ESI **Paper I**). Upon ligand exchange with 2,3-dihydroxynaphthalene (H_2DHN) the ^{13}C MAS NMR spectrum of **MS2** displays two signals, too: one signal at 35 ppm and one at 40 ppm (see Figure S17, ESI **Paper I**). In **Paper II**, the presence of $HNMe_2$ groups in complex **5b** has been proven by several analytical tools (*vide supra*) and the signal at 40 ppm in the ^{13}C NMR spectrum in C_6D_6 of complex **5b** was assigned to the methyl-carbon atoms of $HNMe_2$

(see Figure S12, ESI **Paper II**). Therefore, the signal at 40 ppm for **MS2** can be assigned to surface coordinated $HNMe_2$. The signal at 35 ppm is then ascribed to residues of the bipodal **MS1** species $[(\equiv SiO)_2Ti(NMe_2)_2]$ in **MS2** (see Figures S16 & S17, ESI **Paper I**). Upon grafting of the heteroleptic molecular complex **2a** onto KIT-6, the ^{13}C MAS NMR spectrum of the obtained material **MC1** displays a signal at 40 ppm, too (see Figure S18, ESI **Paper I**), which

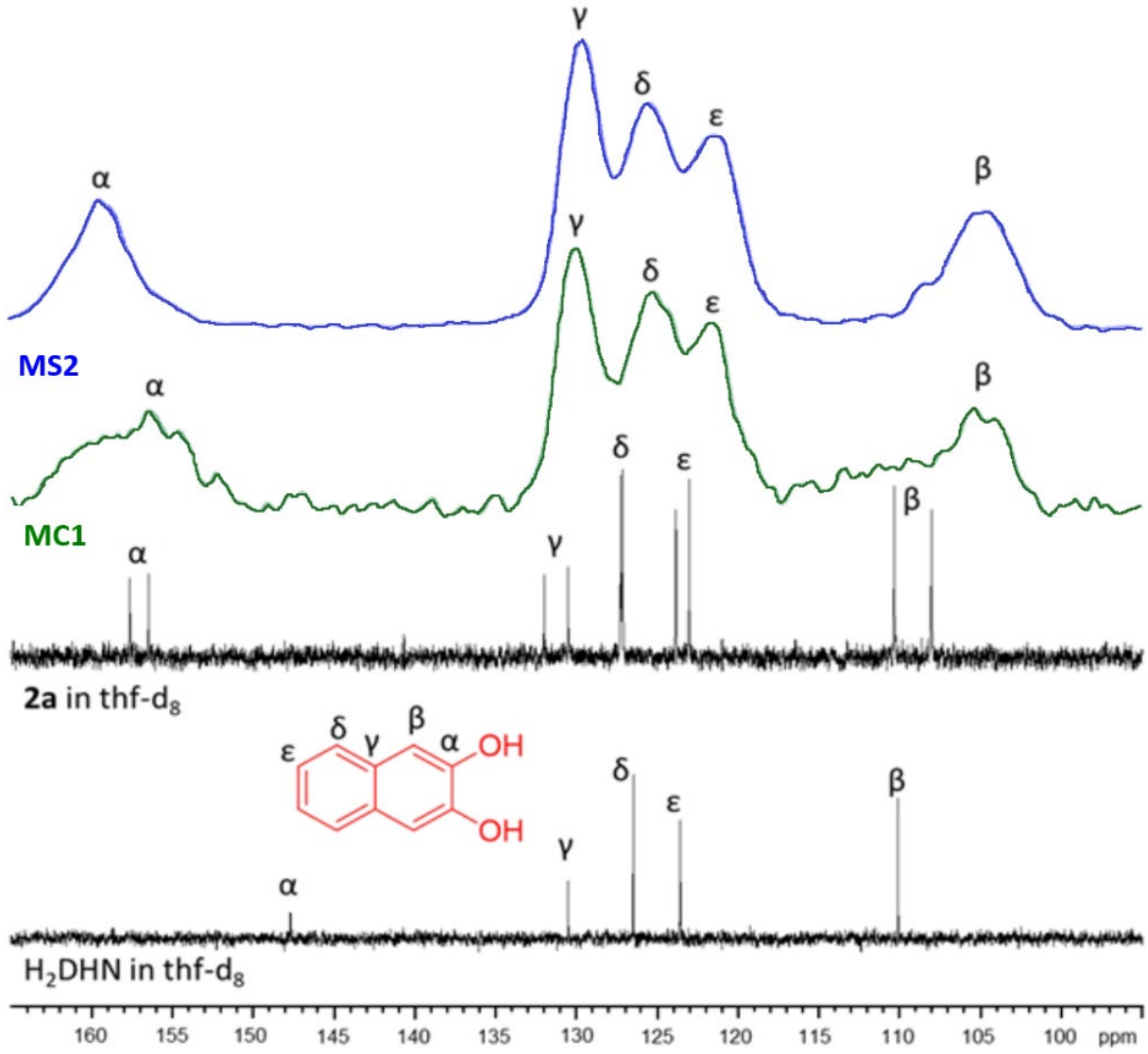

Figure 5: ^{13}C NMR spectra from bottom to top: H_2DHN (100MHz, thf-d_8), $[Ti(DHN)(NMe_2)_2]_2$ (**2a**) (100MHz, thf-d_8), $[Ti(DHN)(NMe_2)_2]_2$@[KIT-6] (**MC1**) (75 MHz, CP/MAS, 10 kHz rotation), H_2DHN@$Ti(NMe_2)_4$@[KIT-6] (**MS2**) (75 MHz, CP/MAS, 10 kHz rotation).

is assigned to surface coordinated $HNMe_2$ as in the case of material **MS2**. The second ^{13}C signal of **MC1** at 47 ppm is in the same position as the signal of the NMe_2 group carbons in the ^{13}C NMR spectrum of the dimeric molecular complex **2a** in thf-d_8 (see Figure S20, ESI **Paper I**), what implies, at least for the partial preservation of the dimeric structure upon immobilization of the heteroleptic complex **2a** onto KIT-6. A stacked plot of ^{13}C NMR spectra with focus on the amido carbon region is found in Figure S21 of the ESI of **Paper I**.

Consequently, the immobilization of $Ti(NMe_2)_4$ onto KIT-6 resulted in bipodal and monopodal surface species giving material **MS1**. The subsequent ligand exchange with H_2DHN was only partially successful, as residues of both, the bipodally anchored **MS1** species and $HNMe_2$, are present in **MS2**, too. The convergent approach did not exclusively give the desired bipodally anchored species with only one dihydroxynaphthaleno ligand, as to be expected from the ligand scrambling experiments before (*vide supra*), but also $HNMe_2$ residues and a surface species, which completely retained the dimeric structure of the molecular complex **2a**.

3.2. Monomeric neopentanolato complex @KIT-6 (Paper II)

The preservation of the dimeric structure of the amido complex **2a** at the KIT-6 surface implied, that the monomeric catecholato neopentoxide complex [Ti(CAT*t*Bu-3,6)(OCH_2*t*Bu)$_2$($HNMe_2$)$_2$] (**5b**) would react analogously, when it is utilized in the convergent approach instead of **2a**. For comparison, the sequential route and an aqueous route were also performed, as depicted in Scheme 2.

In the first step of the sequential route, Ti(IV) neopentoxide [Ti(OCH_2*t*Bu)$_4$] (**6**) has been immobilized onto KIT-6 (**M1a**) giving Ti(OCH_2*t*Bu)$_4$@[KIT-6] (**M1S1**), which was followed by a ligand exchange with 3,6-di-*tert*-butylcatechol (H_2CAT*t*Bu-3,6) to yield H_2CAT*t*Bu-3,6@Ti(OCH_2*t*Bu)$_4$@[KIT-6] (**M1S2**) in the second step. For the convergent approach, the monomeric heteroleptic complex [Ti(CAT*t*Bu-3,6)(OCH_2*t*Bu)$_2$($HNMe_2$)$_2$] (**5b**) has been directly immobilized onto KIT-6 (**M1a**) to obtain [Ti(CAT*t*Bu-3,6)(OCH_2*t*Bu)$_2$($HNMe_2$)$_2$] @[KIT-6] (**M1C1**). The aqueous route consisted of three steps: The immobilization of Ti(IV) isopropoxide [Ti(O*i*Pr)$_4$] onto KIT-6 to obtain Ti(O*i*Pr)$_4$@[KIT-6] (**M1A1**), which was hydrolysed to afford the desired titania overlayer Ti$(OH)_x$@[KIT-6] (**M1A2**) for the reaction with 3,6-di-*tert*-butylcatechol (H_2CAT*t*Bu-3,6), which should simulate the latter´s reaction on

Scheme 6: Overview on the three grafting strategies (aqueous, sequential, and convergent) and proposed surface species **M1A2** and **M1A3** (aqueous route), **M1S1** and **M1S2** (sequential route) and **M1C1** (convergent route).

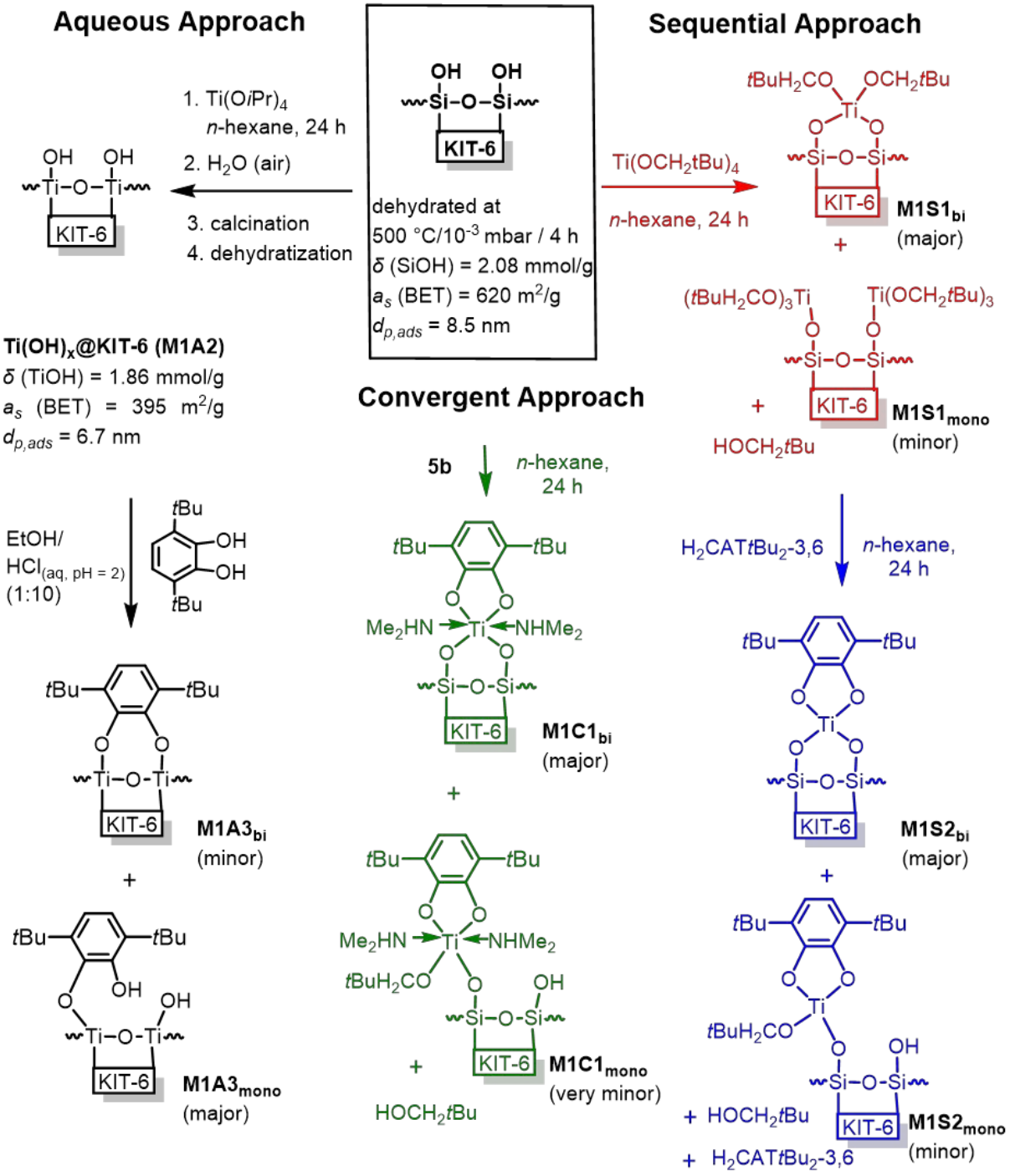

titania surfaces in acidic aqueous media,[16] and resulted in H_2CAT*t*Bu-3,6@$Ti(OH)_x$@[KIT-6] (**M1A3**). The pore volume decreased from KIT-6 (**M1a**) to **M1S2,** and from KIT-6 (**M1a**) to **M1C1,** respectively, whereby the type IV isotherms with H1 hysteresis loops were retained,

indicating absence of pore blocking (see Figure 6). Further on, the pore volume of **M1S2** and **M1C1** are nearly identical, which implies a similar spatial demand of the obtained surface species in the sequential and convergent approaches. Interestingly, the pore volume of **M1S1** is smaller than that of **M1S2**. This may point towards leaching of a fraction of the immobilized surface species in material **M1S2** after the ligand exchange reaction. For the aqueous approach from KIT-6 (**M1a**) to **M1A3** the pore volume was only reduced to half of the extent of the materials **M1S2** and **M1C1** in the other two approaches, which may give rise to less surface coverage in the material **M1A3** compared to **M1S2** and **M1C1**.

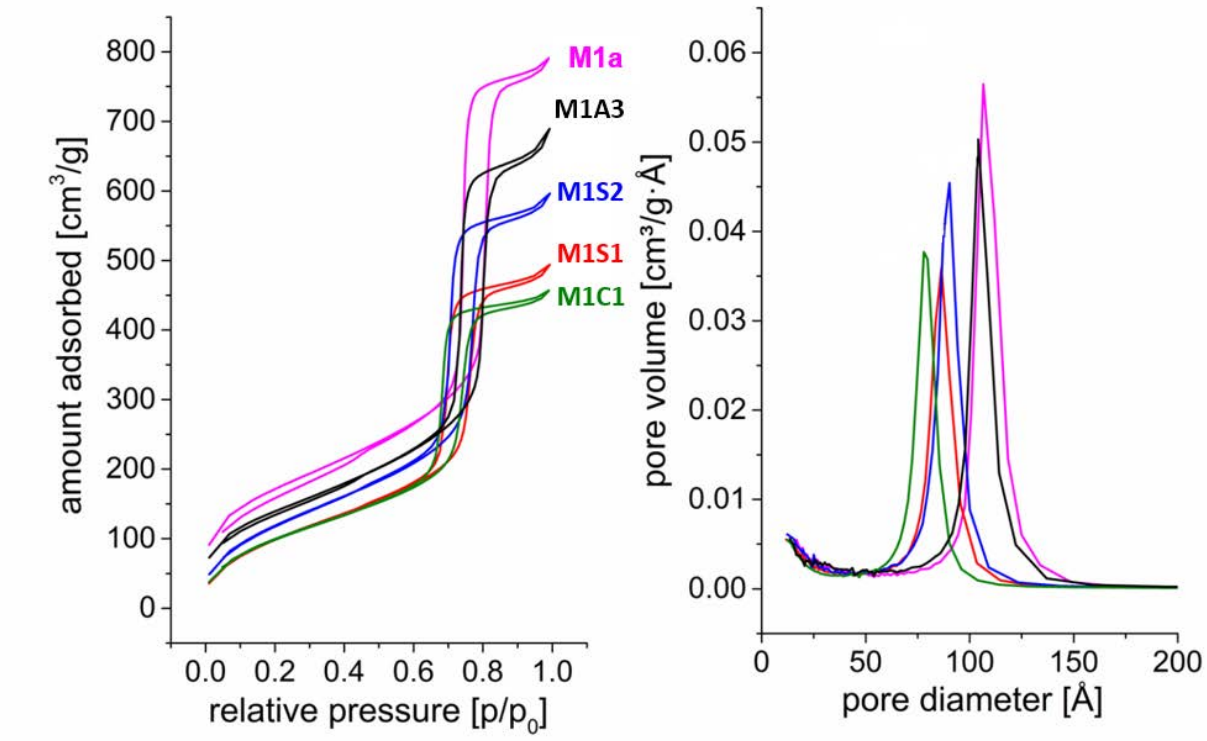

Figure 6: Nitrogen adsorption/desorption isotherms at 77.4 K *(left)* and the corresponding BJH pore size distributions *(right),* derived from the respective isotherm adsorption branch, of KIT-6 (**M1a**), the aqueous route material **M1A3**, the sequential route materials **M1S1** and **M1S2**, and of the convergent route material **M1C1**.

All the DRIFTS spectra of **M1S2**, **M1C1**, and **M1A3** still contain an SiO–H band in the region between 3701-3741 cm^{-1}, which accounts for inaccessible OH groups in all three approaches (see Figures S24, S25 & S22 in ESI of **Paper II**). ^{13}C MAS NMR spectroscopy of **M1S1** revealed two carbon signals in the methyl carbon region at 73 ppm and 89 ppm, whereas the

^{13}C NMR spectrum of the precursor [Ti(OCH$_2$*t*Bu)$_4$] (**6**) in C_6D_6 displayed only a signal at 86 ppm (see Figure 7). Thus, the signal at 89 ppm in the spectrum of **M1S1** is attributed to titanium-bound neopentoxy-methyl carbon-atoms and the signal at 73 ppm to methyl-carbon atoms of neopentanol on the surface of the material **M1S1**. The latter signal is also found in the

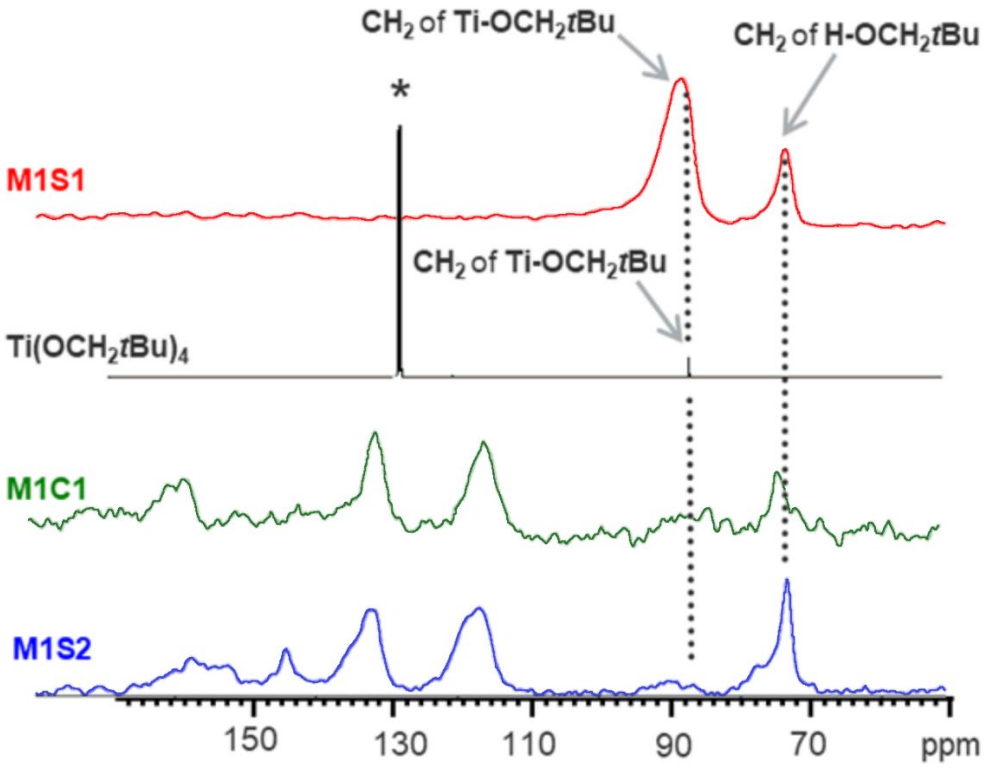

Figure 7: ^{13}C NMR spectra from bottom to top: H$_2$CAT*t*Bu$_2$-3,6@Ti(OCH$_2$*t*Bu)$_4$@[KIT-6] (**M1S2**), and [Ti(CAT*t*Bu$_2$-3,6)(OCH$_2$*t*Bu)$_2$(HNMe$_2$)$_2$]@[KIT-6] (**M1C1**) (75 MHz, CP/MAS, 10 kHz rotation), Ti(OCH$_2$*t*Bu)$_4$ (**6**) in solution (100 MHz, C_6D_6 = *) and of material Ti(OCH$_2$*t*Bu)$_4$@[KIT-6] (**M1S1**) (75 MHz, CP/MAS, 10 kHz rotation).

^{13}C MAS NMR spectra of **M1S2** and **M1C1** (see Figure 7), which indicates residues of neopentanol on the surfaces of both materials after the protonolysis reactions. It is known from the immobilization of Ti(O*i*Pr)$_4$ onto porous silica, that the alcohol, which was generated during the grafting reaction, stayed on the silica surface by interactions with the surface-silanol groups.[38] Thus, the neopentanol residues are blocking reactive surface sites, what explains the

presence of the SiO–H vibrations in the DRIFTS spectra of the materials **M1S1**, **M1S2**, and **M1C1**.

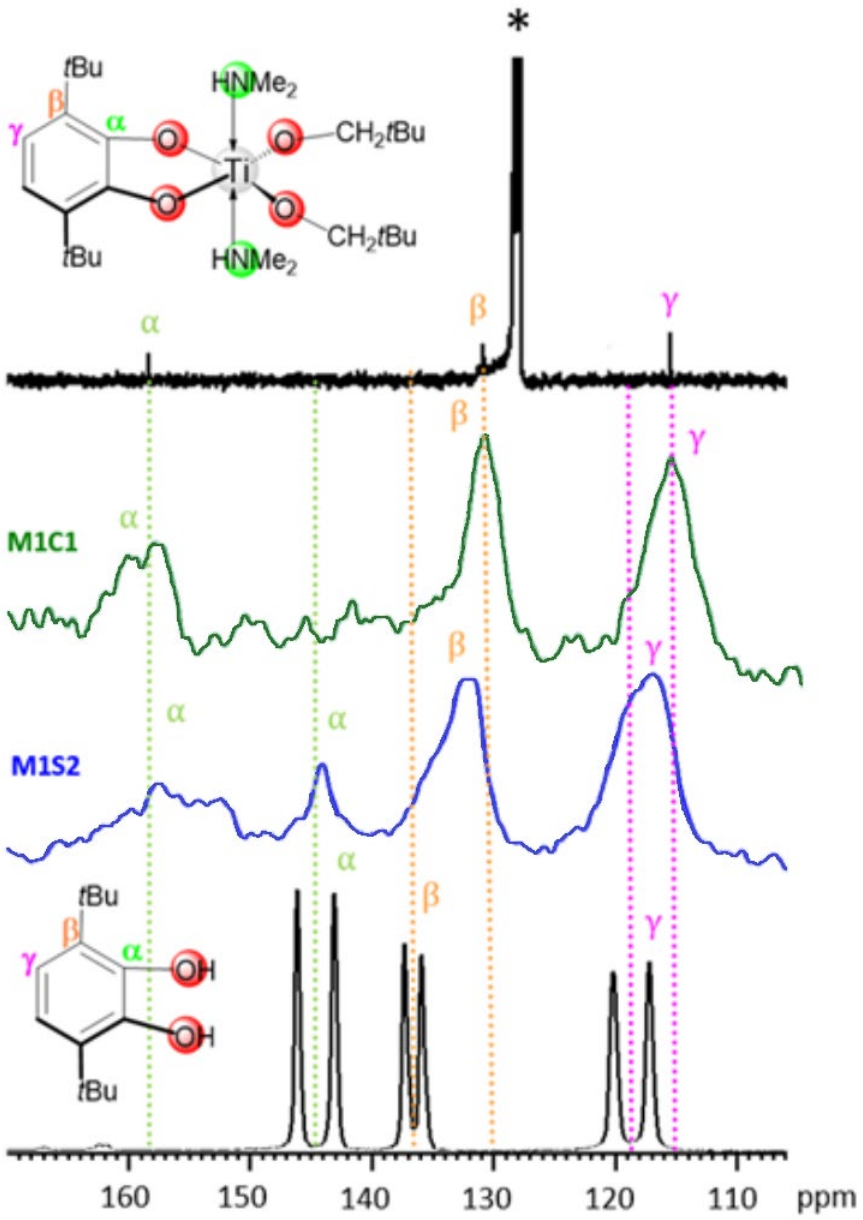

Figure 8: ^{13}C NMR spectra from bottom to top: H_2CAT*t*Bu_2-3,6, H_2CAT*t*Bu_2-3,6@Ti(OCH_2*t*Bu)$_4$@[KIT-6] (**M1S2**), and [Ti(CAT*t*Bu_2-3,6)(OCH_2*t*Bu)$_2$($HNMe_2$)$_2$]@[KIT-6] (**M1C1**) (75 MHz, CP/MAS, 10 kHz rotation), [Ti(CAT*t*Bu_2-3,6)(OCH_2*t*Bu)$_2$($HNMe_2$)$_2$] (**5b**) in solution (100 MHz, C_6D_6 = *).

The ^{13}C MAS NMR spectra of **M1S2** and **M1C1** display an upfield shift of their β-C signal (from 136 ppm to 133 ppm (**M1S2**) and to 131 ppm (**M1C1**)) and a downfield shift of the α-C

signals (from 145 ppm to 158 ppm (**M1S2**) and 157 ppm (**M1C1**)) compared to the signal in the ^{13}C MAS NMR spectrum of the proligand 3,6-di-*tert*-butylcatechol (see Figure 8). These findings account for a chelating catecholato binding to the Ti(IV) center, and also indicate quite similar surface species for **M1S2** and **M1C1**, as corroborated by the similar space demand of the nitrogen physisorption analysis. For **M1S2** a second α-C signal at 144 ppm implies for residues of the proligand, what is confirmed by the occurrence of an aromatic O–H vibration at 3573 cm^{-1} in the DRIFTS spectrum of **M1S2** (see Figure S24 in ESI of **Paper II**) and can be explained by blocked surface sites through the above mentioned neopentanol residues. In the ^{13}C MAS NMR spectrum of **M1A3** the signal intensity in the aromatic region is extremely weak up to not present (see Figure S13 in ESI of **Paper II**), which is why no assignments can be made here and it can be assumed, that the surface coverage with 3,6-di-*tert*-butylcatechol is very low, what explains the presence of the SiO–H vibration and the absence of any characteristic aromatic vibration in the DRIFTS spectrum of material **M1A3**.

The neopentanol residues in the materials **M1S1**, **M1S2**, and **M1C1**, and the additional 3,6-di-*tert*-butylcatechol residues in **M1S2** also had an influence on the elemental analysis results, where they caused very high carbon contents: The C/Ti ratio, which was calculated from the carbon and titanium contents obtained from elemental analyses, was 14:1 for **M1S1**, 36:1 for **M1S2** and 22:1 for **M1C1**. The ratio of accessible surface-hydroxyl groups to the titanium loading was 5.7 : 1.0 (see p.S21 ff. in ESI of **Paper II**) and suggested predominantly bipodally anchored $[(\equiv SiO)_2Ti(OCH_2tBu)_2]$ in material **M1S1** as well as an incomplete surface-hydroxyl consumption. For this surface species the C/Ti ratio to be expected is 10:1 for **M1S1**, which is about 1/3 less carbon than experimentally found. For **M1S2** the above mentioned very high C/Ti ratio of 36:1 does not only originate from neopentanol and proligand residues, but was also caused by the leaching of grafted Ti(IV) species upon the ligand exchange reaction of **M1S1** with 3,6-di-*tert*-butylcatechol, as indicated by the much lower Ti loading of **M1S2** (0.368 mmol/g) compared to **M1S1** (0.961 mmol/g), (see p.S22 in ESI of **Paper II**). For **M1C1** the ratio of accessible surface-hydroxyl groups to the titanium content was 2.7 : 1.0 (see p.S23 in ESI of **Paper II**) and suggested exclusively bipodally anchored $[(\equiv SiO)_2Ti(CAT tBu_2\text{-}3,6)(OCH_2tBu)_2(HNMe_2)_2]$ and an incomplete consumption of the surface hydroxyls of KIT-6, due to blocking by neopentanol residues (*vide supra*). Moreover, the N/Ti ratio to be expected for complex $[Ti(CAT tBu_2\text{-}3,6)(OCH_2tBu)_2(HNMe_2)_2]$ (**5b**) is 2:1, what has been maintained upon grafting of **5b** onto KIT-6 (**M1a**) as proven by the N/Ti ratio of 1.93 : 1.00, which was calculated from the nitrogen and titanium contents obtained from elemental analyses of **M1C1**,

(see p.S23 in ESI of **Paper II**). Thus, the molecular structure of **5b** has been preserved in material **M1C1**, as desired.

3.3. Convergent approach with the monomeric, heteroleptic neopentoxy complex @m-TiO_2 (Paper II)

To investigate the influence of the novel complex [Ti(CAT*t*Bu_2-3,6)(OCH_2*t*Bu)$_2$($HNMe_2$)$_2$] (**5b**) on the optical and electronic properties of m-TiO_2, the convergent approach, which is depicted in Scheme 2, was also applied on m-TiO_2 (**M2**), where the material [Ti(CAT*t*Bu_2-3,6)(OCH_2*t*Bu)$_2$($HNMe_2$)$_2$]@[m-TiO_2] (**M2C1**) was obtained. For comparison, the aqueous route, which is also shown in Scheme 2, has been transferred from silica to titania, as well, starting directly with the immobilization of the free catechol H_2CAT*t*Bu_2-3,6 onto m-TiO_2 (**M2**) to yield H_2CAT*t*Bu_2-3,6@[m-TiO_2] (**M2A1**).

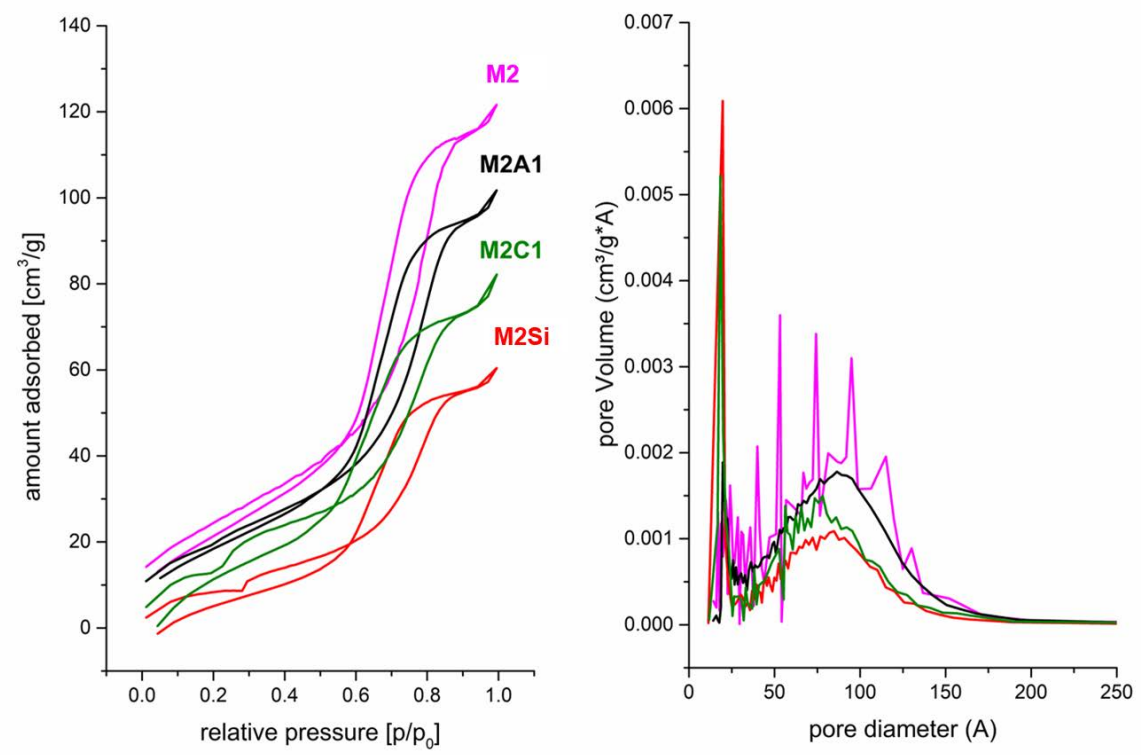

Figure 9: Nitrogen adsorption/desorption isotherms at 77.4 K *(left)* and the corresponding BJH pore size distributions *(right),* derived from the respective isotherm adsorption branch, of m-TiO_2 (**M2**), the aqueous route material **M2A1**, the convergent route material **M2C1** and of the silylated material HN($SiHMe_2$)$_2$@[m-TiO_2] (**M2Si**), where the latter was used to determine the number of accessible surface Ti–OH groups of the m-TiO_2.

The pore volume decreased from m-TiO_2 (**M2**) to **M2A1,** and from m-TiO_2 to **M2C1,** respectively, whereby the type IV isotherms with H1 hysteresis loops were retained, indicating absence of pore blocking (see Figure 9). Interestingly, the pore volume of **M2C1** is smaller than that of **M2A1**: For the aqueous approach from m-TiO_2 (**M2**) to **M2A1** the pore volume was only half as much reduced as that of the material **M2C1** in the convergent approach, which may imply for less surface coverage in the material **M2A1** compared to **M2C1**. This resembles the findings for the functionalized KIT-6 materials **M1A3** and **M1C1** in the previous subchapter.

Compared to the DRIFTS spectrum of m-TiO_2, the spectrum of the material **M2A1** still contains the broad TiO–H vibration at ~3400 cm^{-1}, but no characteristic novel features, whereas the TiO–H band nearly vanished in the DRIFTS spectrum of **M2C1** (see Figure S27 in ESI of **Paper II**). In the latter´s spectrum three new signals appeared at 3252, 2959-2955 and 1456 cm^{-1}, which can be assigned to Ar–H, C–H and C–C/C=C vibrations, which account for a successful grafting reaction of the complex **5b** onto m-TiO_2.

4. Optical and electronic investigations

4.1. X-ray photoelectron spectroscopy (*XPS*) (Paper II)

The nitrogen physisorption and DRFITS spectroscopy results from the previous chapters revealed, that the small amount of accessible surface-OH groups on m-TiO_2 compared to KIT-6, as well as the resulting lower surface coverage with catecholate species in material **M2C1** and especially in material **M2A1** would hardly be analyzable *via* conventional analytical methods, like elemental analysis and ^{13}C MAS NMR spectroscopy. The latter two methods had already reached their limits within the analysis of the aqueous route material (**M1A3**) obtained from KIT-6.

Therefore, the strong surface sensitivity of X-ray photoelectron spectroscopy seemed useful to get direct information on the surface to bulk characteristics of the synthesized compounds: Within the C1s core-level spectrum of the mesoporous TiO_2 (**M2**, Figure 10a), a pronounced, symmetric peak at 286.2 eV is visible, which may seem surprising, as the elemental analysis results of the calcined material (see experimental section of **Paper II**) gave a value for the carbon content of only 0.03 wt%, which is below the resolution limit (0.05 wt%) for C,H,N-elemental analysis (*EA*) with TPD columns. In the field of synthesis chemistry, the m-TiO_2 (**M2**) is therefore defined as pure concerning residual compounds from the synthesis, as the carbon content is negligible. The sensitivity is three magnitudes higher in XPS than in EA.[81-83] Therefore, the pronounced, symmetric peak at 286.2 eV within the C1s spectrum of **M2** implies for trace impurities from the synthesis process, which are located on the m-TiO_2 surface. The peak position is pointing toward alcohol molecules,[84] where HO*i*Pr from the hydrolyzed precursor (Ti(O*i*Pr)$_4$) or EtOH from the final rinsing process (before drying and calcination) are possible residues (see p.S26 in ESI of **Paper II**).

Comparing the C1s peak of the mesoporous TiO_2 (**M2**) with the studies of *Kim and Barteau*,[84] the C1s peak in Figures 6 and 7 of HO*i*Pr at TiO_2 therein is of pronounced asymmetric nature and does not resemble the appearance of **M2**, whereas the EtOH at TiO_2 exhibits a symmetric C1s peak,[84] which is comparable to the one of **M2**. This implies, that the C1s peak within the XPS spectrum of **M2** in Figure 10a stems from EtOH residues.
The other two C1s spectra in Figure 10a both display a broadened, asymmetric main peak,

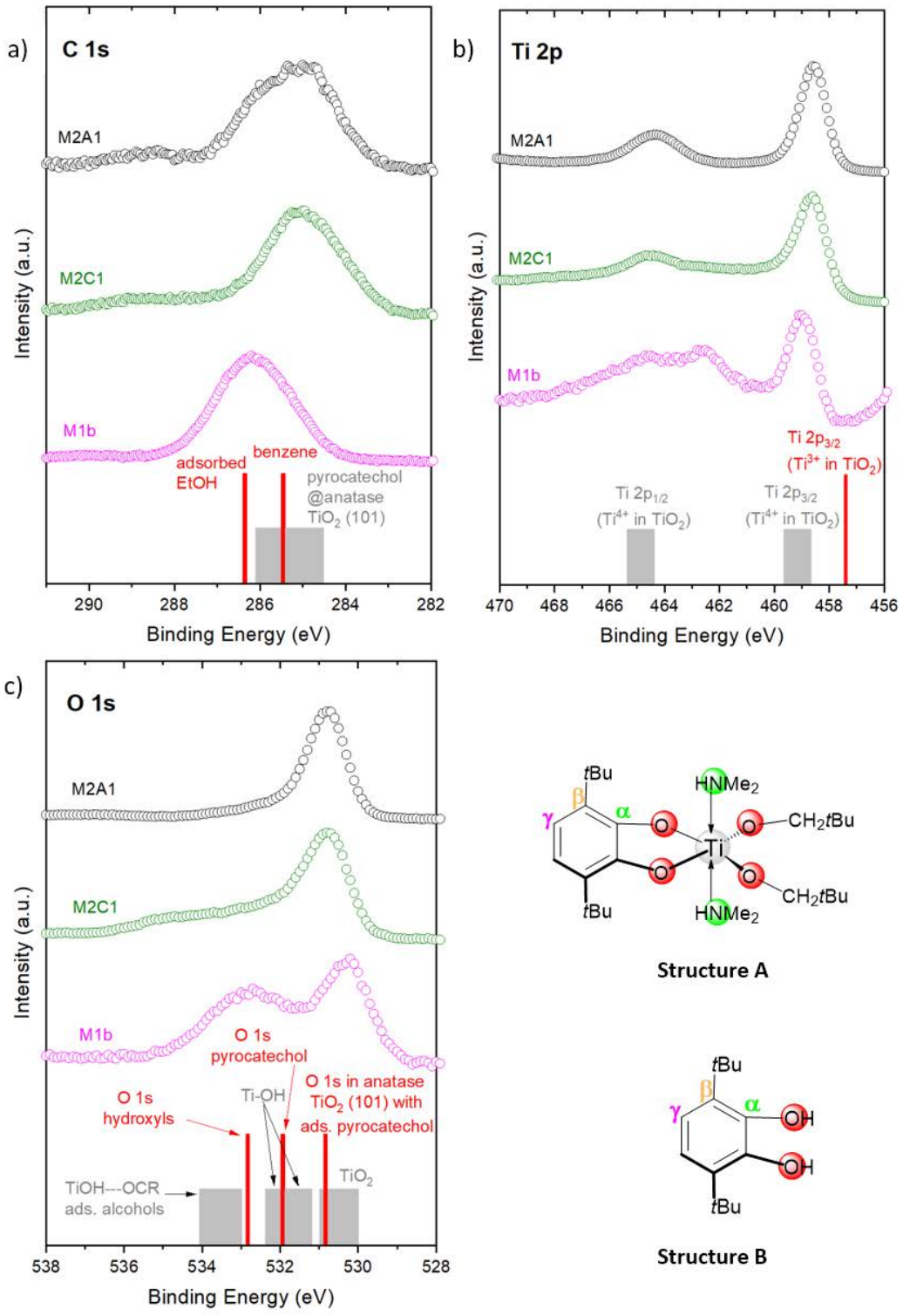

Figure 10: (a) C 1s, (b) Ti 2p and (c) O 1s core-level spectra (XPS) of **M2**, **M2C1**, and **M2A1**. The bar charts display the binding energies for contributions of (a) C 1s species (refs [84-86]), (b) Ti 2p species (refs [86-88]), and (c) O 1s species (refs [86-89]). Structures of the molecular precursors to obtain **M2C1** (structure A) and **M2A1** (structure B). In panel (b), the intensities at around 455 and 463 eV are due to In $3d_{5/2}$ and indium plasmon loss, respectively, also overlapping with the Ti 2p intensity.[90-91] These are especially intense in **M2** because of the smaller amount of powder covering the indium substrate.

centered at 285.0 eV. The shift of the main peak toward lower binding energy implies for new surface species on both materials **M2A1** and **M2C1** compared to the mother material **M2**. The surface species to be expected for **M2A1** and **M2C1** have a benzene backbone – according to *Rocco et al.*[85] the C1s main peak of benzene is located at 285.45 eV and is slightly shifted toward lower binding energy, if the number of inequivalent carbon atoms is increased. This shift is also described by *Kerber et al.*[92] in the C1s spectra of 1,8-bis(dimethylamino)naphthalene, having a broadened main peak, centered at 285.0 eV, which they also ascribe to the non-equivalent carbon atoms. The asymmetry of the main peaks of **M2A1** and **M2C1**, each point toward several carbon components, which are contained therein.[93] Interestingly, the C1s line shape in the spectrum with highest catechol coverage at the anatase TiO_2 surface by *Li et al.*[94] as well as the C1s spectra of pyrocatechol at TiO_2 by *Syres et al.*[86] look very similar to the one of **M2A1**, but the extent of the asymmetry and of the C1s main peak-broadening is more pronounced for **M2A1**. *Syres et al.*[86] have fitted two different species (C–O and $C_{arom.}$) into the C1s main peak of pyrocatechol, which resembles chemically and symmetrically inequivalent carbon atoms. For **M2A1** carbon is either connected to oxygen (C–O), to another carbon (C–C and C=C) or to hydrogen (C–H), which would give at least three types of non-equivalent carbon species, but regarding the structure of the molecular precursor **5b** (see: Figure 10, structure A), even 5 inequivalent carbon species should be considered concerning the symmetry, which may explain the comparatively more pronounced asymmetry and peak broadening, which is also present in the C1s spectrum of **M2C1**.
The peak broadening in the C1s spectra of **M2A1** and **M2C1** is also visible in the ones of differently substituted pentacene molecules,[95-96] which is described to be typical for acenes and even extends to high binding energy tails in the latter case,[85] as, upon core electron excitation, many non-equivalent carbon species contribute to spectral features (due to several possible symmetry reductions).[85]

The O1s spectrum of m-TiO_2 (**M2** in Figure 10b) displays an intensive peak centered at 530.2 eV, which is overlapping with a less intensive peak at 532.7 eV. The intensive main peak is in the common range for O1s in TiO_2 (530.0-530.9 eV).[86-88, 92] Regarding the C1s assignments for **M2**, the smaller peak in the O1s spectrum at 532.7 eV might be correlated to adsorbed EtOH. In contrast, *Jayaweera et al.*[97] show that no additional peak is occurring in the O1s spectrum upon EtOH adsorption on a TiO_2 (110) single crystal: only the O1s main peak´s intensity is reduced and the line-shape becomes slightly asymmetric, whereas the EtOH adsorption itself is confirmed in their C1s spectra. *Stefanov et al.*[89] assume that the shoulder at

532.1 eV in their O1s spectrum of TiO_2 might originate from a partially hydroxide-covered TiO_2 surface. *Kerber et al.*[92] assign a peak at 532.8 eV within the O1s spectrum of "water exposed TiO_2" to C–OH/alcohol and refer to one of their earlier studies:[98] Therein, they correlate the peak at 532.5 eV to O1s of $4TiO_2 \cdot nH_2O$ as well as to C–OH. Regarding the fact that **M2** has quite a few surface-OH groups (see Table 2) and EtOH residues are present, too (as shown in the C1s spectrum of **M2**), an overlay of the O1s signals of both species is assumed.

The other two O1s spectra in Figure 10b both show a main peak at 530.8 eV with broadened full width at half-maximum (fwhm), whereas the latter is much more pronounced for **M2C1** (1.48 eV) than for **M2A1** (1.10 eV). The main peak shift toward a higher binding energy, compared to the substrate material **M2**, accounts for new surface species in **M2A1** and **M2C1**. The differences in line broadening can be explained by the introduction of a different number of oxygen atoms: by grafting **5b** onto m-TiO_2 four oxygen atoms per molecule are introduced in **M2C1**, whereas the immobilization of the bare 3,6-di-*tert*-butylcatechol leads to only two oxygen atoms per molecule in **M2A1**. The huge second peak at 532.7 eV in the O1s spectrum of the m-TiO_2 (**M2**) is not present any more within the O1s spectra of **M2C1** and **M2A1**, which implies for the consumption of a considerable amount of hydroxyl groups and for the displacement of EtOH residues at the m-TiO_2 surface. This is another indicator for a successful surface functionalization with novel species.

Syres et al.[86] have fitted three different species into the O1s spectrum of pyrocatechol@anatase-TiO_2(101): they ascribe 75% contribution to O1s from the TiO_2 crystal (peak at 530.9 eV), 20% to O1s from pyrocatechol after the reaction with the TiO_2 surface (peak at 531.9 eV) and 5% to O1s presumably from surface hydroxyls on TiO_2 and from monopodally anchored pyrocatechol, giving an explanation for the tiny high binding energy feature, which is also present in the O1s spectra of **M2A1** and **M2C1**, as mentioned above. The fact that the O1s high binding energy feature is more pronounced for **M2C1** than for **M2A1** can be explained by the higher complexity of the immobilized surface species in **M2C1**, which may cause more complex relaxation processes upon core hole creation and therefore lead to small satellite peaks.[85, 99-100]

The Ti2p spectrum of m-TiO_2 (**M2** in Figure 10c) contains three peaks: the most intensive peak is centered at 459.0 eV, followed by one at 462.6 eV, which is strongly overlapping with a peak at 464.6 eV. The distance between the latter and the intensive peak is 5.6 eV is in a typical range

for the distance between $Ti2p_{3/2}$ (lower binding energy, higher intensity) and $Ti2p_{1/2}$ (higher binding energy, lower intensity) of TiO_2.[89] The peak at 462.6 eV is not present in the Ti2p spectra of the functionalized materials **M2A1** and **M2C1**, which gives rise to the assumption, that this peak in the Ti2p spectrum of **M2** originates from surface hydroxyls at the m-TiO_2, which are consumed in large amounts during the surface functionalizations. The other two peaks ($Ti2p_{3/2}$ and $Ti2p_{1/2}$) are still present in the Ti2p spectra of **M2A1** and **M2C1**, but are slightly shifted to lower binding energy, while roughly keeping the distance between each other ($Ti2p_{3/2}$ at 458.6 eV and $Ti2p_{1/2}$ at 464.3 eV, intensity 2:1 for **M2A1**; $Ti2p_{3/2}$ at 458.6 eV and $Ti2p_{1/2}$ at 464.5 eV, intensity 2:1 for **M2C1**). A shift to lower binding energy of these two peaks about 0.1-0.3 eV was observed by *Syres et al.*, as well, after the immobilization of pyrocatechol at anatase-TiO_2.[86]

Generally, the obtained XPS data display that virgin m-TiO_2 (**M2**) contains the desired Ti–OH groups and EtOH residues from the rinsing process of the synthesis. The surface hydroxyl groups were consumed and the traces of EtOH were displaced during the surface reactions afterwards. EtOH was only physisorbed at the m-TiO_2 surface, as it caused supplementary peaks within the O1s and Ti2p spectra of **M2**. The O1s and Ti2p spectra of the functionalized materials **M2A1** and **M2C1** do not exhibit such additional peaks. Instead, the binding energy-positions of their main peaks are shifted, which implies for strong interactions with electronic participation of the respective surface species with the m-TiO_2 substrate in materials **M2A1** and **M2C1** and thus, for a more efficient screening of the core hole and thus, for successful surface functionalization reactions.

4.2. Solid-state UV/vis spectroscopy (*SS UV/vis*) (Paper II)

To probe the optical properties of these materials, solid-state ultraviolet visible (*SS UV/vis*) measurements were performed with two setups – an Ulbricht sphere (see Figure S33 in ESI of **Paper II**) and a Praying Mantis setup (see Fig.11a). Two setups have been used, since there were no available data about the stability of the materials, especially concerning **M2C1**, as the isolated molecular complex **5b**, which is shown in Figure 10 (structure A), is sensitive to humidity. For the two setups, the size of the exposed and measured sample areas was different (for details see Table S8 and text below, in ESI of **Paper II**).

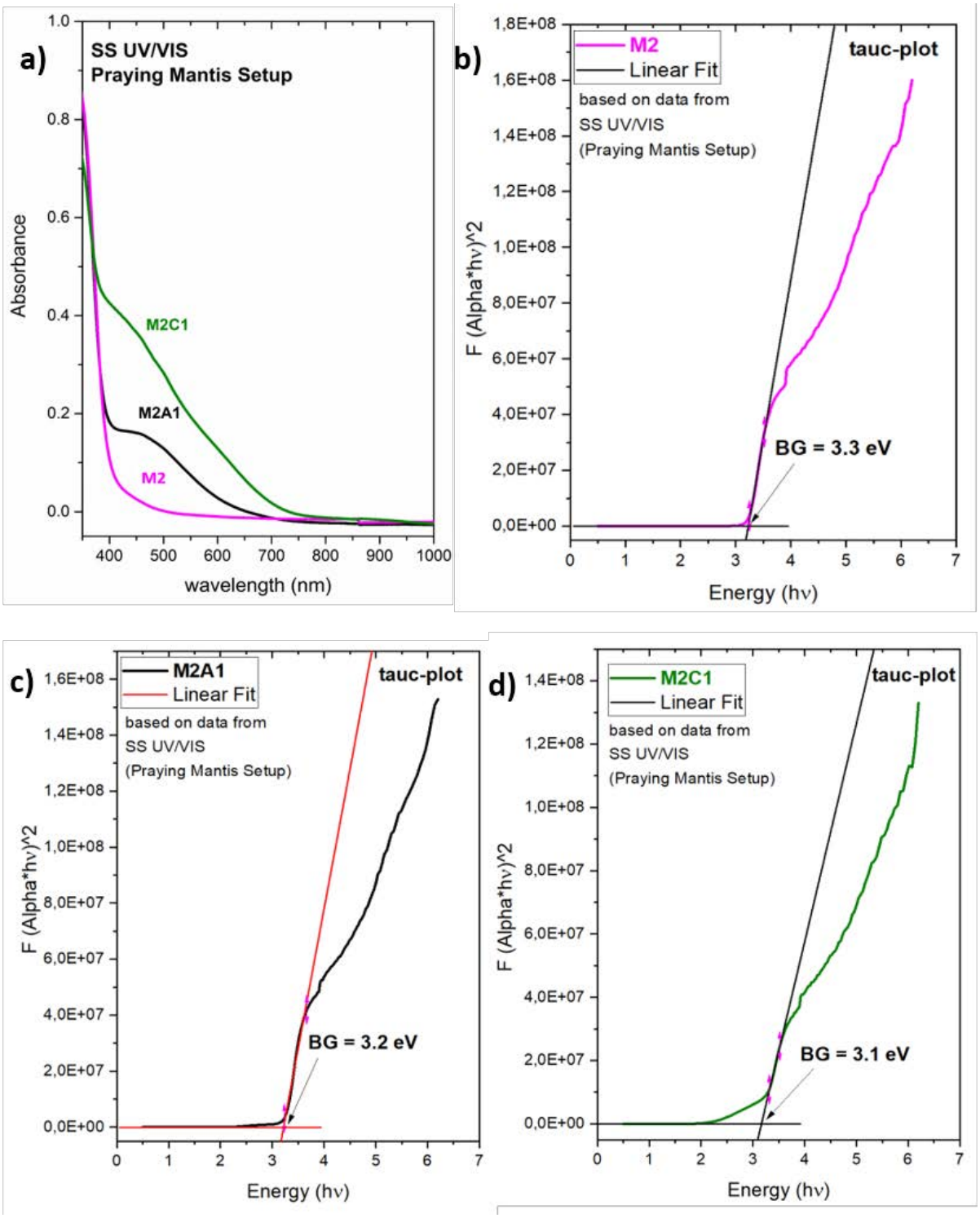

Figure 11: (a) Solid-state UV/vis spectra of **M2**, **M2C1** and **M2A1** (Praying Mantis setup), and the corresponding tauc-plots of (b) **M2**, (c) **M2A1** and (d) **M2C1**.

The absorption curves data from the Solid-state UV/vis measurements of the materials **M2**, **M2A1** and **M2C1** were utilized to obtain the corresponding bandgap values (E_{BG}) *via* tauc-plot

analyses. A tauc-plot is used to determine bandgaps of non-crystalline semiconductors and is named after its inventor Jan Tauc.[101] A linear fit analysis of the steep, near-linear curve range in the low-energy region is performed. The resulting linear curve is extrapolated to obtain the x-intercept giving the bandgap value E_{BG} of the material (see Figure 11). With both setups the same bandgap values were obtained, as displayed in Figures S34-36 in the ESI of **Paper II**. Therefore, the material **M2C1** does not display the same sensitivity to humidity as the precursor complex **5b**. The bandgap for **M2** (~3.3 eV) is consistent with known values for anatase TiO_2.[102-107] It is reduced to ~3.2 eV in **M2A1** and to ~3.1 eV **M2C1**. The latter material contains the bidentate chelating catecholate surface species and proves the greater optical absorption redshift for this species, which has been only theoretically calculated before.[23]

4.3. Ultraviolet photoelectron spectroscopy (*UPS*) (Paper II)

To obtain information about the origin of the optical phenomena the electronic nature of the materials **M2**, **M2A1** and **M2C1** was investigated by using ultraviolet photoelectron spectroscopy (*UPS*), where electrons are removed from a solid specimen by excitation with irradiation in the UV-range ($h\nu \leq 100$ eV).[82-83]

From features in the UPS spectra, which are exemplarily shown in Figure 12, characteristic values, such as the workfunction (φ), were calculated, which are giving information about the electronic nature of the materials. The spectrum width was obtained from the distance between the energy position of the secondary electron-cutoff (E_{SECO}) and the energy position of the fermi level (E_F).

The workfunction was then obtained by the difference of the energy of the incident He-I radiation (21.2 eV) and the spectrum width. With 4.8 eV, the workfunction for m-TiO_2 (**M2**) herein corresponds to typical values for anatase.[103-104, 108-109] The other characteristic values can be found in Table 5 and the derived energy-level alignment is illustrated in Scheme 3. More details about the calculations can be found in **Paper II** and in Figures S37-39 and Table S7+8 in the corresponding ESI.

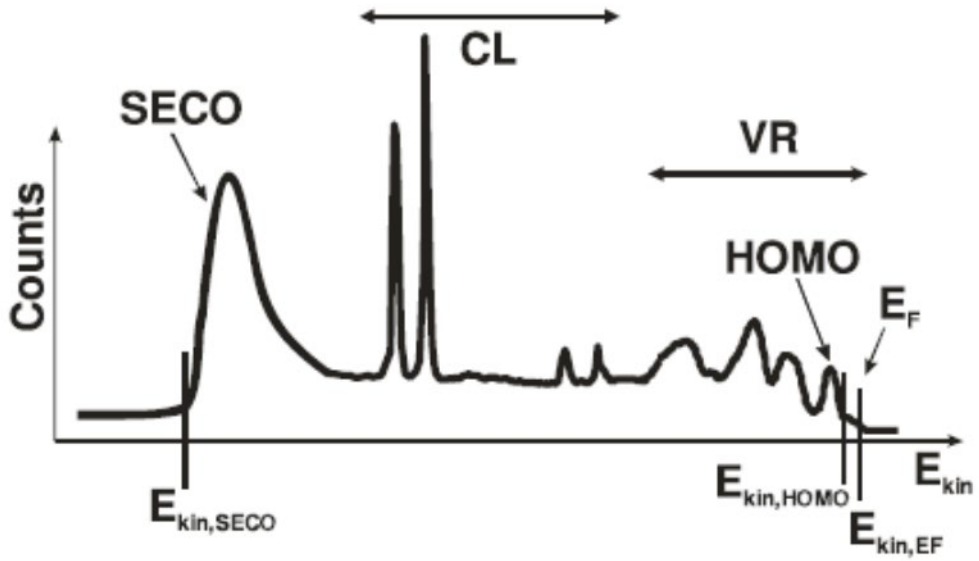

Figure 12: Common features in an exemplaric UPS spectrum according to Figure 1 of reference [110] (CL = core levels, VR = valence region).

Table 5: Energy levels and parameters obtained and/or calculated from UPS and UV/vis spectral data of **M2**, **M2A1** and **M2C1**

Material	**M2**	**M2A1**	**M2C1**
φ [eV]	4.8	4.2	5.0
E_{HOES} [eV]	–1.9	–1.8	–2.1
E_{BG} [eV]	3.3 (3.3)	3.2 (3.2)	3.1 (3.1)
E_{LUES} [eV]	1.4	1.6	1.0
HIB [eV]	1.9	1.8	2.1
IP [eV]	6.7	6.0	7.1
EA [eV]	3.4	2.8	4.0

φ = workfunction, E_{HOES} = highest occupied electronic states, E_{BG} = bandgap, E_{LUES} = lowest unoccupied electronic states, HIB = hole injection barrier, IP = ionization potential, EA = electron affinity.

In Scheme 3 we can see that the highest occupied electronic states (*HOES*) of **M2A1** are higher in energy than those of m-TiO_2. This energetic situation for catechol on titania is described in literature: the catechol´s highest occupied molecular orbital (*HOMO* = the HOES of the

molecular catechol) is energetically located within the bandgap of titania, creating filled electronic states above the valence band (*VB* = HOES of titania) of TiO_2, wherefrom electrons are directly injected into the conduction band (*CB* = lowest unoccupied electronic stated (*LUES*) of titania) of TiO_2.[22, 111] Therefore, less energy is needed than for pure anatase excitation and the excitation mechanism is described as type-II.[80] For **M2C1**, the LUES is energetically located within the bandgap of m-TiO_2. On the one side, the reduction of the energy levels shows that chelating ligands are energetically stabilizing metal centers, which was described in the introduction. On the other hand, it implies for a different excitation mechanism compared to the one described above for **M2A1**, which makes the material itself and the synthesis approach very interesting for potential applications in the field of biomedicine, such as light-induced targeted drug-delivery to fight cancer cells.

Scheme 7: Illustration of the energy-level alignment of **M2**, **M2A1**, and **M2C1**.

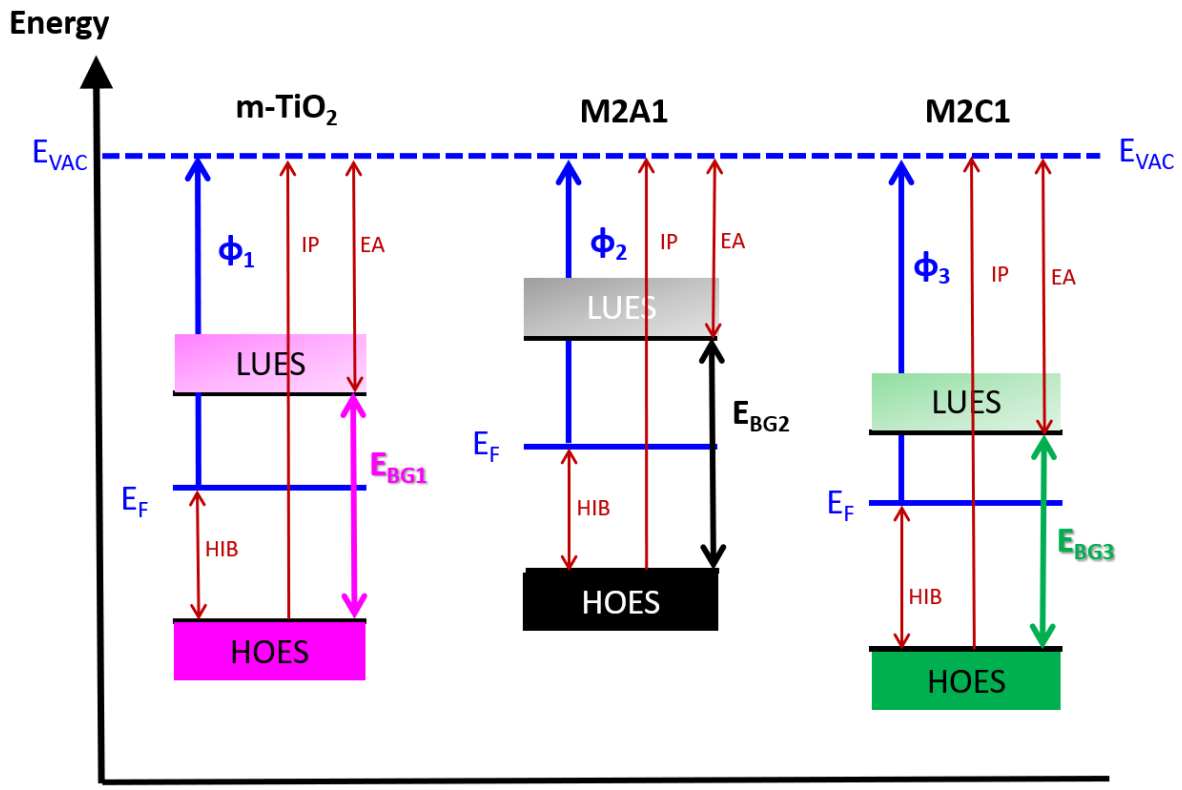

The mechanism for **M2C1** needs to be explored, as, to our knowledge, the bidentate-chelating catecholate species has not been experimentally obtained before on bulk m-TiO_2, but only on

very small titania nanoparticles (see: Introduction). The comparison of one surface species on very small titania nanoparticles with another surface species on bulk-TiO_2 would have involved the morphological effects of two different substrate types, and would not have been suitable to exclusively investigate the effect of the surface structures. Herein, we were able to investigate the influence of two catecholate species on the energy levels of the same substrate type (bulk m-TiO_2).

C

Bibliography

1. Wiberg, N., XXV. Die Titangruppe - 1. Das Titan. In *Lehrbuch der Anorganischen Chemie*, 102 ed.; Holleman, A. F.; Wiberg, N.; Wiberg, E., Eds. Walter de Gruyter & Co.: 10785 Berlin, **2007**; pp 1520-1533.

2. Tschauner, O.; Ma, C.; Lanzirotti, A.; Newville, M. G., Riesite, A New High Pressure Polymorph of TiO_2 from the Ries Impact Structure. *Minerals* **2020**, *10*, 78.

3. Nie, X.; Zhuo, S.; Maeng, G.; Sohlberg, K., Doping of Polymorphs for Altered Optical and Photocatalytic Properties. *Int. J. Photoenergy* **2009**, 294042.

4. Tay, Q.; Liu, X.; Tang, Y.; Jiang, Z.; Sum, T. C.; Chen, Z., Enhanced Photocatalytic Hydrogen Production with Synergistic Two-Phase Anatase/Brookite TiO_2 Nanostructures. *J. Phys. Chem. C* **2013**, *117*, 14973-14982.

5. Zhang, J.; Zhou, P.; Liu, J.; Yu, J., New understanding of the difference of photocatalytic activity among anatase, rutile and brookite TiO_2. *Phys. Chem. Chem. Phys.* **2014**, *16*, 20382-20386.

6. Crossland, E. J. W.; Noel, N.; Sivaram, V.; Leijtens, T.; Alexander-Webber, J. A.; Snaith, H. J., Mesoporous TiO_2 single crystals delivering enhanced mobility and optoelectronic device performance. *Nature* **2013**, *495*, 215-219.

7. Taurino, A. M.; Capone, S.; Siciliano, P.; Toccoli, T.; Boschetti, A.; Guerini, L.; Iannotta, S., Nanostructured TiO_2 thin films prepared by supersonic beams and their application in a sensor array for the discrimination of VOC. *Sens. Actuators, B* **2003**, *92*, 292-302.

8. Chen, D.; Huang, F.; Cheng, Y.-B.; Caruso, R. A., Mesoporous Anatase TiO_2 Beads with High Surface Areas and Controllable Pore Sizes: A Superior Candidate for High-Performance Dye-Sensitized Solar Cells. *Adv Mater* **2009**, *21*, 2206-2210.

9. Wisitsoraat, A.; Tuantranont, A.; Comini, E.; Sberveglieri, G.; Wlodarski, W., Characterization of n-type and p-type semiconductor gas sensors based on NiO_x doped TiO_2 thin films. *Thin Solid Films* **2009**, *517*, 2775-2780.

10. Zhuyi, W.; Liyi, S.; Fengqing, W.; Shuai, Y.; Yin, Z.; Meihong, Z., The sol–gel template synthesis of porous TiO_2 for a high performance humidity sensor. *Nanotechnology* **2011**, *22*, 275502.

11. Yoshikazu, T.; Mao, Y.; Norimichi, K.; Tsutomu, M., Anticancer Effect of Dye-sensitized TiO_2 Nanocrystals by Polychromatic Visible Light Irradiation. *Chem. Lett.* **2006**, *35*, 496-497.

12. Lopez, T.; Ortiz, E.; Alvarez, M.; Navarrete, J.; Odriozola, J. A.; Martinez-Ortega, F.; Páez-Mozo, E. A.; Escobar, P.; Espinoza, K. A.; Rivero, I. A., Study of the stabilization of zinc phthalocyanine in sol-gel TiO_2 for photodynamic therapy applications. *Nanomed. Nanotechnol.* **2010**, *6*, 777-785.

13. Rajh, T.; Dimitrijevic, N. M.; Elhofy, A.; Rozhkova, E., *Handbook of Nanophysics - Vol. Functional Nanomaterials*. CRC-Press: Ed. Sattler, K. D., Boca Raton, **2010**.

14. Paramaguru, G.; Solomon, R. V.; Venuvanalingam, P.; Renganathan, R., Spectroscopic Studies on TiO_2 Enhanced Binding of Hypocrellin B with DNA. *J. Fluoresc.* **2011**, *21*, 1887-1895.

15. Rajh, T.; Dimitrijevic, N. M.; Bissonnette, M.; Koritarov, T.; Konda, V., Titanium Dioxide in the Service of the Biomedical Revolution. *Chem. Rev.* **2014**, *114*, 10177-10216.

16. Luo, L.; Guo, Y.; Yang, J.; Liu, Y.; Chu, S.; Kong, F.; Wang, Y.; Zou, Z., An efficient visible light controlled protein delivery system. *Chem. Commun.* **2011**, *47*, 11243-11245.

17. Bai, J.; Zhou, B., Titanium Dioxide Nanomaterials for Sensor Applications. *Chem. Rev.* **2014**, *114*, 10131-10176.

18. Kurokawa, Y.; Sano, T.; Ohta, H.; Nakagawa, Y., Immobilization of enzyme onto cellulose–titanium oxide composite fiber. *Biotechnol. Bioeng.* **1993**, *42*, 394-397.

19. DeLearie, L. A.; Pierpont, C. G., Catecholate complexes of high oxidation state metal ions. Synthesis and characterization of tris(3,5-di-tert-butylcatecholato)rhenium(VI). *J. Am. Chem. Soc.* **1986**, *108*, 6393-6394.

20. Kwolek, P.; Oszajca, M.; Szaciłowski, K., Catecholate and 2,3-acenediolate complexes of d^0 ions as prospective materials for molecular electronics and spintronics. *Coord. Chem. Rev.* **2012**, *256*, 1706-1731.

21. Dugandzic, I. M.; Jovanovic, D. J.; Mancic, L. T.; Zheng, N.; Ahrenkiel, S. P.; Milosevic, O. B.; Saponjic, Z. V.; Nedeljkovic, J. M., Surface modification of submicronic TiO_2 particles prepared by ultrasonic spray pyrolysis for visible light absorption. *J. Nanopart. Res.* **2012**, *14*, 1157-1168.

22. W. R. Duncan; Prezhdo, O. V., Theoretical Studies of Photoinduced Electron Transfer in Dye-Sensitized TiO_2. *Annu. Rev. Phys. Chem.* **2007**, *58*, 143-184.

23. Luppi, E.; Urdaneta, I.; Calatayud, M., Photoactivity of Molecule–TiO_2 Clusters with Time-Dependent Density-Functional Theory. *J. Phys. Chem. A* **2016**, *120*, 5115-5124.

24. Jankovic, I. A.; Saponjic, Z. V.; Comor, M. I.; Nedeljlkovic, J. M., Surface Modification of Colloidal TiO_2 Nanoparticles with Bidentate Benzene Derivatives. *J. Phys. Chem. C* **2009**, *113*, 12645-12652.

25. Savic, T. D.; Comor, M. I.; Nedeljkovic, J. M.; Veljkovic, D. Z.; Zaric, S. D.; Rakic, V. M.; Jankovic, I. A., The effect of substituents on the surface modification of anatase nanoparticles with catecholate-type ligands: a combined DFT and experimental study. *Phys. Chem. Chem. Phys.* **2014**, *16*, 20796-20805.

26. Chen, L. X.; Rajh, T.; Wang, Z.; Thurnauer, M. C., XAFS Studies of Surface Structures of TiO_2 Nanoparticles and Photocatalytic Reduction of Metal Ions. *J. Phys. Chem. B* **1997**, *101*, 10688-10697.

27. Anwander, R., SOMC@PMS. Surface Organometallic Chemistry at Periodic Mesoporous Silica†. *Chem. Mater.* **2001**, *13*, 4419-4438.

28. Chang, J. S.; Hwang, J. S.; Park, S. E., Preparation and application of nanocatalysts via surface functionalization of mesoporous materials. *Res. Chem. Intermediat.* **2003**, *29*, 921-938.

29. Anwander, R., Immobilization of Molecular Catalysts. In *Handbook of Heterogeneous Catalysis*, Wiley-VCH Verlag GmbH & Co. KGaA: **2008**.

30. Basset, J. M.; Psaro, R.; Roberto, D.; Ugo, R.; (Eds.), *Modern Surface Organometallic Chemistry*. Wiley-VCH Verlag GmbH & Co. KGaA, Weinheim: **2009**.

31. Coperet, C.; Comas-Vives, A.; Conley, M. P.; Estes, D. P.; Fedorov, A.; Mougel, V.; Nagae, H.; Nunez-Zarur, F.; Zhizhko, P. A., Surface Organometallic and Coordination Chemistry toward Single-Site Heterogeneous Catalysts: Strategies, Methods, Structures, and Activities. *Chem. Rev.* **2016**, *116*, 323-421.

32. Liang, Y.; Anwander, R., Nanostructured catalysts via metal amide-promoted smart grafting. *Dalton Trans.* **2013**, *42*, 12521-12545.

33. Liang, Y. C.; Erichsen, E. S.; Anwander, R., Functionalization of large-pore periodic mesoporous silicas: metal silylamide and isopropoxide molecular grafting and secondary surface ligand exchange. *Dalton Trans.* **2013**, *42*, 6922-6935.

34. Schindler, P. W.; Gamsjäger, H., Acid — base reactions of the TiO_2 (Anatase) — water interface and the point of zero charge of TiO_2 suspensions. *Kolloid Z. Z. Polym.* **1972**, *250*, 759-763.

35. Satur, J.; Hiroyoshi, N.; Tsunekawa, M.; Ito, M.; Okamoto, H., Carrier-microencapsulation for preventing pyrite oxidation. *Int. J. Miner. Process.* **2007**, *83*, 116-124.

36. Clayden, J.; Greeves, N.; Warren, S., Organic Chemistry, 17: Elimination reactions. *Organic Chemistry, 2nd Edition, Oxford University Press, Oxford* **2012**, 382-387.

37. Babonneau, F.; Doeuff, S.; Leaustic, A.; Sanchez, C.; Cartier, C.; Verdaguer, M., XANES and EXAFS study of titanium alkoxides. *Inorg. Chem.* **1988**, *27*, 3166-3172.

38. Widenmeyer, M.; Grasser, S.; Köhler, K.; Anwander, R., TiOx overlayers on MCM-48 silica by consecutive grafting. *Microporous Mesoporous Mater.* **2001**, *44*, 327-336.

39. Murahashi, S.-I.; Imada, Y.; Kawakami, T.; Harada, K.; Yonemushi, Y.; Tomita, N., Enantioselective Addition of Ketene Silyl Acetals to Nitrones Catalyzed by Chiral Titanium Complexes. Synthesis of Optically Active β-Amino Acids. *J. Am. Chem. Soc.* **2002**, *124*, 2888-2889.

40. Deschner, T.; Lonstad, B.-T.; Widenmeyer, M.; Anwander, R., Functionalization of MCM-41 and SBA-1 with titanium(IV) (silyl)amides. *J. Mater. Chem.* **2011**, *21*, 5620-5628.

41. Hair, M. L.; Hertl, W., Acidity of surface hydroxyl groups. *J. Phys. Chem.* **1970**, *74*, 91-94.

42. Kruk, M.; Cao, L., Pore Size Tailoring in Large-Pore SBA-15 Silica Synthesized in the Presence of Hexane. *Langmuir* **2007**, *23*, 7247-7254.

43. Sun, J.; Zhang, H.; Ma, D.; Chen, Y.; Bao, X.; Klein-Hoffmann, A.; Pfänder, N.; Su, D. S., Alkanes-assisted low temperature formation of highly ordered SBA-15 with large cylindrical mesopores. *Chem. Commun.* **2005**, 5343-5345.

44. Zhao, D.; Feng, J.; Huo, Q.; Melosh, N.; Fredrickson, G. H.; Chmelka, B. F.; Stucky, G. D., Triblock Copolymer Syntheses of Mesoporous Silica with Periodic 50 to 300 Angstrom Pores. *Science* **1998**, *279*, 548-552.

45. Roux, E. L.; Liang, Y.; Storz, M. P.; Anwander, R., Intramolecular Hydroamination/Cyclization of Aminoalkenes Catalyzed by $Ln[N(SiMe_3)_2]_3$ Grafted onto Periodic Mesoporous Silicas. *J. Am. Chem. Soc.* **2010**, *132*, 16368-16371.

46. Kim, T.-W.; Kleitz, F.; Paul, B.; Ryoo, R., MCM-48-like Large Mesoporous Silicas with Tailored Pore Structure: Facile Synthesis Domain in a Ternary Triblock Copolymer−Butanol−Water System. *J. Am. Chem. Soc.* **2005**, *127*, 7601-7610.

47. Kleitz, F.; Hei Choi, S.; Ryoo, R., Cubic Ia3d large mesoporous silica: synthesis and replication to platinum nanowires, carbon nanorods and carbon nanotubes. *Chem. Commun.* **2003**, 2136-2137.

48. Matthies, A., Synthesis and Catalytical Characterization of REO-Aero- and Xerogels. *Bachelorthesis, Bremen* **2011**.

49. Akimov, Y. K., Fields of Application of Aerogels (Review). *Instruments and Experimental Techniques* **2003**, *46*, 287-299.

50. Hench, L. L.; West, J. K., The sol-gel process. *Chem. Rev.* **1990**, *90*, 33-72.

51. Hüsing, N.; Schubert, U., Aerogels—Airy Materials: Chemistry, Structure, and Properties. *Angew. Chem., Int. Ed.* **1998**, *37*, 22-45.

52. Kresge, C. T.; Leonowicz, M. E.; Roth, W. J.; Vartuli, J. C.; Beck, J. S., Ordered mesoporous molecular sieves synthesized by a liquid-crystal template mechanism. *Nature* **1992**, *359*, 710-712.

53. Beck, J. S.; Vartuli, J. C.; Roth, W. J.; Leonowicz, M. E.; Kresge, C. T.; Schmitt, K. D.; Chu, C. T. W.; Olson, D. H.; Sheppard, E. W., A new family of mesoporous molecular sieves prepared with liquid crystal templates. *J. Am. Chem. Soc.* **1992**, *114*, 10834-10843.

54. Wang, H.; Cheng, X.; Xiao, B.; Wang, C.; Zhao, L.; Zhu, Y., Surface Carbon Activated NiMo/TiO_2 Catalyst Towards Highly Efficient Hydrodesulfurization Reaction. *Catal. Surv. Asia* **2015**, *19*, 78-87.

55. Kim, D. S.; Han, S. J.; Kwak, S.-Y., Synthesis and photocatalytic activity of mesoporous TiO_2 with the surface area, crystallite size, and pore size. *J. Colloid Interface Sci.* **2007**, *316*, 85-91.

56. Naboulsi, I.; Lebeau, B.; Michelin, L.; Carteret, C.; Vidal, L.; Bonne, M.; Blin, J.-L., Insights into the Formation and Properties of Templated Dual Mesoporous Titania with Enhanced Photocatalytic Activity. *ACS Appl. Mater. Interfaces* **2017**, *9*, 3113-3122.

57. Antonelli, D. M.; Ying, J. Y., Synthesis of Hexagonally Packed Mesoporous TiO_2 by a Modified Sol–Gel Method. *Angew. Chem. Int. Ed.* **1995**, *34*, 2014-2017.

58. Zhou, W.; Fu, H. G., Mesoporous TiO_2: Preparation, Doping, and as a Composite for Photocatalysis. *Chemcatchem* **2013**, *5*, 885-894.

59. Zimny, K.; Ghanbaja, J.; Carteret, C.; Stébé, M.-J.; Blin, J.-L., Highly ordered mesoporous titania with semi crystalline framework templated by large or small nonionic surfactants. *New J. Chem.* **2010**, *34*, 2113-2117.

60. Kang, C.; Jing, L.; Guo, T.; Cui, H.; Zhou, J.; Fu, H., Mesoporous SiO_2-Modified Nanocrystalline TiO_2 with High Anatase Thermal Stability and Large Surface Area as Efficient Photocatalyst. *J. Phys. Chem. C* **2009**, *113*, 1006-1013.

61. Zhang, J.; Deng, Y.; Gu, D.; Wang, S.; She, L.; Che, R.; Wang, Z.-S.; Tu, B.; Xie, S.; Zhao, D., Ligand-Assisted Assembly Approach to Synthesize Large-Pore Ordered Mesoporous Titania with Thermally Stable and Crystalline Framework. *Adv. Energy Mater.* **2011**, *1*, 241-248.

62. Tian, G.; Fu, H.; Jing, L.; Xin, B.; Pan, K., Preparation and Characterization of Stable Biphase TiO_2 Photocatalyst with High Crystallinity, Large Surface Area, and Enhanced Photoactivity. *J. Phys. Chem. C* **2008**, *112*, 3083-3089.

63. Zhou, W.; Sun, F.; Pan, K.; Tian, G.; Jiang, B.; Ren, Z.; Tian, C.; Fu, H., Well-Ordered Large-Pore Mesoporous Anatase TiO_2 with Remarkably High Thermal Stability and Improved Crystallinity: Preparation, Characterization, and Photocatalytic Performance. *Adv. Funct. Mater.* **2011**, *21*, 1922-1930.

64. Tian, G.; Fu, H.; Jing, L.; Tian, C., Synthesis and photocatalytic activity of stable nanocrystalline TiO_2 with high crystallinity and large surface area. *J. Hazard Mater.* **2009**, *161*, 1122-1130.

65. Yang, P.; Zhao, D.; Margolese, D. I.; Chmelka, B. F.; Stucky, G. D., Generalized syntheses of large-pore mesoporous metal oxides with semicrystalline frameworks. *Nature* **1998**, *396*, 152-155.

66. Brinker, C. J.; Scherer, G. W., CHAPTER 2 - Hydrolysis and Condensation I: Nonsilicates. In *Sol-Gel Science*, Brinker, C. J.; Scherer, G. W., Eds. Academic Press: San Diego, **1990**; pp 20-95.

67. Vioux, A., Nonhydrolytic Sol−Gel Routes to Oxides. *Chem. Mater.* **1997**, *9*, 2292-2299.

68. Arnal, P.; Corriu, R. J. P.; Leclercq, D.; Mutin, P. H.; Vioux, A., A Solution Chemistry Study of Nonhydrolytic Sol−Gel Routes to Titania. *Chem. Mater.* **1997**, *9*, 694-698.

69. Brunauer, S.; Emmett, P. H.; Teller, E., Adsorption of Gases in Multimolecular Layers. *J. Am. Chem. Soc.* **1938**, *60*, 309-319.

70. Barrett, E.; Joyner, L.; Halenda, P., The Determination of Pore Volume and Area Distributions in Porous Substances. I. Computations from Nitrogen Isotherms. *J. Am. Chem. Soc.* **1951**, *73*, 373-380.

71. König, S., Manganese, Chromium, and Cobalt Surface-Functionalized Cubic Mesoporous Silica KIT-6 and MCM-48 *Diplomathesis, Tübingen* **2009**.

72. Sing, K. S. W.; Everett, D. H.; Haul, H. R. A. W.; Moscou, L.; Pierotti, R. A.; Rouquérol, J.; Siemieniewska, T., REPORTING PHYSISORPTION DATA FOR GAS/SOLID SYSTEMS with Special Reference to the Determination of Surface Area and Porosity. *Pure Appl. Chem.* **1985**, *57*, 603-619.

73. Bubnov, M. P.; Teplova, I. A.; Druzhkov, N. O.; Fukin, G. K.; Cherkasova, A. V.; Cherkasov, V. K., Catecholato complexes of cobalt and nickel with 1,4-disubstituted-1,4-diazabutadiens-1,3 and 1,2-bis(diphenylphosphino)ethane. *J. Chem. Sci.* **2015**, *127*, 527-535.

74. Pierpont, C. G.; Buchanan, R. M., Transition metal complexes of o-benzoquinone, o-semiquinone, and catecholate ligands. *Coord. Chem. Rev.* **1981**, *38*, 45-87.

75. Lange, C. W.; Conklin, B. J.; Pierpont, C. G., Radical Superexchange in Semiquinone Complexes Containing Diamagnetic Metal Ions. 3,6-Di-tert-butyl-1,2-semiquinoate Complexes of Zinc(II), Cobalt(III), Gallium(III), and Aluminum(III). *Inorg. Chem.* **1994**, *33*, 1276-1283.

76. Boyle, T. J.; Barnes, D. L.; Heppert, J. A.; Morales, L.; Takusagawa, F.; Connolly, J. C., Kinetics and thermodynamics of intra-and intermolecular rearrangement in binaphtholate complexes of titanium (IV). *Organometallics* **1992**, *11*, 1112-1126.

77. Benedict, J. B.; Coppens, P., The Crystalline Nanocluster Phase as a Medium for Structural and Spectroscopic Studies of Light Absorption of Photosensitizer Dyes on Semiconductor Surfaces. *J. Am. Chem. Soc.* **2010**, *132*, 2938-2944.

78. Davidson, M. G.; Jones, M. D.; Lunn, M. D.; Mahon, M. F., Synthesis and X-ray Structures of New Titanium(IV) Aryloxides and Their Exploitation for the Ring Opening Polymerization of ε-Caprolactone. *Inorg. Chem.* **2006**, *45*, 2282-2287.

79. Wallace, W. A.; Potvin, P. G., Structurally Diverse Aggregating Condensations of Ti(IV) Catecholates. *Inorg. Chem.* **2007**, *46*, 9463-9472.

80. Finkelstein-Shapiro, D.; Davidowski, S. K.; Lee, P. B.; Guo, C.; Holland, G. P.; Rajh, T.; Gray, K. A.; Yarger, J. L.; Calatayud, M., Direct Evidence of Chelated Geometry of Catechol on TiO_2 by a Combined Solid-State NMR and DFT Study. *J. Phys. Chem. C* **2016**, *120*, 23625-23630.

81. Vickerman, J. C., 1_Introduction. In *Surface Analysis - The Principal Techniques*, 2nd ed.; Vickerman, J. C.; Gilmore, I. S., Eds. John Wiley & Sons Ltd, United Kingdom: Chichester, **2009**; pp 1-8.

82. Ratner, B. D.; Castner, D. G., 3_Electron Spectroscopy for Chemical Analysis. In *Surface Analysis - The Principal Techniques*, 2nd ed.; Vickerman, J. C.; Gilmore, I. S., Eds. John Wiley & Sons Ltd, United Kingdom: Chichester, **2009**; pp 47-112.

83. Hüfner, S., *Photoelectron Spectroscopy: Principles and Applications*. 3rd ed.; Springer, Germany: Berlin Heidelberg, **2003**.

84. Kim, K. S.; Barteau, M. A., Reactions of aliphatic alcohols on the {011}-facetted TiO_2 (001) surface. *J. Mol. Catal.* **1990**, *63*, 103-117.

85. Rocco, M. L. M.; Haeming, M.; Batchelor, D. R.; Fink, R.; Scholl, A.; Umbach, E., Electronic relaxation effects in condensed polyacenes: A high-resolution photoemission study. *J. Chem. Phys.* **2008**, *129*, 074702.

86. Syres, K. L.; Thomas, A. G.; Flavell, W. R.; Spencer, B. F.; Bondino, F.; Malvestuto, M.; Preobrajenski, A.; Grätzel, M., Adsorbate-Induced Modification of Surface Electronic Structure: Pyrocatechol Adsorption on the Anatase TiO_2 (101) and Rutile TiO_2 (110) Surfaces. *J. Phys. Chem. C* **2012**, *116*, 23515-23525.

87. Diebold, U.; Madey, T. E., TiO_2 by XPS. *Surf. Sci. Spectra* **1996**, *4*, 227-231.

88. Sanjinés, R.; Tang, H.; Berger, H.; Gozzo, F.; Margaritondo, G.; Lévy, F., Electronic structure of anatase TiO_2 oxide. *J. Appl. Phys.* **1994**, *75*, 2945-2951.

89. Stefanov, P.; Shipochka, M.; Stefchev, P.; Raicheva, Z.; Lazarova, V.; Spassov, L., XPS characterization of TiO_2 layers deposited on quartz plates. *J. Phys. Conf. Ser.* **2008**, *100*, 012039.

90. Detweiler, Z. M.; Wulfsberg, S. M.; Frith, M. G.; Bocarsly, A. B.; Bernasek, S. L., The oxidation and surface speciation of indium and indium oxides exposed to atmospheric oxidants. *Surf. Sci.* **2016**, *648*, 188-195.

91. Thompson, A. C.; Vaughan, D.; Optics, C. f. X.-r.; optics, C. f. X.-r.; source, a. l.; Source, L. B. N. L. A. L., *X-ray Data Booklet*. Lawrence Berkeley National Laboratory, University of California: **2001**; https://xdb.lbl.gov/.

92. Kerber, S. J.; Bruckner, J. J.; Wozniak, K.; Seal, S.; Hardcastle, S.; Barr, T. L., The nature of hydrogen in x-ray photoelectron spectroscopy: General patterns from hydroxides to hydrogen bonding. *J. Vac. Sci. Technol. A* **1996**, *14*, 1314-1320.

93. Schöll, A.; Zou, Y.; Jung, M.; Schmidt, T.; Fink, R.; Umbach, E., Line shapes and satellites in high-resolution x-ray photoelectron spectra of large π-conjugated organic molecules. *J. Chem. Phys.* **2004**, *121*, 10260-10267.

94. Li, S.-C.; Losovyj, Y.; Diebold, U., Adsorption-Site-Dependent Electronic Structure of Catechol on the Anatase TiO_2(101) Surface. *Langmuir* **2011**, *27*, 8600-8604.

95. Savu, S.-A.; Casu, M. B.; Schundelmeier, S.; Abb, S.; Tönshoff, C.; Bettinger, H. F.; Chassé, T., Nanoscale assembly, morphology and screening effects in nanorods of newly synthesized substituted pentacenes. *RSC Advances* **2012**, *2*, 5112-5118.

96. Savu, S.-A.; Sonström, A.; Bula, R.; Bettinger, H. F.; Chassé, T.; Casu, M. B., Intercorrelation of Electronic, Structural, and Morphological Properties in Nanorods of 2,3,9,10-Tetrafluoropentacene. *ACS Appl. Mater. Interfaces* **2015**, *7*, 19774-19780.

97. Jayaweera, P. M.; Quah, E. L.; Idriss, H., Photoreaction of Ethanol on TiO_2(110) Single-Crystal Surface. *J. Phys. Chem. C* **2007**, *111*, 1764-1769.

98. Kerber, S. J., Bioreactivity of titanium implant alloys. *J. Vac. Sci. Technol. A* **1995**, *13*, 2619-2623.

99. Greczynski, G.; Hultman, L., A step-by-step guide to perform x-ray photoelectron spectroscopy. *J. Appl. Phys.* **2022**, *132*, 011101.

100. Sen, S. K.; Riga, J.; Verbist, J., 2s and 2p X-ray photoelectron spectra of Ti^{4+} ion in TiO_2. *Chem. Phys. Lett.* **1976**, *39*, 560-564.

101. Tauc, J., Optical properties and electronic structure of amorphous Ge and Si. *Mater. Res. Bull.* **1968**, *3*, 37-46.

102. Henningsson, A.; Rensmo, H.; Sandell, A.; Siegbahn, H.; Södergren, S.; Lindström, H.; Hagfeldt, A., Electronic structure of electrochemically Li-inserted TiO_2 studied with synchrotron radiation electron spectroscopies. *J. Chem. Phys.* **2003**, *118*, 5607-5612.

103. Kumarasinghe, A. R.; Flavell, W. R.; Thomas, A. G.; Mallick, A. K.; Tsoutsou, D.; Chatwin, C.; Rayner, S.; Kirkham, P.; Warren, S.; Patel, S.; Christian, P.; O'Brien, P.; Grätzel, M.; Hengerer, R., Electronic properties of the interface between p-CuI and anatase-phase n-TiO_2 single crystal and nanoparticulate surfaces: A photoemission study. *J. Chem. Phys.* **2007**, *127*, 114703.

104. Li, H.; Xie, C.; Liao, Y.; Liu, Y.; Zou, Z.; Wu, J., Characterization of Incidental Photon-to-electron Conversion Efficiency (IPCE) of porous TiO_2/SnO_2 composite film. *J. Alloys Compd.* **2013**, *569*, 88-94.

105. Maheu, C.; Cardenas, L.; Puzenat, E.; Afanasiev, P.; Geantet, C., UPS and UV spectroscopies combined to position the energy levels of TiO_2 anatase and rutile nanopowders. *Phys. Chem. Chem. Phys.* **2018**, *20*, 25629-25637.

106. Scanlon, D. O.; Dunnill, C. W.; Buckeridge, J.; Shevlin, S. A.; Logsdail, A. J.; Woodley, S. M.; Catlow, C. R. A.; Powell, M. J.; Palgrave, R. G.; Parkin, I. P.; Watson, G. W.; Keal, T. W.; Sherwood, P.; Walsh, A.; Sokol, A. A., Band alignment of rutile and anatase TiO_2. *Nat. Mater.* **2013**, *12*, 798-801.

107. Tang, H.; Berger, H.; Schmid, P. E.; Lévy, F., Optical properties of anatase (TiO_2). *Solid State Commun.* **1994**, *92*, 267-271.

108. Kashiwaya, S.; Morasch, J.; Streibel, V.; Toupance, T.; Jaegermann, W.; Klein, A., The Work Function of TiO_2. *Surfaces* **2018**, *1*, 73-89.

109. Yew, R.; Karuturi, S. K.; Liu, J.; Tan, H. H.; Wu, Y.; Jagadish, C., Exploiting defects in TiO_2 inverse opal for enhanced photoelectrochemical water splitting. *Opt. Express* **2019**, *27*, 761-773.

110. Koch, N., Energy levels at interfaces between metals and conjugated organic molecules. *J. Phys.: Condens. Matter* **2008**, *20*, 12.

111. Higashimoto, S.; Nishi, T.; Yasukawa, M.; Azuma, M.; Sakata, Y.; Kobayashi, H., Photocatalysis of titanium dioxide modified by catechol-type interfacial surface complexes (ISC) with different substituted groups. *J. Catal.* **2015**, *329*, 286-290.

D

Paper I

ChemPubSoc Europe

DOI: 10.1002/ejic.201801269

EurJIC European Journal of Inorganic Chemistry

Full Paper

Surface Organotitanium Chemistry

Titanium(IV) Catecholate-Grafted Mesoporous Silica KIT-6: Probing Sequential and Convergent Immobilization Approaches

Andrea Sonström,[a] David Schneider,[a] Cäcilia Maichle-Mössmer,[a] and Reiner Anwander*[a]

Abstract: Molecular Ti^{IV} catecholates were obtained as dimeric complexes from protonolysis reactions of $Ti(NMe_2)_4$ with pyrocatechol (H_2CAT), 4-*tert*-butylcatechol (H_2CAT*t*Bu-4), 3,5-di-*tert*-butylcatechol (H_2CAT*t*Bu_2–3,5), 2,3-dihydroxynaphthalene (H_2DHN) and 3,6-di-*tert*-butylcatechol (H_2CAT*t*Bu_2–3,6). The heteroleptic monocatecholate amide complexes were characterized by X-ray structure analysis but only $[Ti(CAT)(NMe_2)_2]_2$ and $[Ti(DHN)(NMe_2)_2]_2$ were obtained as pure compounds. The solid-state structures revealed Ti^{IV} centers bridged by two catecholato ligands adopting a $[\kappa^2(O,\mu\text{-}O')]$ coordination mode except for complex $[Ti(CAT$*t*Bu_2–3,6$)(NMe_2)_2]$ featuring one bridging catecholato and one bridging amido ligand. Heteroleptic complex $[Ti(DHN)(NMe_2)_2]_2$ was grafted onto large-pore periodic mesoporous silica KIT-6 (*convergent approach*) and the resulting Ti^{IV} surface species compared with the established *sequential approach*, i.e., grafting of $Ti(NMe_2)_4$ onto the KIT-6 material and subsequent ligand exchange with H_2DHN. Dimeric complex $[Ti(DHN)(NMe_2)_2]_2$ proved to be sufficiently reactive for a direct grafting yielding the same dominant surface species as obtained according to the sequential approach, as revealed by nitrogen physisorption, elemental analysis, and DRIFT/^{13}C CP MAS spectroscopy.

Introduction

Post-synthesis surface functionalization of oxidic materials like silica displays a feasible tool for the synthesis of various kinds of hybrid materials.[1] Prominent examples are mixed metal oxide(s) at silica surfaces and (metal)organic-inorganic hybrids emerging from the immobilization of organometallics on silica supports.[1] In particular, the latter surface organometallic chemistry (SOMC) approach provides access to a vast range of heterogeneous catalysts in the context of more cost-efficient and environmentally benign productions.[1e,2] Moreover, periodic mesoporous silicas (PMSs) with defined pore structure and adjustable pore size offer promising support materials in the field of catalysis.[1c,1d,3]

Commonly, SOMC involves the grafting of a reactive organometallic complex onto an oxidic material (like PMS) followed optionally by a secondary ligand exchange to generate the desired surface species.[4] The advantage of this *sequential strategy*[1e] originates from the possibility to conduct such second-step ligand exchanges with multiple proligands in adjustable ratios simultaneously or successively.[1a] However, this approach suffers from the drawback that already the initial grafting of the organometallic complex may create different surface species. Consequently, the feasibility of the secondary ligand exchange will depend on the steric and reactivity constraints of the proligand and the organometallic precursor, respectively.[1a,1d,5] If a single defined surface species is desired, the *convergent strategy*[1e] is more favorable. Here, a tailor-made heteroleptic organometallic precursor is grafted onto the silica support via the reactive ligands,[6] usually undergoing protonolysis with the surface silanol groups, while retaining the functional ligand at the metal center (e.g., chiral ligand for enantioselective catalysis or ligand controlling any luminescent properties).[1a,2]

We have previously reported on the immobilization of (*R*)-H_2BINOL [(*R*)-(+)-1,1′-bi-2-naphthol] on PMS MCM-41 via the sequential approach using $Ti(NMe_2)_4$ as a precursor.[7] Overall, such amido/phenol-type Brønsted-acid-base reactions are driven by the high basicity of the amido ligand and the formation of gaseous $HNMe_2$ (Scheme 1).[8] Unfortunately, at that time the corresponding convergent approach employing $Ti(NMe_2)_2$(*R*-BINOL) as the grafting precursor has not been examined. The latter heteroleptic complex was only obtained in very low yields and could not be structurally characterized.[7]

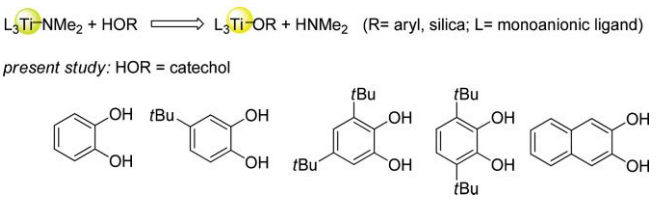

Scheme 1. Protonolysis of titanium(IV) amide with alcoholic substrates.

On the other hand, catechols (benzene derivatives with vicinal diols) impart also a stabilizing ligand (chelate) environment for oxophilic metal centers and their relevance for catalysis has been pointed out. For example, *Murahashi* et al. used mixed (S)-BINOLato-catecholato titanium(IV) complexes as enantioselective catalysts for the synthesis of optically active β-amino

[a] *Institut für Anorganische Chemie, University of Tübingen (EKUT), Auf der Morgenstelle 18, 72076, Germany*
E-mail: reiner.anwander@uni-tuebingen.de
http://uni-tuebingen.de/syncat-anwander

Supporting information and ORCID(s) from the author(s) for this article are available on the WWW under https://doi.org/10.1002/ejic.201801269.

acids.[9] The catalyst synthesis was accomplished by adding both proligands subsequently to the $Ti(OiPr)_4$ precursor solution, which argues for a similar reactivity behavior of BINOL and catechol. Furthermore, catechols are known as efficient complexation agents for free metal ions[10] as well as for oxide surfaces: phenolic OH groups are quite acidic [pK_{a1}(catechol) = 9.25 and pK_{a2}(catechol) = 13.0 in H_2O][11] when compared to aliphatic alcohols in general [pK_a(alcohol) ca. 17 in H_2O] and can readily react with Brønsted-basic functional groups.[12]

Thus, we decided to investigate two strategies outlined in Scheme 2: A) immobilization of $Ti(NMe_2)_4$ on PMS, and subsequent ligand exchange with a catechol (*sequential approach*); B) synthesis of a heteroleptic Ti^{IV}-catecholate complex (according to Scheme 1), and its subsequent immobilization on PMS material (*convergent approach*).

This second approach is assumed to have two major advantages: a) a molecular complex is easier to characterize than grafted materials and the knowledge of its crystal structure should allow for a better predictability of the SOMC of the heteroleptic titanium(IV) catecholate complex than in the case of the sequential approach, and b) it should save one grafting step including posttreatment and time-consuming analyses.

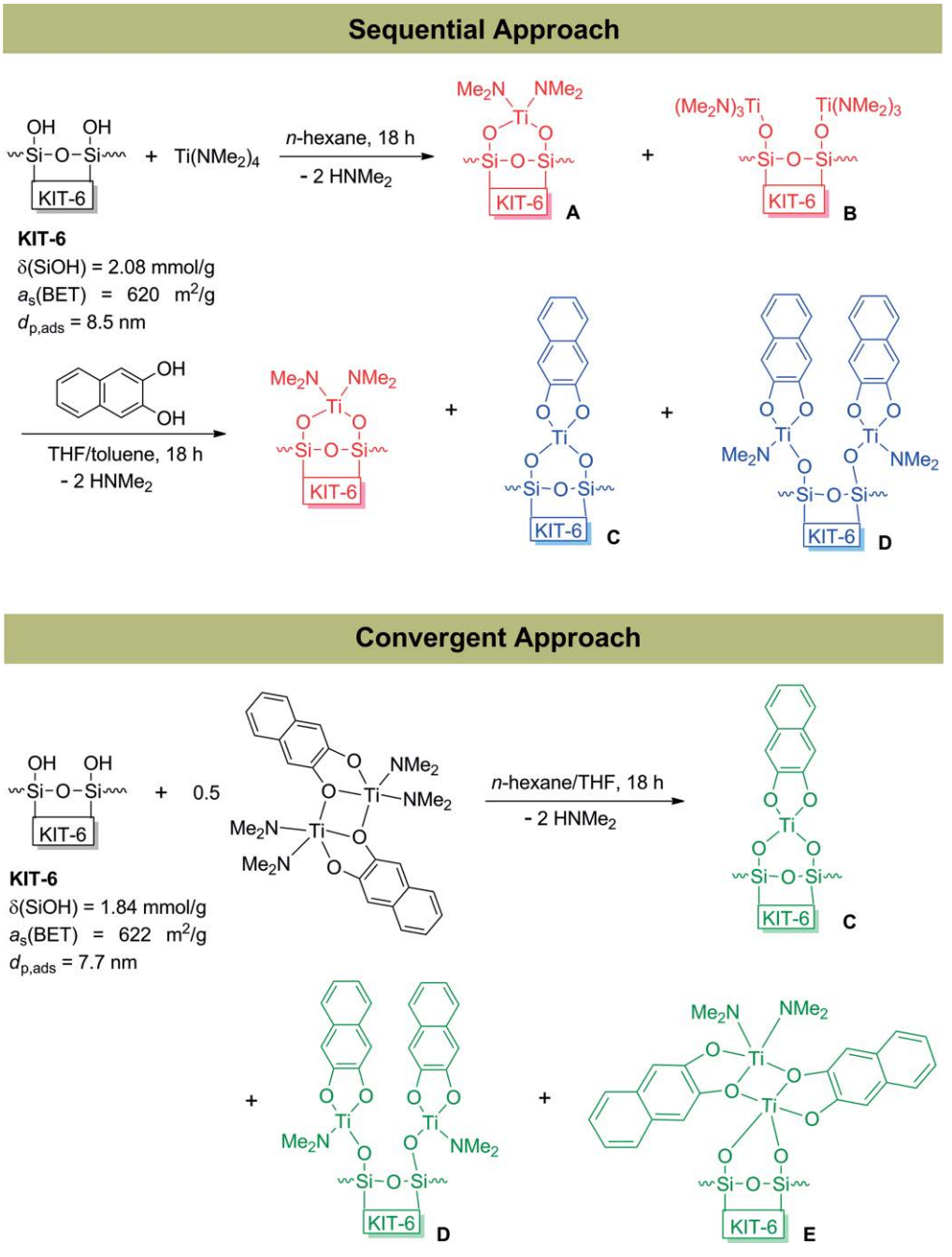

Scheme 2. Schematic illustration of potential surface species: the KIT-6 parent materials **M1a**/**M1b** (black); after grafting of $Ti(NMe_2)_4$ according to the sequential approach (red); and after ligand exchange with H_2DHN according to the sequential approach (blue) or after grafting of **2a** according to the convergent approach (green).

Results and Discussion

Titanium(IV) Grafting Precursors

In order to implement the convergent approach of a molecular heteroleptic titanium(IV) catecholate complex onto a PMS material, the respective molecular complexes were initially synthesized. Using $Ti(NMe_2)_4$ as a precursor and commercially available pyrocatechol and 2,3-dihydroxynaphthalene as proligands, dimeric titanium(IV) catecholate complexes $[Ti(CAT)(NMe_2)_2]_2$ (**1a**) and $[Ti(DHN)(NMe_2)_2]_2$ (**2a**) were obtained and successfully crystallized (cf., Scheme 1).

The solid-state structure of dimeric $[Ti(CAT)(NMe_2)_2]_2$ (**1a**) revealed two 5-coordinate Ti^{IV} centers being bridged by one of their catecholato oxygen atoms each (see Figure 1). Such catecholato bridging was also detected in the anionic complex $[Et_3NH]_2[Ti(CAT\textit{t}Bu_2\text{–}3,5)_2(HCAT\textit{t}Bu_2\text{–}3,5)]_2{\cdot}2CHCl_3$ featuring 6-coordinate Ti^{IV} centers.[13] Aiming at a monomeric complex for better comparability with the envisaged "monomeric" surface complexes, crystallization of **1a** was attempted from thf/*n*-pentane at ambient temperature, instead of toluene/*n*-hexane, at –35 °C. However, the crystal structure analysis of **1a(thf)** showed again a dimeric arrangement with one 5-coordinate and one 6-coordinate Ti^{IV} center bridged by one of their catecholato oxygen atoms each (see Figure 1). Thus, thf adduct formation does not prevent the complexes from dimerization. As expected, the Ti–N distances of the thf-free Ti1 of **1a** [av. 1.880 Å] are comparable to the ones found in **1a(THF)** [av. 1.874 Å], but longer for the thf-coordinated Ti2 center of **1a(thf)** [av. 1.915 Å]. This also affects the N–Ti–N bond angles which are more acute at the 6-coordinate Ti2 of **1a(thf)** [97.86(7) °] compared to those at the 5-coordinate Ti centers of **1a** and **1a(thf)** (ca. 105.0°). In general the Ti–O distances in **1a** and in **1a(thf)** are similar and in accordance with the ones reported for other Ti^{IV} catecholate complexes (see Table 1, and right column of Table S1 in the Supporting Information).[13] In **1a(thf)**, the distances of the two bridging oxygen atoms to their respective adjacent titanium atoms are not equivalent [Ti2–O1 2.0258(13) Å and Ti1–O3 1.9883(13) Å], but comparable to those found for the bridging ligands in $[Et_3NH]_2[Ti(CAT\textit{t}Bu_2\text{–}3,5)_2(HCAT\text{-}\textit{t}Bu_2\text{–}3,5)]_2{\cdot}2CHCl_3$ [Ti–O3′ 2.041(2) Å and Ti′–O3 2.079(1) Å].[13] In **1a** however, the two bridging oxygen atoms are equivalent [Ti1–O1a = Ti1a–O1 2.0014(11) Å].

For $[Ti(DHN)(NMe_2)_2]_2$ (**2a**) only the thf adduct **2a(thf)** could be obtained in crystalline form via vapor diffusion crystallization using thf/*n*-pentane at ambient temperature. Surprisingly, the crystal system of **2a(thf)** is triclinic, whereas that of **1a(thf)** is monoclinic (see Tables 1 and S3 in the Supporting Information). On the other hand, the metrical trends involving the

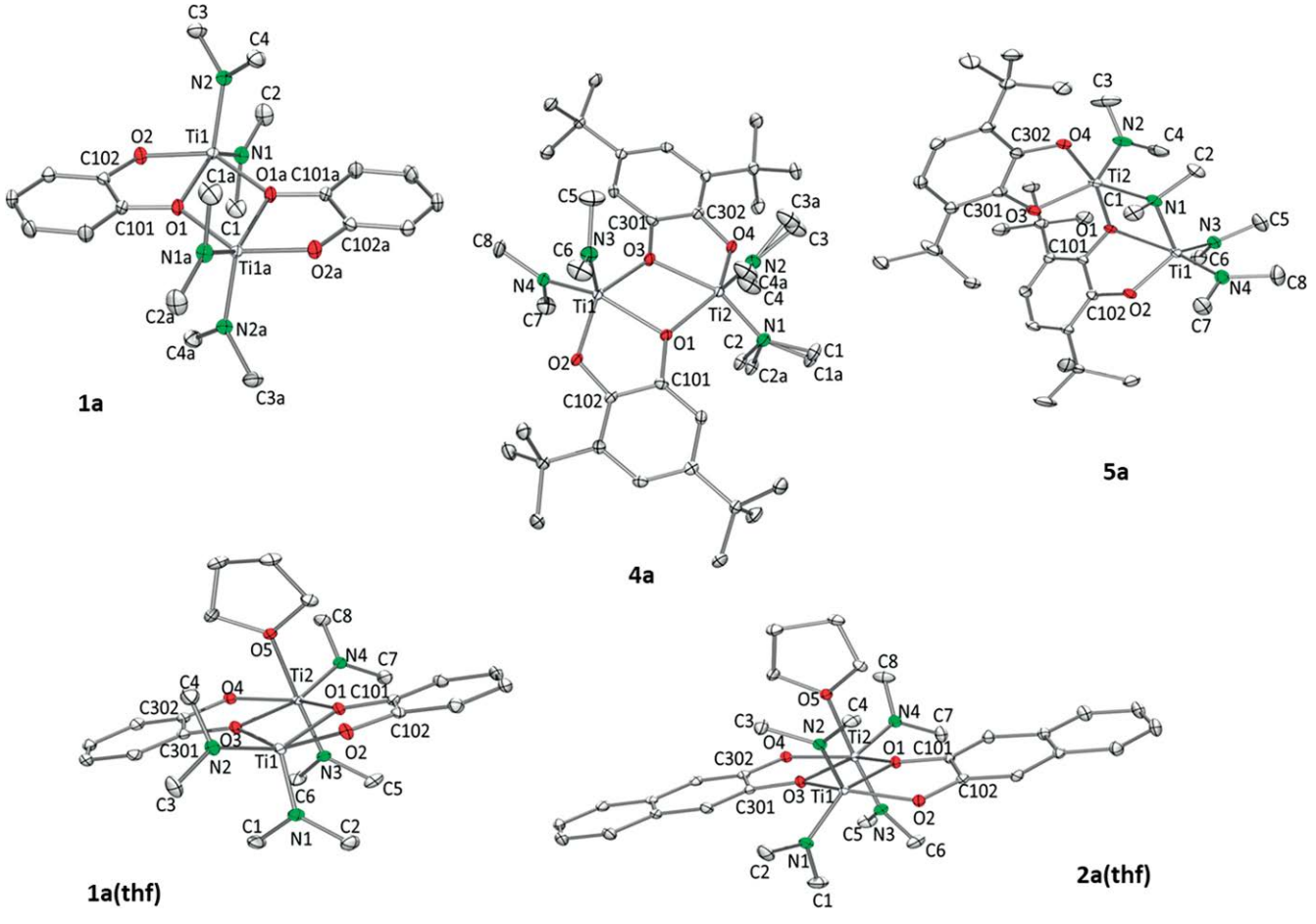

Figure 1. Molecular structures of **1a**, **1a(thf)**, **2a(thf)**, **4a** (twin), and **5a** with atomic displacement parameters set at the 50 % level. Hydrogen atoms are omitted for clarity. For representative interatomic distances and angles, see Table 1).

Table 1. Interatomic distances [Å] and angles [°] of **1a**, **1a(thf)**, **4a**, **2a(thf)**, and **5a**

1a			
Ti1–N1	1.8805(13)	O1a–Ti1–O1	69.95(5)
Ti1–N2	1.8680(14)	O1–C101	1.3710(19)
N1–Ti1–N2	105.00(6)	O2–C102	1.3522(18)
Ti1–O1	2.0995 (11)	C101–C102	1.407(2)
Ti1–O2	1.9356(12)	N2–Ti1–Ti1a	110.29(4)
O1–Ti1–O2	77.64(4)	N1–Ti–Ti1a	126.35(5)
Ti1–O1a	2.0014 (11)	Ti1····Ti1a	3.3609(5)
Ti1a–O1	2.0014 (11)		
1a(thf)			
Ti1–N1	1.8711(17)	Ti2–O4	1.9165(13)
Ti1–N2	1.8895(16)	O3–Ti2–O4	77.58(5)
N1–Ti1–N2	105.24(7)	O1–C101	1.367(2)
Ti2–N3	1.8950(16)	O2–C102	1.352(2)
Ti2–N4	1.9359(16)	O4–C302	1.348(2)
N3–Ti2–N4	97.86(7)	O3–C301	1.361(2)
Ti2–O3	2.1788(13)	C101–C102	1.402(3)
Ti1–O1	2.1380(14)	C301–C302	1.415(3)
Ti1–O2	1.9234(13)	N1–Ti1–Ti2	104.66(5)
O1–Ti1–O2	77.32(5)	N2–Ti1–Ti2	131.84(5)
Ti1–O3	1.9883(13)	N3–Ti2–Ti1	89.67(5)
Ti2–O1	2.0258(13)	N4–Ti2–Ti1	148.52(5)
O2–Ti1–O3	144.44(6)	Ti1····Ti2	3.3587(4)
2a(thf)			
Ti1–N1	1.8853(13)	Ti2–O5	2.2612(11)
Ti1–N2	1.8698(13)	O1–C101	1.3632(17)
N1–Ti1–N2	103.61(6)	O2–C102	1.3492(17)
Ti2–N3	1.8947(13)	O4–C302	1.3451(17)
Ti2–N4	1.9376(13)	O3–C301	1.3589(17)
N3–Ti2–N4	96.39(6)	C101–C102	1.431(2)
Ti2–O3	2.1776(11)	C301–C302	1.437(2)
Ti1–O1	2.1255(11)	N1–Ti1–Ti2	/
Ti1–O2	1.9263(11)	N2–Ti1–Ti2	/
O1–Ti1–O2	77.39(4)	N3–Ti2–Ti1	/
Ti2–O1	2.0165(11)	N4–Ti2–Ti1	/
Ti2–O4	1.9388(11)	Ti1····Ti2	/
O3–Ti2–O4	77.65(4)		
4a			
Ti1–N1	1.8850(16)	Ti2–O4	1.9057(13)
Ti1–N2	1.8699(17)	O3–Ti2–O4	77.00(5)
N1–Ti1–N2	102.95(7)	O1–C101	1.361(2)
Ti2–N3	1.8679(17)	O2–C102	1.375(2)
Ti2–N4	1.8789(15)	O4–C302	1.359(2)
N3–Ti2–N4	105.14(7)	O3–C301	1.378(2)
Ti2–O3	2.1192(13)	C101–C102	1.407(3)
Ti1–O1	2.1084(13)	C301–C302	1.400(3)
Ti1–O2	1.9011(13)	N1–Ti1–Ti2	132.79(5)
O1–Ti1–O2	77.55(5)	N2–Ti1–Ti2	105.82(5)
Ti1–O3	2.0118(13)	N3–Ti2–Ti1	105.52(5)
Ti2–O1	2.0091(13)	N4–Ti2–Ti1	130.74(5)
O1–Ti1–O3	70.72(5)	Ti1····Ti2	3.3412(5)
5a			
Ti1–N3	1.8881(15)	Ti2–O4	1.8986(12)
Ti1–N4	1.8966(14)	O3–Ti2–O4	78.87(5)
N3–Ti1–N4	104.56(6)	O1–C101	1.3740(19)
Ti1–N1	2.1235(14)	O2–C102	1.3620(19)
Ti2–N1–Ti1	99.25(6)	O4–C302	1.360(2)
Ti2–N1	1.8950(16)	O3–C301	1.351(2)
Ti2–N2	1.8988(15)	C101–C102	1.410(2)
N1–Ti2–N2	103.70(6)	C301–C302	1.409(2)
Ti2–O3	1.9374(12)	N1–Ti2–Ti1	41.07(4)
Ti1–O1	2.2978(11)	N2–Ti2–Ti1	107.78(5)
Ti1–O2	1.8528(11)	N1–Ti1–Ti2	39.68(4)
O1–Ti1–O2	74.20(4)	N4–Ti1–Ti2	137.24(5)
Ti2–O1	1.9704(11)	N3–Ti1–Ti2	104.44(5)
		Ti1····Ti2	3.1905(4)

Ti–N distances and N–Ti–N angles of **2a(thf)** and **1a(thf)** are quite comparable.

In order to enhance the solubility of the heteroleptic catecholate complexes, as well as counteract their agglomeration, $Ti(NMe_2)_4$ was treated with *tert*-butyl-substituted pyrocatechols. The resulting titanium(IV) complexes $[Ti(CAT\textit{t}Bu\text{-}4)(NMe_2)_2]_2$(**3a**),$[Ti(CAT\textit{t}Bu_2\text{–}3,5)(NMe_2)_2]_2$(**4a**)and$[Ti(CAT\textit{t}Bu_2\text{–}3,6)(NMe_2)_2]_2$ (**5a**) were obtained in high yield, while the solid-state structures of **4a** and **5a** were analyzed. Despite numerous attempts, complex **3a** could not be obtained in single-crystalline form, but it is believed to be dinuclear based on the other similar compounds. As in the case of complex **1a**, single crystals of **4a** were obtained by recrystallization from toluene/*n*-hexane at –35 °C. Similarly to **1a**, the structure analysis revealed two 5-coordinate Ti^{IV} centers being bridged by one of their catecholato oxygen atoms each (see Figure 1). The Ti–N distances in **4a** [e.g., av. Ti1–N 1.885 Å] match those found in **1a** [e.g., av. Ti1–N 1.874 Å]. The Ti–O bond lengths of **4a** [e.g., Ti1–O1 2.1084(13) Å, see also Table 1, and S2 in the Supporting Information] are similar to the ones in **1a** [e.g. Ti1–O1 2.0995(11) Å, see also Tables 1 and S1 in the Supporting Information], but the distances of the bridging oxygen atoms to their respective adjacent titanium atoms are not equivalent in **4a** [Ti1–O3 2.0118(13) Å and Ti2–O1 2.0091(13) Å], like found in **1a(thf)** [Ti2–O1 2.0258(13) Å and Ti1–O3 1.9883(13) Å] and in the homoleptic complex from literature [Ti–O3′ 2.041(2) Å and Ti′–O3 2.079(1) Å].[13] In general, the Ti–O distances are longer for the bridging catecholato oxygen atoms – in all the discussed crystalline complexes **1a**, **1a(thf)**, **4a**, and **2a(thf)** – than for the terminal ones, which is in agreement with the known dimeric isopropoxide complexes supported by differently substituted catecholato ligands {X-CAT: $[Ti(X\text{-}CAT)(O\textit{i}Pr)_2(HO\textit{i}Pr)]_2$ (X = H; Me-4; *t*Bu-4; $\textit{t}Bu_2$–3,5; OMe-3; NO_2–4; DHN)}.[14]

From these data, it can be concluded that the crystallized catecholato Ti^{IV} amides **1a** - **4a** prefer to form dimers, as known for the catecholato Ti^{IV} isopropoxide[14] and the *meso*-BINOLato Ti^{IV} isopropoxide complexes.[15] For further comparison, the Ti^{IV} catecholate complex $[Et_3NH]_2[Ti(CAT\textit{t}Bu_2\text{–}3,5)_2(HCAT\text{-}\textit{t}Bu_2\text{–}3,5)]_2 \cdot 2CHCl_3$ features also a dimeric composition of the anionic unit in the solid state.[13] Crucially, *Lange* et al. showed that sterically demanding substituents at the catecholato rings in positions adjacent to the oxygen atoms, that is use of 3,6-substituted derivatives, counteract oligomerization of homoleptic catecholate complexes of Ga^{III}, Al^{III} and Co^{III} efficiently.[16] This strategy has been successfully applied to the *meso*-BINOLato Ti^{IV} isopropoxide complex: by implementing $SiMe_2\textit{t}Bu$ groups at the BINOLATE-carbon atoms adjacent to the oxygen atoms, *Boyle* et al. finally obtained a monomeric *meso*-BINOLato Ti^{IV} isopropoxide complex.[17] Much to our surprise, complex $[Ti(CAT\textit{t}Bu_2\text{–}3,6)(NMe_2)_2]_2$ (**5a**), single crystals of which were obtained from *n*-hexane after several weeks at –35 °C, revealed also a dimeric composition. In this case, however, one catecholato oxygen atom (O1) and one amido nitrogen atom (N1) reside in the bridging positions, resulting in TiO_3N_2 and TiO_2N_3 environments. Such a bridging arrangement seems unprecedented in heteroleptic titanium(IV) catecholate complexes (see also Table 1, and Tab. S3 in the Supporting Information). The interatomic distances of complex **5a** are all in the same range as those of the previously obtained complexes (see Table 1), ex-

cept for the fairly elongated Ti1–N1 distance involving the bridging amido ligand [2.1235(14) Å, Table 1]. Striking is also the markedly shortened Ti···Ti interatomic distance of 3.1905(4) Å in **5a** compared to those in complexes **1a**–**4a**, which range from 3.3414(5) – 3.3609(5) Å. Overall, the catecholato C–O and C–C(ring) bond lengths in all titanium complexes under study are in the range typical for dianionic ligands.[18]

Table 2. Nitrogen physisorption data of KIT-6 materials under study

KIT-6[a]	a_S(BET)[b] [$m^2\ g^{-1}$]	$V_{p,des}$[c] [$cm^3\ g^{-1}$]	$d_{p,ads}$[d] [nm]
M1a (dehydrated)	620	1.19	8.5
M2a (silylated)	500	0.97	7.2
$Ti(NMe_2)_4$@[KIT-6] (**M3a**)	440	0.79	7.0
H_2DHN@$Ti(NMe_2)_4$@[KIT-6] (**M4a**)	393	0.60	6.0
M1b (dehydrated)	622	1.24	7.7
M2b (silylated)	503	1.03	6.7
$[Ti(DHN)(NMe_2)_2]_2$@[KIT-6] (**M5b**)	428	0.68	5.6

[a] Pretreatment temperature: for **M1a** and **M1b**: calcination at 813 K, 4 h, followed by dehydration at 773 K, 4 h, 10^{-3} mbar, followed by degassing at r.t., 1 h, 10^{-3} mbar (before N_2 physisorption); for **M2a** and **M2b**: degassing at 383 K, 3 h, 10^{-3} mbar; for **M3a**: degassing at r.t., 4 h, 10^{-3} mbar; for **M4a** and **M5b**: degassing at 323 K, 1 h, 10^{-3} mbar. [b] Specific BET surface area. [c] BJH desorption cumulative pore volume of pores between 1.0–50 nm diameter. [d] BJH adsorption average pore diameter.

A comparison of the ^{1}H NMR spectra of the unreacted catechols (Figures S2–S6) with those of the titanium(IV) complexes (Figures S7–S11) supports the formation of the heteroleptic bis(dimethylamido) catecholate derivatives envisaged. The catecholato signals of complexes **1a**–**4a** are shifted downfield, and the multiplets of the aromatic hydrogen atoms are broadened, while the signal(s) of the dimethylamido hydrogen atoms remain(s) in the region around 3 ppm (Figures S7–S10). Additionally, the COH proton signals (8.34 ppm for H_2DHN, 7.73 ppm for H_2CAT, 7.55 ppm for H_2CAT*t*Bu-4, 3.54 ppm, 5.33 ppm for H_2CAT*t*Bu_2–3.5 and 4.76 ppm for H_2CAT*t*Bu_2–3,6) shown in Figures S2–S5 had vanished in the product spectra (Figures S7–S10). In addition, the coordination of one catecholato ligand per Ti^{IV} center is corroborated by the expected integral ratios of the NMe_2 and aromatic catecholato protons.

The spectrum of the heteroleptic complex **4a** shows the presence of small amounts of side products (Figure S9),[19] which seem to form over time upon dissolution of analytically pure crystalline samples (side product signals are also observable in the crude product). Also, the ^{1}H NMR spectrum of the crystallized heteroleptic complex **5a** (Figure S11) indicated the occurrence of side reactions, which is also manifested in its elemental analysis. Thus, in situ ^{1}H, ^{13}C, and HC-HSQC NMR studies concerning complex **5a** were performed (Figures S13–S15). The broad signal around 2.48 ppm in the ^{1}H NMR spectrum, the characteristic *ν(N-H)* at 3296 and 3251 cm^{-1} in the DRIFT spectrum (see experimental section and Figure S30), and several higher-mass peaks in the mass spectrum of complex **5a** than the molecular ion peak (712 amu) of the dimer (see Figure S34 in the Supporting Information), all imply a by-product containing coordinated $HNMe_2$ groups, which are not found in the crystal structure of complex **5a**. This is similar to the catecholato Ti^{IV} isopropoxides reported previously exhibiting additionally coordinated HO*i*Pr.[14]

Titanium-Amide Grafting onto KIT-6 – The Mesoporous Host

In a previous work[20] we reported on the grafting of $Ti(NMe_2)_4$ onto mesoporous silica MCM-48 featuring a three-dimensional cubic mesopore structure. To ensure an efficient intrapore chemistry with the sterically demanding dimeric catecholate complexes (*convergent approach*), we decided to use mesoporous silica KIT-6. Like MCM-48, this material has a three-dimensional cubic $Ia\bar{3}d$ symmetry, but its mesopores are considerably larger, being stabilized by an additional microporous network.[20] Two KIT-6 samples, **M1a** and **M1b**, of suitable quality were synthesized according to a slightly modified route described by *Kleitz* et al., which uses a mixture of triblock-copolymer Pluronic P123, *n*-butanol, and TEOS under acidic conditions.[21] The structure/pore arrangement was determined by powder X-ray diffraction (PXRD, Figure S34),[21,22] and the surface areas and pore volumes found in the range common for KIT-6 materials (Table 2).[21]

The amount of surface silanol groups was calculated from the carbon contents of materials **M2a** and **M2b**, obtained via surface silylation with $HN(SiHMe_2)_2$, as 2.08 and 1.84 mmol hydroxyl groups per gram KIT-6, respectively.[20,23] Complete silanol consumption was confirmed by DRIFT spectroscopy via the disappearance of the OH stretching vibration (Figure S31). The detected surface silanol sites display the reactive sites in the following grafting reactions.

The N_2 adsorption-desorption isotherms of the parent materials **M1a** and **M1b** were confirmed to be of type IV with H1 hysteresis loops [which appear at a relative pressure (P/P_0) of 0.7–0.88 respectively], indicating characteristic mesoporous structures with cylindrical pores (Figure 2).[24] The t-plot analysis from N_2 adsorption revealed that **M1a** and **M1b** possess micropore volumes of 0.020 $cm^3\ g^{-1}$ and 0.076 $cm^3\ g^{-1}$, respectively, which is caused by cross-packing of the copolymer template during the synthesis procedure. This differs from MCM-48 routinely prepared by using (gemini) alkyl ammonium salts as surfactants under basic conditions. The respective silylated materials **M2a** and **M2b** showed similar isotherms and hysteresis loops (Figure S36), but markedly decreased surface areas, pore diameters as well as pore volumes compared to the parent materials (Table 2). Moreover, materials **M1a** and **M1b** displayed narrow Barrett–Joyner–Halenda (BJH) pore size distributions (PSDs) (Figure 2). The narrow PSDs are retained in silylated materials and **M2a** and **M2b** (see S19 in the Supporting Information), but the t-plot analyses demonstrated that the micropores disappeared. Furthermore, the space demand of the silyl groups could be estimated from the N_2 physisorption isotherm. The maximum nitrogen amount adsorbed for KIT-6 materials **M1a** and **M2a** was 791 and 659 $cm^3\ g^{-1}$, respectively, the difference of which (132 $cm^3\ g^{-1}$) corresponding to the volume occupied by intrapore-silyl groups per gram material. Correspondingly, **M1b** (812 $cm^3\ g^{-1}$) and **M2b** (686 $cm^3\ g^{-1}$) would afford a very similar silyl group volume of 126 cm^3 per gram material.

Sequential Approach: Material **M1a** was treated with an excess of $Ti(NMe_2)_4$ to yield yellow hybrid material $Ti(NMe_2)_4$@[KIT-6] (**M3a**). Subsequent treatment of pre-isolated **M3a** with an excess of 2,3-dihydroxynaphthalene (H_2DHN) gave an orange pow-

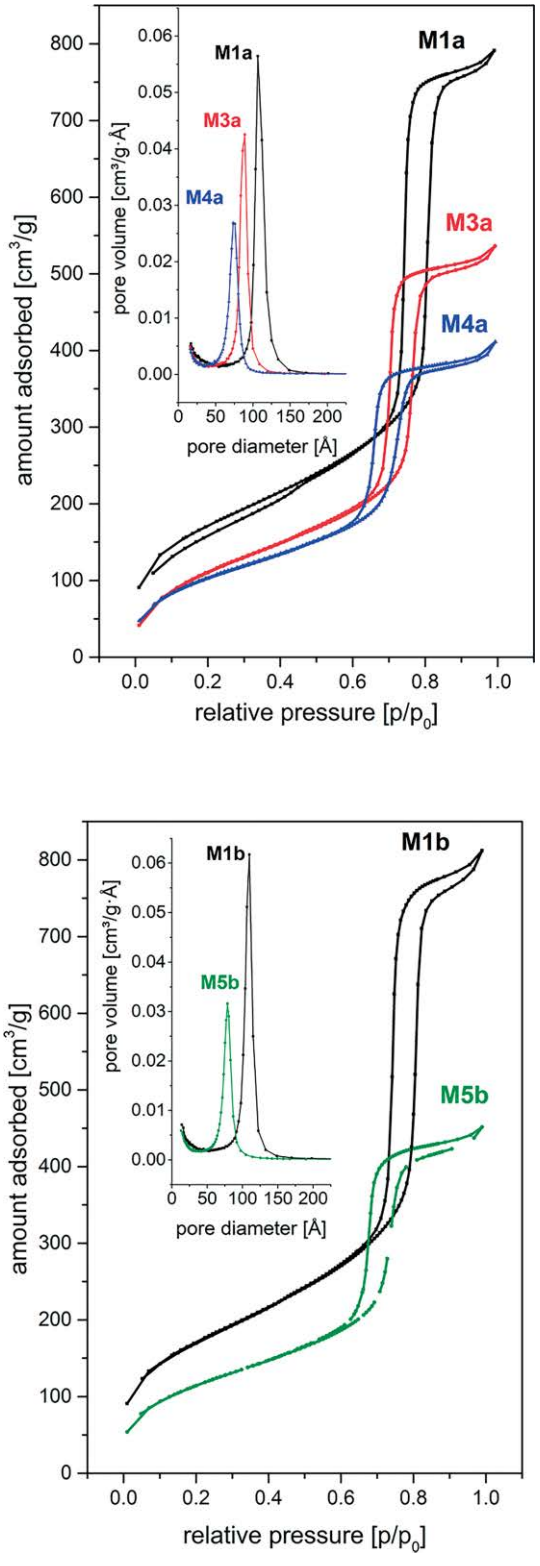

Figure 2. Nitrogen adsorption/desorption isotherms at 77.4 K and the corresponding BJH size distributions. *Top*: dehydrated KIT-6 (**M1a**), $Ti(NMe_2)_4$@[KIT-6] (**M3a**) and $H_2DHN@Ti(NMe_2)_4$@[KIT-6] (**M4a**). *Bottom*: dehydrated KIT-6 (**M1b**) and $[Ti(DHN)(NMe_2)_2]_2$@[KIT-6] (**M5b**).

der, denoted as $H_2DHN@Ti(NMe_2)_4$@[KIT-6] (**M4a**). Such amide grafting and subsequent ligand exchange with H_2DHN did not change the type of isotherm and hysteresis loop (Figure 2), but the obtained hybrid materials showed a markedly decreased specific BET surface area, pore diameter as well as pore volume compared to parent material **M1a** (Table 2). The t-plot analysis from N_2 adsorption revealed the absence of any micropore structure in $Ti(NMe_2)_4$-grafted material **M3a**. The negative isotherm shift along the y-axis of **M3a** with respect to **M1a**, and of **M4a** compared to **M3a** was observed as expected: the maximum nitrogen amount adsorbed in [$cm^3\ g^{-1}$] decreased from **M1a** (791) > **M3a** (536) > **M4a** (411), because of the space occupied by the grafted Ti amide species (255 $cm^3\ g^{-1}$) as well as the DHN ligands (125 $cm^3\ g^{-1}$) – total 380 $cm^3\ g^{-1}$. This also led to a successive reduction of pore diameter within the KIT-6 series (Table 2).

Convergent Approach: The dimeric complex $[Ti(DHN)(NMe_2)_2]_2$ (**2a**) was selected as a representative bulky precursor [the approximate molecular dimension of complex **2a(thf)** is 15.16 Å × 7.27 Å, as obtained from the ORTEP plot]. It was reacted (also in excess) with KIT-6 material **M1b**, giving an orange powder, denoted as $[Ti(DHN)(NMe_2)_2]_2$@[KIT-6] (**M5b**). Again, DRIFT spectroscopy confirmed the complete consumption of the surface silanol groups. Interestingly, material **M5b** displayed an isotherm and hysteresis loop similar to hybrid material **M4a** obtained via the sequential approach (Figure 2), along with the same implications for specific BET surface area, pore diameter and pore volume (Table 2). The maximum nitrogen amount adsorbed in [$cm^3\ g^{-1}$] decreased from **M1b** (812) > **M5b** (452), meaning that the intrapore-grafted Ti-complex occupied ca. 360 cm^3 per gram material.

Nature of the Surface Species: Although the nitrogen physisorption nicely pictures the pore filling according to such sequential and convergent approaches, the covalent attachment was only revealed by DRIFT (see Figure 3). The distinct SiO-H stretching vibration[25,23] at 3745 cm^{-1} in the spectra of activated silica materials **M1a** and **M1b** disappeared completely upon grafting of $Ti(NMe_2)_4$ (**M3a**) or of complex **4a** (**M5b**). For the grafted PMS materials **M3a**, **M4a** and **M5b**, the observed C-H stretching[26] and rocking[7] vibrations between 2800 and 3000 cm^{-1}, as well as at 1421 cm^{-1} (only for material **M3a**) can be ascribed to the amido methyl groups, whereas it shall be noted that the characteristic Si–OTi stretching vibrations at 945 and 598 cm^{-1} might overlap with ν *(NC$_2$)* in the first- or with ν_{as} *(Ti-N)* in the second case and cannot be taken into account for a potentially successful grafting or ligand exchange procedure.[7,27] The DHN-containing samples **M4a** and **M5b** still displayed weak CH signals around 2800 cm^{-1} indicative of some remaining NMe_2 groups. The occurrence of Ti–O-C vibrations at (1458, 1163 and) 741 cm^{-1},[7] in materials **M4a** and **M5b**, together with the vanished SiO-H vibration, indicate a successful ligand exchange for **M4a** and a successful grafting of the molecular complex for **M5b**.

In order to allow a comparison between the grafting behavior of Ti^{IV} species onto MCM-48 (previous work)[20] and onto KIT-6 (present work), the molar C/N-ratios of the directly grafted materials (**M3a** and **M5b**) and of the one after ligand exchange (**M4a**) were calculated (see S31 in the Supporting Information). As expected, the C/N ratio of 2.09 for **M3a** exactly corresponds to an NMe_2 group. For materials $H_2DHN@Ti(NMe_2)_4$@[KIT-6]

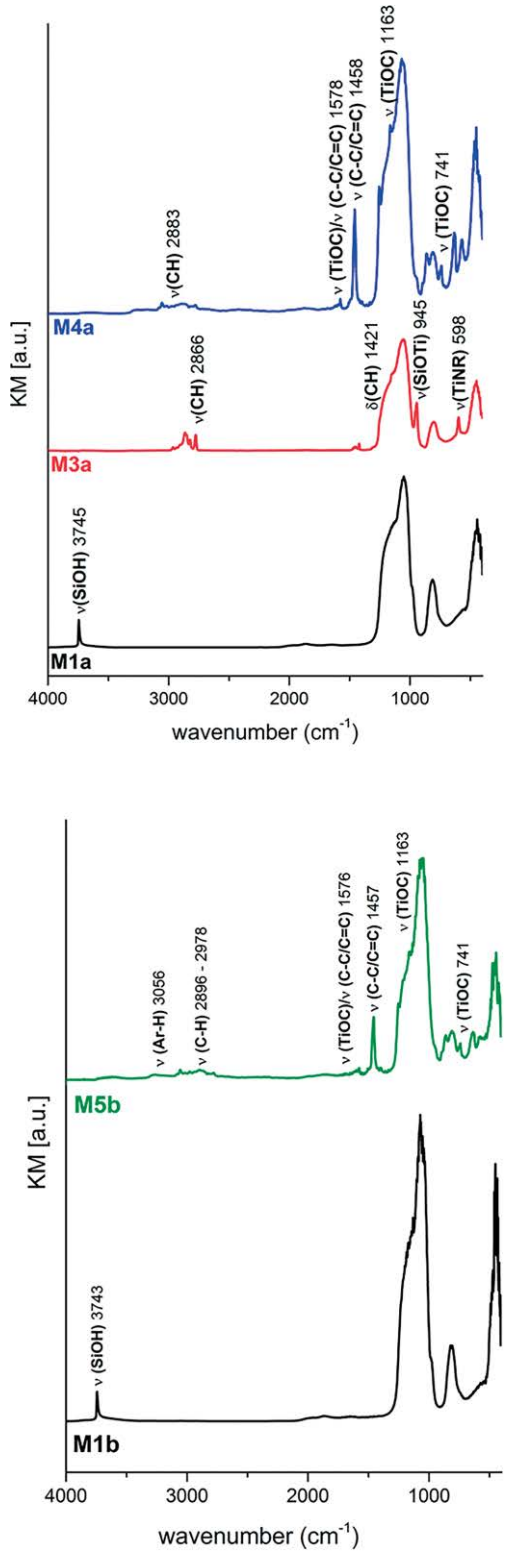

Figure 3. DRIFT spectra of the synthesized materials diluted with KBr powder. *Top*: dehydrated KIT-6 (**M1a**), $Ti(NMe_2)_4$@[KIT-6] (**M3a**) and H_2DHN@$Ti(NMe_2)_4$@[KIT-6] (**M4a**). *Bottom*: dehydrated KIT-6 (**M1b**) and $[Ti(DHN)(NMe_2)_2]_2$@[KIT-6] (**M5b**).

(**M4a**) and $[Ti(DHN)(NMe_2)_2]_2$@[KIT-6] (**M5b**) on the other hand, we obtained values of 8.65 and 8.44, respectively, implying a considerable amount of residual NMe_2 groups. As the latter values are nearly the same, the residual NMe_2 groups might originate from ligand exchange at monopodally grafted species $SiO–Ti(NMe_2)_3$ and from the grafting of dimeric complex **2a**, respectively (Scheme 2; neglecting donor coordination of released $HNMe_2$). This is not surprising, as we already reported on 80 % (2.2 out of 2.7 mmol g^{-1}) monopodally grafted Ti species at MCM-48, when using $Ti(NMe_2)_4$.[20] This scenario is supported by the microanalytical data which can be used to calculate the number of surface sites δ (Si-OH), required for each postulated surface species (see Scheme 2). For material **M3a**, full coverage with surface species **A** (1st step of the sequential approach assuming a monofunctional surface reaction) would require δ (Si-OH) = 4.45 mmol/g, whereas 100 % surface species **B** would only require 1.44 mmol/g surface silanols. As the KIT-6 material **M1a** has 2.08 mmol/g accessible surface silanol groups only and the carbon atom population is ca. 8.6 mmol/g, the monopodal species can be assumed the dominant species.[20] This will directly affect the 2nd step of the sequential approach and the formation of species **C** and **D** of the resulting material **M4a**. Given that **B** is the prevailing species on material **M3a**, **D** might be the one on **M4a**.

For the convergent approach, full coverage with species **C** would require 3.66 mmol/g silanol groups, while the theoretical value for **D** would be 1.54 mmol/g. Given the silanol population of material **M1b** as 1.84 mmol/g, the carbon elemental analysis suggests **D** as the dominant surface species of material **M5b**. As the dimeric complex **2a** was grafted onto KIT-6 material **M1b**, one might also propose a surface species like **E**, which in turn is identical to **D** concerning its atomic composition. To find out whether both synthesis strategies yield the same or different final surface species, we had a closer look at the DRIFT spectra of materials $Ti(NMe_2)_4$@[KIT-6] (**M3a**), H_2DHN@$Ti(NMe_2)_4$@[KIT-6] (**M4a**), $[Ti(DHN)(NMe_2)_2]_2$@[KIT-6] (**M5b**), $Ti(NMe_2)_4$, H_2DHN, and complex **2a** (Figures S32 and S33). Vibrations above 3200 cm^{-1} only belong to the proligand H_2DHN, whereas the vibrations between 2950–3100 cm^{-1} are present in the spectra of H_2DHN, complex **2a**, and materials **M4a**/**M5b**, and can thus be ascribed to C-H vibrations of the DHN moiety. The vibrations between 2750 and 2950 cm^{-1} are present in all spectra except for the one of H_2DHN, and hence can be assigned to C-H vibrations of the NMe_2 ligands. Since the characteristic pattern is nearly identical in materials **M4a** and **M5b**, if one neglects the difference in intensity, the presence of different surface species on these materials cannot be assessed on the basis of DRIFT spectroscopy.

Finally, solid-state NMR spectroscopy of materials **M3a**, **M4a**, and **M5b** was performed and the ^{13}C CP/MAS spectra compared with the ^{13}C NMR spectra of $Ti(NMe_2)_4$ and complex **2a** recorded in C_6D_6 (Figures S16–S21), as well as of H_2DHN and complex **2a** in $[D_8]$thf (Figure 4). *Finkelstein-Shapiro* et al. pointed out[28] that the shifts of the alpha-, beta- and gamma-carbon atoms of surface catecholate species (DHN), compared to the ones of the free catechol [H_2DHN: 146.8 ppm,[29] 147.7 ppm in $[D_8]$thf (Figures 4 and S22)] are specific for the surface binding mode. The alpha-carbon signal of material **M5b** at 157 ppm (Figures 4 and S18) is close to the one of the dimeric molecular complex **2a** (Figures 4, S20, and S23) in solu-

tion (156–158 ppm), whereas the alpha-carbon resonance of material **M4a** (Figure 4 and Figure S17) appears shifted to lower field (160 ppm). This points out the presence of different surface species in materials **M4a** and **M5b**, possibly favoring dimeric species **E** (not expected for **M4a**) over monopodal **D** in material **M5b** (Scheme 2). The gamma-carbon signal remains unchanged for all the materials shown in Figure 4, while the beta-carbon signal of **M4a** and **M5b** is shifted upfield implying for a chelating surface species.

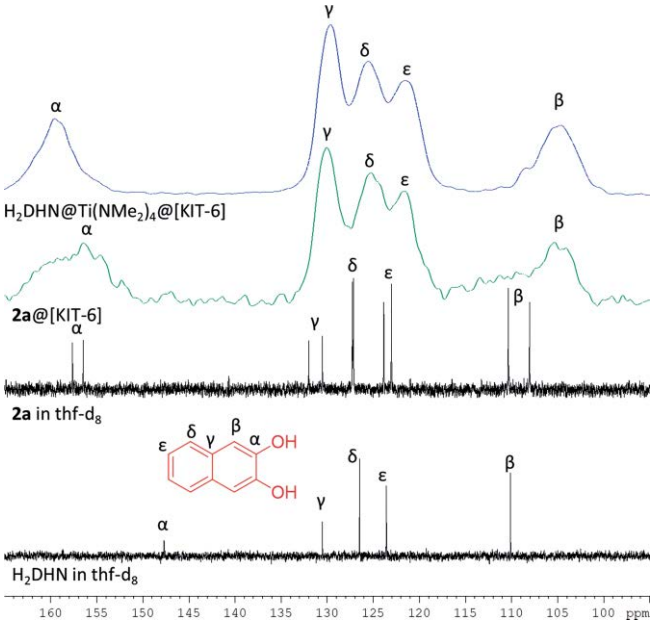

Figure 4. ^{13}C NMR spectra (some solid-state and some in solution) from top to bottom: $H_2DHN@Ti(NMe_2)_4@[KIT-6]$ (**M4a**) (^{13}C NMR, 75 MHz, CP/MAS, 10 kHz rotation), $[Ti(DHN)(NMe_2)_2]_2@[KIT-6]$ (**M5b**) (^{13}C NMR, 75 MHz, CP/MAS, 10 kHz rotation), $[Ti(DHN)(NMe_2)_2]_2$ (**2a**) (^{13}C NMR, 100 MHz, $[D_8]$thf) and H_2DHN (^{13}C NMR, 100 MHz, $[D_8]$thf).

Moreover, the amide precursor $Ti(NMe_2)_4$ shows a single ^{13}C signal in solution at 44.0 ppm (Figure S19), whereas material **M3a** displays two signals for the NMe_2 groups assignable to monopodal (43.1 ppm) and bipodal Ti^{IV} surface species (35.8 ppm) (Figure S16). The ^{13}C CP/MAS spectrum of material **M4a** revealed that some of the bipodal Ti^{IV}-amido species are preserved upon (incomplete) surface ligand exchange (**M3a**–**M4a**: 35 ppm, Figures S17 and S21), whereas another "NMe_2" species occurred (**M4a**: 40 ppm, Figure S21). The latter "NMe_2" species also formed upon grafting of **2a** (**M5b**: 40 ppm, Figure S18 and S21) onto KIT-6 and might therefore represent any coordinated $HNMe_2$, considering the affinity of unsaturated metal centers for donor molecules, as shown for complex **5a** and also in surface grafting reactions involving liberated alcohols.[20] Overall, the presence of NMe_2 or $HNMe_2$ groups on hybrid materials **M4a** and **M5b** is also consistent with their nitrogen contents of 2.01 and 2.21 wt.-%, respectively. Furthermore, the signal at 46 ppm in the ^{13}C spectra of complex **2a** and material **M5b** accounts for the preservation of (at least a fraction of) the dimeric structure of complex **2a** upon grafting onto KIT-6 (Figure S21). Significant fluxional behavior of the catecholato and amido ligands can be assumed in solution. Examining equimolar solutions of complexes **1a** and **2a** in C_6D_6 by ^1H NMR spectroscopy not only revealed the typical signals of **1a** and **2a** but also the appearance of a signal at 3.11 ppm assignable to $Ti(NMe_2)_4$, and the formation of a precipitate which was not further investigated (Figure S24).

Conclusions

The equimolar protonolysis reaction of $Ti(NMe_2)_4$ with a series of catechols gave access to heteroleptic dimeric Ti^{IV} catecholates of which $[Ti(CAT)(NMe_2)_2]_2$ (CAT = pyrocatechol) and $[Ti(DHN)(NMe_2)_2]_2$ (DHN = 2,3-dihydroxynaphthalene) could be obtained as pure compounds. The solid-state structures revealed Ti^{IV} centers bridged by two catecholato ligands and two terminal amido groups each, but the sterically more demanding 3,6-di-*tert*-butylcatechol ($H_2CAT tBu_2$–3,6) yielded complex $[Ti(CAT tBu_2–3,6)(NMe_2)_2]_2$ featuring one bridging catecholato and one bridging amido ligand. Exploiting the high carbon content of DHN, it could be successfully employed as ligand in SOTiC studies on periodic mesoporous silica KIT-6 (SOTiC = surface organotitanium chemistry). Interestingly, nitrogen physisorption indicated similar space consumption of the grafted metal complex in hybrid materials $H_2DHN@Ti(NMe_2)_4@[KIT-6]$ and $[Ti(DHN)(NMe_2)_2]_2@[KIT-6]$, emerging from sequential and convergent approaches, respectively. However, the presence of distinct surface species was suggested by solid-state NMR spectroscopy.

Experimental Section

General Considerations: All operations were performed with rigorous exclusion of air and water, if not otherwise noted, using standard Schlenk and glovebox techniques (MB Braun MB150B-G-II <1 ppm O_2, <1 ppm H_2O) under argon atmosphere. Solvent pretreatment was performed with Grubbs-type columns (MB Braun, MB SPS-800). C_6D_6, $[D_8]$toluene, and $[D_8]$thf were obtained from Eurisotop, degassed and dried with NaK for 24 h, stored in a glovebox, and freshly filtered before use. The other chemicals [including $Ti(NMe_2)_4$ in >99.999 % purity] were obtained from Aldrich and used as received, except for the catechols (4-*tert*-butylcatechol, 3,5-di-*tert*-butylcatechol and pyrocatechol), which were degassed prior to use.

NMR measurements were performed on a Bruker Avance-II+ 400-PFT-NMR spectrometer (^1H: 400.11 MHz, ^{13}C: 100.61 MHz). ^1H- and ^{13}C-shifts were referenced to internal solvent resonances and are reported relative to TMS (tetramethylsilane). On several occasions a very minor contamination of C_6D_6 was observed at 7.36 ppm in the ^1H NMR spectra. The NMR spectra of air- and moisture-sensitive compounds were recorded in NMR tubes with J.-Young-valves. ^{13}C CP/MAS NMR spectra were obtained at ambient temperature on a Bruker ASX 300 instrument equipped with magic angle spinning (MAS) hardware, using a 3 mm ZrO_2 rotor. The ^{13}C spectra were recorded using cross polarization and proton decoupling and were referenced to adamantane (^{13}C: 28.46 and 37.85 ppm).

Mass spectra were obtained, using an MSD 5977 spectrometer (Agilent, Waldbronn) with DIP by SIM, Oberhausen. DRIFT measurements were performed on a NICOLET 6700 FTIR spectrometer (Thermo SCIENTIFIC) and dried KBr powder was used as a dilution matrix (10 wt.-% analyte related to $m_{analyte} + m_{KBr} = 100$ %). The

sample/KBr mixture was carefully mixed by grinding in an agate mortar prior to the measurements and put into a DRIFT cell with KBr windows. The collected data were converted using the Kubelka–Munk refinement.

Elemental analyses were carried out on an Elementar Vario MICRO cube instrument using the CHNS mode.

Single crystals suitable for X-ray diffraction (XRD) were selected in a glovebox, covered in Paratone-N (Hampton Research) and mounted onto a microloop. XRD data were collected on a Bruker APEX2 Duo at 100(2) K, except for **4a(thf)** [200(2) K], by use of QUAZAR optics and Mo-K_α radiation (λ = 0.71073 Å) with ω and φ scans. The data were collected using the COSMO program[30] and SAINT for integration and data reduction.[31] Numerical absorption effect corrections were done using SADABS.[32,33] Structure solution was performed with SHELXS-97[34] and structure refinement with SHELXL-2013.[35,33] The structure was solved by direct methods and refined against all data by full-matrix least-squares methods on F^2 using SHELXTL and SHELXLE.[35] **3a** was refined as a twin. The two domains were separated using APEX2 RLATT, integration and data reduction were also done with SAINT. For absorption correction the program TWINABS was used.[36] All crystal structure graphics were created with ORTEP-III[37] and POV-Ray.[38] CCDC 1862528 [for **1a**], 1862531 [for **1a(thf)**], 1862529 [for **2a(thf)**], 1862530 [for **4a**], and 1862532 [for **5a**] contain the supplementary crystallographic data for this paper. These data can be obtained free of charge from The Cambridge Crystallographic Data Centre.

Powder X-ray diffraction analyses (PXRD) were performed on a Bruker Advance D8 instrument in the step/scan mode using Cu-K_α radiation (λ = 1.5418 Å). The small-angle diffractograms were recorded in the 2θ range of 0.5–9.99° with a scan speed of 2. Nitrogen physisorption measurements were performed on an ASAP 2020 volumetric adsorption apparatus (Micromeritics) at 77 K [$a_m(N_2, 77\ K)$ = 0.162 nm^2]. Prior to analysis the samples were degassed at ambient temperature or the expected temperature for at least 1 h under vacuum (≈ 10^{-3} mbar).

The Brunauer–Emmett–Teller (BET) specific surface area was obtained from the nitrogen adsorption branch of the isotherm in the relative pressure range from 0.10 to 0.2. Pore size distributions were calculated from the adsorption branches using the Barrett–Joyner–Halenda (BJH) method. Application of prolonged vacuum to titanium amido surface species should be avoided due to possible decomposition to imide species.[39]

Bis(dimethylamido-)benzene-1,2-diolato-titanium(IV) (1a): $Ti(NMe_2)_4$ (225 mg, 1.00 mmol), diluted in 2 mL *n*-pentane, was added dropwise to a stirred suspension of pyrocatechol (110 mg, 1.00 mmol) in 3 mL *n*-pentane, causing a color change from yellow to orange to red. After 17 h stirring at ambient temperature a bright orange powder had formed. Upon removal of solvent residues under vacuum, complex $[Ti(CAT)(NMe_2)_2]_2$ (**1a**) was obtained as a yellow powder in 98 % yield (239 mg, 0.977 mmol). **1a** (100 mg, 0.410 mmol) was crystallized from a saturated toluene/*n*-hexane solution at –35 °C, giving orange-yellow needles in 89 % yield (89 mg, 0.365 mmol) after two days. Elemental analysis calculated for $C_{10}H_{16}N_2O_2Ti$ (M = 244.11 g mol^{-1}): C, 49.20; H, 6.61; N, 11.48 wt.-%; found C, 49.45; H, 6.51; N, 11.45 wt.-%. ^{1}H NMR (400 MHz, C_6D_6, 26 °C): δ = 3.09 (s, 12H, *NMe*$_2$), 6.94 (m, 2H, *Ar-H*), 7.06 (d, 2H *Ar-H*), 7.36 (s, 0.05 H, *O-H*) ppm. DRIFT (KBr): 3052(w) ν*(Ar-H)*; 2962(w), 2903(m), 2864(m), 2809(m) ν*(C-H), CH*$_3$, *CH*$_2$, 2768(w/m) ν*(C-H), N-CH*$_3$, 1585(w), 1575(w) ν*(C=C), aromatic ring* + ν*(Ti-O-C)*, 1482(s), 1458(m), 1414(w) ν*(C=C), aromatic ring*, 942(s) ν_S*(NC*$_2$*)*; 735(m) ν*(Ti-O-C)*, 605(s/m) ν_{as}*(Ti-N)* cm^{-1}.

Bis(dimethylamido-)naphthalene-2,3-diolato-titanium(IV) (2a): $Ti(NMe_2)_4$ (224 mg, 1.00 mmol), diluted in 1 mL *n*-pentane, was added dropwise to a stirred suspension of 2,3-dihydroxynaphthalene (160 mg, 0.999 mmol) in 2 mL *n*-pentane. A color change from clear yellow to opaque orange was observed as well as strong warming of the sample noticed. After 19 h of stirring at ambient temperature an orange powder had formed. Upon removal of solvent residues under vacuum, $[Ti(DHN)(NMe_2)_2]_2$ (**2a**) was obtained quantitatively as a yellow powder (294 mg, 0.999 mmol). Elemental analysis calculated for $C_{14}H_{18}N_2O_2Ti$ (M = 294.17 g mol^{-1}): C, 56.16; H, 6.17; N, 9.52 wt.-%; found C, 56.16; H, 6.13; N, 9.52 wt.-%. ^{1}H NMR (400 MHz, C_6D_6): δ [ppm] = 3.14 (s, 12H, 2 × *NMe*$_2$), 7.26–7.28 (dd/m, 2H, *Ar-H in pos.6+7*), 7.36 (s, 2H, *Ar-H in pos. 1+4*), 7.67–7.76 (d/m, 2H, *Ar-H in pos. 5+8*). ^{13}C NMR (100 MHz, C_6D_6): δ[ppm] = 45.1 (*N-Me*$_2$), 109.6 (β+β' *carbons*), 128.1 (overlain by C_6D_6), 156.0 (α+α'*carbons*). ^{13}C NMR (100 MHz, [D$_8$]thf): δ [ppm] = 47.3 (*N-Me*$_2$), 108.1 + 110.4 (β+β' *carbons*), 123.0 + 123.9 (ε+ε'*carbons*), 127.2 + 127.3 (δ+δ'*carbons*), 130.5 + 132.0 (γ+γ'*carbons*), 156.5 + 157.6 (α+α'*carbons*). DRIFT (KBr): 3046(w) ν*(Ar-H)*, 2966(w), 2860(m), 2814(w) ν*(C-H), CH*$_3$, *CH*$_2$, 2771(w/m) ν*(C-H), N-CH*$_3$, 1598(w), 1576(w) ν*(C=C), aromatic ring* + ν*(Ti-O-C)*, 1469(m), 1498(w), 1461(s), 1414(w) ν*(C=C), aromatic ring*, 945(s/m) ν_S*(NC*$_2$*)*, 744(m) ν*(Ti-O-C)*, 607(s) ν_{as}*(Ti-N)* cm^{-1}.

Bis(dimethylamido-)(4-*tert*-butyl)benzene-1,2-diolatotitanium-(IV) (3a): $Ti(NMe_2)_4$ (244 mg, 1.00 mmol) was added dropwise to a stirred solution of 4-*tert*-butylcatechol (300 mg, 1.00 mmol) in 5 mL *n*-hexane. In the meantime, a color change from yellow to dark red was observed as well as a strong warming of the sample noticed. After 19 h stirring at ambient temperature a clear orange-red solution had formed. Upon removal of the solvent and volatiles under vacuum, the crude product was obtained as a mixture of yellow and orange powders. Solvent residues could not be completely removed even after prolonged degassing in vacuum. Therefore the crude product was washed several times with small amounts of *n*-hexane (total volume: 5 mL) and the final solid product $[Ti(CAT\textit{t}Bu\text{-}4)(NMe_2)_2]_2$ (**3a**) was then collected via centrifugation separation (yellow powder) in 70 % yield (196 mg, 0.653 mmol). Elemental analysis calculated for $C_{14}H_{24}N_2O_2Ti$ (M = 300.22 g mol^{-1}): C, 56.01; H, 8.06; N, 9.33 wt.-%; found C, 55.64; H, 8.10; N, 9.14 wt.-%. ^{1}H NMR (400 MHz, C_6D_6, 26 °C): δ = 1.37 (s, 9H, *tert-butyl*), 3.11–3.16 (t, 12H, 2 × *NMe*$_2$), 6.96–7.02 (m, 2H, *Ar-H*), 7.21 (s, 1H, *Ar-H*), 7.36 (s, 0.1H, *O-H*) ppm. DRIFT (KBr): 3059(w) ν*(Ar-H)*, 2960(s/m), 2899(m), 2860(s/m), 2810(m) ν*(C-H), CH*$_3$, *CH*$_2$, 2765(w/m) ν*(C-H), N-CH*$_3$, 1598(w), 1570(w) ν*(C=C), aromatic ring* + ν*(Ti-O-C)*, 1494(s), 1460(w), 1446(w), 1417(m) ν*(C=C), aromatic ring*; 941(s) ν_S*(NC*$_2$*)*, 604(s/m) ν_{as}*(Ti-N)* cm^{-1}.

Bis(dimethylamido-)(3,5-di-*tert*-butyl)benzene-1,2-diolato-titanium(IV) (4a): $Ti(NMe_2)_4$ (247 mg, 1.10 mmol) was added dropwise to a stirred solution of 3,5-di-*tert*-butylcatechol (222 mg, 1.00 mmol) in 5 mL *n*-hexane. A color change from clear yellow to dark red was observed as well as a strong warming of the sample noticed. After 18 h of stirring at ambient temperature, a red-brown suspension had formed, which was transferred into centrifugation tubes and washed with *n*-hexane until the supernatant stayed colorless. The solid was transferred back into a vial with as little *n*-hexane as possible. Upon removal of the solvent under vacuum, $[Ti(CAT\textit{t}Bu_2\text{–}3,5)(NMe_2)_2]_2$ (**4a**) was obtained as a gold-colored powder in 75 % yield (266 mg, 0.747 mmol). Compound **4a** (30 mg, 0.0842 mmol) was crystallized from a saturated toluene/*n*-hexane solution at –35 °C to afford golden-yellow plates in 60 % yield (18 mg, 0.051 mmol) after one week. Elemental analysis calculated for $C_{18}H_{32}N_2O_2Ti$ (M = 356.33 g mol^{-1}): C, 60.67; H, 9.05; N, 7.86 wt.-%; found C, 59.95; H, 8.63; N, 7.32 wt.-%. ^{1}H NMR (400 MHz, C_6D_6,

26 °C): δ = 1.18 (s, 3H, *tert-butyl of extradiol C*), 1.33 (bs, 3H, *tert-butyl of intradiol A*), 1.45 (s, 3H, *tert-butyl of extradiol B*), 1.48 (s, 9H, *tertbutyl of* ***4a*** *in pos. 3*), 1.72 (s, 9H, *tertbutyl of* ***4a*** *in pos. 5*), 3.16 (s, 12H, *2 × NMe$_2$ of* ***4a***), 7.12 (s, 0.4H *Ar-H of intradiol A and of extradiols B+C*), 7.21 (d, 1H, *Ar-H of* ***4a*** *in pos. 6*), 7.26 (d, 1H, *Ar-H of* ***4a*** *in pos. 4*) ppm.[19] ^{13}C NMR (100 MHz, C_6D_6, 26 °C): δ = 30.2 (*CH$_3$ of tert-butyl in pos. 5 of* ***4a***), 32.5 (*CH$_3$ of tert-butyl in pos. 3 of* ***4a***), 45.3 (*=C-OR of extradiol B+C*), 110.7 (*Ar-H in pos. 6 of* ***4a***), 115.8 (*Ar-H in pos. 4 of* ***4a***), 122.2 (*Ar-C=O of extradiol B + intradiol A*), 128.1 (t, C_6D_6), 133.9 (*Ar-OTi in pos. 2 of* ***3a***), 140.9 (*Ar-tert-butyl in pos. 3+5 of* ***4a***), 151.5 (*-O-C=O of extradiols B+C*), 154.8 (*O=C-O-C=O anhydride Cs of intradiol A*) ppm.[19] DRIFT (KBr): 2952(s), 2899(s/m), 2862(s), 2820(w) ν*(C-H), CH$_3$, CH$_2$*, 2773(w/m) ν*(C-H), N-CH$_3$*, 1597(w), 1563(w) ν*(C=C), aromatic ring* + ν*(Ti-O-C)*, 1469(m), 1443(m), 1416(s) ν*(C=C), aromatic ring*, 942(s) ν_s*(NC$_2$)*, 754(m) ν*(Ti-O-C)*, 606(s) ν_{as}*(Ti-N)* cm^{-1}.

Bis(dimethylamido-)(3,6-di-*tert*-butyl)benzene-1,2-diolato-titanium(IV) (5a): Ti(NMe$_2$)$_4$ (359 mg, 1.60 mmol) was added dropwise to a stirred solution of 3,6-di *tert*-butylcatechol (333 mg, 1.50 mmol) in 5 mL *n*-hexane. A color change from clear yellow to dark red was observed as well as a strong warming of the sample noticed. After 18 h of stirring at ambient temperature a red-brown solution had formed, which was transferred into centrifugation tubes and washed with *n*-hexane to remove Ti-precursor residues. The solid was transferred back into a vial with as little *n*-hexane as possible. Upon removal of the solvent under vacuum, [Ti(CAT*t*Bu$_2$-3,6)(NMe$_2$)$_2$]$_2$ (**5a**) was obtained as a dark reddish-brown powder in 65 % yield (350 mg, 0.983 mmol). Compound **5a** was recrystallized from *n*-hexane for several weeks at –35 °C. Elemental analysis calculated for $C_{18}H_{32}N_2O_2Ti$ (M = 356.33 g mol^{-1}): C, 60.67; H, 9.05; N, 7.86 wt.-%. Found (2 samples): C, 59.25/62.43; H, 7.68/9.54; N, 7.43/9.89 wt.-%. Found (crystals): C, 62.25; H, 9.64; N, 7.22 wt.-%. ^{1}H NMR (400 MHz, C_6D_6, 26 °C): δ = 0.89 & 1.24 (*n-hexane residues*), 1.41(m, 0.4H),1.52–1.56(m,36H,*tert-butylof* ***5a***),1.70(s,3H,*tert-butyl*),1.92–2.06 (bd/m, 3.5H), 2.29 (d, 1H), 2.88 (bs, 1H), 2.92 (s, 2H), 3.02 (bs, 12H, *2 × NMe$_2$*), 3.12 (s, 1H), 3.34 (bs, 1H), 6.77 (s, 0.3H, *Ar-H*), 6.84 (bs, 1H, *Ar-H*), 6.88 (bs, 0.6H, *Ar-H*), 6.95 (bs, 2H, *Ar-H*), 7.00 (s, 0.3H, *Ar-H*), 7.16 (s, 2H, *C_6D_6*), 7.36 (bs, 0.03H, *O-H*) ppm. DRIFT (KBr): 3296(w), 3251(w) ν*(N-H)*, 3080(w) ν*(Ar-H)*, 2953(s), 2901(s), 2863(s), 2818(m/w) ν*(C-H), CH$_3$, CH$_2$*, 2772(m/w) ν*(C-H), N-CH$_3$*, 1484(m), 1463(m), 1393(s), 1374(s), 1354(m) ν*(C=C), aromatic ring*, 939(s) ν_s*(NC$_2$)*, 735(m) ν*(Ti-O-C)* cm^{-1}.

Ti(NMe$_2$)$_4$@[KIT-6] (M3a): To a stirred suspension **M1a** (300 mg, 0.624 mmol) in *n*-hexane (6 mL), which was milky but colorless, Ti(NMe$_2$)$_4$ (140 mg, 0.625 mmol) was added dropwise and rinsed with another 2 mL *n*-hexane. After the addition of the first drop of the titanium precursor the milky but colorless suspension turned orange. The suspension was stirred at ambient temperature for 24 h. Then, the solid was collected by centrifugation and washed three times with each 2–4 mL of *n*-hexane and centrifuged after each washing step. After solvent removal in vacuo, **M3a** was obtained as an orange-yellow solid (287 mg). N$_2$ physisorption: a_S(BET) = 440 m^2 g^{-1}; $V_{P,des.}$ = 0.79 cm^3 g^{-1}; $d_{P,ads.}$ = 7.0 nm. Elemental analysis: C, 8.23; H, 1.70; N, 4.60 wt.-%;; C/N = 2.09. DRIFT (KBr): 2866(m) ν*(C-H)*, 1421(w) δ*(C-H)*, 1056(vs) ν_{as}*(Si-O-Si)*, 945(s) ν*(Si–OTi) &* ν*(NC$_2$)*, 808(s) ν_s*(Si-O-Si)*, 598(s) ν*(Ti-NR)*, 449(vs) ν_s*(O-Si-O)* cm^{-1}. ^{13}C NMR (75 MHz, CP/MAS, 10 kHz rotation, 26 °C): δ = 35.82 [*-Ti(NMe$_2$)$_3$*], 43.06 [*=Ti(NMe$_2$)$_2$*] ppm.

H$_2$DHN@Ti(NMe$_2$)$_4$@[KIT-6] (M4a): A clear, colorless solution of 2,3-dihydroxynaphthalene (H$_2$DHN) (23 mg, 0.139 mmol) in toluene (3 mL) was added dropwise to an orange suspension of **M3a** (100 mg) in toluene (1 mL), which then turned red and became darker over time. The mixture was stirred at ambient temperature for 14 h. A dark-red solid had formed, which needed 30 min to settle at the bottom of the vial. Meanwhile a lighter-red, clear supernatant was forming. For easier solvent removal, the supernatant was pipetted off and the solid was suspended in *n*-hexane (4 mL) and transferred into centrifuge tubes. The solid was collected by centrifugation and washed once with 2 mL of toluene, then three times with each 2–4 mL of *n*-hexane and centrifuged after each washing step. After solvent removal in vacuo, **M4a** remained as a shiny orange solid (108 mg). N$_2$ physisorption: a_S(BET) = 393 m^2 g^{-1}; $V_{P,des.}$ = 0.60 cm^3 g^{-1}; $d_{P,ads.}$ = 6.0 nm. Elemental analysis: C, 19.41; H, 2.01; N, 2.62 wt.-%; C/N = 8.65. DRIFT (KBr): 3056(vw) ν*(Ar-H)*, 2883(vw) ν*(C-H)*, 1578(w) ν*(TiO-C) or* ν*(C-C/C=C)*, 1458(s) ν*(C-C/C=C)*, 1163(shoulder) ν*(TiO-C)*, 1068(vs) ν_{as}*(Si-O-Si)*, 862(m) ν*(Si-N)*, 812(m), 633(m) and 569(m) ν_s*(Si-O-Si)*, 741(m) ν*(TiO-C)*, 451(vs) ν_s*(O-Si-O)* cm^{-1}. ^{13}C NMR (75 MHz, CP/MAS, 10 kHz rotation, 26 °C): δ = 25.0 (*THF*), 40.0 [*-Ti(DHN)(NMe$_2$)*], 46.7 {*-[Ti(DHN)]$_2$(NMe$_2$)$_2$*} 67.2 (*THF*), 105.4 (β+β' *carbons*), 121.5 (ε+ε'*carbons*), 125.2 (δ+δ'*carbons*), 130.0 (γ+γ'*carbons*), 156.5 (α+α'*carbons*) ppm.

[Ti(DHN)(NMe$_2$)$_2$]$_2$@[KIT-6] (M5b): To a stirred suspension of **M1b** (300 mg, 0.606 mmol) in *n*-hexane (3 mL), which was milky but colorless, the dimeric complex **2a** (108 mg, 0.367 mmol), dissolved in a mixture of 3 mL *n*-hexane and 6 mL of thf, was added dropwise. The resulting dark-red suspension was stirred at ambient temperature for 22 h. The solid was collected by centrifugation, washed with thf once, then twice with *n*-hexane and centrifuged after each washing step. The solid was finally suspended in 2 mL *n*-hexane and transferred into a vial. After solvent removal in vacuo **M5b** remained as an orange solid (244 mg). N$_2$ physisorption: a_S(BET) = 428 m^2 g^{-1}; $V_{P,des.}$ = 0.68 cm^3 g^{-1}; $d_{P,ads.}$ = 5.6 nm. Elemental analysis: C, 16.00; H, 1.94; N, 2.21 wt.-%; C/N = 8.44. DRIFT (KBr): 3056(vw) ν*(Ar-H)*, 2878–2978(vw) ν*(C-H)*, 1576(w) ν*(TiO-C) or* ν*(C-C/C=C)*, 1457(s) ν*(C-C/C=C)*, 1163(shoulder) ν*(TiO-C)*, 1068(vs) ν_{as}*(Si-O-Si)*, 862(m) ν*(Si-N)*, 812(m), 633(m) and 569(m) ν_s*(Si-O-Si)*, 741(m) ν*(TiO-C)*, 451(s) ν_s*(O-Si-O)* cm^{-1}. ^{13}C NMR (75 MHz, CP/MAS, 10 kHz rotation, 26 °C): δ = 25.0 (*THF*), 35.0 [*-Ti(NMe$_2$)$_3$*], 40.2 [*-Ti(DHN)(NMe$_2$)*], 67.2 (*THF*), 105.0 (β+β' *carbons*), 121.5 (ε+ε'*carbons*), 126.0 (δ+δ'*carbons*), 130.0 (γ+γ'*carbons*), 160.0 (α+α'*carbons*) ppm.

Supporting information (see footnote on the first page of this article): Crystallographic data for complexes **1a**, **1a(thf)**, **2a(thf)**, **4a**, and **5a**; NMR spectra of reactants and molecular complexes; IR spectra of the molecular complexes, EI-mass spectrum of complex **5a**; nitrogen adsorption/desorption isotherms at 77.4 K and the corresponding BJH size distributions of materials **M1a, M2a**, **M1b**, and **M2b**; DRIFT spectra of materials **M1a, M2a**, **M1b**, and **M2b**. PXRD diagrams of parent materials **M1a** and **M1b**.

Acknowledgments

We thank *ams Sensors Germany GmbH* for financial support. We are grateful to Dr. Yucang Liang and Lena Merten for their support in the synthesis of KIT-6, Dr. Daniel Werner and Elke Niquet for support in X-ray structure analyses and Tatiana Spallek for assistance with the grafting reactions.

Keywords: Titanium · N ligands · Catechol · Grafting · Mesoporous materials

[1] a) R. Anwander, *Chem. Mater.* **2001**, *13*, 4419–4438; b) J. S. Chang, J. S. Hwang, S. E. Park, *Res. Chem. Intermed.* **2003**, *29*, 921–938; c) J. M. Basset,

R. Psaro, D. Roberto, R. Ugo (Eds.), *Modern Surface Organometallic Chemistry*, Wiley-VCH Verlag GmbH & Co. KGaA, Weinheim, **2009**; d) C. Copéret, A. Comas-Vives, M. P. Conley, D. P. Estes, A. Fedorov, V. Mougel, H. Nagae, F. Nunez-Zarur, P. A. Zhizhko, *Chem. Rev.* **2016**, *116*, 323–421; e) R. Anwander, in *Handbook of Heterogeneous Catalysis*, Wiley-VCH Verlag GmbH & Co. KGaA, **2008**. ***((<=PM: CrossRef notyet done))***.

[2] E. Le Roux, *Coord. Chem. Rev.* **2016**, *306*, 65–85.

[3] a) J. S. Chang, S. H. Jhung, Y. K. Hwang, S. E. Park, J. S. Hwang, *IJNT* **2006**, *3*, 150–180; b) B. Albela, L. Bonneviot, *New J. Chem.* **2016**, *40*, 4115–4131; c) J. M. Campos, J. P. Lourenco, H. Cramail, M. R. Ribeiro, *Prog. Polym. Sci.* **2012**, *37*, 1764–1804; d) F. Lefebvre, in *Atomically-Precise Methods for Synthesis of Solid Catalysts* (Eds.: S. Hermans, T. V. DeBocarme), **2015**, pp. 1–26. *RSC Books, Catalysis Series,* DOI: 10.1039/9781782628439-00001.

[4] Y. Liang, R. Anwander, *Dalton Trans.* **2013**, *42*, 12521–12545.

[5] Y. Liang, E. S. Erichsen, R. Anwander, *Dalton Trans.* **2013**, *42*, 6922–6935.

[6] R. Anwander, H. W. Görlitzer, G. Gerstberger, C. Palm, O. Runte, M. Spiegler, *J. Chem. Soc., Dalton Trans.* **1999**, 3611–3615.

[7] T. Deschner, B.-T. Lønstad, M. Widenmeyer, R. Anwander, *J. Mater. Chem.* **2011**, *21*, 5620–5628.

[8] A. O. Bouh, G. L. Rice, S. L. Scott, *J. Am. Chem. Soc.* **1999**, *121*, 7201–7210.

[9] S.-I. Murahashi, Y. Imada, T. Kawakami, K. Harada, Y. Yonemushi, N. Tomita, *J. Am. Chem. Soc.* **2002**, *124*, 2888–2889.

[10] L. A. DeLearie, C. G. Pierpont, *J. Am. Chem. Soc.* **1986**, *108*, 6393–6394.

[11] N. Schweigert, A. J. B. Zehnder, R. I. L. Eggen, *Environ. Microbiol.* **2001**, *3*, 81–91.

[12] J. Clayden, N. Greeves, S. Warren, *Organic Chemistry*, 2nd Edition, Oxford University Press, Oxford **2012**, pp. 382–387.

[13] B. A. Borgias, S. R. Cooper, Y. B. Koh, K. N. Raymond, *Inorg. Chem.* **1984**, *23*, 1009–1016.

[14] a) M. G. Davidson, M. D. Jones, M. D. Lunn, M. F. Mahon, *Inorg. Chem.* **2006**, *45*, 2282–2287; b) W. A. Wallace, P. G. Potvin, *Inorg. Chem.* **2007**, *46*, 9463–9472; c) J. B. Benedict, P. Coppens, *J. Am. Chem. Soc.* **2010**, *132*, 2938–2944.

[15] a) K. M. Waltz, P. J. Carroll, P. J. Walsh, *Organometallics* **2004**, *23*, 127–134; b) J. P. Corden, W. Errington, P. Moore, M. G. Partridge, M. G. Wallbridge, *Dalton Trans.* **2004**, 1846–1851.

[16] C. W. Lange, B. J. Conklin, C. G. Pierpont, *Inorg. Chem.* **1994**, *33*, 1276–1283.

[17] T. J. Boyle, D. L. Barnes, J. A. Heppert, L. Morales, F. Takusagawa, J. C. Connolly, *Organometallics* **1992**, *11*, 1112–1126.

[18] M. P. Bubnov, I. A. Teplova, N. O. Druzhkov, G. K. Fukin, A. V. Cherkasova, V. K. Cherkasov, *J. Chem. Sci.* **2015**, *127*, 527–535.

[19] S. Paria, P. Halder, B. Chakraborty, T. Kanti Paine, *Indian J. Chem. Sect. A* **2011**, *50*, 420.

[20] M. Widenmeyer, S. Grasser, K. Köhler, R. Anwander, *Microporous Mesoporous Mater.* **2001**, *44*, 327–336.

[21] F. Kleitz, S. Hei Choi, R. Ryoo, *Chem. Commun.* **2003**, 2136–2137.

[22] a) T.-W. Kim, F. Kleitz, B. Paul, R. Ryoo, *J. Am. Chem. Soc.* **2005**, *127*, 7601–7610; b) Ref. [5].

[23] R. Anwander, I. Nagl, M. Widenmeyer, G. Engelhardt, O. Groeger, C. Palm, T. Röser, *J. Phys. Chem. B* **2000**, *104*, 3532–3544.

[24] K. S. W. Sing, D. H. Everett, H. R. A. W. Haul, L. Moscou, R. A. Pierotti, J. Rouquérol, T. Siemieniewska, *Pure Appl. Chem.* **1985**, *57*, 603–619.

[25] Y. Liang, R. Anwander, *J. Mater. Chem.* **2007**, *17*, 2506–2516.

[26] S. Herres, P. Hesemann, Joël J. E. Moreau, *Eur. J. Org. Chem.* **2003**, 99–105.

[27] D. C. Bradley, M. H. Gitlitz, *J. Chem. Soc. A* **1969**, *0*, 980–984.

[28] D. Finkelstein-Shapiro, S. K. Davidowski, P. B. Lee, C. Guo, G. P. Holland, T. Rajh, K. A. Gray, J. L. Yarger, M. Calatayud, *J. Phys. Chem. C* **2016**, *120*, 23625–23630.

[29] SDBS No. 1626CDS-12–413, ^{13}C NMR (15 MHz) of 2,3-naphthalenediol in [D_6]DMSO, Spectral Database for Organic Compounds SDBS; http://sdbs.db.aist.go.jp/sdbs/cgi-bin/direct_frame_disp.cgi?sdbsno = 1626, Wed. 28/02/**2018**.

[30] *APEX2*, COSMO, **2012**, version 2012.10 0, Bruker AXS Inc., Madison, WI.

[31] *APEX2*, SAINT, **2010**, version 7.99 A, Bruker AXS Inc., Madison, WI.

[32] *APEX2*, SADABS, **2012**, version 2012/1, G. M. Sheldrick, Bruker AXS Inc., Madison, WI.

[33] G. M. Sheldrick, *Acta Crystallogr., Sect. A* **2008**, *64*, 112–122.

[34] *SHELXS-97*, **1997**, G. M. Sheldrick, Göttingen, Germany.

[35] *SHELXL-**2013***, **2013**, G. M. Sheldrick, Göttingen, Germany. SHELXLE **2011**; C. B. Hubschle, G. M. Sheldrick, B. Dittrich, *J. Appl. Crystallogr.* **2011,** *44*, 1281–1284; SHELXTL, *Acta Cryst.* **2015,** *A71*, 3–8.

[36] *TWINABS*, **2007**, G. M. Sheldrick, Bruker AXS Scaling for twinned crystals, version 2007/3, & SADABS, Göttingen, Germany.

[37] L. J. Farrugia, *J. Appl. Crystallogr.* **1997**, *30*, 565.

[38] POV-Ray, **2004**, version 3.6, Persistence of Vision Pty. Ltd., Williamstown, Victoria, http://www.povray.org/.

[39] M. Beaudoin, S. L. Scott, *Organometallics* **2001**, *20*, 237–239.

Received: October 16, 2018

Supporting Information

Titanium(IV) Catecholate-Grafted Mesoporous Silica KIT-6: Probing Sequential and Convergent Immobilization Approaches

Andrea Sonström, David Schneider, Cäcilia Maichle-Mössmer, and Reiner Anwander*

ejic201801269-sup-0001-SupMat.pdf

Supporting Information

Contents

Experimental Data

KIT-6 (M1a and M1b).

Triblock-copolymer Pluronic P123 (11.6 g, 2.00 mmol) and an aqueous solution of 35% HCl (20.3 g, 195 mmol) in deionized water (399.8 g, 22.21 mol) were stirred at 35.0 °C until P123 dissolved completely. Then *n*-butanol (11.5 g, 155 mmol) was added slowly. After being stirred at 35.0 °C for 30 min, TEOS (24.78 g, 119 mmol) was added dropwise. A cloudy solution was obtained and continuously stirred at 35 °C for 24 h. The resulting suspension was transferred into a PTFE-lined stainless steel autoclave and aged at 130 °C for 24 h. The white precipitate was collected by a suction filter before cooling and dried at ambient temperature in a ceramic crucible overnight. The organic residues were removed by calcination of the as-made precipitate at 540 °C for 4 h to obtain 6.58 g (109 mmol, 93%) of the mesoporous silica as a white powder. The calcined material was characterized by powder X-ray diffraction analysis and nitrogen physisorption. For the latter the sample was degassed at 270 °C for 4 h before the measurement. PXRD: 2θ = 0.91°; d_{211} = 9.71 nm; a = 23.8 nm. N_2 physisorption: a_S(BET) = 629 m^2 g^{-1}; $V_{P,\,cum.des.}$ = 1.20 cm^3 g^{-1}; $d_{P,\,ads.}$ = 8.3 nm. The KIT-6 sample was ground to a fine powder and activated at 500 °C for 12 h by using a temperature-controlled program and a high-vacuum system (HV). The activated KIT-6_{500} sample was denoted as **M1a** and stored in an Ar-filled glovebox for use. Material **M1a** was characterized by powder X-ray diffraction analysis and nitrogen physisorption as well as DRIFT spectroscopy. Prior to the nitrogen physisorption measurement the sample was degassed at ambient temperature for 1 h at the physisorption device. PXRD: 2θ = 0.91°, 1.65°; d_{211} = 9.71 nm; a = 23.8 nm. N_2 Physisorption: a_S (BET) = 620 m^2 g^{-1}; $V_{P,\,cum.des}$ = 1.19 cm^3 g^{-1}; $d_{P,\,ads.}$ = 8.5 nm. DRIFTS (KBr, [cm^{-1}]): 3745(m) *ν(SiOH)*; 1051(vs) ν_{as}*(Si-O-Si)*; 814(vs) ν_s*(Si-O-Si)*; 444(vs) ν_s*(O-Si-O)*.

Using the same procedure, a second synthesis gave 6.04 g (100 mmol, 85% yield) of the mesoporous silica as a white powder. PXRD: 2θ = 0.9°; d_{211} = 10.3 nm; a = 25.0 nm. N_2 physisorption: a_S(BET) = 638 m^2 g^{-1}; $V_{P,cum.des.}$ = 1.28 cm^3 g^{-1}; $d_{P,\,ads.}$ = 7.9 nm. The activated KIT-6_{500} sample was called **M1b** and stored in an Ar-filled glovebox for use. PXRD: 2θ = 0.86°, 1.59°; d_{211} = 10.3 nm; a = 25.0 nm. N_2 physisorption: a_S(BET) = 622 m^2 g^{-1}; $V_{P,cum.des.}$ = 1.24 cm^3 g^{-1}; $d_{P,\,ads.}$ = 7.7 nm. DRIFTS (KBr, [cm^{-1}]): 3743(m) *ν(SiOH)*; 1070(vs) ν_{as}*(Si-O-Si);* 819(s) ν_s*(Si-O-Si);* 451(s) ν_s*(O-Si-O)*.

$HN(SiHMe_2)_2$@[KIT-6] (M2a and M2b).

M1a (202 mg, 0.420 mmol) was suspended in 5 mL of dry *n*-hexane in a vial. A solution of 1,1,3,3-tetramethyldisilazane (400 mg, 3.00 mmol) in 5 mL of dry *n*-hexane was added. The mixture was stirred at ambient temperature for 24 h. The solid was collected by centrifugation and washed four times with *n*-hexane (2 mL each). The final solid was dispersed in fresh *n*-hexane and transferred into a vial, dried in vacuum until constant weight to yield 190 mg of material **M2a**. **M2a** was degassed and further dried at the physisorption device (p = 10^{-3} mbar) at 110 °C for 3 h before performing elemental analysis, DRIFTS and nitrogen physisorption. N_2 physisorption: a_S(BET) = 500 m^2 g^{-1}; $V_{P,cum.des.}$ = 0.97 cm^3 g^{-1}; $d_{P,\,ads.}$ = 7.2 nm. Elemental analysis [wt%]: C, 4.46; H, 0.50; N, 0.03; δ (SiOH) = 2.08 mmol g^{-1}; α (SiOH) = 2.02 $\frac{\mathbf{OH-groups}}{\mathbf{nm^2}}$. DRIFTS (KBr, [$cm^{-1}$]): 2966(w) *ν(C-H);* 2154(m) *ν(Si-H)*; 1051(vs) ν_{as}*(Si-O-Si)*; 908(s) *δ(O-Si-H);* 814(vs) ν_s*(Si-O-Si);* 436(vs) ν_s*(O-Si-O)*.

For **M2b**, **M1b** (202 mg, 0.420 mmol) was suspended in 5 mL of dry *n*-hexane following the same procedure as for the synthesis of **M2a**. N_2 Physisorption: a_S(BET) = 503 m^2 g^{-1}; $V_{P,cum.des.}$ = 1.03 cm^3 g^{-1}; $d_{P,ads.}$ = 6.7 nm. Elemental analysis [wt%]: C, 4.01; H, 1.27; N, 0.00. δ (SiOH) = 1.84 mmol g^{-1}; α (SiOH) = 1.78 $\frac{\mathbf{OH-groups}}{\mathbf{nm^2}}$. DRIFTS (KBr, [$cm^{-1}$]): 2965(w) *ν(C-H);* 2153(m) *ν(Si-H)*; 1058(vs) ν_{as}*(Si-O-Si)*; 909(s) *δ(O-Si-H);* 811(vs) ν_s*(Si-O-Si);* 440(vs) ν_s*(O-Si-O)*.

Crystallographic Details

Table S1: Selected bond lengths and interatomic distances [Å] as well as selected bond angles [°] of the dimeric complexes [Ti(CAT)(NMe_2)] (**1a**) and [Ti(CAT)(NMe_2)(thf)] (**1a(thf)**) compared to a dimeric anion of a homoleptic Ti(IV) catecholate complex known from literature[1]

1a		**1a(thf)**		**Dimeric anion in $[Et_3NH]_2$ $[Ti(tBu_2CAT)_2(HtBu_2CAT)]$[1]**	
bond/angle	**length [Å]/ angle [°]**	**bond/angle**	**length [Å]/ angle [°]**	**bond/angle**	**length [Å]/ angle [°]**
Ti1-N1	1.8805(13)	Ti1-N1	1.8711(17)	/	/
Ti1-N2	1.8680(14)	Ti1-N2	1.8895(16)	/	/
N1-Ti1-N2	105.00(6)	N1-Ti1-N2	105.24(7)	/	/
/	/	Ti2-N3	1.8950(16)	/	/
/	/	Ti2-N4	1.9359(16)	/	/
/	/	N3-Ti2-N4	97.86(7)	/	/
/	/	Ti2-O3	2.1788(13)	/	/
Ti1-O1	2.0995 (11)	Ti1-O1	2.1380(14)	Ti-O3	2.079(1)
Ti1-O2	1.9356(12)	Ti1-O2	1.9234(13)	Ti-O4	1.885(2)
O1-Ti1-O2	77.64(4)	O1-Ti1-O2	77.32(5)	O3-Ti-O4	77.5(1)
Ti1-O1a	2.0014 (11)	Ti1-O3	1.9883(13)	Ti-O3´	2.041(2)
Ti1a-O1	2.0014 (11)	Ti2-O1	2.0258(13)	Ti´-O3	2.079(1)
O1a-Ti1-O1	69.95(5)	O1-Ti1-O3	72.41(5)	O3´-Ti-O3	72.4(1)
/	/	Ti2-O4	1.9165(13)	/	/
/	/	O3-Ti2-O4	77.58(5)	/	/
/	/	Ti2-O5	2.2718(14)	Ti-O5	1.936(2)
O1-C101	1.3710(19)	O1-C101	1.367(2)	O3-C21	1.372(3)
O2-C102	1.3522(18)	O2-C102	1.352(2)	O4-C22	1.353(3)
/	/	O4-C302	1.348(2)	/	/
/	/	O3-C301	1.361(2)	/	/
Ti1····Ti1a (distance)	3.3609(5)	Ti1····Ti2 (distance)	3.3587(4)	Ti····Ti´ (distance)	3.326(1)

* Here only the data of the HCATtBu$_2$ ligand and the data of the CATtBu$_2$ ligand, which participates in the bridging to the second Ti(IV) center, are presented.

Table S2: Selected bond lengths and interatomic distances [Å] as well as selected bond angles [°] of the dimeric complexes of [Ti(CAT*t*Bu$_2$-3,5)(NMe$_2$)] (**4a**), and [Ti(DHN)(NMe$_2$)(thf)] (**2a(thf)**) compared to a dimeric anion of a homolepticTi(IV) catecholate complex known from literature[1]

4a		**2a(thf)**		**5a**		**Dimeric anion in [Et$_3$NH]$_2$ [Ti(*t*Bu$_2$CAT)$_2$(H*t*Bu$_2$CAT)][1]**	
bond/angle	**length [Å]/ angle [°]**	**bond/angle**	**length [Å]/ angle [°]**	**bond/angle**	**length [Å]/ angle [°]**	**bond/angle**	**length [Å]/ angle [°]**
Ti1-N1	1.8850(16)	Ti1-N1	1.8853(13)	Ti1-N3	1.8881(15)	/	/
Ti1-N2	1.8699(17)	Ti1-N2	1.8698(13)	Ti1-N4	1.8966(14)	/	/
N1-Ti1-N2	102.95(7)	N1-Ti1-N2	103.61(6)	N3-Ti1-N4	104.56(6)	/	/
/	/	/	/	Ti1-N1	2.1235(14)	/	/
/	/	/	/	Ti2-N1-Ti1	99.25(6)	/	/
Ti2-N3	1.8679(17)	Ti2-N3	1.8947(13)	Ti2-N1	2.0641(14)	/	/
Ti2-N4	1.8789(15)	Ti2-N4	1.9376(13)	Ti2-N2	1.8988(15)	/	/
N3-Ti2-N4	105.14(7)	N3-Ti2-N4	96.39(6)	N1-Ti2-N2	103.70(6)	/	/
Ti2-O3	2.1192(13)	Ti2-O3	2.1776(11)	Ti2-O3	1.9374(12)	/	/
Ti1-O1	2.1084(13)	Ti1-O1	2.1255(11)	Ti1-O1	2.2978(11)	Ti-O3	2.079(1)
Ti1-O2	1.9011(13)	Ti1-O2	1.9263(11)	Ti1-O2	1.8528(11)	Ti-O4	1.885(2)
O1-Ti1-O2	77.55(5)	O1-Ti1-O2	77.39(4)	O1-Ti1-O2	74.20(4)	O3-Ti-O4	77.5(1)
Ti1-O3	2.0118(13)	Ti1-O3	2.0071(11)	/	/	Ti-O3´	2.041(2)
Ti2-O1	2.0091(13)	Ti2-O1	2.0165(11)	Ti2-O1	1.9704(11)	Ti´-O3	2.079(1)
O2-Ti1-O3	70.72(5)	O1-Ti1-O3	71.07(4)	/	/	O3´-Ti-O3	72.4(1)
Ti2-O4	1.9057(13)	Ti2-O4	1.9388(11)	Ti2-O4	1.8986(12)	/	/
O3-Ti2-O4	77.00(5)	O3-Ti2-O4	77.65(4)	O3-Ti2-O4	78.87(5)	/	/
		Ti2-O5	2.2612(11)	/	/	Ti-O5	1.936(2)
O1-C101	1.361(2)	O1-C101	1.3632(17)	O1-C101	1.3740(19)	O3-C21	1.372(3)
O2-C102	1.375(2)	O2-C102	1.3492(17)	O2-C102	1.3620(19)	O4-C22	1.353(3)
O4-C302	1.359(2)	O4-C302	1.3451(17)	O4-C302	1.360(2)	/	/
O3-C301	1.378(2)	O3-C301	1.3589(17)	O3-C301	1.351(2)	/	/
Ti1···Ti2 (distance)	3.3412(5)	Ti1···Ti2 (distance)	/	Ti1···Ti2 (distance)	3.1905(4)	Ti···Ti´ (distance)	3.326(1)

* Here only the data of the HCAT*t*Bu$_2$ ligand and the data of the CAT*t*Bu$_2$ ligand, which participates in the bridging to the second Ti(IV) center, are presented.

Table S3: Crystallographic data for complexes **1a**, **1a(thf)**, **4a**, **2a(thf)**, and **5a**

	1a	**1a (thf)**	**4a**	**2a (thf)**	**5a**
CCDC#	1862528	1862531	1862530	1862529	1862532
Formula	$C_{20}H_{32}N_4O_4Ti_2$	$C_{24}H_{40}N_4O_5Ti_2$	$C_{36}H_{64}N_4O_4Ti_2$	$C_{32}H_{44}N_4O_5Ti_2$	$C_{36}H_{64}N_4O_4Ti_2$
M_w	488.29	560.40	712.71	661.52	712.71
color/shape	yellow/needles	Red/huge needles	Gold-yellow/plates	Red/ huge needles	Clear orange/ irregular needles
crystal dimensions [mm³]	0.033 0.086 0.188	0.329 0.228 0.196	0.070 0.170 0.200	0.061 0.142 0.162	0.244 0.124 0.105
crystal system	triclinic	monoclinic	triclinic	triclinic	Monoclinic
space group	$P\bar{1}$	Cc	$P\bar{1}$	$P\bar{1}$	$P2_1/c$
a [Å]	7.6628(2)	18.6649(6)	10.4984(6)	8.5561(4)	13.4391(9)
b [Å]	8.0764(2)	11.3034(4)	13.8961(8)	13.0639(6)	20.4412(14)
c [Å]	10.0856(3)	14.5943(8)	15.6303(9)	15.3118(7)	15.4533(11)
α [°]	71.069(2)	90	109.716(2)	99.563(2)	90
β [°]	81.822(2)	118.37	101.103(2)	104.570(2)	112.3888(11)
γ [°]	80.954(2)	90	103.449(2)	100.136(2)	90
V [Å³]	580.28(3)	2709.3(2)	1994.1(2)	1590.34(13)	3925.2(5)
Z	1	4	2	2	4
T [K]	173(2)	100(2)	100(2)	100(2)	100(2)
ρ_{calcd} [gcm^{-3}]	1.397	1.374	1.187	1.379	1.206
μ [mm^{-1}]	0.720	0.629	0.440	0.548	0.447
F(000)	256	1184	768	696	1536
θ range [°]	2.705/28.270	2.187/28.282	1.644/27.101	1.624/28.282	1.639/28.299
index ranges	-10 ≤ h ≤ 10 -10 ≤ k ≤ 10 -13 ≤ l ≤ 13	-24 ≤ h ≤ 24 -15 ≤ k ≤ 15 -19 ≤ l ≤ 19	/	-11 ≤ h ≤ 11 -17 ≤ k ≤ 17 -20 ≤ l ≤ 20	-17 ≤ h ≤ 17 -27 ≤ k ≤ 25 -20 ≤ l ≤ 20
total reflns	9325	34134	30881	50091	71979
unique reflns / R_{int}	2869/0.0261	6722/0.0274	8788/0.0386	7890/0.0403	9732/0.0582
observed reflns (I > 2σ)*	2594	6583	7036	6752	8038
data/parameters/ restraints	2869/140/0	6722/324/2	8788/441/2	7890/396/408	9732/436/0
R1/wR2 (I > 2σ)*	0.0304/0.0733	0.0197/0.0499	0.0403/0.0911	0.0317/0.0774	0.0400/0.0914
R1/wR2 (all data)*	0.0357/0.0758	0.0205/0.0498	0.0575/0.0969	0.0398/0.0822	0.0551/0.0993
GOF*	1.080	1.039	1.035	1.065	1.079

NMR Spectra

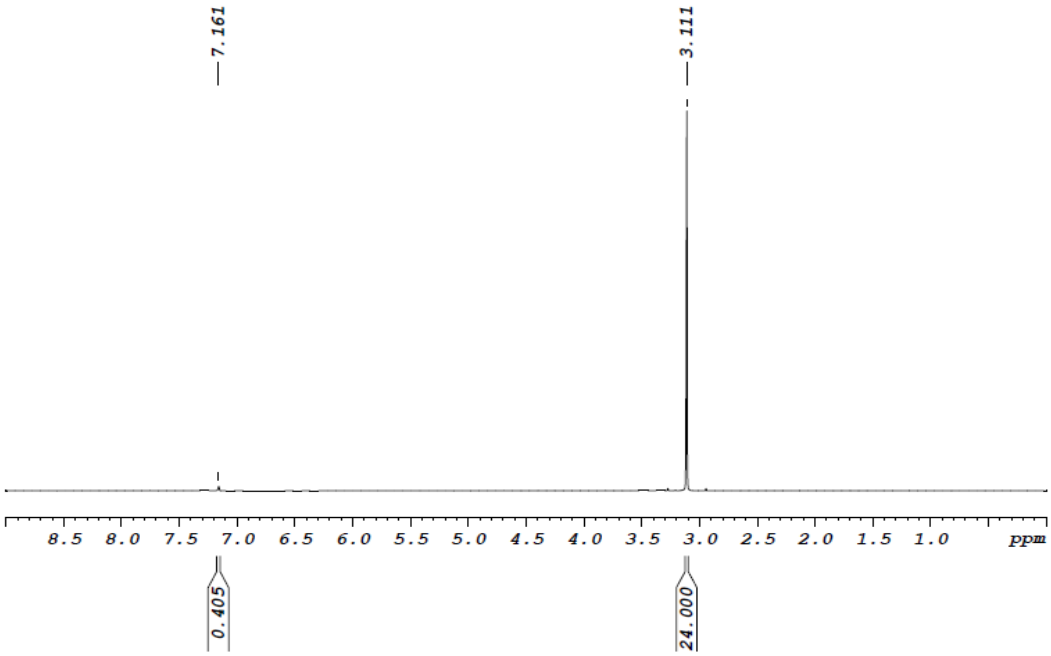

Figure S1: ^{1}H NMR spectrum (400 MHz, C_6D_6) of $Ti(NMe_2)_4$ at 26 °C.

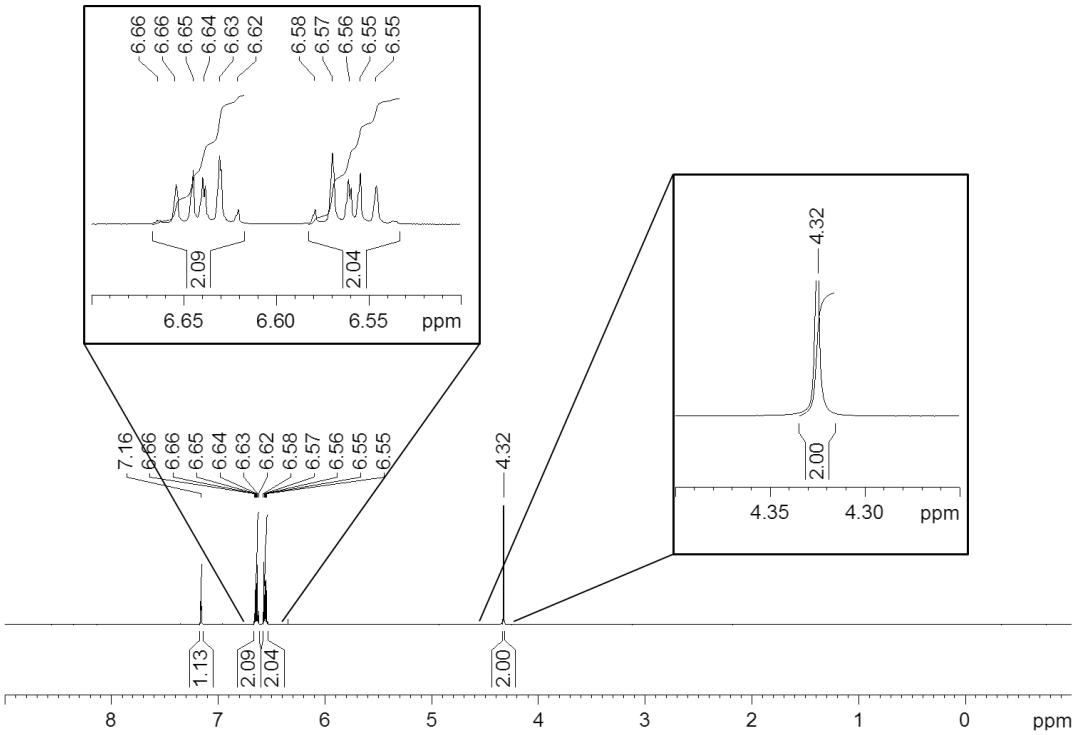

Figure S2: ^{1}H NMR spectrum (400 MHz, C_6D_6) of H_2CAT at 26 °C.

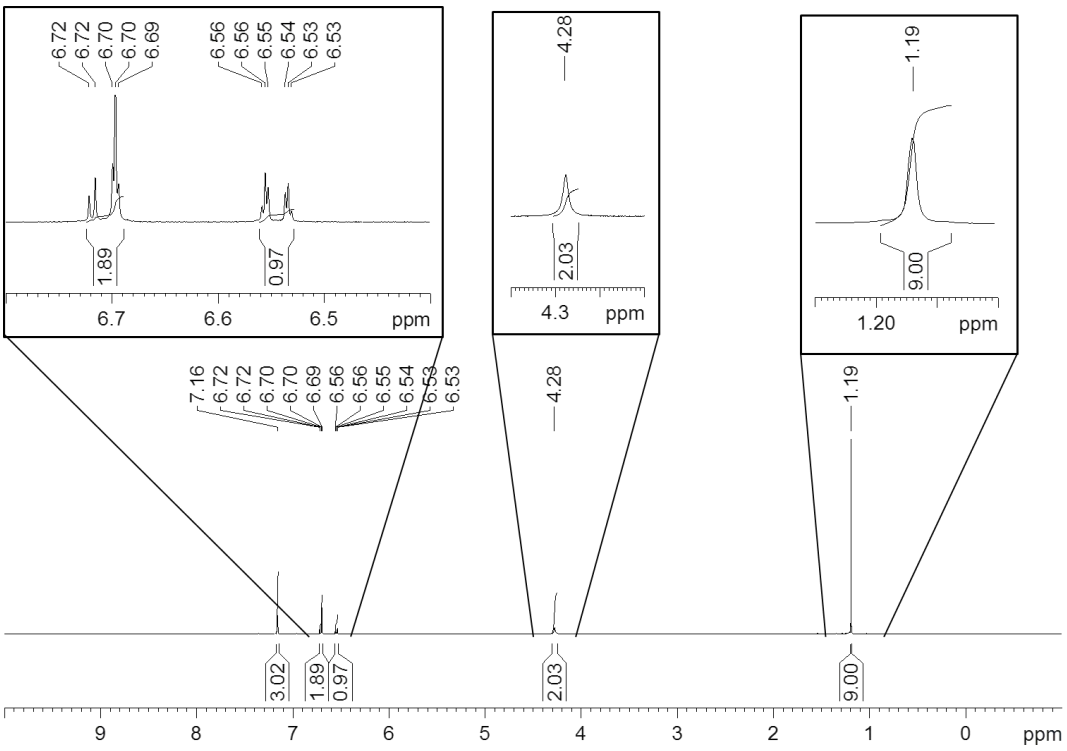

Figure S3: ^{1}H NMR spectrum (400 MHz, C_6D_6) of H_2CAT*t*Bu-4 at 26 °C.

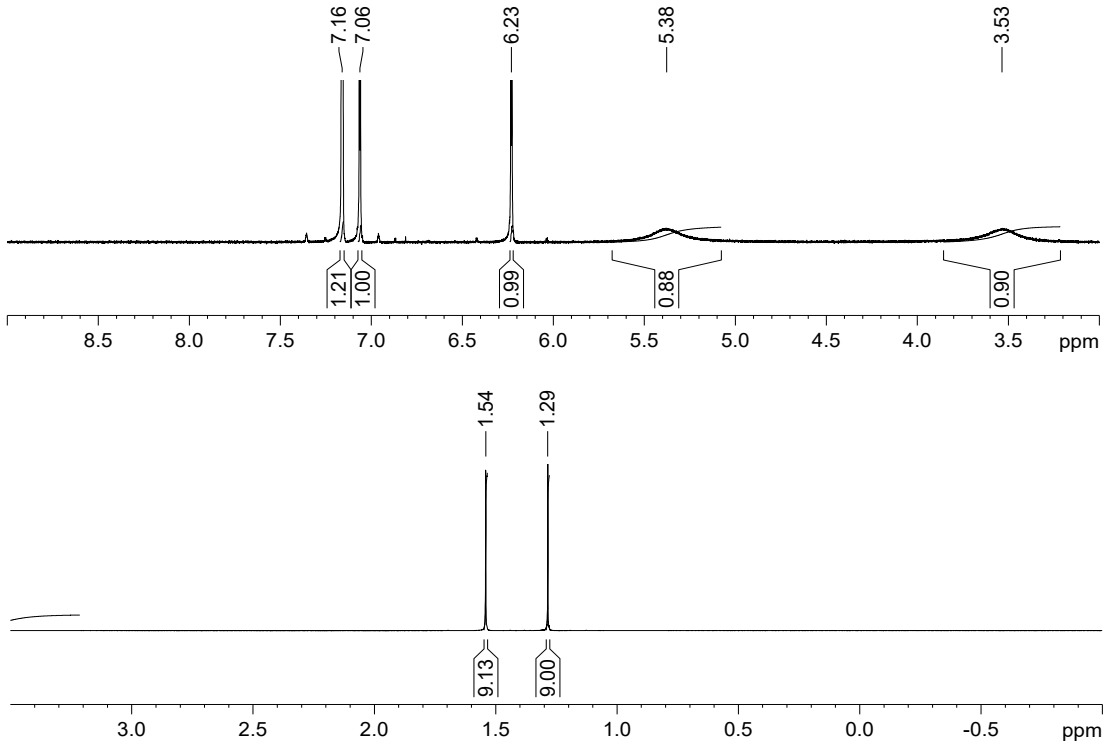

Figure S4: ^{1}H NMR spectrum (400 MHz, C_6D_6)of H_2CAT*t*Bu$_2$-3,5 at 26 °C.

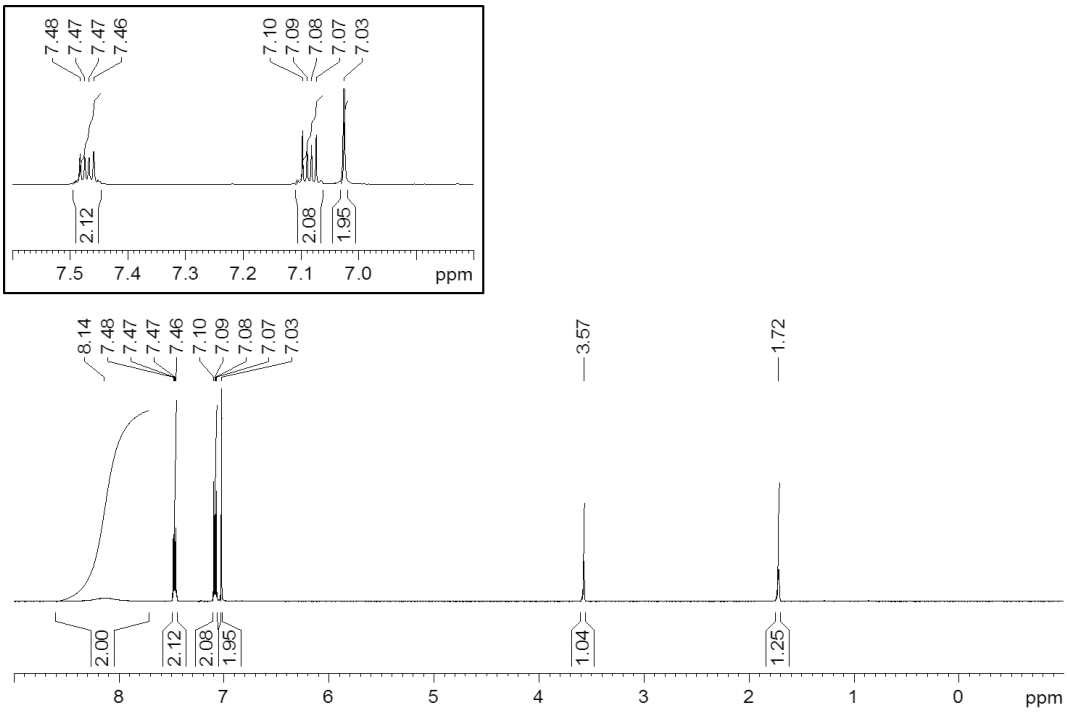

Figure S5: ^{1}H NMR spectrum (400 MHz, thf-d_8) of H_2DHN at 26 °C.

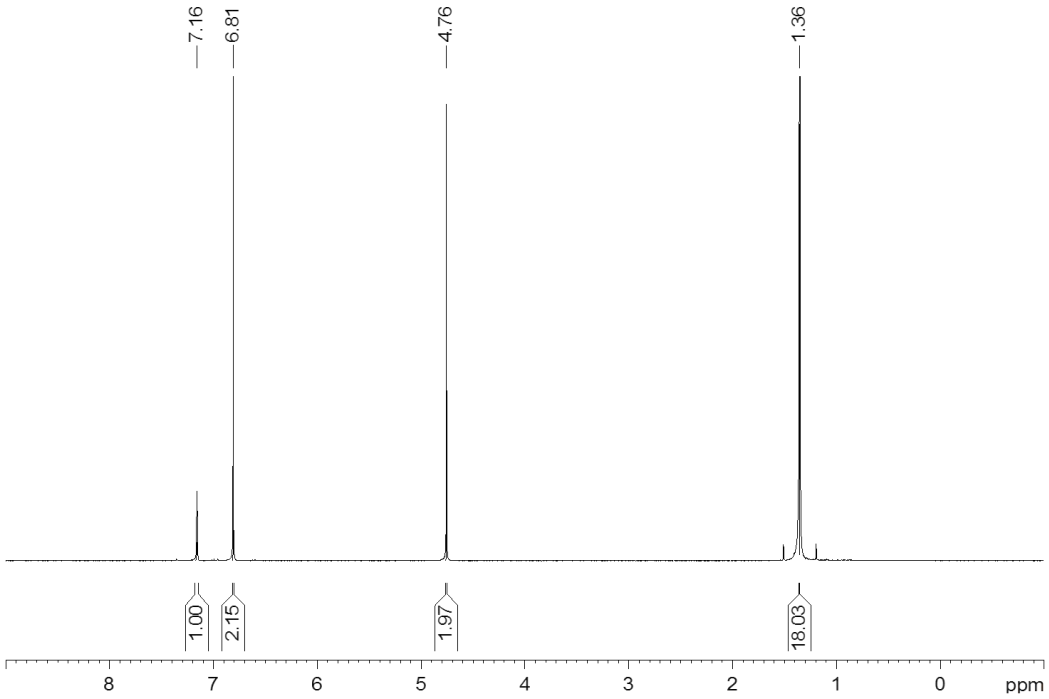

Figure S6: ^{1}H NMR spectrum (400 MHz, C_6D_6) of H_2CAT*t*Bu$_2$-3,6 at 26 °C.

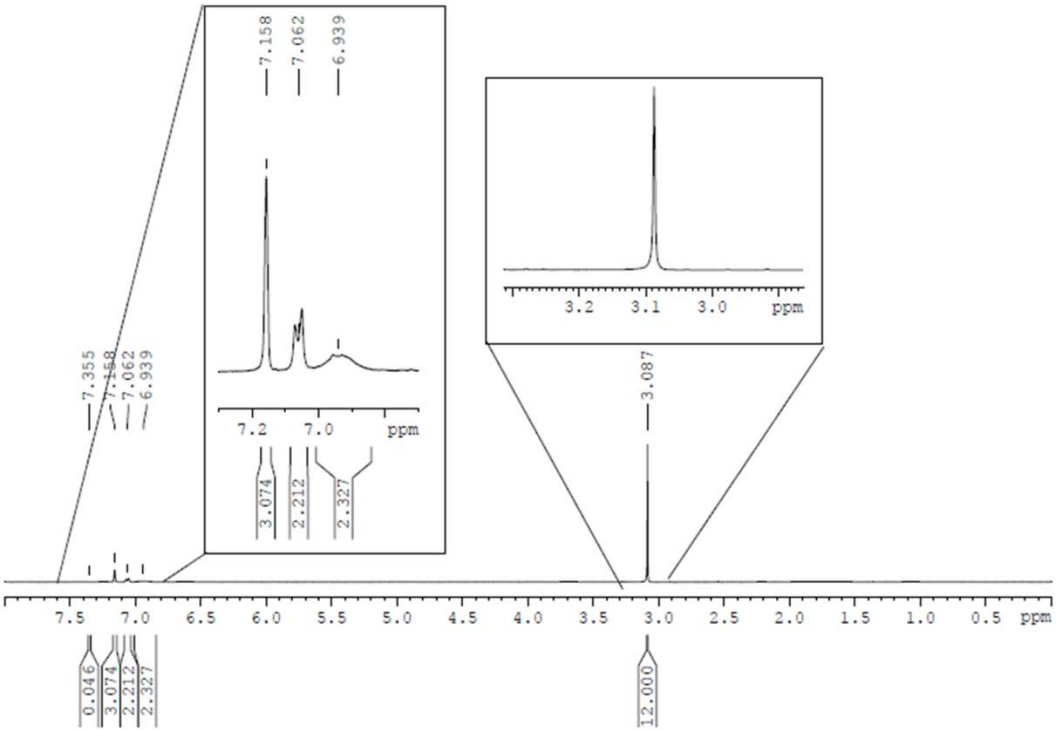

Figure S7: ^{1}H NMR spectrum (400 MHz, C_6D_6) of $[Ti(CAT)(NMe_2)_2]_2$ **(1a)** at 26 °C.

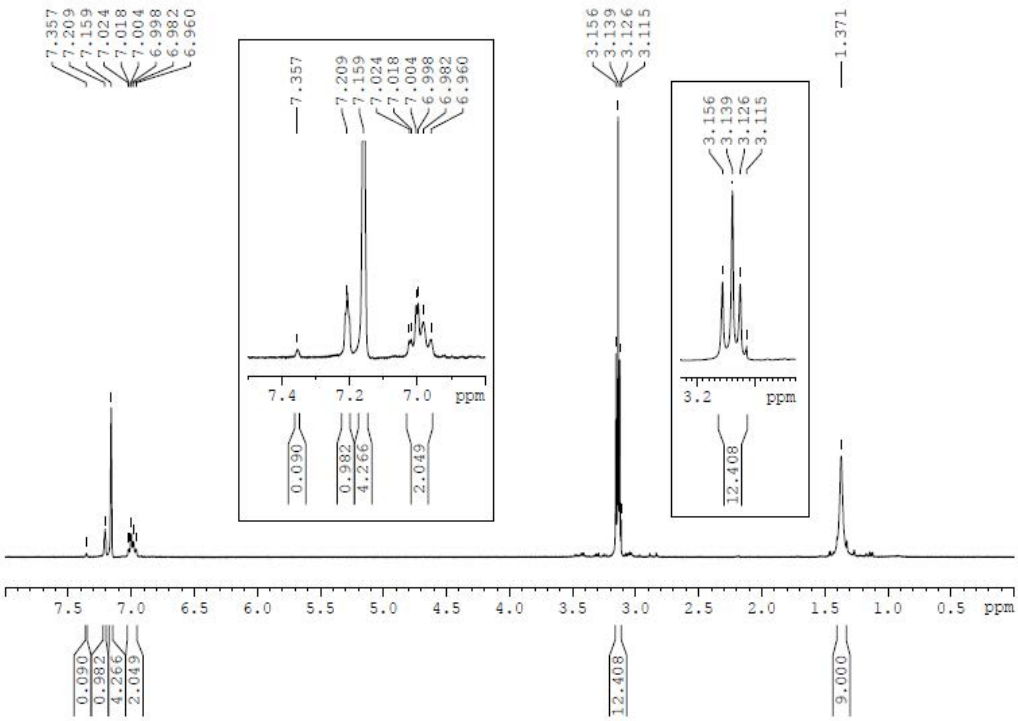

Figure S8: ^{1}H NMR spectrum (400 MHz, C_6D_6) of $[Ti(CAT\textit{t}Bu\text{-}4)(NMe_2)_2]_x$ **(3a)** at 26 °C.

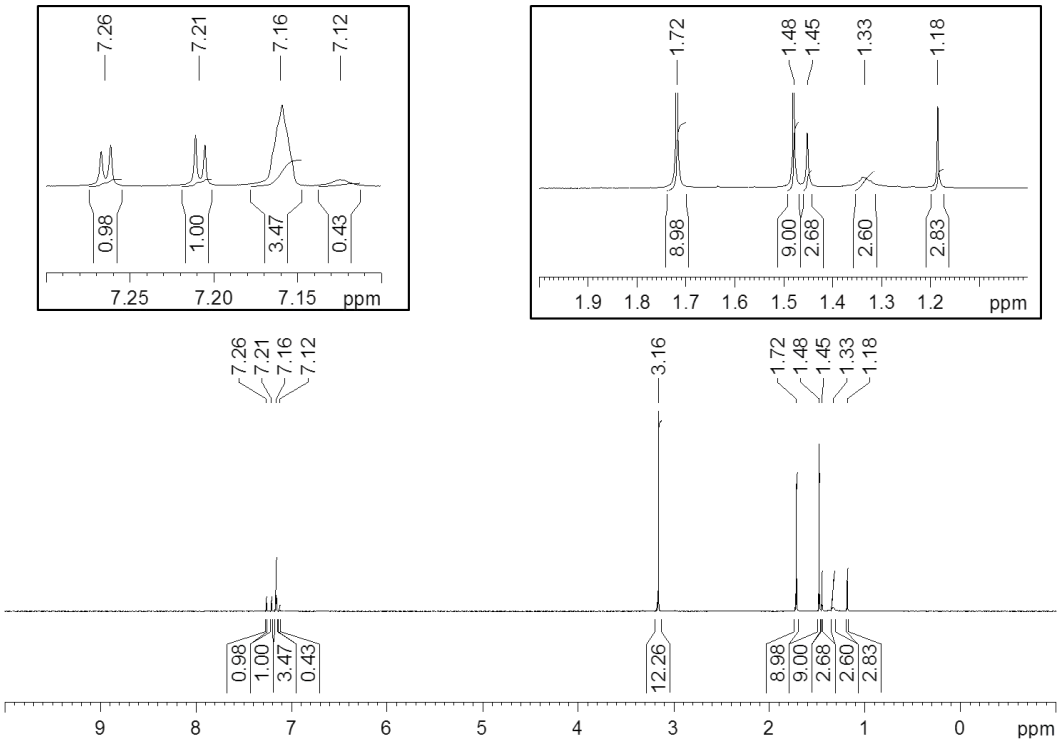

Figure S9: ^{1}H NMR spectrum (400 MHz, C_6D_6) of $[Ti(CAT^{t}Bu_2\text{-}3,5)(NMe_2)_2]_2$ **(4a)** at 26 °C.

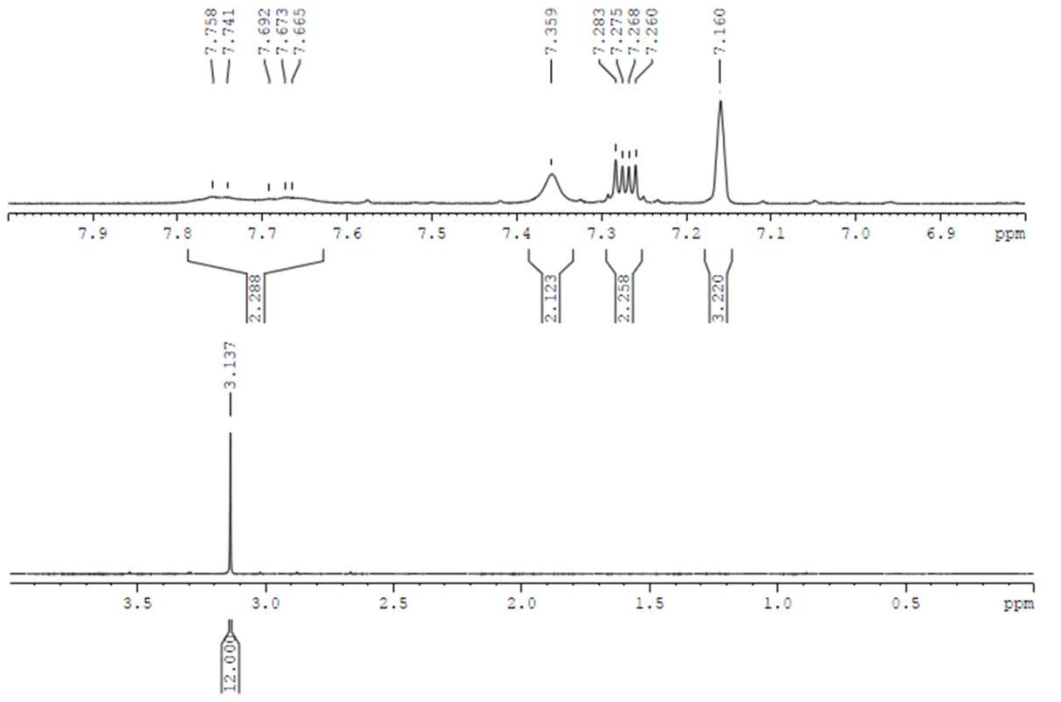

Figure S10: ^{1}H NMR spectrum (400 MHz, C_6D_6) of $[Ti(DHN)(NMe_2)_2]_2$ **(2a)** at 26 °C.

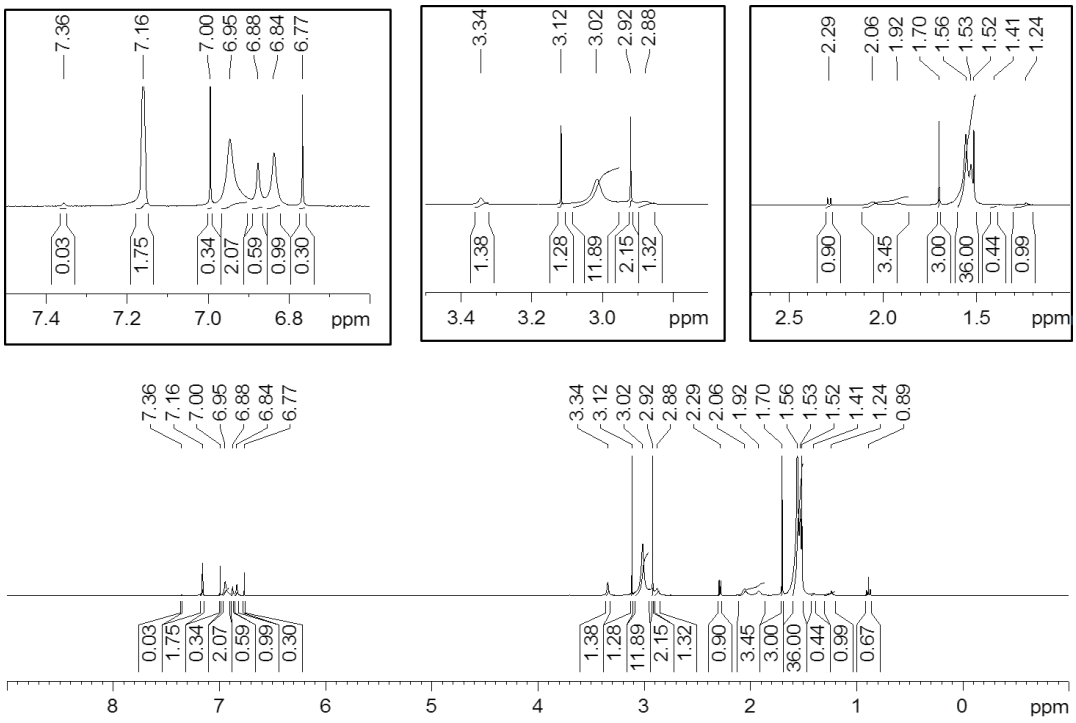

Figure S11: ^{1}H NMR spectrum (400 MHz, C_6D_6) of [Ti(CAT*t*Bu$_2$-3,6)(NMe$_2$)$_2$]$_2$ **(5a)** at 26 °C.

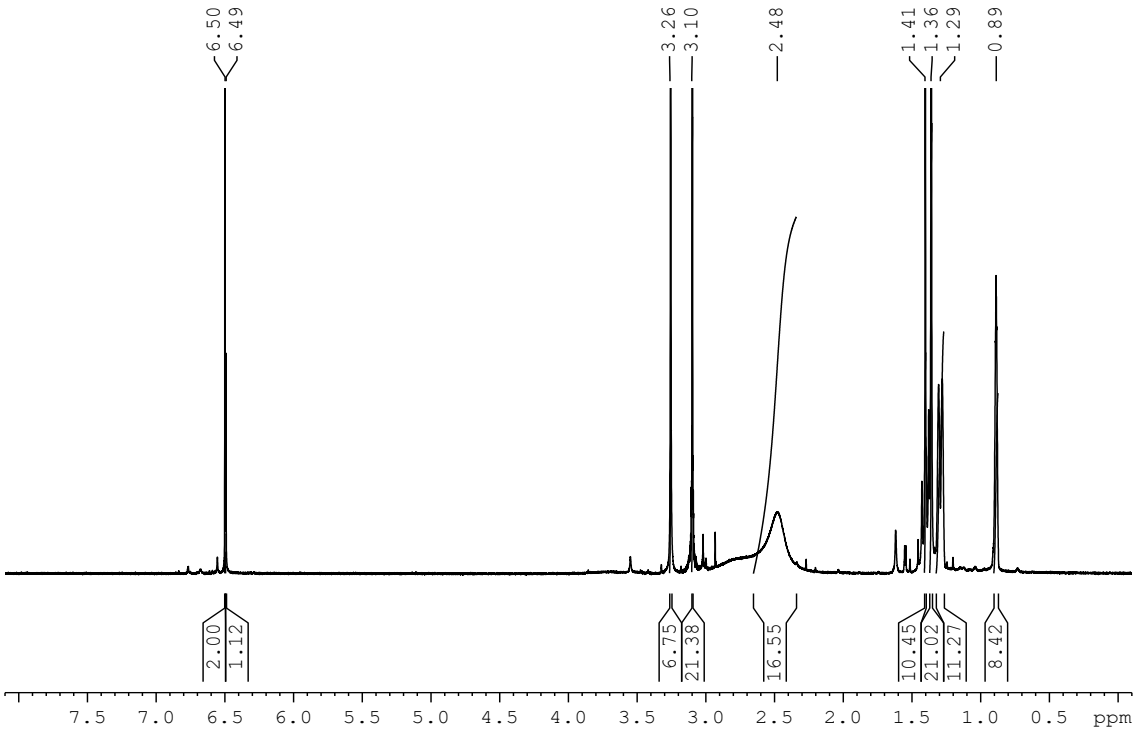

Figure S12: ^{1}H NMR spectrum (400 MHz, hexane-d$_{14}$) of [Ti(CAT*t*Bu$_2$-3,6)(NMe$_2$)$_2$]$_2$ **(5a)** in situ after 1 h at 26 °C.

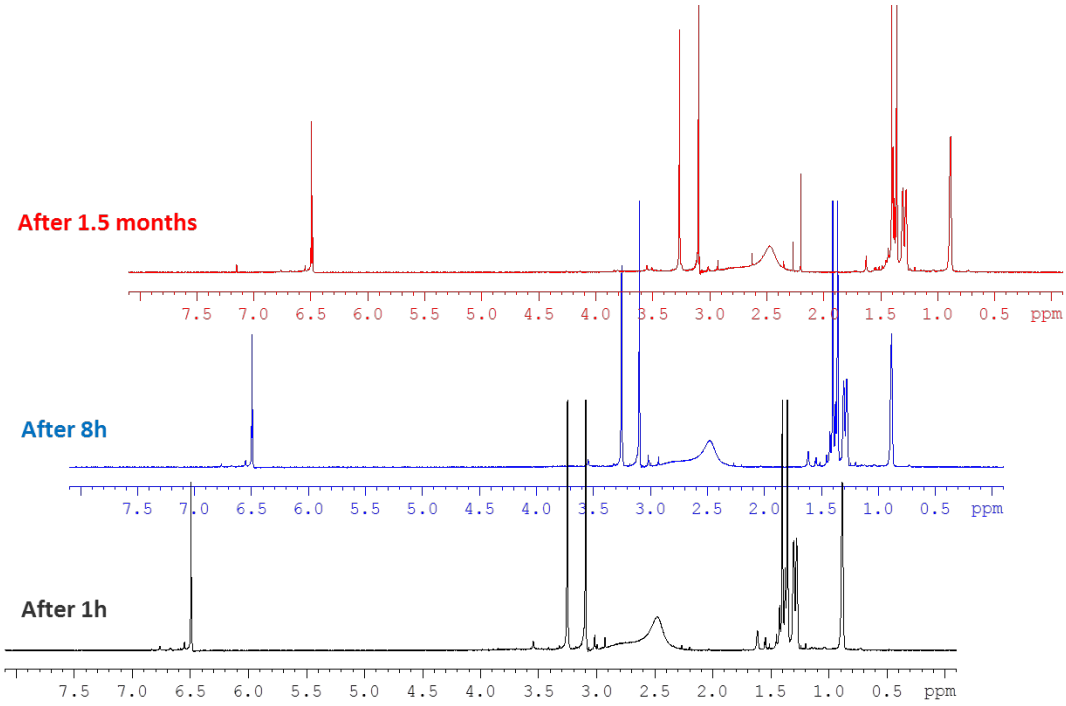

Figure S13: ^{1}H NMR spectrum (400 MHz, hexane-d_{14}) of [Ti(CAT*t*Bu$_2$-3,6)(NMe$_2$)$_2$]$_2$ **(5a)** in situ after 1 h, 8 h and 1.5 months at 26 °C.

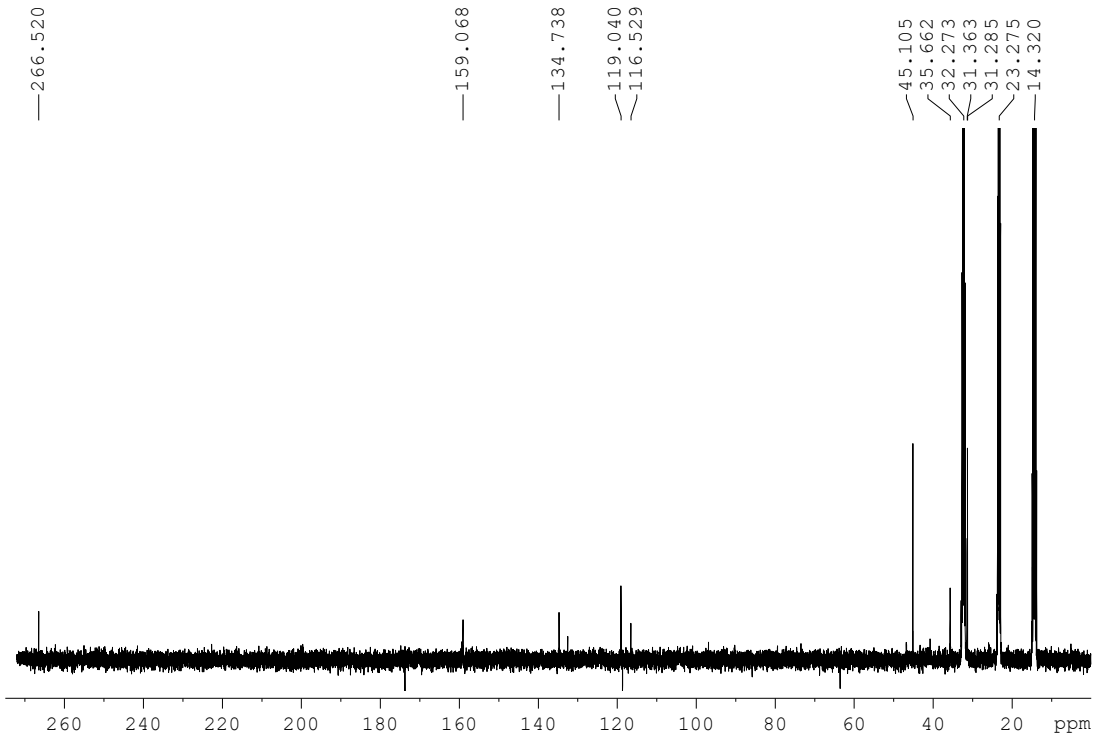

Figure S14: ^{13}C NMR spectrum (100 MHz, hexane-d_{14}) of[Ti(CAT*t*Bu$_2$-3,6)(NMe$_2$)$_2$]$_2$ **(5a)** in situ after 8 h at 26 °C.

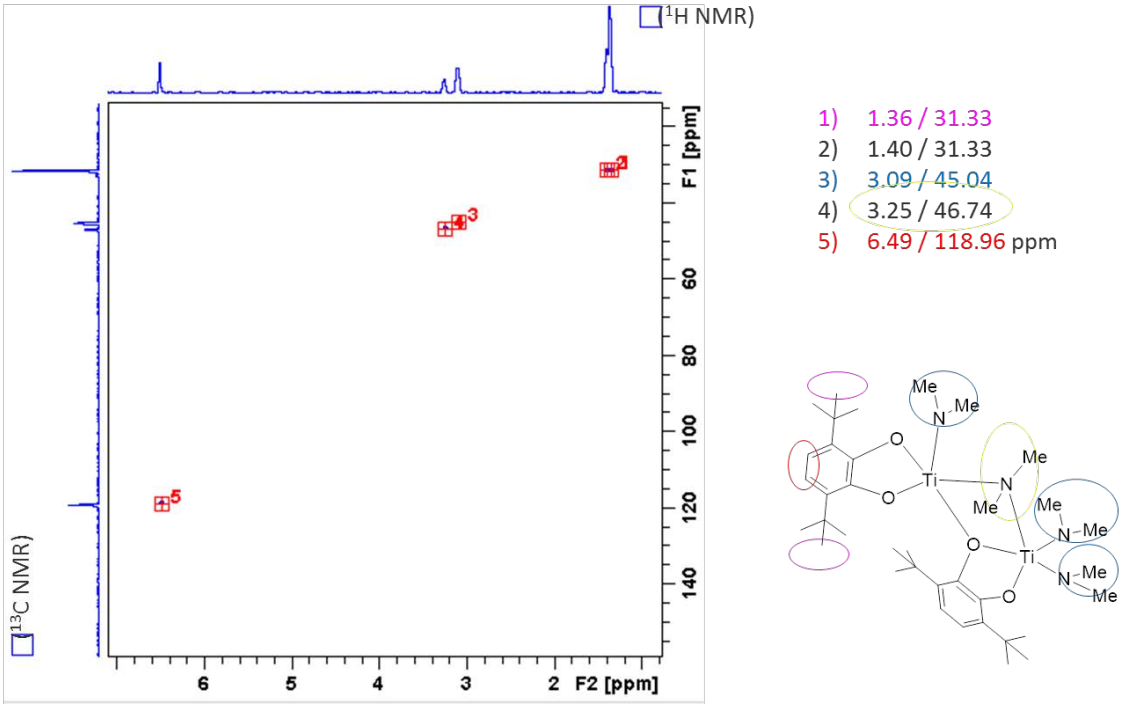

Figure S15: HC-HSQC spectrum (hexane-d_{14}) of [Ti(CAT*t*Bu$_2$-3,6)(NMe$_2$)$_2$]$_2$ **(5a)** in situ after 8 h at 26 °C.

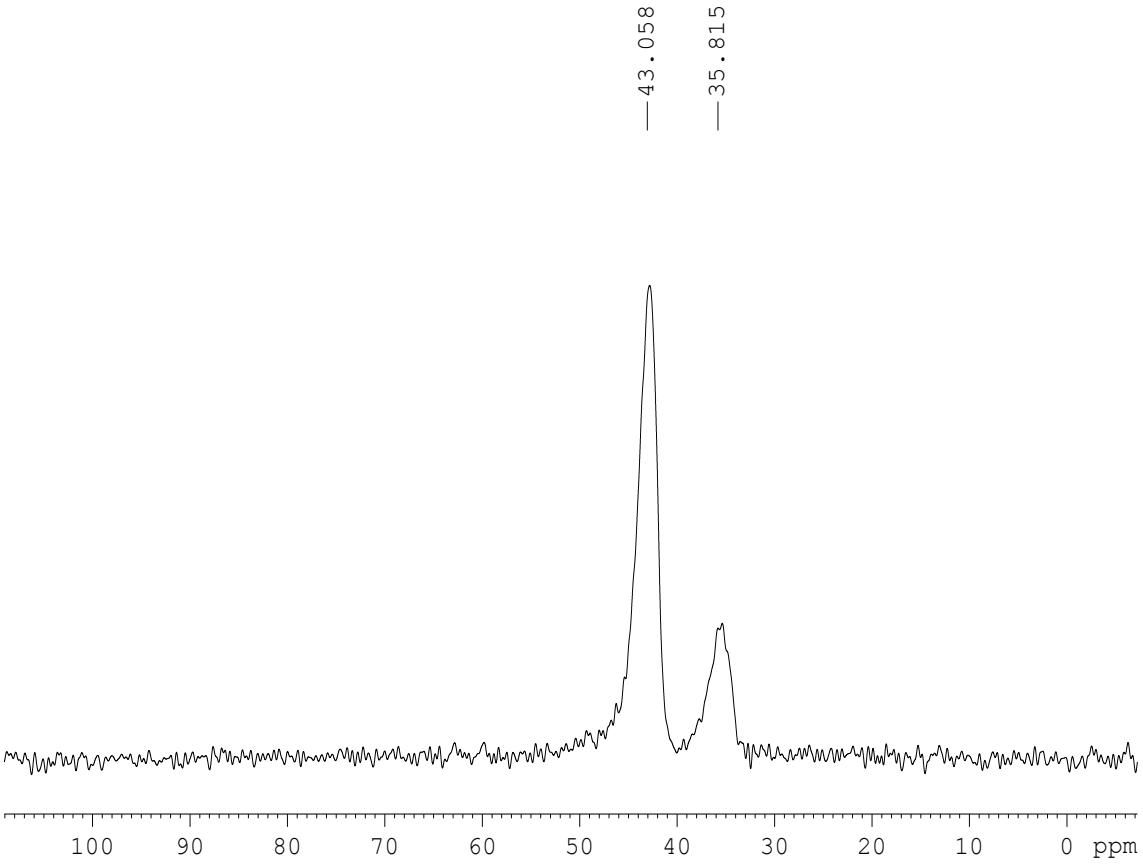

Figure S16: ^{13}C NMR spectrum (75 MHz, cp/MAS, 10 kHz rotation) of $Ti(NMe_2)_4$@[KIT-6] (**M3a**) at 26 °C.

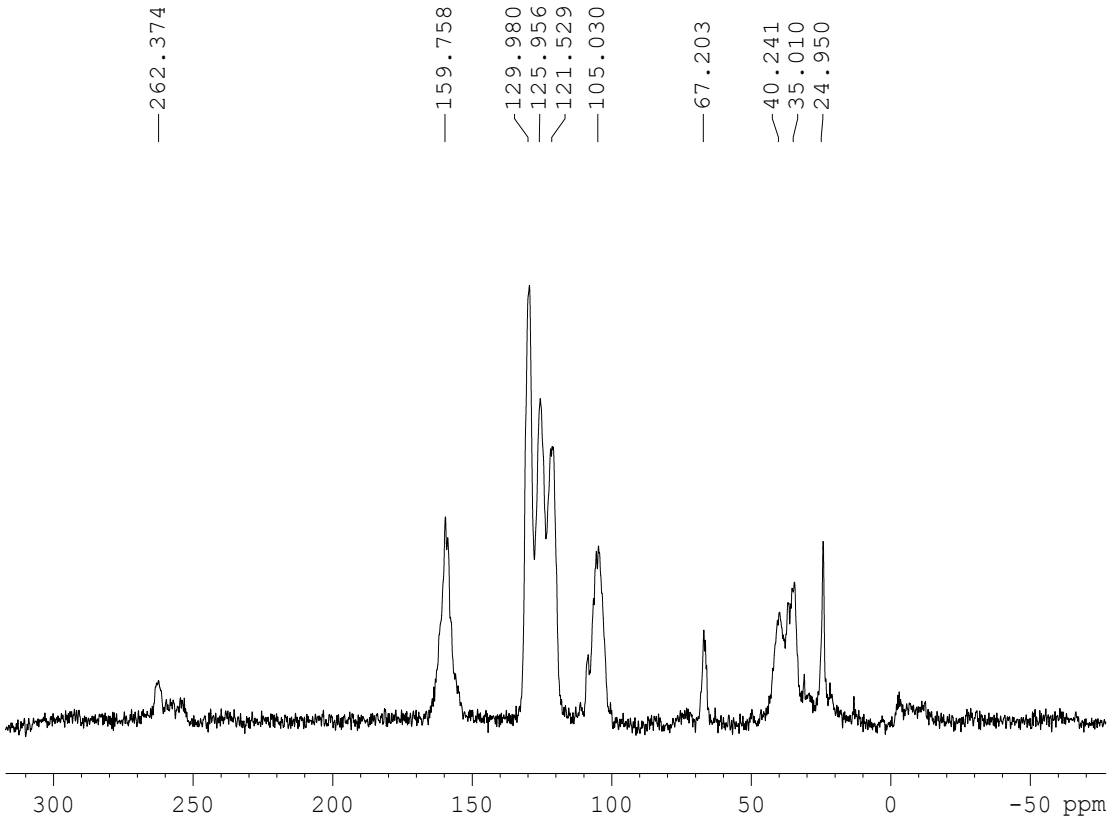

Figure S17: ^{13}C NMR spectrum (75 MHz, cp/MAS, 10 kHz rotation) of H_2DHN@$Ti(NMe_2)_4$@[KIT-6] (**M4a**) at 26 °C.

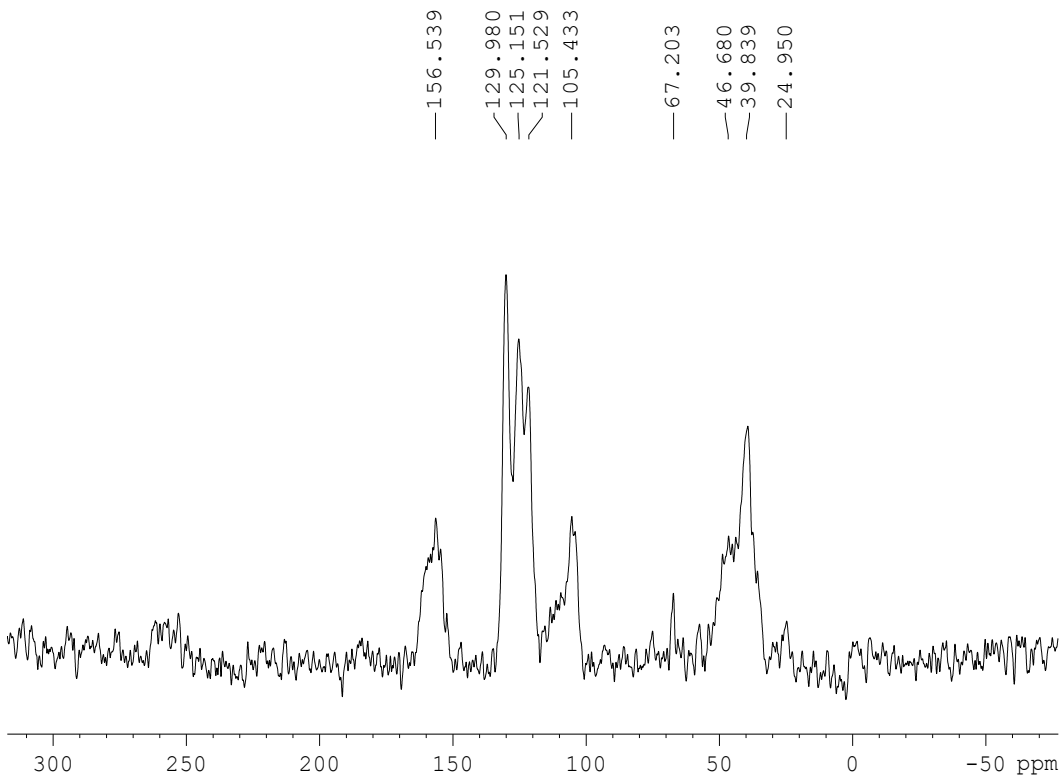

Figure S18: ^{13}C NMR spectrum (75 MHz, cp/MAS, 10kHz Rotation) of $[Ti(DHN)(NMe_2)_2]_2$@[KIT-6] (**M5b**) at 26 °C.

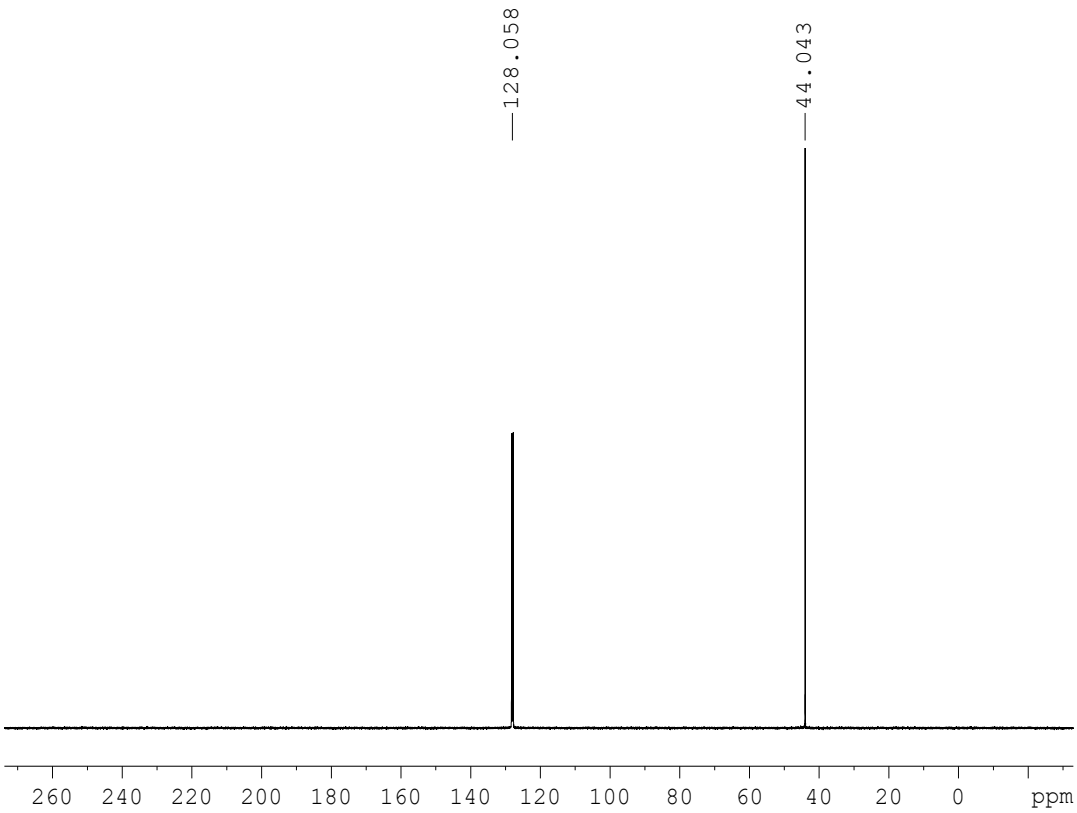

Figure S19: ^{13}C NMR spectrum (100 MHz, C_6D_6) of $Ti(NMe_2)_4$ at 26 °C.

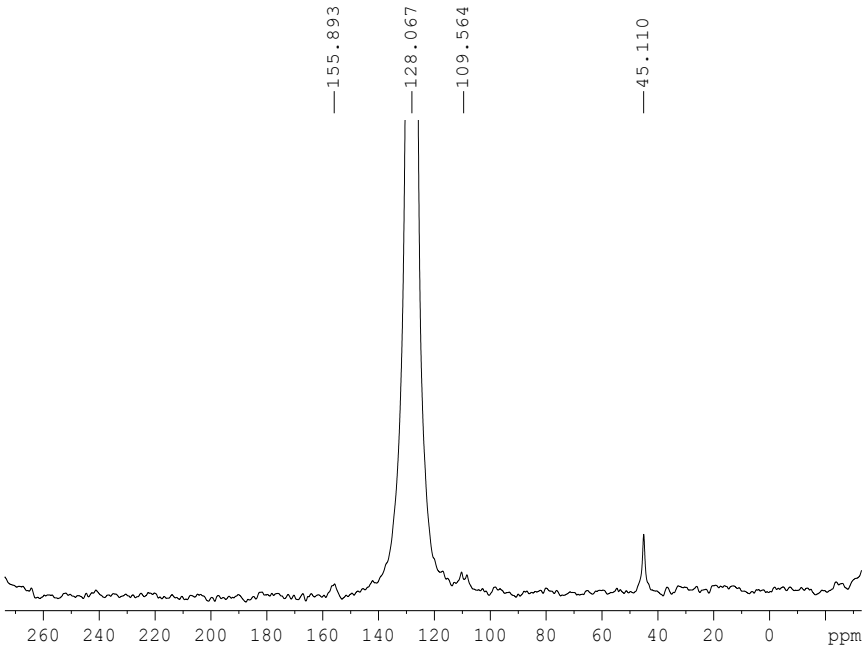

Figure S20: ^{13}C NMR spectrum (100 MHz, C_6D_6) of $[Ti(DHN)(NMe_2)_2]_2$ (**2a**) at 26 °C.

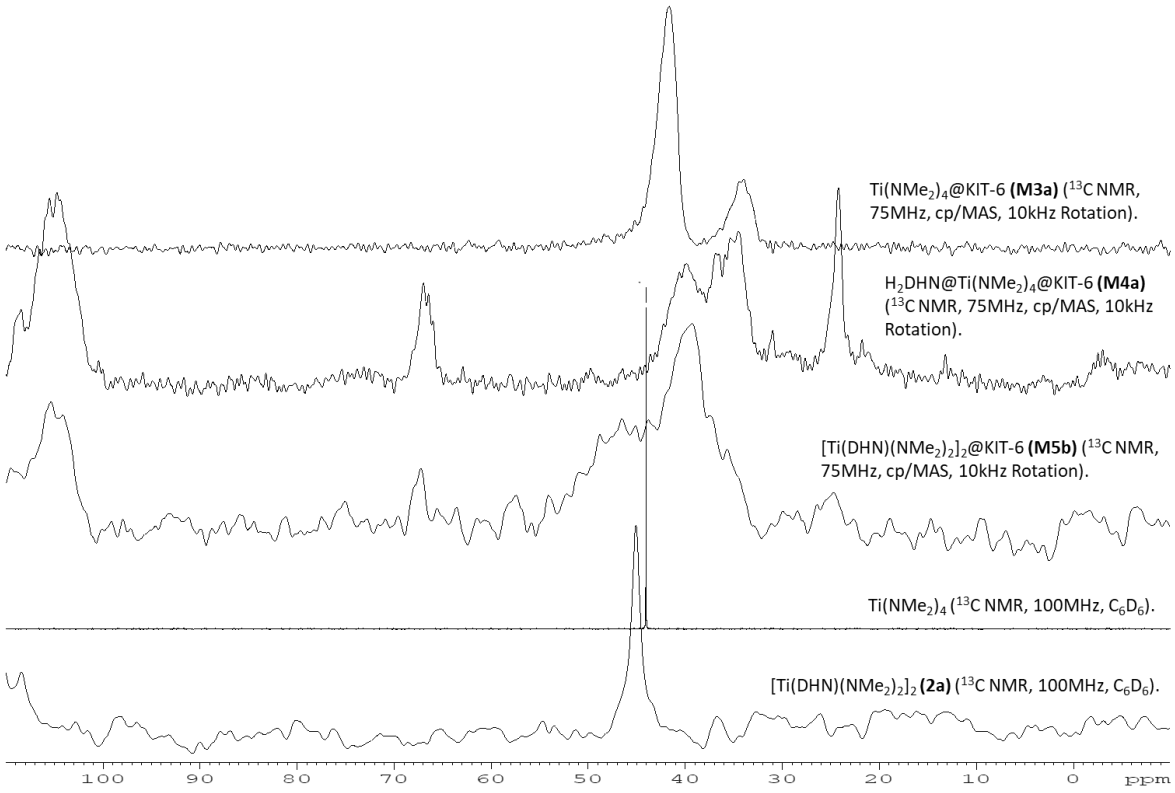

Figure S21: ^{13}C NMR spectra (some solid-state and some in solution) from top to bottom: of $Ti(NMe_2)_4$@[KIT-6] (**M3a**) (75MHz, cp/MAS, 10kHz Rotation), $H_2DHN@Ti(NMe_2)_4$@[KIT-6] (**M4a**) (75MHz, cp/MAS, 10 kHz Rotation), $[Ti(DHN)(NMe_2)_2]_2$@[KIT-6] (**M5b**) (75 MHz, cp/MAS, 10 kHz Rotation), $Ti(NMe_2)_4$ (100 MHz, C_6D_6) and $[Ti(DHN)(NMe_2)_2]_2$ (**2a**) (100 MHz, C_6D_6).

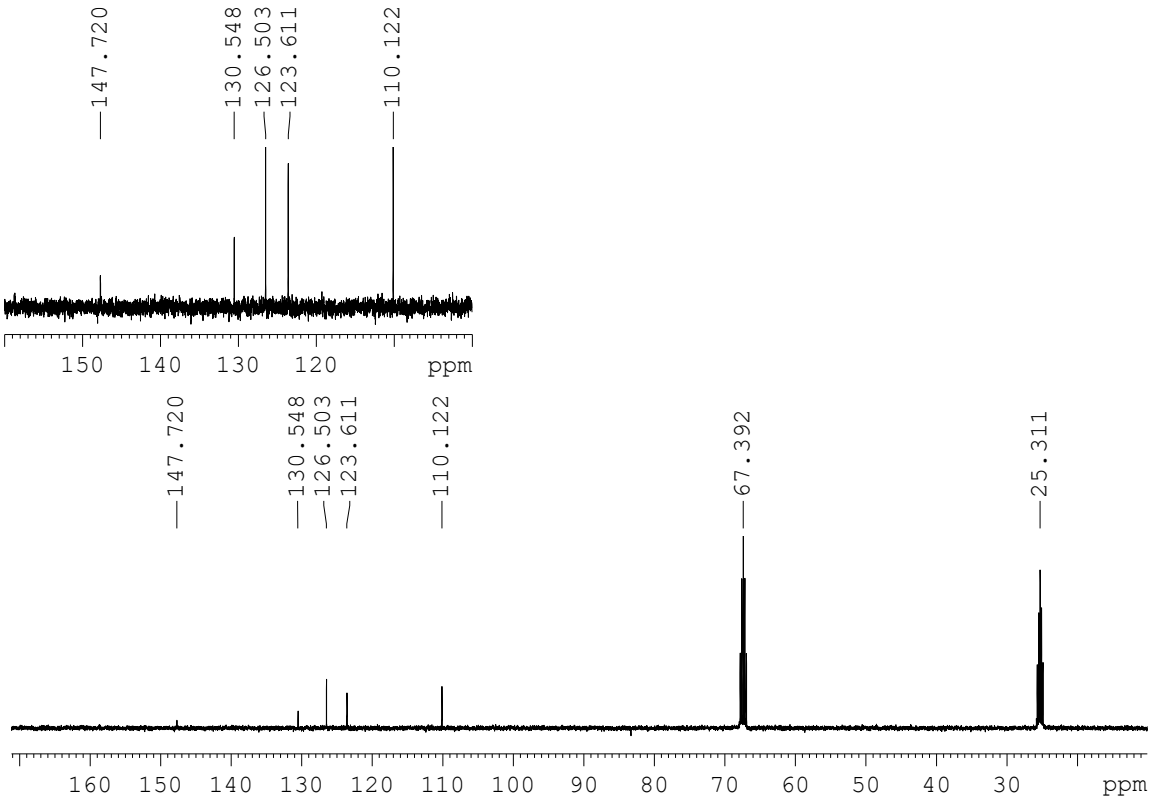

Figure S22: ^{13}C NMR spectrum (100 MHz, thf-d_8) of H_2DHN at 26 °C.

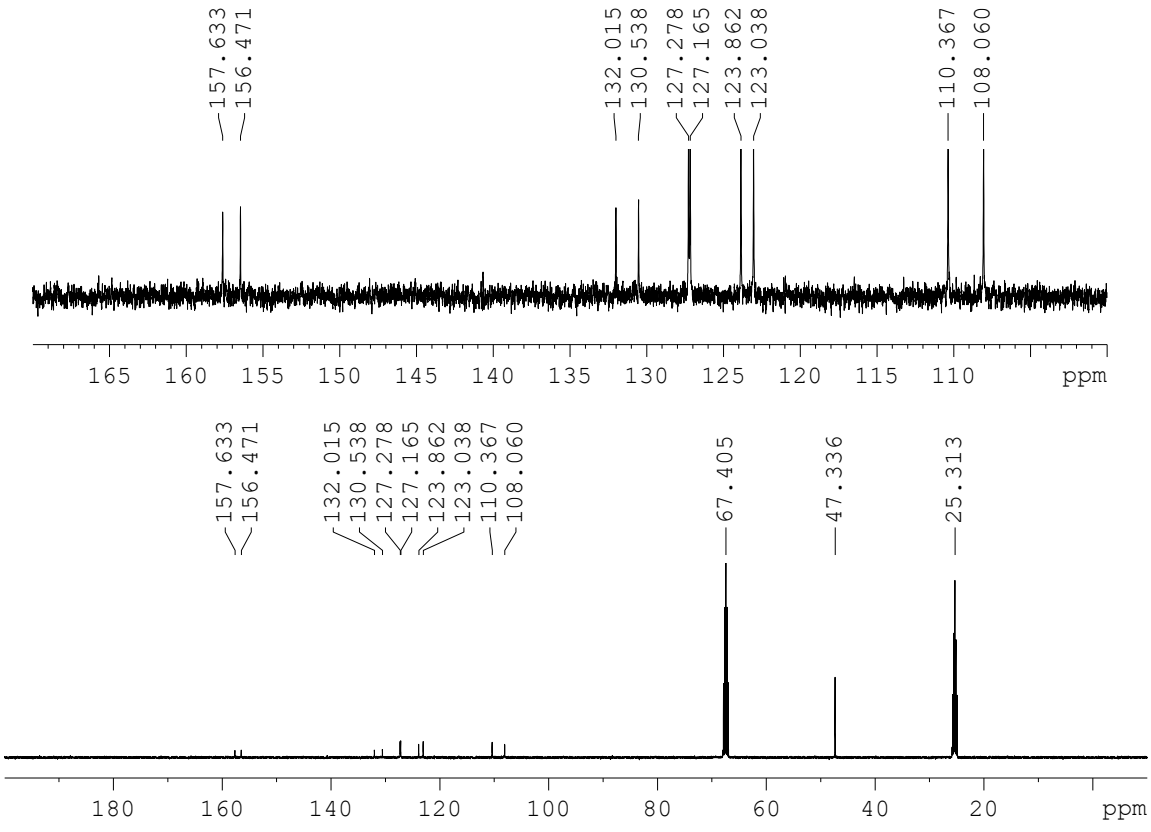

Figure S23: ^{13}C NMR spectrum (100 MHz, thf-d_8) of $[Ti(DHN)(NMe_2)_2]_2$ (**2a**) at 26 °C.

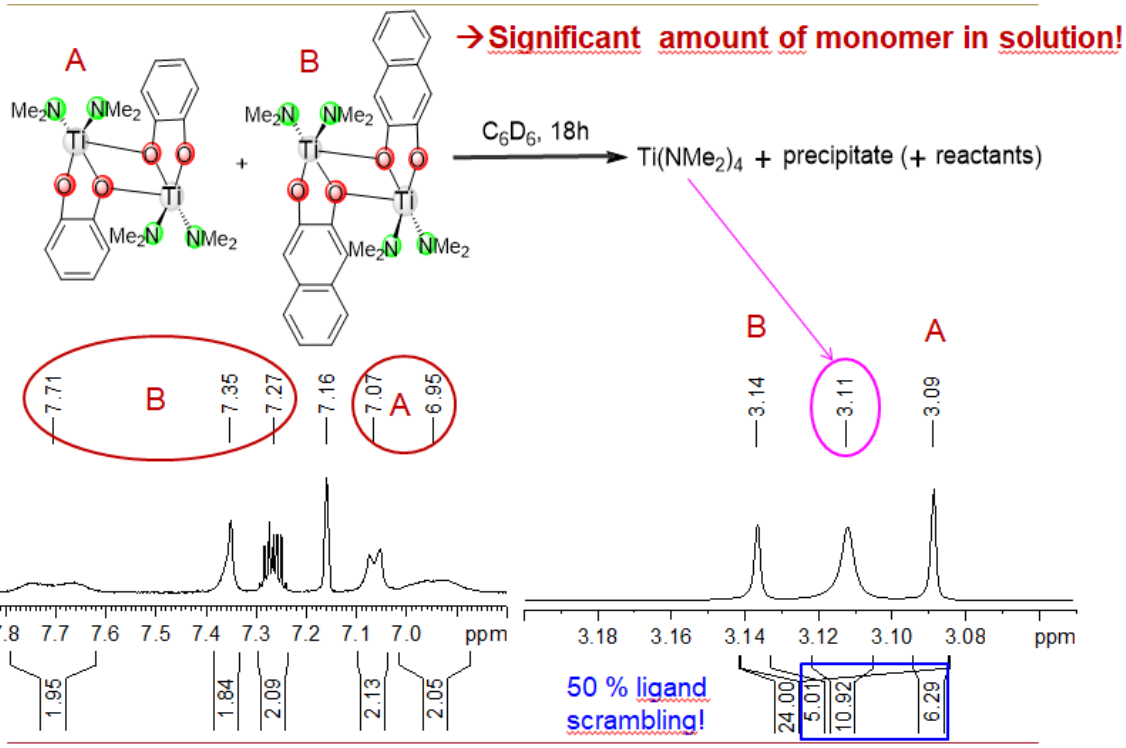

Figure S24: ^{1}H NMR spectrum (400 MHz, C_6D_6) of $[Ti(CAT)(NMe_2)_2]_2$ (**1a →A**) and $[Ti(DHN)(NMe_2)_2]_2$ (**2a→B**) at 26 °C, after 18h reaction time.

DRIFT Spectra

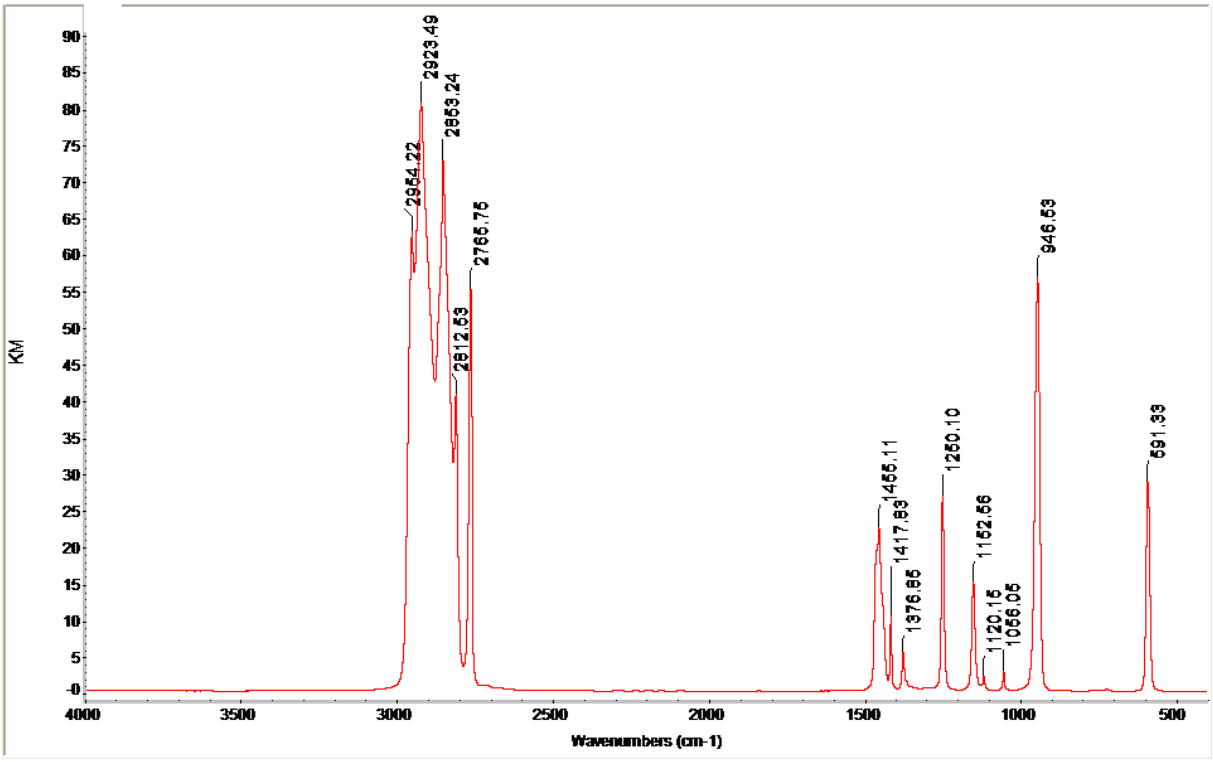

S25: DRIFT spectrum of $Ti(NMe_2)_4$.

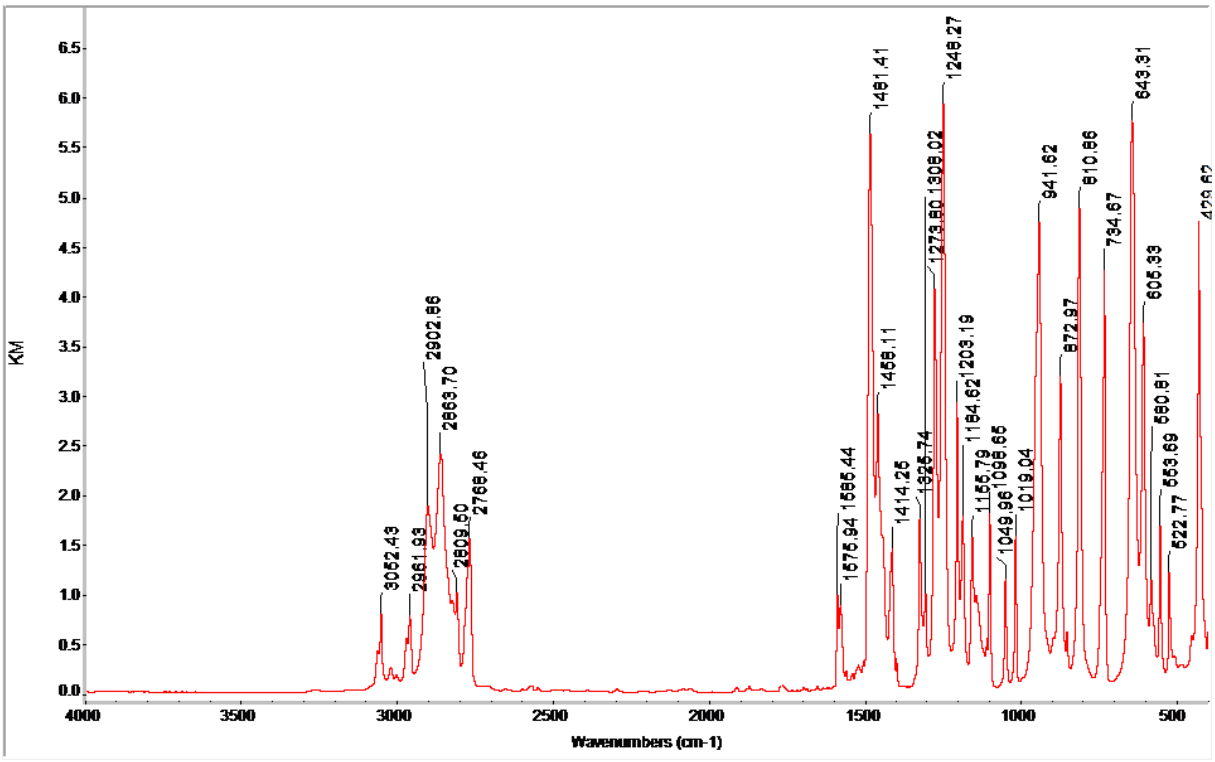

S26: DRIFT spectrum of $[Ti(CAT)(NMe_2)_2]_2$ (**1a**).

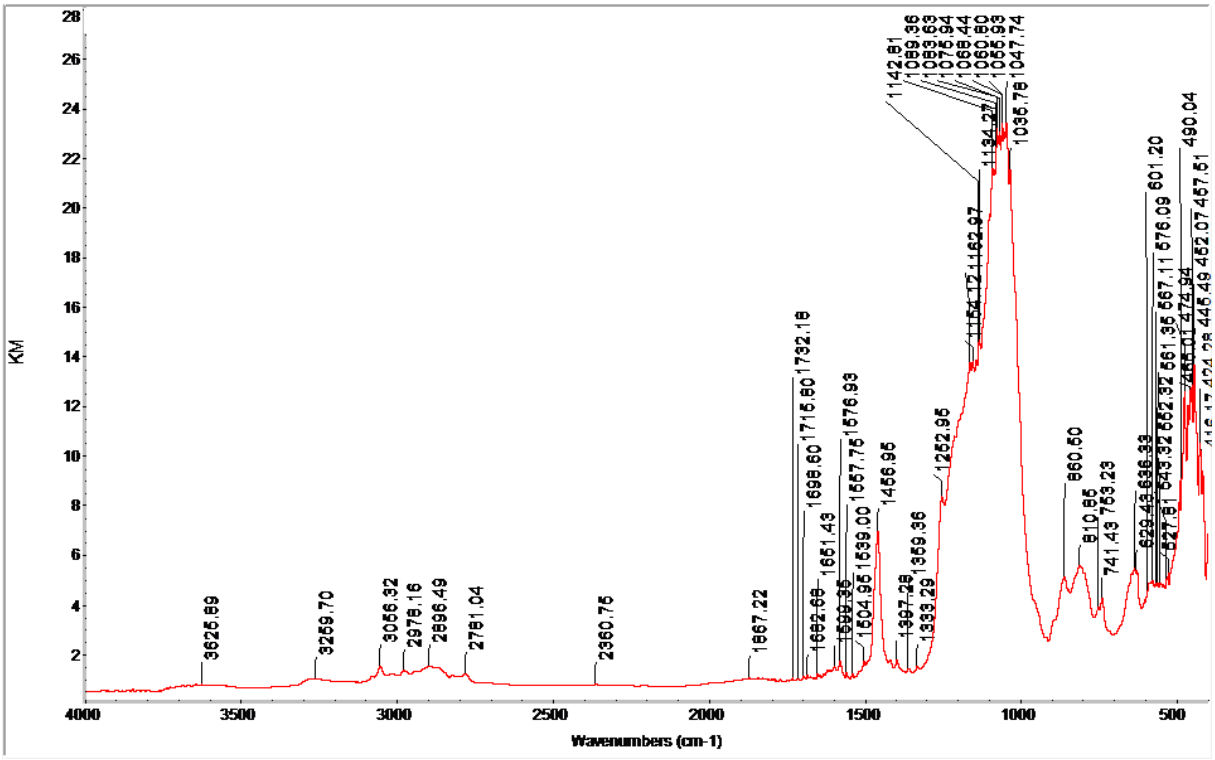

S27: DRIFT spectrum of [Ti(DHN)$(NMe_2)_2]_2$ (**2a**).

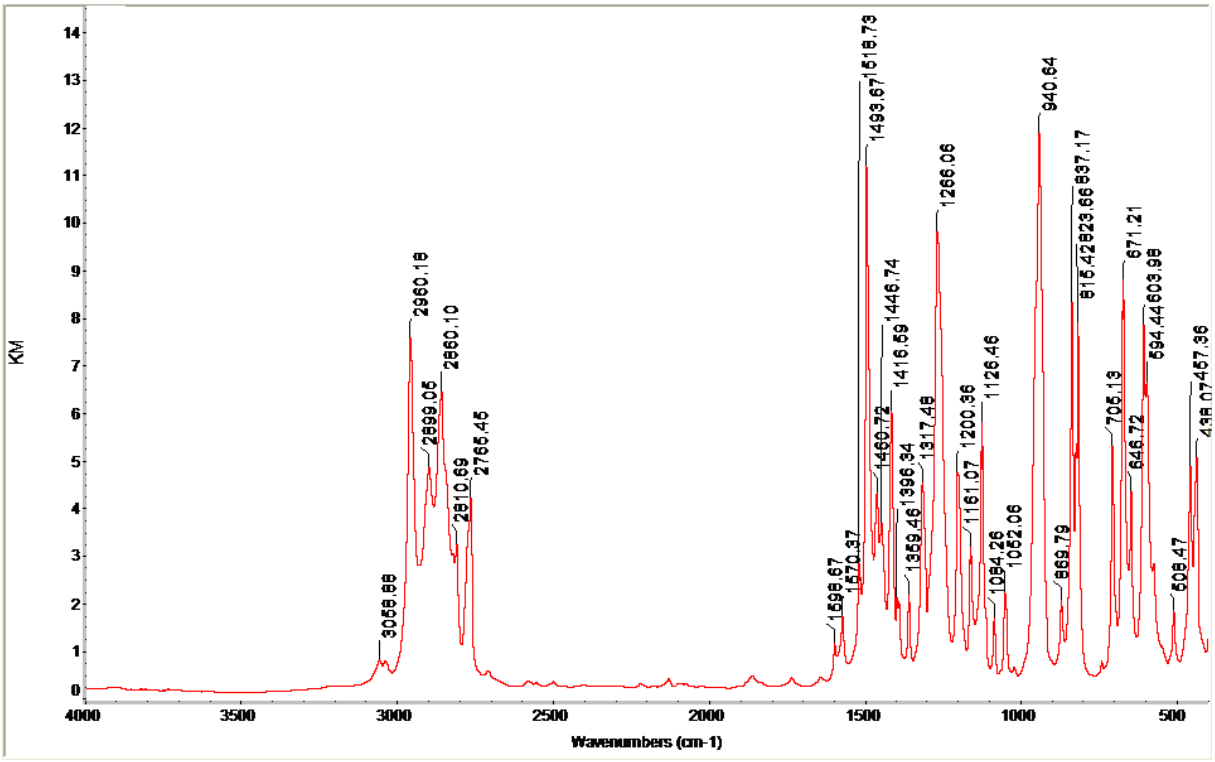

S28: DRIFT spectrum of [Ti(CAT*t*Bu-4)$(NMe_2)_2]_2$ (**3a**).

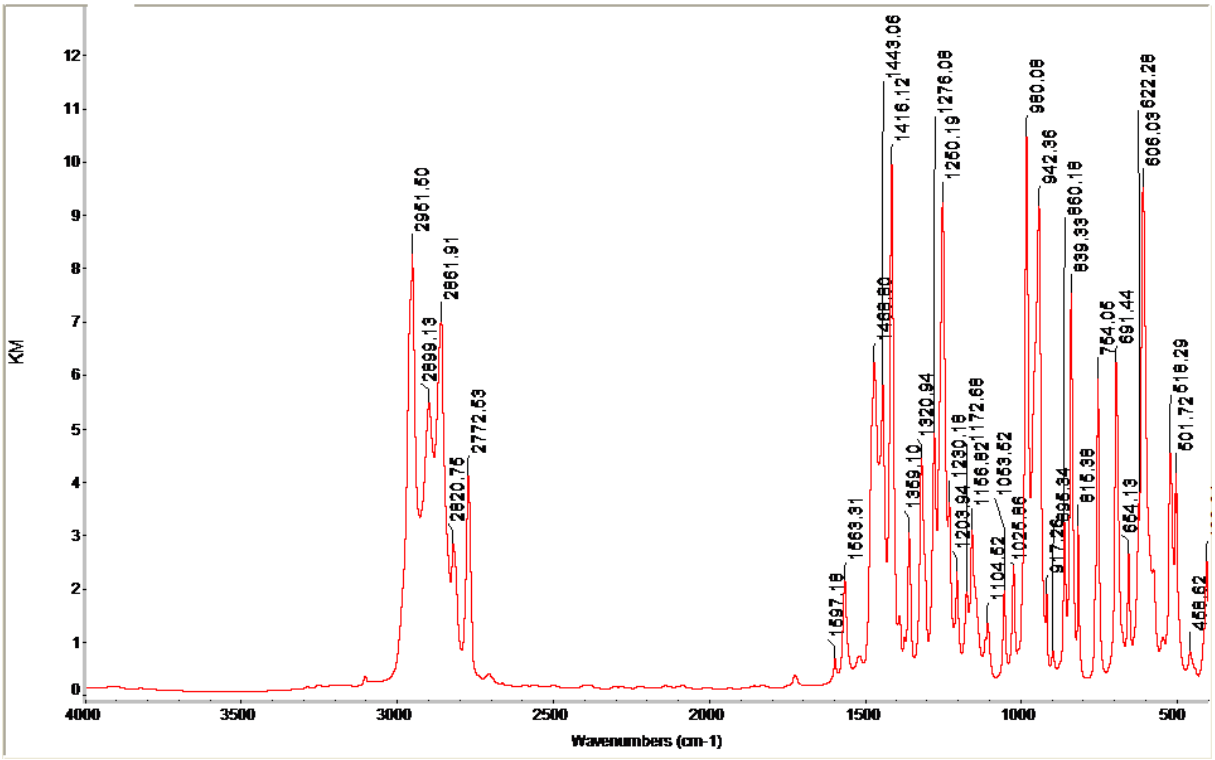

S29: DRIFT spectrum of [Ti(CAT*t*Bu$_2$-3,5)(NMe$_2$)$_2$]$_2$ (**4a**).

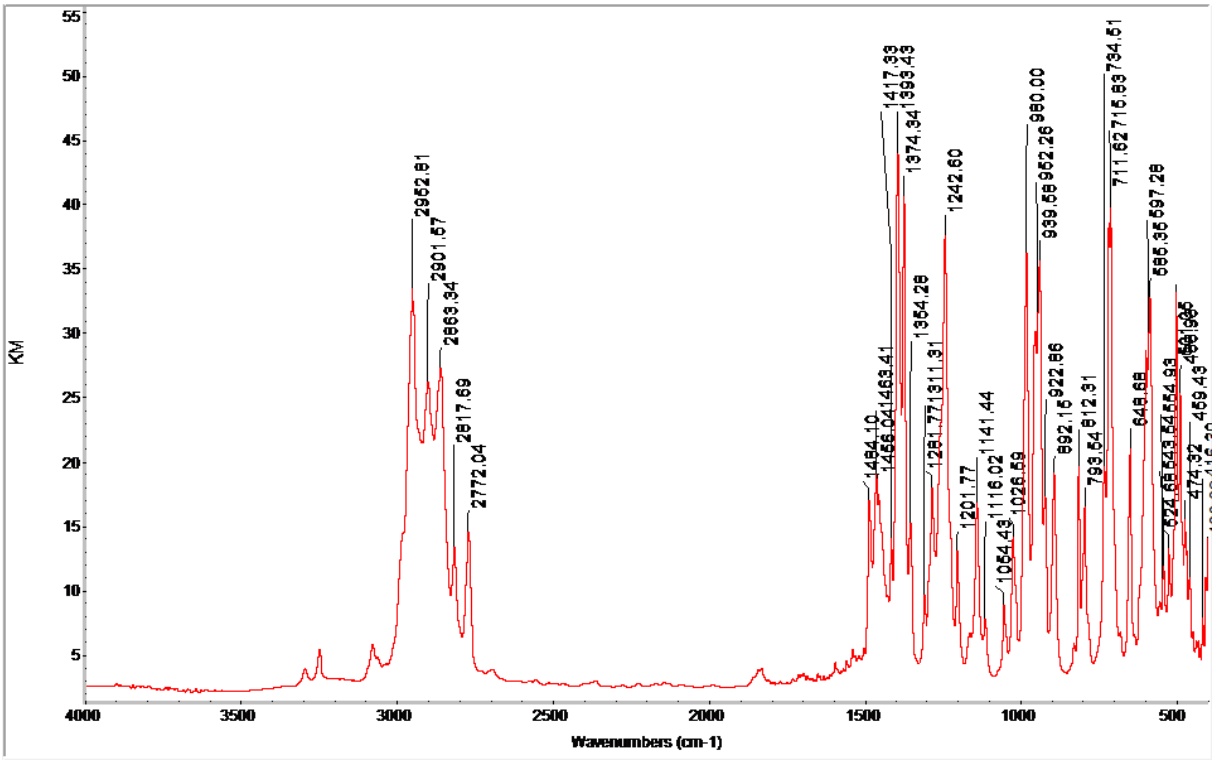

S30: DRIFT spectrum of [Ti(CAT*t*Bu$_2$-3,6)(NMe$_2$)$_2$]$_2$ (**5a**).

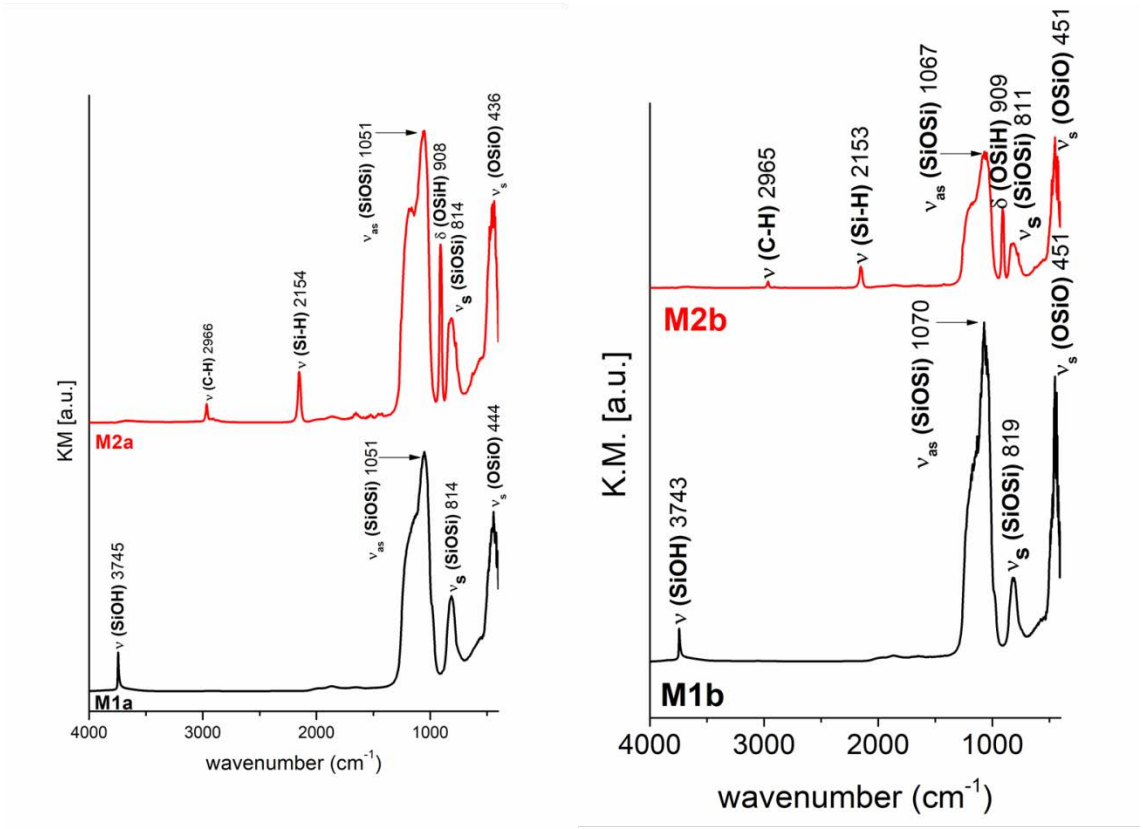

Figure S31: DRIFT spectra of the synthesized materials diluted with KBr powder. *Left*: dehydrated KIT-6 (**M1a**) and silylated KIT-6 (**M2a**). *Right*: dehydrated KIT-6 (**M1b**) and silylated KIT-6 (**M2b**).

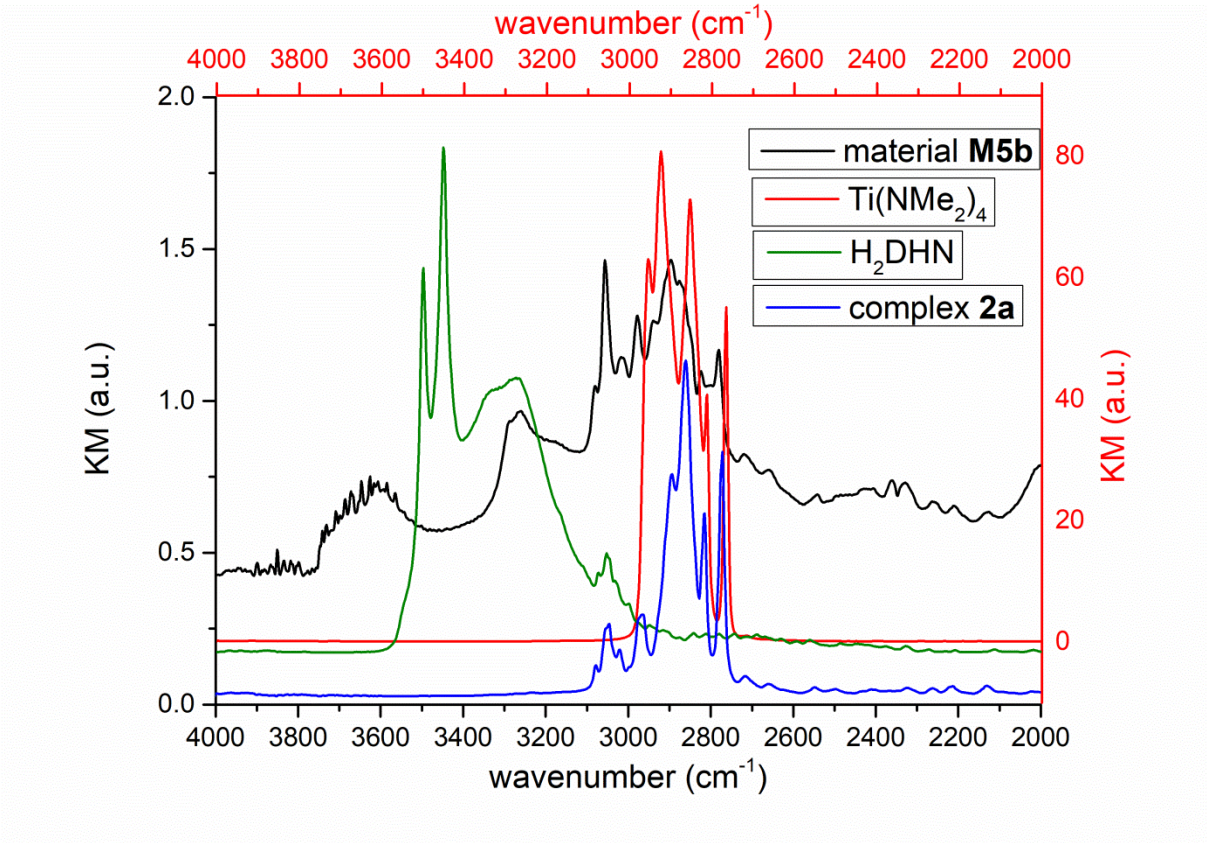

Figure S32: Stacked DRIFT spectra of the synthesized materials diluted with KBr powder: $[Ti(DHN)(NMe_2)_2]_2$@[KIT-6] (**M5b**), $Ti(NMe_2)_4$, H_2DHN and $[Ti(DHN)(NMe_2)_2]_2$ (**2a**).

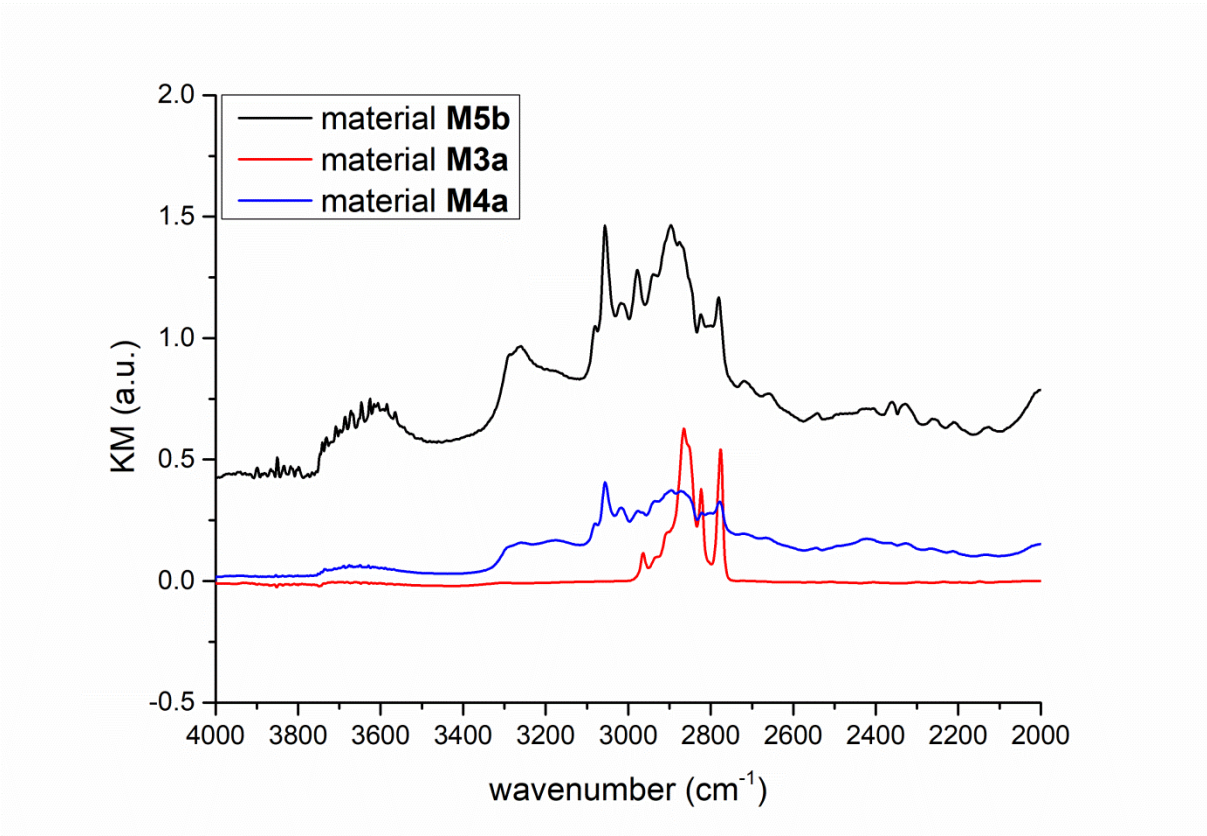

Figure S33: Stacked DRIFT spectra of the synthesized materials diluted with KBr powder: [KIT-6]$Ti(DHN)_y$ (**M5b**), $Ti(NMe_2)_4$@[KIT-6] (**M3a**), H_2DHN@$Ti(NMe_2)_4$@[KIT-6] (**M4a**).

Mass Spectrometry

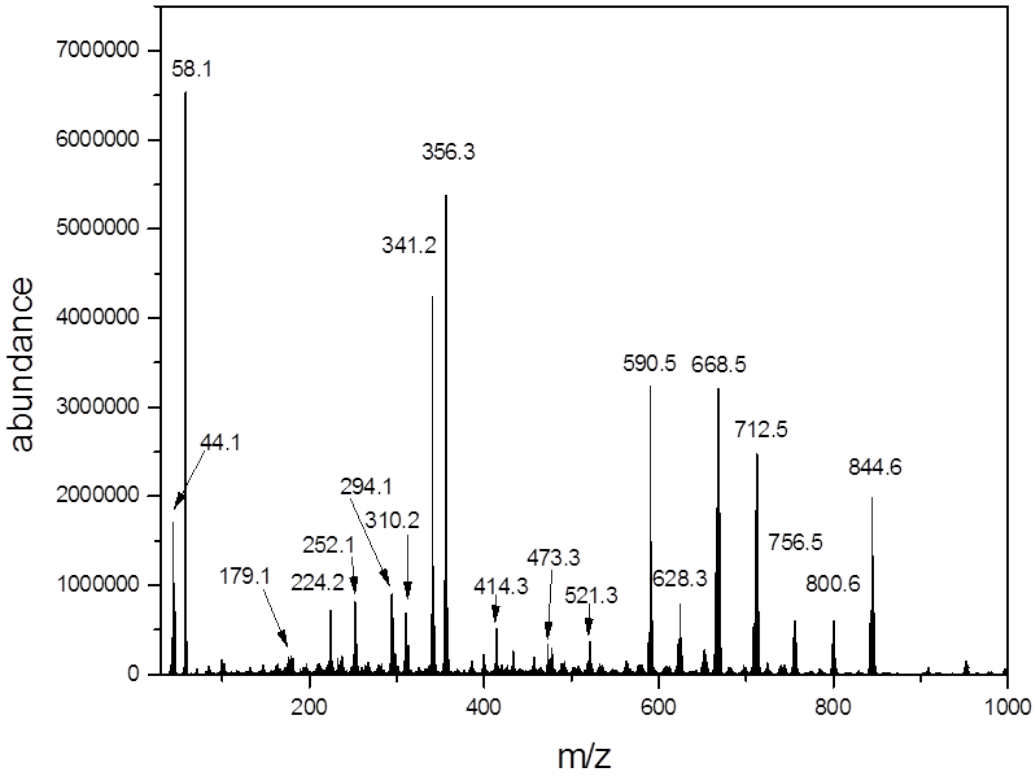

Figure S34: Mass spectrum (EI with CI source, 230 °C, 70 eV) of [Ti(CAT*t*Bu$_2$-3,6)(NMe$_2$)$_2$]$_2$ **(5a)**.

Powder X-ray Diffraction

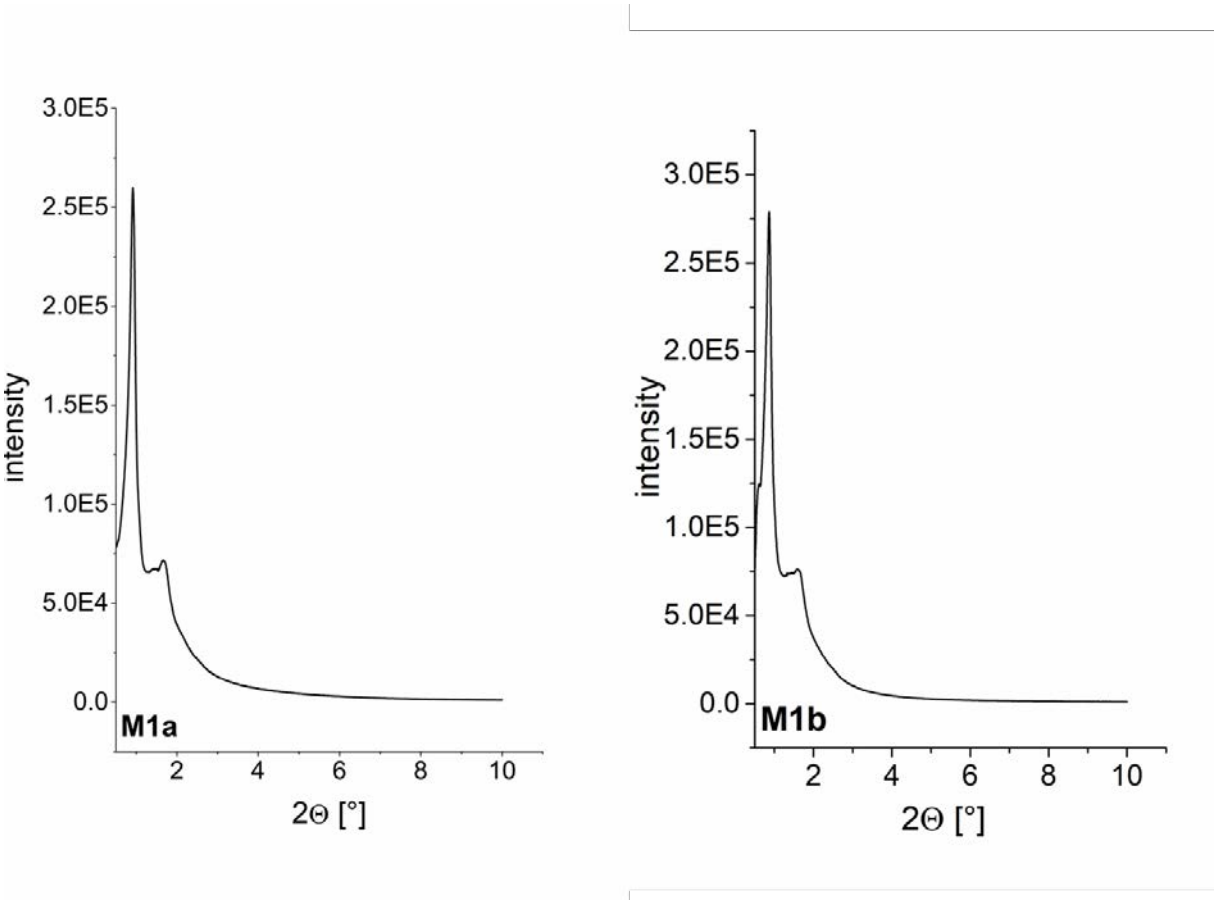

Figure S35: PXRDs. *Left*: dehydrated KIT-6 (**M1a**). *Right*: dehydrated KIT-6 (**M1b**). The reflex at 2θ = 0.91° and 0.90° was indexed as (211) plane respectively, which is in agreement with the KIT-6 materials reported in literature.[2,3] The d_{211} spacings were calculated with Bragg´s law and therefrom the unit cell parameters a were received as 23.8 nm (**M1a**) and 25.0 nm (**M1b**) respectively, derived from the equation for a cubic structure:[3] $a = d_{hkl} * (\sqrt{h^2 + k^2 + l^2}) = \sqrt{6} \cdot d_{211}$.

Nitrogen Physisorption

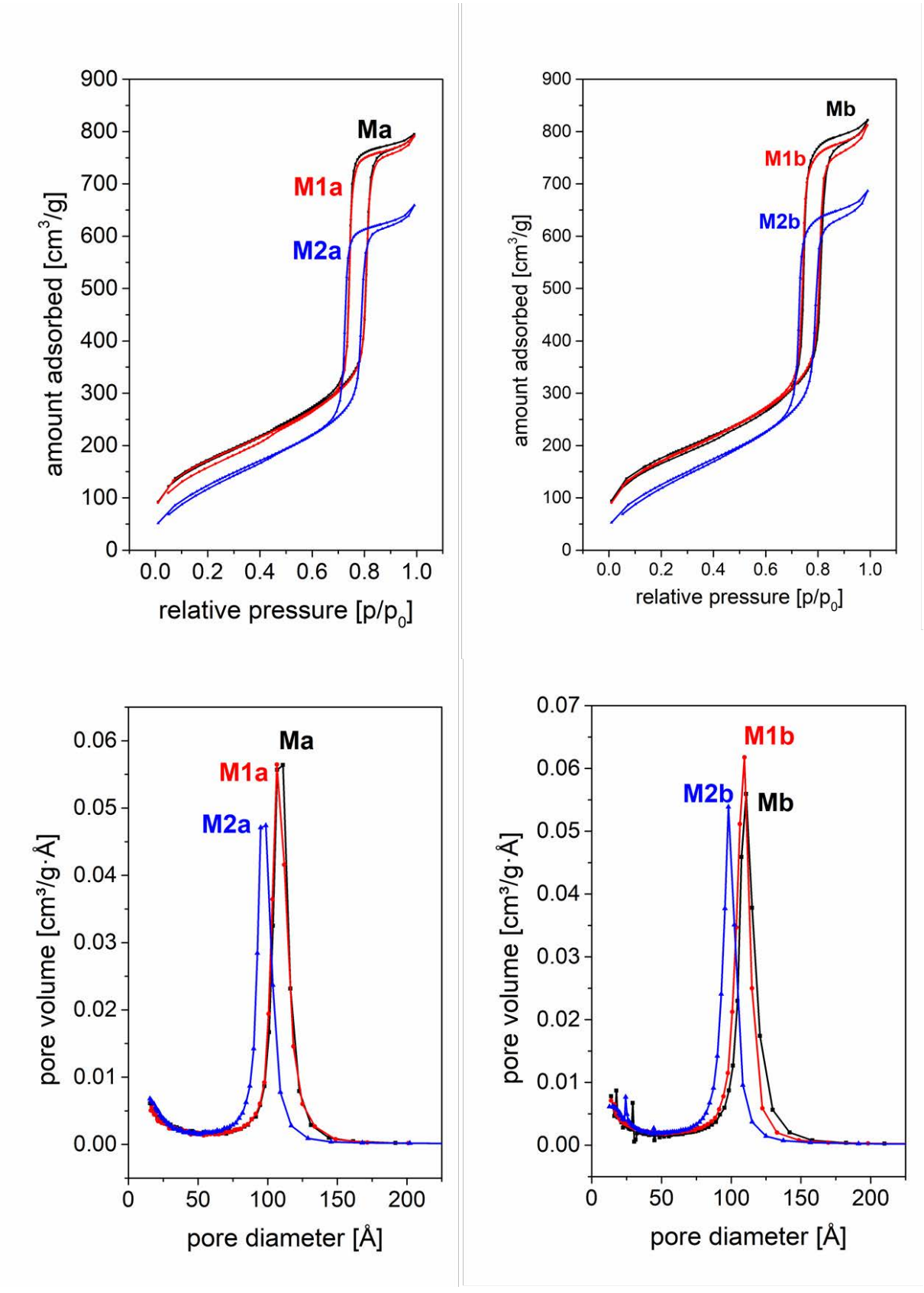

Figure S36: Nitrogen ad-/desorption isotherms at 77.4 K and the corresponding BJH size distributions. *Left*: calcined KIT-6 (**Ma**), dehydrated KIT-6 (**M1a**) and silylated KIT-6 (**M2a**). *Right*: calcined KIT-6 (**Mb**), dehydrated KIT-6 (**M1b**) and silylated KIT-6 (**M2b**).

References

1. B. A. Borgias, S. R. Cooper, Y. B. Koh, K. N. Raymond, *Inorg. Chem.* **1984**, *23*, 1009-1016.
2. F. Kleitz, S. Hei Choi, R. Ryoo, *Chem. Commun.* **2003**, 2136-2137.
3. T.-W. Kim, F. Kleitz, B. Paul, R. Ryoo, *J. Am. Chem. Soc.* **2005**, *127*, 7601-7610.

Paper II

Inorganic Chemistry

pubs.acs.org/IC Article

Titanium(IV) Surface Complexes Bearing Chelating Catecholato Ligands for Enhanced Band-Gap Reduction

Andrea Sonström, Barbara Boldrini, Daniel Werner, Cäcilia Maichle-Mössmer, Karsten Rebner, Maria Benedetta Casu,* and Reiner Anwander*

Cite This: *Inorg. Chem.* 2023, 62, 715−729 Read Online

ACCESS | Metrics & More | Article Recommendations | Supporting Information

ABSTRACT: Protonolysis reactions between dimethylamido titanium(IV) catecholate $[Ti(CAT)(NMe_2)_2]_2$ and neopentanol or tris(*tert*-butoxy)silanol gave catecholato-bridged dimers $[(Ti(CAT)(OCH_2tBu)_2)(HNMe_2)]_2$ and $[Ti(CAT)\{OSi(OtBu)_3\}_2(HNMe_2)_2]_2$, respectively. Analogous reactions using the dimeric dimethylamido titanium(IV) (3,6-di-*tert*-butyl)catecholate $[Ti(CAT tBu_2\text{-}3,6)(NMe_2)_2]_2$ yielded the monomeric $Ti(CAT tBu_2\text{-}3,6)(OCH_2tBu)_2(HNMe_2)_2$ and $Ti(CAT tBu_2\text{-}3,6)[OSi(OtBu)_3]_2(HNMe_2)_2$. The neopentoxide complex $Ti(CAT tBu_2\text{-}3,6)(OCH_2tBu)_2(HNMe_2)_2$ engaged in further protonolysis reactions with Si−OH groups and was consequentially used for grafting onto mesoporous silica KIT-6. Upon immobilization, the surface complex $[Ti(CAT tBu_2\text{-}3,6)(OCH_2tBu)_2(HNMe_2)_2]$@[KIT-6] retained the bidentate chelating geometry of the catecholato ligand. This convergent grafting strategy was compared with a sequential and an aqueous approach, which gave either a mixture of bidentate chelating species with a bipodally anchored Ti(IV) center along with other physisorbed surface species or not clearly identifiable surface species. Extension of the convergent and aqueous approaches to anatase mesoporous titania (m-TiO_2) enabled optical and electronic investigations of the corresponding surface species, revealing that the band-gap reduction is more pronounced for the bidentate chelating species (convergent approach) than for that obtained via the aqueous approach. The applied methods include X-ray photoelectron spectroscopy, ultraviolet photoelectron spectroscopy, and solid-state UV/vis spectroscopy. The energy-level alignment for the surface species from the aqueous approach, calculated from experimental data, accounts for the well-known type II excitation mechanism, whereas the findings indicate a distinct excitation mechanism for the bidentate chelating surface species of the material $[Ti(CAT tBu_2\text{-}3,6)(OCH_2tBu)_2(HNMe_2)_2]$@[m-$TiO_2$].

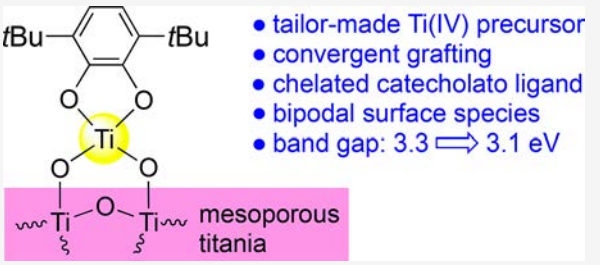

INTRODUCTION

The discovery of titania-promoted water photosplitting[1] triggered immense research efforts in the synthesis of tailor-made titania materials involving both nanostructuring and surface modification.[2−9] Catechol-functionalized titania surfaces belong to the most studied dye-sensitized metal oxide materials, shifting the photoactivity to the visible spectrum.[10−26] Crucially, the surface binding mode of the catechol (enediol) molecule has a decisive effect on the stability and energy band gap of such hybrid materials. Recent density functional theory (DFT) calculations on titania cluster/pyrocatechol interfaces revealed the highest stability for the bidentate bridging species (one pyrocatechol binds to two adjacent surface Ti atoms), while the largest optical absorption red shift was found for the chelating species (one pyrocatechol binds 2-fold to one surface Ti atom).[27] Notably, the stability of enediol/titania composites is also exploited in the field of biomedicine for light-induced targeted drug delivery or for combating cancer cells.[28−31] Weakly absorbing dyes at TiO_2 surfaces/substrates are prone either to be displaced by or to react with (cell) proteins, which have a high affinity to the titania surface. These undesired side reactions of weakly bound dyes or other biomedical molecules can induce death also to healthy cells and/or accidentally change the metabolism of the cells. Enediol ligands, like dopamine [4-(2-aminoethyl)-benzene-1,2-diol], covalently immobilized on titania surfaces, facilitate covalent tethering of bioactive molecules to the catechol backbone, creating stable materials for targeted drug delivery.[32]

Typically, catechol-functionalized bulk titanium oxide and titania particles (>20 nm) exhibit either a bidentate bridging binding mode of the catechol/catecholato at low surface coverage or monodentate catechol/catecholato binding at high surface coverage.[16,23,27,33] The (bidentate) chelating mode can be enforced by decreasing the titania particle size, being

Received: August 8, 2022
Published: January 3, 2023

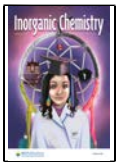

https://doi.org/10.1021/acs.inorgchem.2c02838
Inorg. Chem. 2023, 62, 715−729

Scheme 1. From Dimers to Monomers: Bridging Tendency of Heteroleptic Titanium(IV) Catecholates[a]

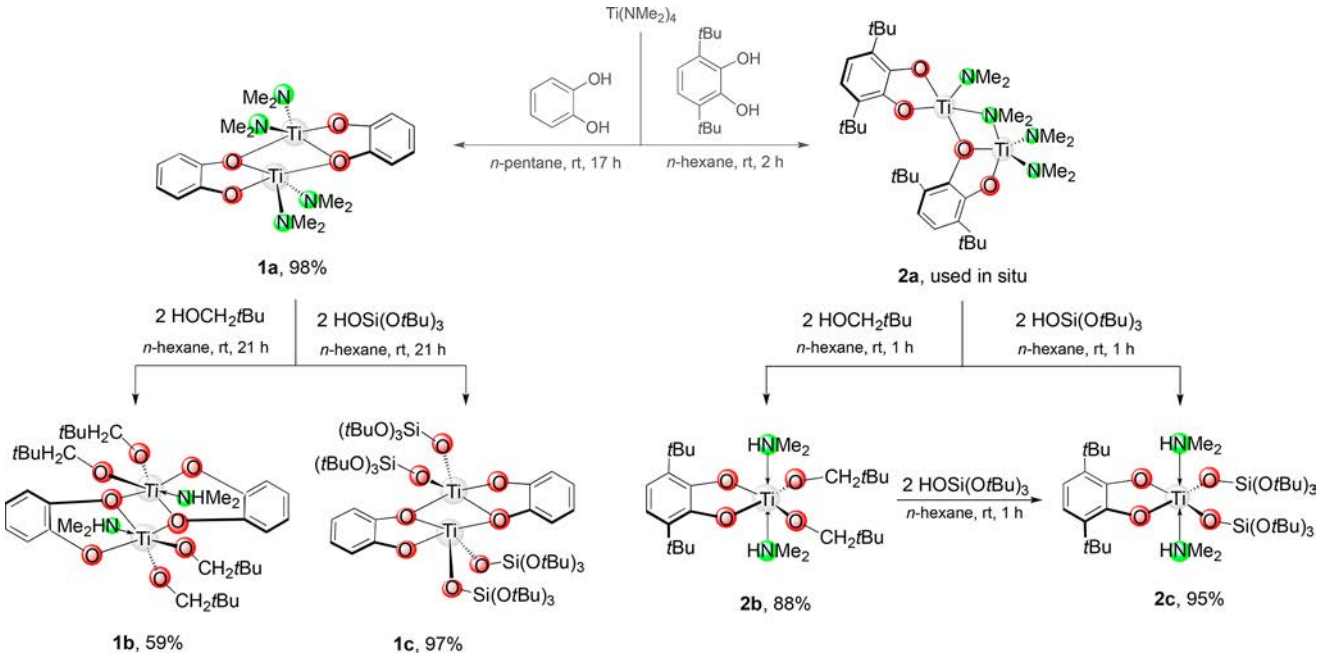

[a]Synthesis of **1a** and **2a** according to ref 40.

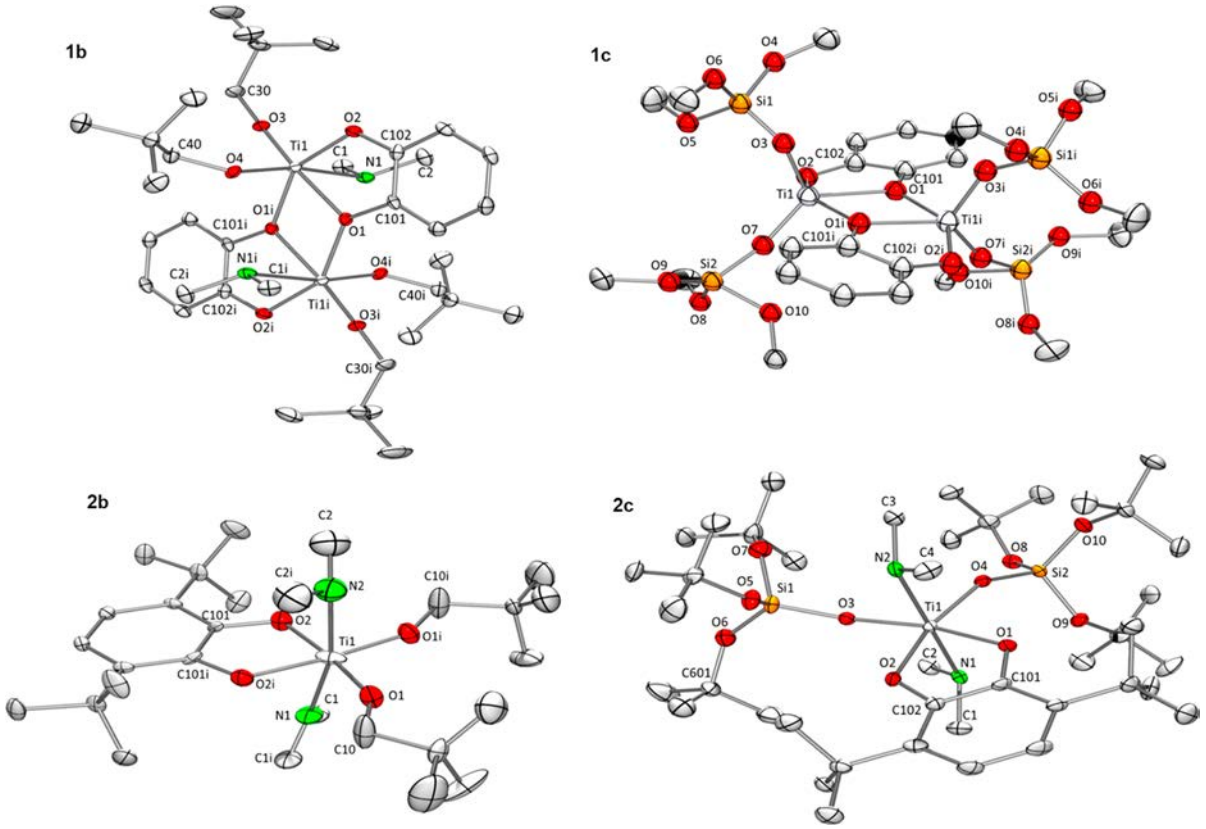

Figure 1. Crystal structures of complexes **1b**, **1c**, **2b**, and **2c** with atomic displacement parameters set at the 50% level. Hydrogen atoms and the *tert*-butyl-methyl groups in **1c** are omitted for clarity. For selected interatomic distances and angles, see Table 1 and the Supporting Information.

exclusive on particles smaller than 4.5 nm. The surface Ti atoms in bulk titanium dioxide exhibit a coordination number of six (octahedral geometry), which is claimed to be energetically more favorable than the square-pyramidal environment observed in nanoparticles smaller than 4.5 nm.[16,23] Chelating ligands, like catechol/catecholato, are considered to have a stabilizing effect on coordinatively unsaturated "open" metal sites,[34] which explains the exclusive occurrence of the bidentate chelating binding mode of pyrocatechol at very small titania nanoparticles. All previous

https://doi.org/10.1021/acs.inorgchem.2c02838
Inorg. Chem. 2023, 62, 715−729

Table 1. Interatomic Distances [Å] of 1b, 1c, 2b, and 2c

	1a[1]	1b	2a[1]	2b	2c
Ti---Ti	3.361(1)	3.364(1)	3.191(1)		
ArC−O	1.362(2)	1.348(3)	1.362(2)	1.357(5)	1.347(5)
		1.365(3)			1.360(5)
OC−CO	1.407(2)	1.409(4)	1.410(1)	1.409(9)	1.400(5)
Ti−N	1.874(1)	2.317(2)	1.895(2)	2.205(15), 2.24(3)	2.227(3), 2.229(3)
Ti−O[a]	1.936(1)−2.000(1)	1.906(2)−2.108(2)	1.901(1)−2.011(1)	1.915(3)	1.936(3)/1.937(3)
Ti−O[b]		1.767(2), 1.843(2)		1.840(3)	1.886(3), 1.886(3)

[a]Ti−O(catecholato). [b]Ti−O(neopentoxy/siloxy).

studies show that the surface binding type of catechol(s) on titania was experimentally controlled/directed by the change of the titania particle size.

Herein, we report the synthesis of a titanium(IV) complex bearing a bidentate chelating catecholato ligand. This discrete complex was grafted according to a convergent approach onto both mesoporous silica KIT-6 for comprehensive hybrid material characterization[35,36] and mesoporous titania (m-TiO_2) for optical and electronic investigations.[37−39] For a better assessment of the immobilization process, a sequential grafting approach and an aqueous route were investigated as well.[20]

RESULTS AND DISCUSSION

Molecular Titanium(IV) Precursors and Surface Models. To obtain a monomeric titanium(IV) complex, we advanced our previous findings on heteroleptic titanium(IV) catecholates. Recently, we reported on dimethylamido/catecholato-bridged titanium(IV) complexes derived from pyrocatechol, 2,3-dihydroxy-naphthalene, 4-*tert*-butylcatechol, 3,5-di-*tert*-butylcatechol, and 3,6-di-*tert*-butylcatechol proligands.[40] Despite additional tetrahydrofuran coordination or increased steric demand of the catecholato ligand, the formation of dimeric complexes could not be impeded. This phenomenon is also known for the corresponding catecholato-bridged titanium(IV) isopropoxides.[41,42] Therefore, we envisaged the use of neopentoxy as a sterically slightly more demanding alkoxy ligand, which is still labile enough for subsequent reactions with surface hydroxyl groups of silica or titania. Moreover, tris(*tert*-butoxy)silanol was considered to be a suitable model surface for [HOSi(OSi≡)$_3$] (Q^3) sites, hence enlightening/mimicking the surface chemistry.[43−45]

Accordingly, the previously described dimeric complexes $[Ti(CAT)(NMe_2)_2]_2$ (**1a**) and $[Ti(CAT^tBu_2\text{-}3,6)(NMe_2)_2]_2$ (**2a**)[40] were treated with 2 equiv of neopentanol (Scheme 1). The alcoholysis products $[Ti(CAT)(OCH_2{}^tBu)_2(HNMe_2)]_2$ (**1b**) and $Ti(CAT^tBu_2\text{-}3,6)(OCH_2{}^tBu)_2(HNMe_2)_2$ (**2b**) were obtained as dimeric and monomeric complexes, respectively, upon crystallization from *n*-hexane at −35 °C (Figure 1). This indicated that the use of the sterically demanding catecholato ligand [CAT^tBu_2-3,6] in combination with neopentoxy coligands can sufficiently counteract dimerization.

The heteroleptic neopentoxide complexes **1b** and **2b** are six-coordinated and feature $HNMe_2$ as additional amine donor ligands, which is evidenced by the longer Ti−N distances (ave. 2.220 and 2.317 Å) compared to the amido ligands in **1a** and **2a** (Ti−N ave. 1.895 Å) (Table 1). Thus, $HNMe_2$ is not completely displaced from the titanium coordination sphere, causing broad methyl resonances at 2.28 and 2.11 ppm in the ^{1}H NMR spectra of compounds **1b** and **2b**, respectively (Figures S2 and S4). The presence of $HNMe_2$ donor coordination is further supported by diffuse-reflectance infrared Fourier-transformed (DRIFT) spectroscopy, showing typical N−H stretch vibrations at 3199 and 3293 cm^{-1}, respectively. Such amine coordination seems to be stronger than that in the case of the five-coordinated amido precursors **1a** and **2a**, the crystal structures of which did not display coordinated $HNMe_2$.[40]

Notwithstanding, the amino-donor coordination observed for **1b** and **2b** seems surprising because the alcoholysis of homoleptic $Ti(NMe_2)_4$ with 4 equiv of neopentanol gave the homoleptic titanium(IV) neopentoxide complex (**3**), devoid of coordinated $HNMe_2$ (see the ^{1}H NMR and DRIFT spectra in Figures S6 and S18). Therefore, $HNMe_2$ seems to have a stabilizing effect specifically for the new heteroleptic complexes by promoting octahedral geometries. The catecholato ligands in complexes **1b** and **2b** adopt [κ^2(O,μ-O′)] and the desired bidentate chelating coordination mode [κ^2(O,O′)], respectively. The Ti−O(catecholato) distances are in the ranges of 1.906(2)−2.108(2) Å (**1b**) and 1.840(3)−1.915(3) Å (**2b**).

To get an idea of the potential surface species emerging from grafting of the neopentoxide complexes **1b** and **2b** onto silica KIT-6 (vide infra), the amide precursors **1a** and **2a** were reacted with tris(*tert*-butoxy)silanol instead of neopentanol as well.[46,47] The resulting heteroleptic siloxide complexes $[Ti(CAT)\{OSi(O^tBu)_3\}_2(HNMe_2)_2]_2$ (**1c**) and $[Ti(CAT^tBu_2\text{-}3,6)\{OSi(O^tBu)_3\}_2(HNMe_2)_2]$ (**2c**) again revealed the formation of a monomeric species in the presence of the sterically demanding ligand CAT^tBu_2-3,6 (Figure 1). Crucially, the monomeric siloxide **2c** was also obtained in nearly quantitative yield, when the neopentoxy complex **2b** (instead of **2a**) was reacted with tris(*tert*-butoxy)silanol via silanolysis,[48−54] which comes even closer to the potential surface reaction to be expected on KIT-6 (vide infra). The Ti−O(siloxy) distances amount to 1.851(9)/1.855(16) Å (**1c**) and 1.886(3)/1.886(3) Å (**2c**) and match those of other mixed alkoxy/siloxy titanium(IV) complexes.[51,53−55] Neopentoxy/siloxy exchange significantly affects the Ti−O(catecholato) bonding due to the increasingly electron-withdrawing behavior of the siloxy ligands (Table 1).

Overall, the ArC−O and OC−CO distances of complexes **1b**, **2b**, and **2c** are in the same range as those in their precursor complexes **1a** and **2a**, supporting preservation of the dianionic nature and bidentate coordination mode of the catecholato ligands and, hence, the formal oxidation state IV of the Ti centers (Table 1).[40]

Titanium Grafting onto Periodic Mesoporous Silica KIT-6. Silica KIT-6 (**M1**) featuring large mesopores ($d_{p,ads}$ = 8.5 nm) of cubic symmetry ($Ia\bar{3}d$) was employed to ensure efficient intrapore chemistry (avoidance of pore blocking).[35,36,40] Moreover, a relatively high surface area (620 m^2 g^{-1}) along with a comparatively high number of surface-

https://doi.org/10.1021/acs.inorgchem.2c02838
Inorg. Chem. 2023, 62, 715−729

Scheme 2. Three Routes toward Surface Titanium(IV) Catecholates: Aqueous, Sequential, and Convergent Approaches

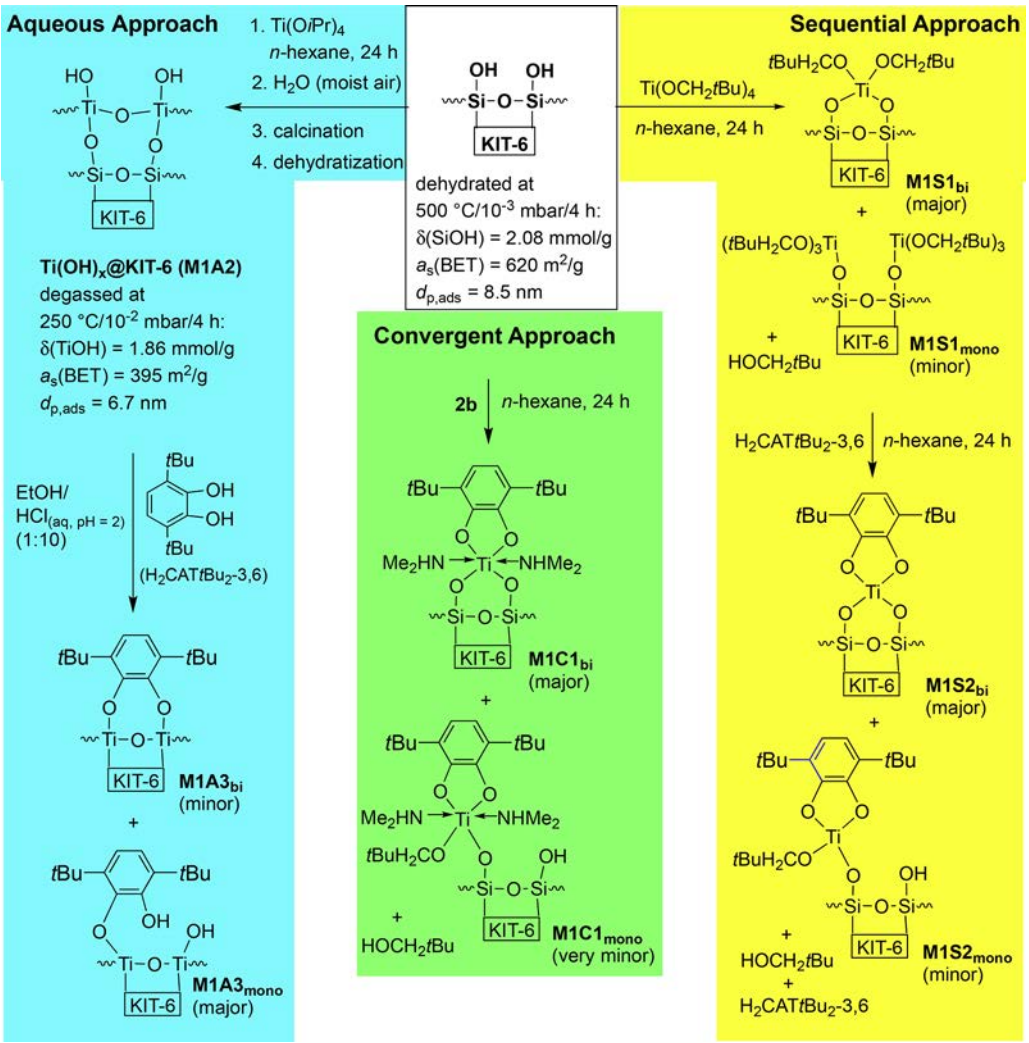

hydroxyl groups should afford a high concentration of surface complexes and, hence, facilitate their characterization. Three grafting strategies were pursued comprising sequential and convergent approaches,[40,45] as well as a procedure drawing on an intermediate aqueous treatment.[20]

Sequential Approach. This surface functionalization sequence was started with homoleptic titanium(IV) neopentoxide $Ti(OCH_2tBu)_4$ (**3**) (Scheme 2). Complex **3** was obtained via alcoholysis of $Ti(NMe_2)_4$ with 4 equiv of neopentanol in *n*-hexane at ambient temperature. A unit cell check [via X-ray diffraction (XRD)] of **3** recrystallized from *n*-hexane at −35 °C matched the cell parameters of dimeric $[Ti(\mu\text{-}OCH_2tBu)(OCH_2tBu)_3]_2$ reported by Boyle et al. in 1997.[55] The latter work also stated that complex **3** is monomeric in a toluene solution, making it a good candidate for immobilization reactions. The hybrid material $Ti(OCH_2tBu)_4$@[KIT-6] (**M1S1**) was obtained by treating parent KIT-6 (dehydrated at 773 K/10^{-3} mbar for 4 h) with a solution of complex **3** in *n*-hexane ("alkoxide grafting").[56−60] Both such alkoxide grafting and "amide grafting" (vide infra) adopt the principles of surface organometallic chemistry.[61−64] The DRIFT spectrum of **M1S1** revealed a significant amount of nonreacted SiOH groups, as indicated by the OH stretching vibration at 3701 cm^{-1} (see the DRIFT spectrum in Figure S23), implying inaccessible OH groups. For a qualitative determination of the surface species, the ^{13}C magic-angle-spinning (MAS) NMR spectrum of the material **M1S1** was recorded and compared to the ^{13}C NMR spectrum of **3** in C_6D_6 (Figure 2). In accordance with a monomeric species in solution, the spectrum of complex **3** shows only one CH_2 signal (86 ppm). In contrast, the solid-state spectrum of the material **M1S1** displays two signals in this region (73 and 89 ppm). The signal at 89 ppm can be assigned to the neopentoxy ligands of grafted titanium species, while the resonance at higher field results from the methylene group of surface-bound neopentanol. It was already pointed out that alcohols liberated by metal-alkoxide grafting are prone to coordinate to surface sites like Ti(IV) centers of enhanced Lewis acidity.[56]

For quantification issues, the amount of accessible surface-SiOH groups of the parent material **M1** was determined as $\delta(SiOH) = 2.08$ mmol g^{-1}, from the C content of the surface-silylated material $HN(SiHMe_2)_2$@[KIT-6] (**M1a**).[65,66] In general, there are two prevailing grafting modes of **3** on the KIT-6 surface: monopodal $[\equiv SiOTi(OCH_2tBu)_3]$ or bipodal $[(\equiv SiO)_2Ti(OCH_2tBu)_2]$. Assuming metalation of all surface OH groups accessible for silylation and the formation of monotitanium surface sites (monofunctional reaction, no clustering), the Ti content of the material **M1S1** of 0.96 mmol g^{-1} (see the Supporting Information) suggested bipodally anchored titanium species as the major surface

https://doi.org/10.1021/acs.inorgchem.2c02838
Inorg. Chem. 2023, 62, 715−729

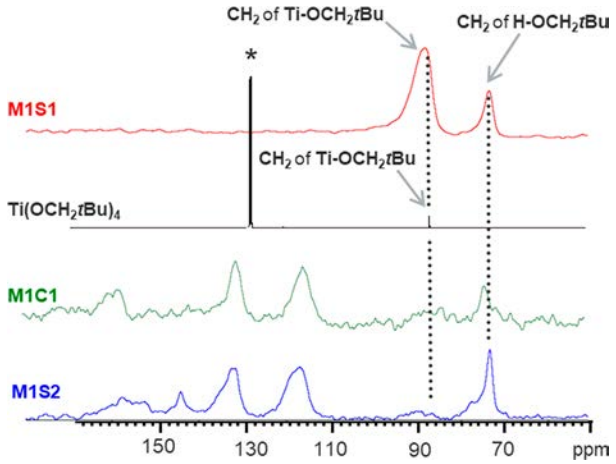

Figure 2. ^{13}C NMR spectra (bottom-up) of the materials **M1S2**, **M1C1**, and **3** in solution (100 MHz, C_6D_6 = *) and of the material **M1S1**. Materials represented by solid-state spectra: 75 MHz, CP/MAS, 10 kHz rotation.

species. The high C/Ti ratio, obtained from the experimental results (14:1), can be ascribed to surface-coordinated neopentanol, which was already identified via ^{13}C MAS NMR of **M1S1**. For comparison, exclusive $[(\equiv SiO)_2Ti(OCH_2tBu)_2]$ surface sites would correspond to a theoretical C/Ti ratio of 10:1.

The second step of the sequential approach involves the surface-promoted ligand exchange of **M1S1** with $H_2CAT tBu_2$-3,6. The signal of the Ti[OCH_2*t*Bu] methylene moieties at 89 ppm in the ^{13}C MAS NMR spectrum of the material **M1S1** nearly vanished in $H_2CAT tBu_2$-3,6@$Ti(OCH_2tBu)_4$@[KIT-6] (**M1S2**; Figure 2), which implies a successful ligand exchange via transalcoholysis. Finkelstein-Shapiro et al.[25] pointed out that, compared to those of the free catechol, the shifts of the *α*-, *β*-, and *γ*-C atoms of surface catecholato species are specific for the surface binding mode. For the material **M1S2**, the position of the *β*-C atom is shifted upfield from 135 to 137 ppm (free catechol) to 133 ppm (Figure 3), which can be assigned to a bidentate (chelating) surface species.[25] However, there are two signals for the *α*-C atoms: one very broad signal is shifted downfield, centered at 158 ppm, and the other is still at the same position as that for the free catechol (144 ppm). Consequently, the overall ^{13}C signal pattern indicates the presence of bidentate chelating surface species, involving both bipodally and monopodally anchored Ti(IV) centers $[(\equiv SiO)_2Ti(CAT tBu_2$-3,6)] and $[(\equiv SiO)Ti(CAT tBu_2$-3,6)-$(OCH_2tBu)]$, respectively, and physisorbed $H_2CAT tBu_2$-3,6 (cf. Scheme 2).

The presence of predominantly bipodal surface species is also suggested by the low titanium concentration of the material **M1S2** of 0.37 mmol g^{-1}. This considerably lower Ti content than that in the precursor material **M1S1** can be ascribed to leaching of the titanium surface species. The experimentally obtained C/Ti ratio (36:1; Table S2) of **M1S2** accounts for a huge C content, which can be ascribed to surface-coordinated neopentanol and nonreacted proligand $H_2CAT tBu_2$-3,6. The ArOH stretching vibration at 3573 cm^{-1} is a further hint for the presence of molecular $H_2CAT tBu_2$-3,6 (Figure S24).

Convergent Approach. $[Ti(CAT tBu_2$-3,6)-$(OCH_2tBu)_2(HNMe_2)_2]$@[KIT-6] (**M1C1**) was obtained via grafting of the monomeric complex **2b** onto KIT-6 (**M1**)

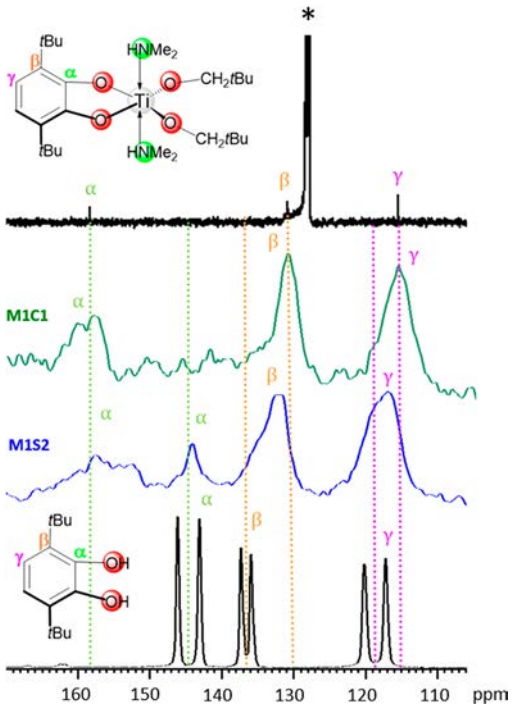

Figure 3. ^{13}C NMR spectra (bottom-up) of $H_2CAT tBu_2$-3,6, **M1S2**, and **M1C1** in the solid state (75 MHz, CP/MAS, 10 kHz rotation) as well as **2b** in solution (100 MHz, C_6D_6 = *).

through a protonolysis reaction in *n*-hexane at ambient temperature (Scheme 2). The disappearance of the Ti-[OCH_2*t*Bu] neopentoxy methylene moieties at 89 ppm in the ^{13}C MAS NMR spectrum of the material **M1C1** (Figures 2 and S11) is in accordance with a successful grafting reaction. This is further supported by the appearance of a methylene carbon resonance at 74 ppm ascribed to surface-attached neopentanol. Both the upfield shift of the *β*-C (from 135 to 137 ppm to 131 ppm) and the downfield shift of the *α*-C (from 145 to 158 ppm) of the catecholato ligand (compared to catechol) suggest a bidentate (chelating) surface species (Figure 3).[25] Also, the position of the *γ*-C at 115 ppm resembles that of the molecular complex **2b** rather than that of the free catechol (Figure 3). The resonance at 40.5 ppm is ascribed to coordinated amine (Figures S11 and S12).

Due to the absence of any C signal originating from Ti[OCH_2*t*Bu] in the ^{13}C MAS NMR spectrum of the material **M1C1** (Figures 2 and S11), bipodally grafted $[(\equiv SiO)_2Ti-(CAT tBu_2$-3,6)$(HNMe_2)_2]$ was proposed as the prevailing surface species. This was corroborated by elemental analysis, revealing a titanium concentration of the material **M1C1** of 0.76 mmol g^{-1} (see the Supporting Information) and the presence of residual SiOH groups, as detected in the DRIFT spectrum (Figure S25). The experimentally determined N/Ti ratio of 1.93:1 is close to the theoretical one (2:1), while the presence of the $HNMe_2$ donor is evidenced by ^{13}C MAS NMR (vide supra) and DRIFT spectroscopy (ν_{NH} = 3295 cm^{-1}; Figure S25).

Aqueous Approach. The aqueous synthesis route to access catecholato-functionalized titanium(IV) surface species was approached from the material $Ti(OiPr)_4$@[KIT-6] (**M1A1**) obtained by grafting of $Ti(OiPr)_4$.[56] Mild hydrolysis of **M1A1** afforded $Ti(OH)_x$@[KIT-6] (**M1A2**), which was subsequently reacted with 3,6-di-*tert*-butylcatechol under

https://doi.org/10.1021/acs.inorgchem.2c02838
Inorg. Chem. 2023, 62, 715−729

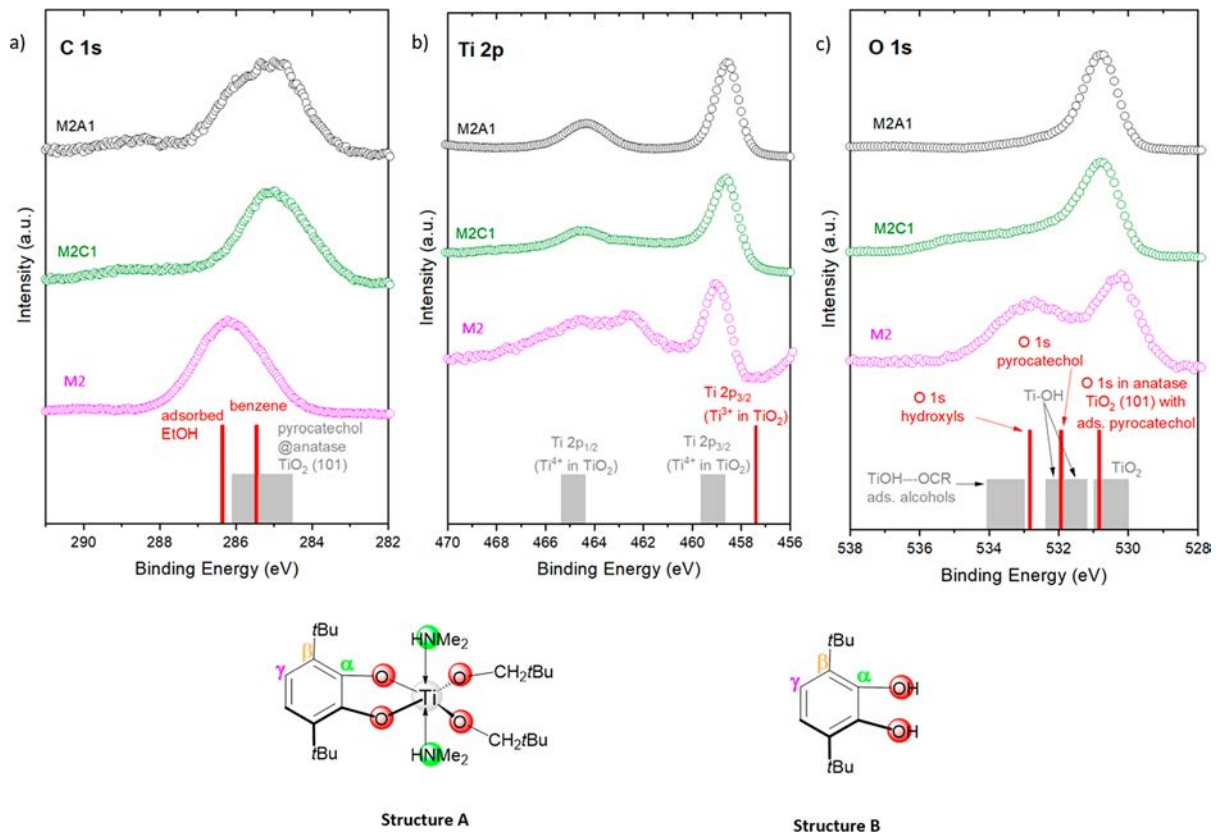

Figure 4. (a) C 1s and (b) Ti 2p core-level spectra (XPS) and (c) O 1s of **M2**, **M2C1**, and **M2A1**. Bar charts indicate the binding energies for the various contributions of (a) C 1s species as reported in refs 67−69, (b) Ti 2p species as reported in refs 69, 71, and 72, and (c) O 1s species as reported in refs 69 and 71−73. Structures of the molecular precursors to obtain **M2C1** (structure A) and **M2A1** (structure B) are also shown. Note that, in part b, the intensities at around 455 and 463 eV are due to In $3d_{5/2}$ and indium plasmon loss, respectively, also overlapping the Ti 2p intensity.[74,75] These are particularly intense in **M2** because of the smaller amount of powder covering the indium substrate.

acidic conditions to yield $H_2CAT tBu_2$-3,6@$Ti(OH)_x$@[KIT-6] (**M1A3**; Scheme 2). The Ti content of the material **M1A2** after calcination was determined as 5.07 wt % corresponding to a titanium surface coverage of 1.27 mmol g^{-1}, therefore pointing to mono- and bipodally grafted $Ti(OiPr)_4$ species in **M1A1**. The catechol/catecholato-functionalized material **M1A3** revealed a significantly lower titanium surface concentration of 0.82 mmol g^{-1}, which is ascribed to some leaching under the applied acidic conditions. Moreover, the low C content (C/Ti = 5.6/1) clearly indicated a weak $Ti_{surface}$−$H_2CAT tBu_2$-3,6 interaction. This is supported by the ^{13}C MAS NMR spectrum of the material **M1A3** showing very weak (if at all) signals in the aromatic region (Figure S13). Furthermore, the DRIFT spectrum of the material **M1A3** clearly revealed the presence of unreacted surface OH groups (ν_{OH} = 3741 cm^{-1}; Figure S22). The amount of maximum surface hydroxyl groups of the dehydrated material **M1A2** was determined via carbon analysis of the silylated material $HN(SiHMe_2)_2$@$Ti(OH)_x$@[KIT-6] (**M1A2a**) as δ(TiOH) = 1.86 mmol g^{-1}.

Extension to m-TiO_2. To probe the electronic and optical properties of a tailor-made bidentate chelating catecholato surface species, complex **2b** was grafted onto a m-TiO_2 material and compared to a material obtained according to the aqueous approach. The latter material should feature a random distribution of bidentate bridging and monodentate catechol/catecholato surface species.[20] The synthesis of m-TiO_2 (**M2**) was inspired by the Blin group[37−39] and modified with respect to our laboratory equipment (see the Experimental Section: a_S(BET) = 93 m^2 g^{-1}; $V_{P,cum.des.}$ = 0.19 cm^3 g^{-1}; $d_{P,ads.}$ = 7.0 nm; δ(TiOH) = 0.76 mmol g^{-1}; anatase type). In analogy to the synthesis of the KIT-6 hybrid materials described above, the aqueous and convergent approaches gave distinct materials denoted as $H_2CAT tBu_2$-3,6@[m-TiO_2] (**M2A1**) and [$Ti(CAT tBu_2$-3,6)-$(OCH_2tBu)_2(HNMe_2)_2$]@[m-TiO_2] (**M2C1**). The convergent approach was favored over the sequential approach because the bipodally grafted [$(\equiv SiO)_2Ti(CAT tBu_2$-3,6)-$(HNMe_2)_2$] emerged as the prevailing surface species on silica.

Electronic and Optical Investigations. Because m-TiO_2 exhibits a smaller surface area and less surface hydroxyl groups than KIT-6, a markedly lower catecholate concentration is found on m-TiO_2 upon functionalization reactions. To shed light on the obtained hybrid materials, X-ray photoelectron spectroscopy (XPS) was applied because it has a much higher surface-to-bulk sensitivity than conventional spectroscopic techniques (like, e.g., ^{13}C MAS NMR spectroscopy). We envisioned that the XPS features, being sensitive to the chemical environment of the single elements, might give evidence of whether the grafting has been successful or not. A successful grafting should be reflected by strong differences in the O 1s core-level curves, as is the case (Figure 4). To prove that our grafting strategy is successful, in the following part, all relevant XPS features are commented on in detail by considering the chemical environments that determine their binding energies, intensities, and shapes.

https://doi.org/10.1021/acs.inorgchem.2c02838
Inorg. Chem. 2023, 62, 715−729

Figure 4 depicts the C 1s, O 1s, and Ti 2p core-level spectra for **M2** and the functionalized materials **M2C1** and **M2A1** (for the survey spectra, see Figure S32). Focusing on the C 1s spectra in Figure 4a, a pronounced, symmetric peak at 286.2 eV was detected for m-TiO_2 (C 1s spectrum of **M2**), which hints at surface-coordinated alcohols.[67] In fact, HO*i*Pr from the hydrolyzed precursor [Ti(O*i*Pr)$_4$] or EtOH from the final rinsing process is a plausible residue. When our data are compared with those in the literature,[67] the symmetric shape of the C 1s peak in the spectrum of **M2** indicates that the carbon contaminants stem from EtOH residues, which were not detectable within C/H/N elemental analysis with temperature-programmed desorption (TPD) columns (for details, see "XPS surface sensitivity" in the Supporting Information).

The **M2A1** and **M2C1** C 1s spectra in Figure 4a both display a broadened, asymmetric main peak, centered at 285.0 eV. In both cases, the peak energy position suggests a different chemical environment of the C atoms, involving a substituted phenylene backbone.[69,70] Substituents change the chemical (e.g., C−C, C−O, and C−H) and symmetrical (e.g. C−C, C≡C, and C−*t*Bu) environment of C atoms, which has an influence on the line width and the binding energy of the respective carbon species.

The Ti 2p spectrum of **M2** (Figure 4b) displays three main features: The two peaks at 459.0 and 464.6 eV can be identified as the doublet Ti 2p$_{3/2}$ and Ti 2p$_{1/2}$ peaks, expected because of spin−orbit splitting.[73] The third feature at 462.6 eV can be assigned to Ti−OH surface species of the virgin **M2**. This feature disappeared in the Ti 2p spectra of **M2C1** and **M2A1**, in agreement with the fact that the surface hydroxyls are consumed during the surface functionalization reactions. The Ti 2p doublet features in the Ti 2p spectra of **M2A1** and **M2C1** show intensities and splitting values in good agreement with the literature (Ti 2p$_{3/2}$ at 458.6 eV and Ti 2p$_{1/2}$ at 464.3 eV and intensity 2:1 for **M2A1**; Ti 2p$_{3/2}$ at 458.6 eV and Ti 2p$_{1/2}$ at 464.5 eV and intensity 2:1 for **M2C1**).[69]

The XPS data show that virgin **M2** contains the desired Ti−OH groups but also traces of EtOH residues from the synthesis. The Ti−OH groups were consumed and the EtOH residues were displaced during the subsequent surface functionalization reactions. The O 1s and Ti 2p spectra of the functionalized materials **M2A1** and **M2C1** do not exhibit such supplementary peaks. Instead, the binding energy positions of their main peaks are shifted. This accounts for a more efficient screening of the core hole with electronic participation of the m-TiO_2 support for **M2A1** and **M2C1**.

The O 1s spectrum of **M2** (Figure 4c) shows an intensive peak centered at 530.2 eV, which is in the range expected for photoelectrons emitted from O atoms in TiO_2 (530.0−530.9 eV).[69−72] A lower-intensity peak at 532.7 eV can be correlated with hydroxyl groups from the TiO_2 surface (Ti−OH)[73] and with adsorbed ethanol (C−OH).[70,76] The latter peak is not present in the **M2C1** and **M2A1** O 1s spectra (Figure 4c), wherein the O 1s main peak is shifted toward higher binding energies (530.8 eV). Moreover, the full width at half-maximum (fwhm) of the **M2A1** O 1s line is narrower than the fwhm of the **M2C1** O 1s line (1.10 and 1.48 eV, respectively). In fact, looking at the structures of the two materials, four new O atoms are introduced per immobilized molecule of **2b** in **M2C1** (see structure A in Figure 4), whereas there are only two O atoms in **M2A1** (see structure B in Figure 4). The presence of a small photoemission feature in the high-binding-energy range, more pronounced for **M2C1** than for **M2A1**, might be due to satellite intensities that stem from the relaxation processes due to the creation of a core hole.[68,77,78] The relaxation is different in the two cases because of the different chemical structures and the presence of very small amounts of oxygen contaminants. This result suggests a successful surface functionalization in both cases.

The electronic nature of the corresponding materials was further investigated by using ultraviolet photoelectron spectroscopy (UPS; the UPS spectra and calculations can be found in Figures S37−S39 and Tables S7 and S8). The results are displayed in Table 2 and visualized as an energy-level diagram

Table 2. Energy Levels Obtained from the UPS Spectra of M2, M2C1, and M2A1[a]

	M2	M2A1	M2C1
φ [eV]	4.8	4.2	5.0
E_{HOES} [eV]	−1.9	−1.8	−2.1
E_{BG} [eV][b]	3.3 (3.3)	3.2 (3.2)	3.1 (3.1)
*E_{LUES} [eV]	1.4	1.6	1.0
HIB [eV]	1.9	1.8	2.1
IP [eV]	6.7	6.0	7.1
*EA [eV]	3.4	2.8	4.0

[a]For details about how these values were obtained, see Tables S7 and S8. [b]Value 1 (value 2) = from the Praying Mantis setup, used for further calculations of *E_{LUES} and *EA (from the Ulbricht sphere setup, only for comparison).

in Scheme 3. The m-TiO_2 work function (φ), 4.8 eV, corresponds to typical values of the anatase TiO_2 crystallographic phase,[79−82] concomitant with the optical band gap obtained experimentally. The optical properties of the materials under study were examined by solid-state UV/vis measurements using an Ulbricht sphere (Figure S33) and a Praying Mantis setup (Figure 5).

The Tauc plots of the spectra are reported in Figures S34−S36, and their results were consistent for both methods. Therefrom, the optical band gaps (E_{BG}) of **M2**, **M2A1**, and **M2C1** were calculated (Table 2). The **M2** optical band gap of ∼3.3 eV is in the typical range for anatase-TiO_2.[81−86] The grafted monomeric Ti(IV) complex reduced the band gap to ∼3.1 eV (**M2C1**), whereas the species **M2A1**, which was synthesized according to an established aqueous approach,[20] exhibited a slightly larger band gap of ∼3.2 eV. Therefore, the bidentate chelating catecholate species on the surface of titania, which is herein represented by the material **M2C1**, leads to a larger optical absorption redshift. Our results show a behavior that has been predicted only theoretically so far and never proven experimentally.[27]

The obtained energy-level alignment is shown in Scheme 3. The highest occupied electronic states (HOES) of **M2A1** are higher than those of **M2**, in agreement with the literature.[27] The catechol's highest occupied molecular orbital (HOMO = the HOES of the molecular catechol) is energetically located within the band gap of titania, creating filled electronic states above the valence band (VB = HOES of titania) of TiO_2, wherefrom electrons are directly injected into the conduction band [CB = lowest unoccupied electronic states (LUES) of titania] of TiO_2.[24,87] Therefore, its excitation requires less energy than pure anatase. This excitation mechanism with direct electronic injection from the catechol's electronic levels into the titania's electronic levels is defined as type II.[25] Scheme 3 also shows that **M2C1** LUES are energetically

https://doi.org/10.1021/acs.inorgchem.2c02838
Inorg. Chem. 2023, 62, 715−729

Scheme 3. Energy-Level Scheme for M2, M2C1, and M2A1 to Visualize the Data Displayed in Table 2[a]

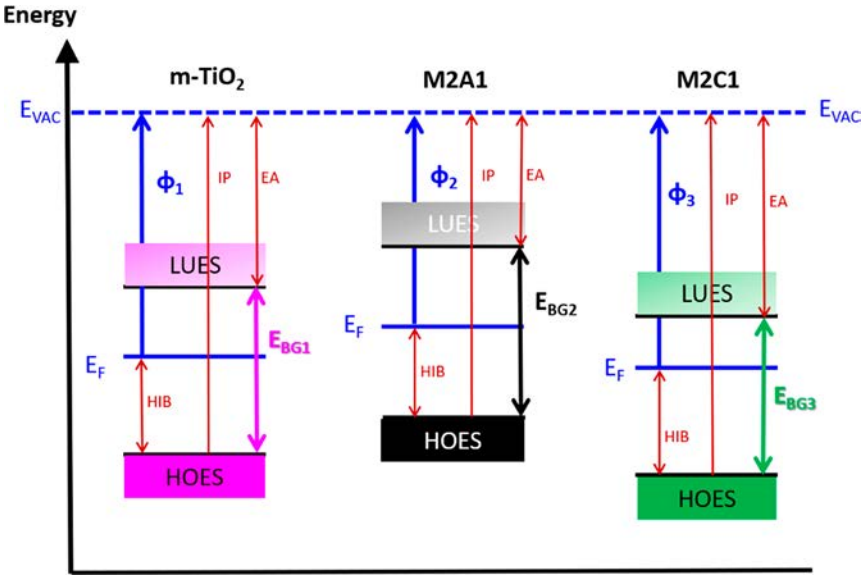

[a]Abbreviations: hole injection barrier, HIB; ionization potential, IP; electron affinity, EA.

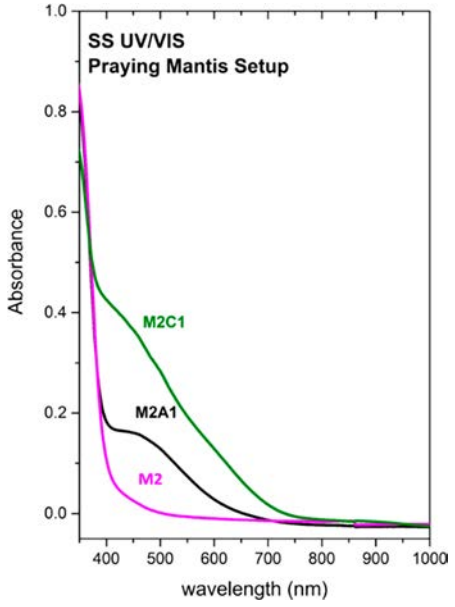

Figure 5. Solid-state UV/vis spectra of **M2**, **M2C1**, and **M2A1** (setup: Praying Mantis).

located within the band gap of **M2**, which indicates a defect structure different from that in the case of material **M2A1**. The reduction of the energy levels mirrors the stabilizing influence of the chelating ligands on metal centers, as mentioned in the Introduction. The exact excitation mechanism within the material **M2C1** still needs to be investigated. In fact, to our knowledge, the bidentate-chelating catecholate species has been experimentally reported only on very small titania nanoparticles but not on mesoporous titania.[16,23,27,33,88]

CONCLUSION

The immobilization of catechol on titanium(IV) surface-functionalized mesoporous silica KIT-6 by applying aqueous conditions provides only very low catechol surface coverage, making identification of the exact surface species essentially impossible. In contrast, metal−organic grafting gave access to considerably higher concentrations of titanium(IV) catecholate surface species. The sequential approach affording the material $H_2CAT{t}Bu_2$-3,6@$Ti(OCH_2{t}Bu)_4$@[KIT-6] exhibits the desired bidentate chelating surface species $(\equiv SiO)_2$[Ti($CAT{t}Bu_2$-3,6)] but also incomplete alcoholysis. Crucially, the convergent approach affording material [Ti($CAT{t}Bu_2$-3,6)$(OCH_2{t}Bu)_2(HNMe_2)_2$]@[KIT-6] ensures exclusive formation of the desired bidentate chelating surface species with bipodally anchored Ti(IV) centers.

Extension of the aqueous and convergent approaches to m-TiO_2 finally enabled investigation of the optical and electronic properties of the obtained materials $H_2CAT{t}Bu_2$-3,6@[m-TiO_2] and [Ti($CAT{t}Bu_2$-3,6)$(OCH_2{t}Bu)_2(HNMe_2)_2$]@[m-TiO_2]. The XPS spectra confirmed that the surface species are linked to the titania surface but that they are not identical. Both functionalized materials exhibit a reduction of the band gap compared to the parent m-TiO_2 support (∼3.3 eV), with grafted [Ti($CAT{t}Bu_2$-3,6)$(OCH_2{t}Bu)_2(HNMe_2)_2$]@[m-TiO_2] displaying a smaller band gap (∼3.1 eV) than the material obtained under aqueous conditions (∼3.2 eV). The corresponding redshift of the optical absorption of the grafted material was previously described as a unique phenomenon for bidentate chelating surface species formed by enediol ligands like catechols via dissociative chemisorption on very small nanoparticles (<20 nm) of metal oxides like titania.[88] Our findings indicate that, on m-TiO_2, the grafted material features the bidentate chelating surface species, while aqueous impregnation seems to favor a different surface species. The energy-level alignment of the titanium catechol/catecholate materials indicates distinct excitation mechanisms for the two materials. Because the grafted material features very stable surface species, the convergent synthesis approach bears promising potential for the exploration of novel pathways for photoreactive materials (e.g., exchange of catechol for dopamine) with tailor-made surface species and for potential applications in the field of biomedicine, such as light-induced targeted drug delivery to fight cancer cells.

https://doi.org/10.1021/acs.inorgchem.2c02838
Inorg. Chem. 2023, 62, 715−729

EXPERIMENTAL SECTION

General Considerations and Procedures. If not otherwise noted, all operations were performed with rigorous exclusion of air and water, using standard Schlenk and glovebox techniques (MB Braun MB150B-G-I; <1 ppm of O_2, <1 ppm of H_2O) under an argon atmosphere. Solvent purification was performed over Grubbs-type columns (MB Braun, MB SPS-800): *n*-pentane [≥99.0% for high-performance liquid chromatography (HPLC), from Sigma-Aldrich] and *n*-hexane (≥97% for HPLC, from Riedel de Haen). C_6D_6 (99.5%, water <0.02%) was obtained from Eurisotop, degassed and dried over NaK for 24 h, stored in the glovebox, and always freshly filtered before use. Pyrocatechol (≥99%, from Aldrich) and 3,6-di-*tert*-butylcatechol (95%, from SynChem) were degassed prior to use and stored in the glovebox. 1,1,3,3-Tetramethyldisilazan ($HN[SiHMe_2]_2$; ≥97%, from ABCR), tetrakis(dimethylamido)titanium(IV) [$Ti(NMe_2)_4$; >99.999%, from Aldrich], titanium(IV) isopropoxide [$Ti(OiPr)_4$; 99.999%, from Aldrich], tris(*tert*-butoxy)silanol (99,999%, from Sigma-Aldrich), and neopentanol (99%, from Alfa Aesar) were stored in the glovebox and used as received. Triblock copolymer Pluronic P123 (M_n ~ 5800, from Aldrich), 37% HCl (ACS reagent ≥37%, from Aldrich), ethanol (99.8%, p.a., from Sigma-Aldrich), and a 25% ammonium hydroxide solution (puriss Pa.a., from Sigma-Aldrich) were used as received. Periodic mesoporous silica KIT-6 (**M1**) was synthesized according to the literature.[35,36] NMR measurements were performed on a Bruker Avance-II+ 400-PFT-NMR spectrometer (^1H, 400.11 MHz; ^{13}C, 100.61 MHz). ^1H and ^{13}C resonances were referenced to internal solvent resonances and reported relative to tetramethylsilane. The NMR spectra of air- and moisture-sensitive compounds were recorded in NMR tubes with J. Young valves. ^{13}C cross-polarization (CP)/MAS NMR spectra were obtained at ambient temperature on a Bruker ASX 300 instrument equipped with MAS hardware, using a 3 mm ZrO_2 rotor. The ^{13}C NMR spectra were recorded using CP and proton decoupling and were referenced to adamantane (^{13}C: 28.46 and 37.85 ppm). Mass spectra were obtained using an MSD 5977 spectrometer (Agilent, Waldbronn) with a Direct Input Probe by SIM GmbH, Oberhausen, Germany. DRIFTS measurements were performed on a Nicolet 6700 FTIR spectrometer (Thermo Scientific), and dried KBr powder was used as the dilution matrix (10 wt % analyte related to $m_{analyte} + m_{KBr} = 100\%$). The sample/KBr mixture was always intimately mixed by grinding in an agate mortar prior to the measurements and put into a DRIFTS cell with KBr windows. The collected data were converted using the Kubelka–Munk refinement.[89] Elemental analyses were carried out on an Elementar Vario MICRO cube instrument using the CHNS mode. Single crystals suitable for XRD were selected in a glovebox, submerged in Paratone-N (Hampton Research), and mounted onto a microloop. XRD data collections were performed on a Bruker APEXII Duo at 100(2) K. The data were collected using the *COSMO* program[90] and *SAINT* for integration and data reduction.[91] Numerical absorption effect corrections were done using *SADABS*.[92] The structures were solved by direct methods and refined against all data by full-matrix least-squares methods on F^2 using *SHELXTL*[93] and *SHELXLE*.[94] For absorption correction of compound **2b**, the program *TWINABS* was used.[95] All crystal structure graphics were created with *ORTEP-III*[96] and *POV-Ray*.[97] Powder X-ray diffraction (PXRD) analyses were performed on a Bruker Advance D8 instrument in the step/scan mode using Cu Kα radiation (λ = 1.5418 Å). The small-angle diffractograms were recorded in the 2θ range of 0.5–9.99° with a scan speed of 2 s step^{-1}. N_2 physisorption measurements were performed on an ASAP 2020 volumetric adsorption apparatus (Micromeritics) at 77 K [$a_m(N_2, 77\ K) = 0.162\ nm^2$]. Prior to analysis, the samples were degassed at ambient temperature or the expected temperature for at least 1 h under vacuum (~10^{-3} mbar). The Brunauer–Emmett–Teller (BET) specific surface area was obtained from the nitrogen adsorption branch of the isotherm in the relative pressure range from 0.10 to 0.2.[98] Pore size distributions were calculated from the adsorption branches using the Barrett–Joyner–Halenda method.[99] The application of prolonged vacuum to titanium amido surface species should be avoided because of possible decomposition to imide species.[100]

*[Ti(CAT)(NMe$_2$)$_2$]$_2$ (**1a**).* The synthesis was performed as described in the literature:[40] $Ti(NMe_2)_4$ (225 mg, 1.00 mmol), diluted in 2 mL of *n*-pentane, was added dropwise to a stirred suspension of pyrocatechol (110 mg, 1.00 mmol) in 1 mL of *n*-pentane. A color change from yellow to orange to red was observed. After 17 h of stirring at ambient temperature, a bright-orange powder precipitated. Upon the removal of solvent residues under vacuum, product **1a** was obtained as a yellow powder in 98% yield (239 mg, 0.977 mmol). ^1H NMR (400 MHz, C_6D_6): δ 3.09 (s, 12H, N-Me_2), 6.94 (m, 2H, Ar-*H*), 7.06 (d, 2H Ar-*H*), 7.16 (s, 1H, C_6D_6).

*[(Ti(CAT)(OCH$_2$tBu)$_2$)(HNMe$_2$)]$_2$ (**1b**).* Neopentanol (53.2 mg, 0.604 mmol), dissolved in 1 mL of *n*-hexane, was added dropwise to a stirred suspension of **1a** (73.4 mg, 0.301 mmol) in 1 mL of *n*-hexane. After 21 h of stirring at ambient temperature, a yellow powder had precipitated, which was washed with *n*-hexane three times. Upon the removal of solvent residues under vacuum, product **1b** was obtained as a yellow powder in 59% yield (58.9 mg, 0.178 mmol). Elem anal. Calcd for $C_{36}H_{66}N_2O_8Ti_2$ (M = 750.66 g mol^{-1}): C, 57.60; H, 8.86; N, 3.73. Found: C, 57.27; H, 8.60; N, 3.81. ^1H NMR (400 MHz, C_6D_6): δ 0.98 (s, 18H, 2 × OCH_2C-Me_3), 2.28 (s, 6H, HN-Me_2), 4.40 (d, 2H, O-CH_2CMe_3), 4.52 (d, 2H, O-CH_2CMe_3), 6.80–6.90 (xm, 3H, 3 × Ar-*H*), 7.16 (s, 1H, C_6D_6), 7.29 (d, 1H, Me_2N-*H*). DRIFTS (KBr, cm^{-1}): 3199(w) [ν(R_2N–H)], 3064(w) [ν(Ar-H)], 2999–2828(w-m) [ν(C–H), CH_3, CH_2], 1573(w), 1517(w) [ν(C=C), aromatic ring + ν(Ti–O–C)], 1479(s), 1452(m), 1408(w), 1477(m), 1462(m), 1391(m), 1361(m) [δ(C–H)], CH_3, CH_2, 741(m) [ν(Ti–O–C)]. Another batch of powder **1b** (54.2 mg, 0.164 mmol) was crystallized from a saturated *n*-hexane solution at −35 °C as orange-yellow crystals in 90% yield (48.5 mg, 0.147 mmol) after 3 weeks.

*[Ti(CAT){OSi(OtBu)$_3$}$_2$(HNMe$_2$)$_2$]$_2$ (**1c**).* Tris(*tert*-butoxy)silanol (217 mg, 0.820 mmol), dissolved in 1 mL of *n*-hexane, was added dropwise to a stirred suspension of **1a** (100 mg, 0.410 mmol) in 1 mL of *n*-hexane. A color change from yellow to dark red was observed. After 21 h of stirring at ambient temperature, a yellow powder had precipitated. Upon the removal of solvent residues under vacuum, product **1c** was obtained as an orange-red powder in 97% yield (308 mg, 0.398 mmol). Elem anal. Calcd for $C_{34}H_{72}N_2O_{10}Si_2Ti$ (M = 772.99 g mol^{-1}): C, 52.83; H, 9.39; N, 3.62. Found: C, 52.78; H, 9.37; N, 3.21. ^1H NMR (400 MHz, C_6D_6): δ 1.39 (s, 2H, 2 × Me_2N-*H*), 1.47 (s, 54H, 2 × OSi(OC-Me_3)$_3$), 2.54 (s, 11H, HN-Me_2), 6.64 (m, 2H, 2 × Ar-*H*), 6.82 (m, 2H, 2 × Ar-*H*), 7.16 (s, 3H, C_6D_6). DRIFTS (KBr, cm^{-1}): 3239(w) [ν(R_2N–H)], 3058(w) [ν(Ar–H)], 2972–2798(w-m) [ν(C–H), CH_3, CH_2], 1575(w) [ν(C=C), aromatic ring + ν(Ti–O–C)], 1479(m), 1470(m), 1415(w), 1388(m), 1364(m) [δ(C–H), CH_3, CH_2], 936(s) [$\nu_S(NC_2)$], 739(m) [ν(Ti–O–C)]. Crystallization of powdery **1c** was performed from a saturated *n*-hexane solution at −78 °C, yielding after 3 weeks very temperature-sensitive orange-red crystals in extremely low yield but suitable for XRD analysis.

*[Ti(CATtBu$_2$-3,6)(NMe$_2$)$_2$]$_2$ (**2a**).* The synthesis was performed as described in the literature:[1] 3,6-di-*tert*-butylcatechol (209 mg, 0.942 mmol), diluted in 2 mL of *n*-hexane was added dropwise to a stirred solution of $Ti(NMe_2)_4$ (211 mg, 0.942 mmol) in 3 mL of *n*-hexane. A color change from yellow to dark red was observed, accompanied by pronounced warming. After 2 h of stirring at ambient temperature, a red-brown solution was obtained, which was directly used for the synthesis of **2b**.

*Ti(CATtBu$_2$-3,6)(OCH$_2$tBu)$_2$(HNMe$_2$)$_2$ (**2b**).* Neopentanol (167 mg, 1.88 mmol), dissolved in 2 mL of *n*-hexane, was added dropwise to a stirred solution of **2a** in 5 mL of *n*-hexane. After 1 h stirring at ambient temperature and subsequent removal of solvent residues under vacuum, the crude product **2b** was obtained as a reddish powder. Recrystallization was performed twice from *n*-hexane at −35 °C, producing single crystals within 1 week. The overall crystal yield was 88% (443 mg, 0.833 mmol). Elem anal. Calcd for $C_{28}H_{54}N_2O_4Ti$ (M = 532.63 g mol^{-1}): C, 63.14; H, 10.60; N, 5.26. Found: C, 62.97; H, 10.47; N, 5.36. ^1H NMR (400 MHz, C_6D_6): δ 0.98 (s, 18H, 2 ×

https://doi.org/10.1021/acs.inorgchem.2c02838
Inorg. Chem. 2023, 62, 715–729

OCH_2CMe_3, 1.67 (s, 18H, 2 × Ar-CMe_3), 2.11 (bs, 12H, HN-Me_2), 4.30 (s, 4H, 2 × O-CH_2CMe_3), 6.86 (s, 2H, 2 × Ar-*H*), 7.16 (s, 2H, C_6D_6). ^{13}C NMR (100 MHz, C_6D_6): δ 26.9 (OCH_2C-Me_3), 30.3 (Ar-CMe_3), 34.4 (Ar-CMe_3 and OCH_2-CMe_3), 40.0 (HN-Me_2), 115.4 (aromatic γ-*C*), 128.0 (C_6D_6), 130.8 (aromatic β-*C*), 158.3 (aromatic α-*C*). DRIFTS (KBr, cm^{-1}): 3294(w) [ν(R_2N−H)], 3074(w) [ν(Ar−H)], 2953−2820(s-m) [ν(C−H), CH_3, CH_2], 1575(w) [ν(C═C), aromatic ring + ν(Ti−O−C)], 1481(m), 1464(m), 1410(w), 1392(s), 1350(m) [δ(C−H), CH_3, CH_2], 749(m) [ν(Ti−O−C)].

Ti(CATtBu$_2$-3,6)(OSi(OtBu)$_3$)$_2$(HNMe$_2$)$_2$ ***(2c)***. Tris(*tert*-butoxy)-silanol (64.5 mg, 0.244 mmol), dissolved in 1.5 mL *n*-hexane, was added dropwise to a stirred orange solution of **2b** (65.0 mg, 0.122 mmol) in 1.5 mL of *n*-hexane. A color change to dark red was observed, accompanied by pronounced warming. After 1 h of stirring at ambient temperature and removal of solvent residues under vacuum, the crude product **2c** was obtained as a red-brown wax in 95% yield (102 mg, 0.115 mmol). Recrystallization from *n*-hexane at −35 °C gave dark-red crystals in 28% yield (30.0 mg, 0.0342 mmol) after 3 days. Elem anal. Calcd for $C_{42}H_{88}N_2O_{10}Si_2Ti$ (M = 885.21 g mol^{-1}): C, 56.99; H, 10.02; N, 3.16. Found: C, 56.74; H, 9.88; N, 3.13. ^{1}H NMR (400 MHz, C_6D_6): δ 1.45 (s, 54H, 2 × OSi(OC-Me_3)$_3$), 1.59 (s, 18H, 2 × ArC-Me_3), 2.56 (bs, 11H, HN-Me_2), 6.80 (s, 2H, 2 × Ar-*H*), 7.16 (s, 4H, C_6D_6). DRIFTS (KBr, cm^{-1}): 3210(w) [ν(R_2N−H)], 3075(w) [ν(Ar−H)], 2971−2796(w-m) [ν(C−H), CH_3, CH_2], 1580(vw) [ν(CC), aromatic ring + ν(Ti−O−C)], 1466(m), 1388(m), 1363(m) [δ(C−H), CH_3, CH_2], 933(s) [ν_s(NC_2)], 731(w) [ν(Ti−O−C)].

[Ti(OCH$_2$tBu)$_4$]$_2$ ***(3)***. Neopentanol (374 mg, 4.24 mmol), dissolved in 2 mL of *n*-hexane, was added dropwise to a stirred solution of Ti(NMe_2)$_4$ (238 mg, 1.06 mmol) in 2 mL of *n*-hexane. After 1 h stirring at ambient temperature and upon reduction of the solvent under vacuum, the product was crystallized from *n*-hexane at −35 °C within 1 week. The overall crystal yield was 86% (363 mg, 0.916 mmol). Elem anal. Calcd for $C_{20}H_{44}O_4Ti$ (M = 396.44 g mol^{-1}): C, 60.60; H, 11.19. Found: C, 60.28; H, 11.13. ^{1}H NMR (400 MHz, C_6D_6): δ 1.00 (s, 36H, 4 × OCH_2C-Me_3), 4.07 (s, 8H, 4 × O-CH_2CMe_3), 7.16 (s, 2H, C_6D_6). ^{13}C NMR (100 MHz, C_6D_6): δ 26.4 (OCH_2CMe_3), 34.1 (OCH_2-CMe_3), 86.4 (O-CH_2CMe_3), 128.1 (C_6D_6). DRIFTS (KBr, cm^{-1}): 2951−2838(s-m) [ν(C−H), CH_3, CH_2], 1477(m), 1462(m), 1392(m), 1360(m) [δ(C−H), CH_3, CH_2]. Cell parameters: a = 11.44(9) Å, b = 12.17(9) Å, c = 19.14(17) Å, α = 84.49(16)°, β = 77.66(18)°, and γ = 62.1(2)°.[55]

Grafting Reactions. Hybrid Materials: MA = Material Aqueous, MS = Material Sequential Grafting, and MC = Material Consecutive Grafting. *KIT-6 (M1).* The material was used as described in the literature[40] with the following characterization results. PXRD: 2θ = 0.91°, 1.65°; d_{211} = 9.71 nm; a = 23.8 nm. N_2 physisorption: a_S(BET) = 620 m^2 g^{-1}; $V_{P,cum.des}$ = 1.19 cm^3 g^{-1}; $d_{P,ads.}$ = 8.5 nm. DRIFTS (KBr, [cm^{-1}]): 3745(m) [ν(SiOH)], 1051(vs) [ν_{as}(Si−O−Si)], 814(vs) [ν_s(Si−O−Si)], 444(vs) [ν_s(O−Si−O)].

HN(SiHMe$_2$)$_2$@[KIT-6] ***(M1a)***. The material was used as described in the literature[40] with the following characterization results. N_2 physisorption: a_S(BET) = 500 m^2 g^{-1}; $V_{P,cum.des}$ = 0.97 cm^3 g^{-1}; $d_{P,ads.}$ = 7.2 nm. Elem anal. Calcd: C, 4.46; H, 0.50; N, 0.03. δ(SiOH) = 2.08 mmol g^{-1}. DRIFTS (KBr, cm^{-1}): 2966(w) [ν(C−H), CH_3, CH_2], 2154(m) [ν(Si−H)], 1051(vs) [ν_{as}(Si−O−Si)], 908(s) [δ(O−Si−H)], 814(vs) [ν_s(Si−O−Si)], 436(vs) [ν_s(O−Si−O)].

Ti(OiPr)$_4$@[KIT-6] ***(M1A1)***. Ti(O*i*Pr)$_4$ (490 mg, 2.53 mmol), dissolved in 4 mL of *n*-hexane, was added dropwise to a stirred suspension of KIT-6 (**M1**; 701 mg, 1.46 mmol of accessible surface OH groups, related to δ(SiOH) = 2.08 mmol g^{-1}) in 6 mL of *n*-hexane. The mixture was stirred at ambient temperature for 24 h. The solid was collected by centrifugation and washed three times with *n*-hexane (2 mL each). The resulting solid was dispersed in fresh *n*-hexane, transferred to a vial, and dried in a vacuum to constant weight changes, yielding 722 mg of the material **M1A1**. **M1A1** was degassed and further kept in the physisorption device (p = 10^{-3} mbar) at 100 °C for 3 h before elemental analysis, DRIFTS, and N_2 physisorption measurements. Elem anal. Found: C, 9.76; H, 1.92; N, 0.01. N_2 physisorption: a_S(BET) = 395 m^2 g^{-1}; $V_{P,cum.des}$ = 0.809 cm^3 g^{-1}; $d_{P,ads}$ = 6.7 nm. DRIFTS (KBr, cm^{-1}): 2973−2874(w-m) [ν(C−H), CH_3, CH_2], 737(w) [ν(Ti−O−C)].

Ti(OH)$_x$@[KIT-6] ***(M1A2)***. **M1A1** (576 mg, 1.20 mmol of accessible surface OH groups, related to δ (SiOH) = 2.08 mmol g^{-1}) were hydrolyzed by exposure to air humidity during calcination (with the following temperature program: room temperature (rt) → 100 °C within 1 h, hold 100 °C for 1 h, heating to 500 °C within 3.5 h, hold 500 °C for 4 h) to yield 545 mg of a white powder. A total of 535 mg of the calcined hydrolyzed product was further degassed and kept in the physisorption device (p = 10^{-3} mbar) at 250 °C for 2 h before elemental analysis, DRIFTS, and N_2 physisorption measurements. Elem anal. Found: C, 0.09; H, 0.43; N, 0.20; Ti, 5.07. N_2 physisorption: a_S(BET) = 552 m^2 g^{-1}; $V_{P,cum.des}$ = 1.13 cm^3 g^{-1}; $d_{P,ads.}$ = 8.0 nm. DRIFTS (KBr, cm^{-1}): 3743(w) [ν(SiO−H)], 1059(vs) [ν_{as}(Si−O−Si)], 447(vs) [ν_s(O−Si−O)].

HN(SiHMe$_2$)$_2$@Ti(OH)$_x$@[KIT-6] ***(M1A2a)***. Calcined material **M1A1** (70.1 mg, 0.146 mmol of accessible surface OH groups, related to δ(SiOH) = 2.08 mmol g^{-1}), suspended in 1 mL of *n*-hexane, were stirred in a vial. A solution of HN($SiHMe_2$)$_2$ (58.2 mg, 0.437 mmol) in 2 mL of *n*-hexane was added. The mixture was stirred at rt for 24 h. The solid was collected by centrifugation and washed three times with *n*-hexane (2 mL each). The final solid was dispersed in fresh *n*-hexane and transferred into a vial and dried in a vacuum until no weight change occurred any more to yield 63.4 mg of the sample material **M1A2a**. **M1A2a** was degassed and further dried in the physisorption device (p = 10^{-3} mbar) at 110 °C for 3 h before elemental analysis, DRIFTS, and N_2 physisorption. N_2 physisorption: a_S(BET) = 407 m^2 g^{-1}; $V_{P,cum.des.}$ = 0.88 cm^3 g^{-1}; $d_{P,ads.}$ = 7.0 nm. Elem anal. Calcd: C, 4.03; H, 1.20; N, 0.24. δ(TiOH) = 1.86 mmol g^{-1}. DRIFTS (KBr, cm^{-1}): 2964(w) [ν(C−H), CH_3, CH_2], 2151(w) [ν(Si−H)], 1080(s) [ν_{as}(Si−O−Si)], 910(m) [δ(O−Si−H)], 805(m) [ν_s(Si−O−Si)], 442(s) [ν_s(O−Si−O)].

H$_2$CATtBu$_2$-3,6@Ti(OH)$_x$@[KIT-6] ***(M1A3)***. 3,6-Di-*tert*-butylcatechol (83.4 mg, 0.375 mmol) was dissolved in a mixture of 50 mL of a 10 mM aqueous HCl solution and 5 mL of EtOH. Upon the addition of **M1A2** (270 mg, 0.502 mmol of accessible surface OH groups, related to δ(TiOH) = 1.86 mmol g^{-1}; or 0.562 mmol of accessible surface OH groups, related to δ(SiOH) = 2.08 mmol g^{-1}), an immediate color change from white to orange-brown was observed. After 2 h stirring (600 rpm) at 60 °C, the suspension became dark brown. After 24 h of stirring (600 rpm) at ambient temperature, the solid was collected by centrifugation, washed three times with an EtOH/water mixture (1:1), and washed a further six times with EtOH. The final solid was transferred to a vial and dried in a vacuum overnight to yield 263 mg of the material **M1A3**. Elem anal. Found: C, 4.92; H, 1.04; N, 0.16; Ti, 3.53. N_2 physisorption: a_S(BET) = 552 m^2 g^{-1}; $V_{P,cum.des}$ = 1.08 cm^3 g^{-1}; $d_{P,ads.}$ = 8.0 nm. DRIFTS (KBr, cm^{-1}): 3742(w) [ν(SiO−H)], 3502(broad, w) [ν(O−H with hydrogen bonds], 2955(w) [ν(C−H), CH_3, CH_2], 1063(vs) [ν_{as}(Si−O−Si)], 802(m) [ν_s(Si−O−Si)], 443(vs) [ν_s(O−Si−O)]. ^{13}C NMR (75 MHz, CP/MAS, 10 kHz rotation): δ 15.8, 27.9 (ArC-Me_3), 59.2.

Ti(OCH$_2$tBu)$_4$@[KIT-6] ***(M1S1)***. Neopentoxide **3** (345 mg, 0.883 mmol of accessible surface OH groups, related to δ(SiOH) = 2.08 mmol g^{-1}), dissolved in 4 mL of *n*-hexane, was added dropwise to a stirred suspension of KIT-6 (**M1**; 420 mg, 0.883 mmol) in 2 mL of *n*-hexane. After 24 h stirring at ambient temperature, the solid was collected by centrifugation and washed with *n*-hexane three times. The final solid was transferred to a vial and dried in a vacuum at ambient temperature to yield 517 mg of the material **M1S1**. Elem anal. Found: C, 12.66; H, 2.36; N, 0.02; Ti, 3.74. N_2 physisorption: a_S(BET) = 400 m^2 g^{-1}; $V_{P,cum.des}$ = 0.769 cm^3 g^{-1}; $d_{P,ads}$ = 6.2 nm. DRIFTS (KBr, cm^{-1}): 3701(w) [ν(SiO−H)], 2957−2870(w) [ν(C−H), CH_3, CH_2], 1480(w), 1396 (w), 1365 (w) [δ(C−H), CH_3, CH_2], 1063(vs) [ν_{as}(Si−O−Si)], 799(w) [ν_s(Si−O−Si)], 711(w) [ν(Ti−O−C)], 448(s) [ν_s(O−Si−O)]. ^{13}C NMR (75 MHz, CP/MAS, 10 kHz rotation): δ 25.3 (OCH_2C-Me_3), 33.4 (OCH_2-CMe_3), 73.5 (HO-CH_2CMe_3), 88.8 (O-CH_2CMe_3).

H$_2$CATtBu$_2$-3,6@Ti(OCH$_2$tBu)$_4$@[KIT-6] ***(M1S2)***. 3,6-Di-*tert*-butylcatechol (120 mg, 0.540 mmol), dissolved in 3 mL of *n*-hexane, was

https://doi.org/10.1021/acs.inorgchem.2c02838
Inorg. Chem. 2023, 62, 715−729

added dropwise to a stirred suspension of **M1S1** (343 mg, 0.713 mmol of accessible surface OH groups, related to δ(SiOH) = 2.08 mmol g^{-1}) in 2 mL of *n*-hexane. After 24 h stirring at ambient temperature, the brown solid was collected by centrifugation and washed with *n*-hexane until the supernatant solution became colorless. The final solid was transferred to a vial and dried in a vacuum at ambient temperature to yield 294 mg of the material **M1S2**. Elem anal. Found: C, 13.12; H, 2.04; N, 0.23; Ti, 1.47. N_2 physisorption: a_S(BET) = 468 m^2 g^{-1}; $V_{P,cum.des}$ = 0.929 cm^3 g^{-1}; $d_{P,ads}$ = 6.6 nm. DRIFTS (KBr, cm^{-1}): 3705(w) [ν(SiO−H)], 3573(w) [ν(ArO−H)], 3089(vw) [ν(Ar−H)], 2959−2873(w) [ν(C−H), CH_3, CH_2], 1481(w), 1417(w), 1397 (w), 1367 (w) [δ(C−H), CH_3, CH_2], 1065(vs) [ν_{as}(Si−O−Si)], 810(m) [ν_s(Si−O−Si)], 717(w) [ν(Ti−O−C)], 440(s) [ν_s(O−Si−O)]. ^{13}C NMR (75 MHz, CP/MAS, 10 kHz rotation): δ 24.7 (OCH_2C-Me_3), 28.3 (ArC-Me_3), 31.6 (OCH_2-CMe_3), 32.8 (Ar-CMe_3), 73.7 (HO-CH_2CMe_3), 117.5 (aromatic γ-C), 132.8 (aromatic β-C), 144.5 + 157.8 (aromatic α-C).

*Ti(CATtBu$_2$-3,6)(OCH$_2$tBu)$_2$(HNMe$_2$)$_2$@[KIT-6] (**M1C1**).* Complex **2b** (122 mg, 0.229 mmol), dissolved in 8 mL of *n*-hexane, was added dropwise to a stirred suspension of KIT-6 (**M1**) (110 mg, 0.229 mmol of accessible surface OH groups, related to δ(SiOH) = 2.08 mmol g^{-1}) in 2 mL of *n*-hexane. After 24 h stirring at ambient temperature, the orange solid was collected by centrifugation and washed with *n*-hexane three times. The final solid was transferred to a vial and dried in a vacuum at ambient temperature to yield 113 mg of the material **M1C1**. Elem anal. Found: C, 15.77; H, 2.54; N, 1.59; Ti, 2.82. N_2 physisorption: a_S(BET) = 395 m^2 g^{-1}; $V_{P,cum.des}$ = 0.713 cm^3 g^{-1}; $d_{P,ads}$ = 6.0 nm. DRIFTS (KBr, [cm^{-1}]): 3694(w) [ν(SiO−H)], 3295(w) [ν(R_2N−H)], 3090(vw) [ν(Ar−H)], 2956−2870(w) [ν(C−H), CH_3, CH_2], 1603(vw) [ν(C═C)], 1468(w), 1395 (w), 1366 (w) [δ(C−H), CH_3, CH_2], 1061(s) [ν_{as}(Si−O−Si)], 812(m) [ν_s(Si−O−Si)], 704(w) [ν(Ti−O−C)], 593(w-m) [ν(Ti−N-R)], 444(s) [ν_s(O−Si−O)]. ^{13}C NMR (75 MHz, CP/MAS, 10 kHz rotation): δ 25.3 (OCH_2C-Me_3), 28.4 (ArC-Me_3), 32.9 + 36.2 (OCH_2-CMe_3) + (Ar-CMe_3), 37.9 + 40.5 (HN-Me_2) 74.2 (HO-CH_2CMe_3)), 115.8 (aromatic γ-C), 131.0 (aromatic β-C), 157.9 + 160.0 (aromatic α-C).

*m-TiO$_2$ (**M2**).* Triblock copolymer Pluronic P123 (1.00 g, 0.172 mmol) and a solution of 37% HCl (2.00 g, 28.4 mmol) in ethanol (20.0 g, 434 mmol) were stirred (440 rpm) at ambient temperature until P123 had dissolved completely. While cooling the solution with an ice bath, Ti(O*i*Pr)$_4$ (3.00 g, 10.6 mmol) was added dropwise. Then deionized water (2,00 g, 111 mmol) was added slowly. After removal of the ice bath, the mixture was stirred at ambient temperature for 30 min and was then transferred to a beaker covered with perforated aluminum foil, which was put under an active vacuum inside a desiccator overnight. The aluminum foil was removed and the beaker, containing a clear viscose gel, was put into an oven at 40 °C for 24 h (evaporation-induced self-assembly, EISA). Deionized water (2.00 mL) and a stirring bar were added to the clear gel (slightly yellowish), which was followed by the dropwise addition of a 25% ammonium hydroxide solution, until the stirring bar was not able to move through the solid white cake any more. Then deionized water (5 mL) was added again, and the dropwise addition of an ammonium hydroxide solution was continued until a total volume of 10 mL of a 25% ammonium hydroxide solution was in the reaction mixture to ensure that *n*(ammonium hydroxide) = 4 × *n*[Ti(O*i*Pr)$_4$]. The mixture was stirred (700 rpm) at ambient temperature for 2 h, while the beaker was covered with a watchglass. The solid was collected by centrifugation, washed three times with water, and washed a further five times with EtOH (20k rpm for 30 s each). The solid was transferred to a ceramic crucible and dried in an oven at 40 °C overnight. The vanilla-colored solid was pestled and tempered with a heating rate of 1 °C min^{-1}, holding at 150 °C and at 350 °C for 1 h, respectively. The organic residues were removed by calcination of the tempered, vanilla-colored powder at 450 °C for 4 h to obtain 550 mg of m-TiO_2 as a white powder. The calcined material was analyzed by PXRD and N_2 physisorption as well as DRIFT spectroscopy. Prior to the N_2 physisorption measurement, the sample was degassed at 250 °C for 4 h in the physisorption device. Small-angle PXRD: 2θ = 0.54°, *d* = 16.3 nm; 2θ = 0.69°, *d* = 12.7 nm. Wide-angle PXRD: 2θ = 25.4° (101); 37.9° (004); 48.1° (200); 54.0° (105); 55.1° (211); 62.7°; anatase. Elem anal. Found: C, 0.03; N, 0.02; H, 0.00. N_2 physisorption: a_S(BET) = 93 m^2 g^{-1}; $V_{P,cum.des}$ = 0.189 cm^3 g^{-1}; $d_{P,ads}$ = 7.0 nm. The calcined and degassed sample was denoted as **M2** and stored in an argon-filled glovebox for use. DRIFTS (KBr, cm^{-1}): 3675(w) [ν(TiO−H)]; 3365(broad, w) [ν(TiO−H with hydrogen bonds)].

*HN(SiHMe$_2$)$_2$@[m-TiO$_2$] (**M2a**).* Mesoporous titania **M2** (50.0 mg, 0.0381 mmol of accessible surface OH groups, related to δ(TiOH) = 0.762 mmol g^{-1}) was suspended in 2 mL of dry *n*-hexane in a vial. A solution of 1,1,3,3-tetramethyldisilazane (100 mg, 0.750 mmol) in 1 mL of dry *n*-hexane was added. The mixture was stirred at ambient temperature for 19 h. The solid was collected by centrifugation and washed four times with *n*-hexane (2 mL each). The final solid was dispersed in fresh *n*-hexane, transferred to a vial, and dried in a vacuum to constant weight to yield 40.3 mg of the material **M2a**. **M2a** was degassed and further kept for 3 h before elemental analysis, DRIFTS and N_2 physisorption measurements. Elem anal. Found: C, 1.75; H, 0.59. δ(TiOH) = 0.762 mmol g^{-1}; α(TiOH) = 4.92 OH groups nm^{-2}. N_2 physisorption: a_S(BET) = 31 m^2 g^{-1}; $V_{P,cum.des}$ = 0.093 cm^3 g^{-1}; $d_{P,ads}$ = 5.8 nm. DRIFTS (KBr, cm^{-1}): 3365(broad, w) [ν(TiO−H with hydrogen bonds)], 2959 + 2923(w) [ν(C−H)], 2360 + 2337(w) [ν(Si−H)].

*H$_2$CATtBu$_2$-3,6@[m-TiO$_2$] (**M2A1**).* 3,6-Di-*tert*-butylcatechol (10.2 mg, 0.0457 mmol of accessible surface OH groups, related to δ(TiOH) = 0.762 mmol g^{-1}) was dissolved in a mixture of 1 mL of a 10 mM aqueous HCl solution and 1 mL of EtOH. The solution was added to a suspension of **M2** (90.0 mg, 0.0686 mmol) in 5.1 mL of a 10 mM aqueous HCl solution. After 2 h of stirring (600 rpm) at 60 °C and a further 24 h of stirring (600 rpm) at ambient temperature, the solid was collected by centrifugation and washed twice with EtOH and water, consecutively. The final solid was transferred to a vial and dried in a vacuum overnight to yield 77.9 mg of the material **M2A1**. **M2A1** was degassed and further dried in the physisorption device (p = 10^{-3} mbar) at 25 °C for 4 h before DRIFTS and N_2 physisorption measurements. The weight of the material **M2A1** after degassing was 64 mg. Elem anal. Found: C, 0.65; H, 0.32; N, 0.04. N_2 physisorption: a_S(BET) = 73 m^2 g^{-1}; $V_{P,cum.des}$ = 0.158 cm^3 g^{-1}; $d_{P,ads}$ = 7.1 nm. DRIFTS (KBr, cm^{-1}): 3446 (broad, w) [ν(TiO−H with hydrogen bonds)].

*Ti(CATtBu$_2$-3,6)(OCH$_2$tBu)$_2$(HNMe$_2$)$_2$@[m-TiO$_2$] (**M2C1**).* Compound **2b** (40.6 mg, 0.0762 mmol), dissolved in 3 mL of *n*-hexane, was added dropwise to a stirred suspension of **M2** (100 mg, 0.0762 mmol of accessible surface OH groups, related to δ(TiOH) = 0.762 mmol g^{-1}) in 1 mL of *n*-hexane. The suspension turned red-brown. After 20 h of stirring at ambient temperature, the light-brown solid was collected by centrifugation and washed with *n*-hexane six times. The final solid was transferred to a vial and dried in a vacuum at ambient temperature to yield 91 mg of the material **M2C1**. **M2C1** was degassed and further kept in the physisorption device (p = 10^{-3} mbar) at 25 °C for 4 h before DRIFTS and N_2 physisorption measurements. Elem anal. Found: C, 2.41; H, 0.63; N, 0.39. N_2 physisorption: a_S(BET) = 44 m^2 g^{-1}; $V_{P,cum.des}$ = 0.122 cm^3 g^{-1}; $d_{P,ads}$ = 5.7 nm. DRIFTS (KBr, cm^{-1}): 3252(vw) [ν(Ar−H)], 2955−2869(w) [ν(C−H), CH_3, CH_2], 1456(vw) [ν(C═C)].

Electronic and Optical Investigations. XPS and UPS measurements were performed in an ultrahigh-vacuum (UHV) system consisting of an analysis chamber [base pressure = (2−4) × 10^{-10} mbar] equipped with a SPECS Phoibos 150 hemispherical electron analyzer, a monochromatic Al Kα source (SPECS Focus 500, 26 mA, 12 kV, spot size: 1 mm × 0.5 mm), and a high-flux helium discharge lamp [UVS 300 SPECS, He(I) = 21.22 eV]. The spectrometer dispersion was adjusted to give a binding energy of 368.21 eV for the Ag $3d_{5/2}$ line of metallic silver, following SPECS specifics. The binding energy was calibrated by using the In $3d_{5/2}$ XPS signal at 443.8 eV. The energy resolution was 0.4 eV. All photoemission measurements were performed in normal emission.

The sample preparation for XPS and UPS was carried out in a glovebox. The powders were embedded in an indium foil by pressing

https://doi.org/10.1021/acs.inorgchem.2c02838
Inorg. Chem. 2023, 62, 715−729

them onto the indium surface. The samples were transported to the UHV system inside an argon-filled shuttle, which was opened only for transferring the sample into the nitrogen-floated transfer chamber of the UHV system (maximum 1−2 min), where it was left to degas overnight, before it was transferred to the analysis chamber. Survey and detailed XPS spectra were measured with a dwell time of 0.1 s, an electron pass energy of 50, a 0.4 eV step width (scan window of +1100 to −5 eV), and 20 eV, 0.1 eV step width (a C 1s scan window of 275−295 eV, a O 1s scan window of 520−550 eV, and a Ti 2p scan window of 440−485 eV), respectively. The number of scans was variable depending on the statics. No beam-induced degradation of the samples was observed on the time scale of all discussed experiments.

The measurements could be performed without any charge compensation, taking advantage of a very low amount of point defects and contaminants. In fact, the XPS lines are not broadened as expected when bad conductive materials are measured.[101]

UV/vis spectroscopy measurements were performed under ambient conditions on a PerkinElmer Precisely Lambda 1050 UV/vis/NIR spectrometer using two setups to allow for a comparison of the data to exclude any artifacts due to potential sample degradation in ambient conditions (the isolated molecular complex **2b** is sensitive to humidity). The first setup consists of an Ulbricht sphere with two detectors (a photomultiplier for UV/vis and a 150 mm InGaAs sphere for NIR) and two lamps for excitation (deuterium and tungsten). A Teflon strip (Spectralon optical Teflon, LabSphere, reflectivity >99%) was placed in a Suprasil 1 mm cuvette, where a 2.5 mm hole was pierced. The sample powders were filled in under ambient conditions. The cuvette was covered with a Suprasil faceplate. The sandwiched system was placed in a sample holder on the back end of the Ulbricht sphere above the internal reference (also Spectralon optical Teflon). Measurements were performed from 2500 to 200 nm with 2 nm slit width and variable amplification (dependent on the light intensity) in order to avoid artifacts when changing from NIR to UV/vis. The second experiment was performed with a Praying Mantis setup with one more detector (PbS for MIR), which enables measurements of up to 3000 nm. The sample holder was half-filled with a Spectralon strip and topped off with a sample powder. The sample holder was positioned in the center of the measurement chamber (as is known for DRIFTS measurements), measurements were performed from 2500 to 200 nm, and the data were reported with respect to the internal reference ($BaSO_4$). The concomitance of the results obtained with the two setups indicates that the materials are not sensitive to humidity.

■ ASSOCIATED CONTENT

Supporting Information

The Supporting Information is available free of charge at https://pubs.acs.org/doi/10.1021/acs.inorgchem.2c02838.

> Supporting figures, detailed crystallographic data including PXRD data of the materials, spectroscopic data (NMR, FTIR, XPS, UV/vis, and UPS), N_2 physisorption, and elemental analysis including calculation procedures (PDF)

Accession Codes

CCDC 2165168−2165171 contain the supplementary crystallographic data for this paper. These data can be obtained free of charge via www.ccdc.cam.ac.uk/data_request/cif, or by emailing data_request@ccdc.cam.ac.uk, or by contacting The Cambridge Crystallographic Data Centre, 12 Union Road, Cambridge CB2 1EZ, UK; fax: +44 1223 336033.

■ AUTHOR INFORMATION

Corresponding Authors

Reiner Anwander − *Institut für Anorganische Chemie, Eberhard Karls Universität Tübingen, Tübingen 72076, Germany*; orcid.org/0000-0002-1543-3787; Email: reiner.anwander@uni-tuebingen.de

Maria Benedetta Casu − *Institut für Physikalische und Theoretische Chemie, Eberhard Karls Universität Tübingen, Tübingen 72076, Germany*; orcid.org/0000-0002-5659-7040; Email: benedetta.casu@uni-tuebingen.de

Authors

Andrea Sonström − *Institut für Anorganische Chemie, Eberhard Karls Universität Tübingen, Tübingen 72076, Germany*

Barbara Boldrini − *Lehr- und Forschungszentrum "Process Analysis and Technology", Fakultät Angewandte Chemie, Hochschule Reutlingen, Reutlingen 72762, Germany*

Daniel Werner − *Institut für Anorganische Chemie, Eberhard Karls Universität Tübingen, Tübingen 72076, Germany*

Cäcilia Maichle-Mössmer − *Institut für Anorganische Chemie, Eberhard Karls Universität Tübingen, Tübingen 72076, Germany*; orcid.org/0000-0001-7638-1610

Karsten Rebner − *Lehr- und Forschungszentrum "Process Analysis and Technology", Fakultät Angewandte Chemie, Hochschule Reutlingen, Reutlingen 72762, Germany*

Complete contact information is available at: https://pubs.acs.org/10.1021/acs.inorgchem.2c02838

Notes

The authors declare no competing financial interest.

■ ACKNOWLEDGMENTS

We thank ams Sensors Germany GmbH for financial support, Dr. Regine Herbst-Irmer for her assistance in solving the twin structure of **2b**, and Alexandros Mortis for assistance with the NMR spectra.

■ REFERENCES

(1) Fujishima, A.; Honda, K. Electrochemical Photolysis of Water at a Semiconductor Electrode. *Nature* **1972**, *238*, 37−38.

(2) Chen, X.; Mao, S. S. Titanium Dioxide Nanomaterials: Synthesis, Properties, Modifications, and Applications. *Chem. Rev.* **2007**, *107*, 2891−2959.

(3) Chen, H.; Nanayakkara, C. E.; Grassian, V. H. Titanium Dioxide Photocatalysis in Atmospheric Chemistry. *Chem. Rev.* **2012**, *112*, 5919−5948.

(4) Jing, L. Q.; Zhou, W.; Tian, G. H.; Fu, H. G. Surface tuning for oxide-based nanomaterials as efficient photocatalysts. *Chem. Soc. Rev.* **2013**, *42*, 9509−9549.

(5) Chen, X.; Selloni, A. Introduction: Titanium Dioxide (TiO_2) Nanomaterials. *Chem. Rev.* **2014**, *114*, 9281−9282.

(6) Fattakhova-Rohlfing, D.; Zaleska, A.; Bein, T. Three-Dimensional Titanium Dioxide Nanomaterials. *Chem. Rev.* **2014**, *114*, 9487−9558.

(7) Kapilashrami, M.; Zhang, Y.; Liu, Y.-S.; Hagfeldt, A.; Guo, J. Probing the Optical Property and Electronic Structure of TiO_2 Nanomaterials for Renewable Energy Applications. *Chem. Rev.* **2014**, *114*, 9662−9707.

(8) Dahl, M.; Liu, Y.; Yin, Y. Composite Titanium Dioxide Nanomaterials. *Chem. Rev.* **2014**, *114*, 9853−9889.

(9) Ma, Y.; Wang, X.; Jia, Y.; Chen, X.; Han, H.; Li, C. Titanium Dioxide-Based Nanomaterials for Photocatalytic Fuel Generations. *Chem. Rev.* **2014**, *114*, 9987−10043.

(10) Moser, J.; Punchihewa, S.; Infelta, P. P.; Graetzel, M. Surface complexation of colloidal semiconductors strongly enhances interfacial electron-transfer rates. *Langmuir* **1991**, *7*, 3012−3018.

(11) Connor, P. A.; Dobson, K. D.; McQuillan, A. J. New Sol-Gel Attenuated Total Reflection Infrared Spectroscopic Method for

Analysis of Adsorption at Metal Oxide Surfaces in Aqueous Solutions. Chelation of TiO_2, ZrO_2, and Al_2O_3 Surfaces by Catechol, 8-Quinolinol, and Acetylacetone. *Langmuir* **1995**, *11*, 4193−4195.
(12) Redfern, P. C.; Zapol, P.; Curtiss, L. A.; Rajh, T.; Thurnauer, M. C. Computational Studies of Catechol and Water Interactions with Titanium Oxide Nanoparticles. *J. Phys. Chem. B* **2003**, *107*, 11419−11427.
(13) Angelome, P. C.; Soler-Illia, G. Organically modified transition-metal oxide mesoporous thin films and xerogels. *Chem. Mater.* **2005**, *17*, 322−331.
(14) Lana-Villarreal, T.; Rodes, A.; Pérez, J. M.; Gómez, R. A Spectroscopic and Electrochemical Approach to the Study of the Interactions and Photoinduced Electron Transfer between Catechol and Anatase Nanoparticles in Aqueous Solution. *J. Am. Chem. Soc.* **2005**, *127*, 12601−12611.
(15) Tachikawa, T.; Takai, Y.; Tojo, S.; Fujitsuka, M.; Majima, T. Probing the Surface Adsorption and Photocatalytic Degradation of Catechols on TiO2 by Solid-State NMR Spectroscopy. *Langmuir* **2006**, *22*, 893−896.
(16) Jankovic, I. A.; Saponjic, Z. V.; Comor, M. I.; Nedeljković, J. M. Surface Modification of Colloidal TiO_2 Nanoparticles with Bidentate Benzene Derivatives. *J. Phys. Chem. C* **2009**, *113*, 12645−12652.
(17) Janković, I. A.; Šaponjić, Z. V.; Džunuzović, E. S.; Nedeljković, J. M. New Hybrid Properties of TiO_2 Nanoparticles Surface Modified With Catecholate Type Ligands. *Nanoscale Res. Lett.* **2010**, *5*, 81.
(18) Benedict, J. B.; Coppens, P. The Crystalline Nanocluster Phase as a Medium for Structural and Spectroscopic Studies of Light Absorption of Photosensitizer Dyes on Semiconductor Surfaces. *J. Am. Chem. Soc.* **2010**, *132*, 2938−2944.
(19) Liu, L.-M.; Li, S.-C.; Cheng, H.; Diebold, U.; Selloni, A. Growth and Organization of an Organic Molecular Monolayer on TiO_2: Catechol on Anatase (101). *J. Am. Chem. Soc.* **2011**, *133*, 7816−7823.
(20) Luo, L.; Guo, Y.; Yang, J.; Liu, Y.; Chu, S.; Kong, F.; Wang, Y.; Zou, Z. An efficient visible light controlled protein delivery system. *Chem. Commun.* **2011**, *47*, 11243−11245.
(21) Kwolek, P.; Oszajca, M.; Szaciłowski, K. Catecholate and 2,3-acenediolate complexes of d^0 ions as prospective materials for molecular electronics and spintronics. *Coord. Chem. Rev.* **2012**, *256*, 1706−1731.
(22) Savic, T. D.; Jankovic, I. A.; Saponjic, Z. V.; Comor, M. I.; Veljkovic, D. Z.; Zaric, S. D.; Nedeljkovic, J. M. Surface modification of anatase nanoparticles with fused ring catecholate type ligands: a combined DFT and experimental study of optical properties. *Nanoscale* **2012**, *4*, 1612−1619.
(23) Savic, T. D.; Comor, M. I.; Nedeljkovic, J. M.; Veljkovic, D. Z.; Zaric, S. D.; Rakic, V. M.; Jankovic, I. A. The effect of substituents on the surface modification of anatase nanoparticles with catecholate-type ligands: a combined DFT and experimental study. *Phys. Chem. Chem. Phys.* **2014**, *16*, 20796−20805.
(24) Higashimoto, S.; Nishi, T.; Yasukawa, M.; Azuma, M.; Sakata, Y.; Kobayashi, H. Photocatalysis of titanium dioxide modified by catechol-type interfacial surface complexes (ISC) with different substituted groups. *J. Catal.* **2015**, *329*, 286−290.
(25) Finkelstein-Shapiro, D.; Davidowski, S. K.; Lee, P. B.; Guo, C.; Holland, G. P.; Rajh, T.; Gray, K. A.; Yarger, J. L.; Calatayud, M. Direct Evidence of Chelated Geometry of Catechol on TiO_2 by a Combined Solid-State NMR and DFT Study. *J. Phys. Chem. C* **2016**, *120*, 23625−23630.
(26) Sredojević, D. N.; Kovač, T.; Džunuzović, E.; Đorđević, V.; Grgur, B. N.; Nedeljković, J. M. Surface-modified TiO_2 powders with phenol derivatives: A comparative DFT and experimental study. *Chem. Phys. Lett.* **2017**, *686*, 167−172.
(27) Luppi, E.; Urdaneta, I.; Calatayud, M. Photoactivity of Molecule-TiO_2 Clusters with Time-Dependent Density-Functional Theory. *J. Phys. Chem. A* **2016**, *120*, 5115−5124.
(28) Rajh, T.; Dimitrijevic, N. M.; Bissonnette, M.; Koritarov, T.; Konda, V. Titanium Dioxide in the Service of the Biomedical Revolution. *Chem. Rev.* **2014**, *114*, 10177−10216.
(29) Tokuoka, Y.; Yamada, M.; Kawashima, N.; Miyasaka, T. Anticancer Effect of Dye-sensitized TiO_2 Nanocrystals by Polychromatic Visible Light Irradiation. *Chem. Lett.* **2006**, *35*, 496−497.
(30) Paramaguru, G.; Solomon, R. V.; Venuvanalingam, P.; Renganathan, R. Spectroscopic Studies on TiO_2 Enhanced Binding of Hypocrellin B with DNA. *J. Fluoresc.* **2011**, *21*, 1887−1895.
(31) Lopez, T.; Ortiz, E.; Alvarez, M.; Navarrete, J.; Odriozola, J. A.; Martinez-Ortega, F.; Páez-Mozo, E. A.; Escobar, P.; Espinoza, K. A.; Rivero, I. A. Study of the stabilization of zinc phthalocyanine in sol-gel TiO_2 for photodynamic therapy applications. *Nanomed. Nanotechnol.* **2010**, *6*, 777−785.
(32) Rajh, T.; Dimitrijevic, N. M.; Elhofy, A.; Rozhkova, E. In *Handbook of Nanophysics: Functional Nanomaterials*; Sattler, K. D., Ed.; CRC Press: Boca Raton, FL, 2010.
(33) Chen, L. X.; Rajh, T.; Wang, Z.; Thurnauer, M. C. XAFS Studies of Surface Structures of TiO_2 Nanoparticles and Photocatalytic Reduction of Metal Ions. *J. Phys. Chem. B* **1997**, *101*, 10688−10697.
(34) DeLearie, L. A.; Pierpont, C. G. Catecholate complexes of high oxidation state metal ions. Synthesis and characterization of tris(3,5-di-tert-butylcatecholato)rhenium(VI). *J. Am. Chem. Soc.* **1986**, *108*, 6393−6394.
(35) Kleitz, F.; Hei Choi, S.; Ryoo, R. Cubic *Ia3d* large mesoporous silica: synthesis and replication to platinum nanowires, carbon nanorods and carbon nanotubes. *Chem. Commun.* **2003**, 2136−2137.
(36) Kim, T.-W.; Kleitz, F.; Paul, R.; Ryoo, R. MCM-41-like Large Mesoporous Silicas with Tailored Pore Structure: Facile Synthesis Domain in a Ternary Triblock Copolymer-Butanol-Water System. *J. Am. Chem. Soc.* **2005**, *127*, 7601−7610.
(37) Zimny, K.; Ghanbaja, J.; Carteret, C.; Stébé, M.-J.; Blin, J.-L. Highly ordered mesoporous titania with semi crystalline framework templated by large or small nonionic surfactants. *New J. Chem.* **2010**, *34*, 2113−2117.
(38) Zimny, K.; Roques-Carmes, T.; Carteret, C.; Stébé, M. J.; Blin, J. L. Synthesis and Photoactivity of Ordered Mesoporous Titania with a Semicrystalline Framework. *J. Phys. Chem. C* **2012**, *116*, 6585−6594.
(39) Naboulsi, I.; Lebeau, B.; Michelin, L.; Carteret, C.; Vidal, L.; Bonne, M.; Blin, J.-L. Insights into the Formation and Properties of Templated Dual Mesoporous Titania with Enhanced Photocatalytic Activity. *ACS Appl. Mater. Interfaces* **2017**, *9*, 3113−3122.
(40) Sonström, A.; Schneider, D.; Maichle-Mössmer, C.; Anwander, R. Titanium(IV) Catecholate-grafted Mesoporous Silica KIT-6: Probing Sequential and Convergent Immobilization Approaches. *Eur. J. Inorg. Chem.* **2019**, 682−692.
(41) Davidson, M. G.; Jones, M. D.; Lunn, M. D.; Mahon, M. F. Synthesis and X-ray Structures of New Titanium(IV) Aryloxides and Their Exploitation for the Ring Opening Polymerization of ε-Caprolactone. *Inorg. Chem.* **2006**, *45*, 2282−2287.
(42) Wallace, W. A.; Potvin, P. G. Structurally Diverse Aggregating Condensations of Ti(IV) Catecholates. *Inorg. Chem.* **2007**, *46*, 9463−9472.
(43) Liang, Y.; Anwander, R. Nanostructured Catalysts via silylamide-based smart grafting. *Dalton Trans.* **2013**, *42*, 12521−12545.
(44) Fischbach, A.; Klimpel, M. G.; Widenmeyer, M.; Herdtweck, E.; Scherer, W.; Anwander, R. Sterospecific Polymerization if Isoprene with Molecular and MCM-41-grafted Lanthanide(III)-Tetramethylaluminates $LnAl_3R_{12}$. *Angew. Chem., Int. Ed.* **2004**, *43*, 2234−2239.
(45) Michel, O.; König, S.; Törnroos, K. W.; Maichle-Mössmer, C.; Anwander, R. Surface Organobarium and -Magnesium Chemistry of Periodic Mesoporous Silica MCM-41: Convergent and Sequential Approaches Traced by Molecular Models. *Chem. Eur. J.* **2011**, *17*, 11857−11867.
(46) Terry, K. W.; Tilley, T. D. Trialkoxysiloxy Complexes as Precursors to MO_2-$4SiO_2$ (M = Ti, Zr, Hf) Materials. *Chem. Mater.* **1991**, *3*, 1001−1003.
(47) Coles, M. P.; Lugmair, C. G.; Terry, K. W.; Tilley, T. D. Titania-Silica Materials from the Molecular Precursor Ti[OSi-

https://doi.org/10.1021/acs.inorgchem.2c02838
Inorg. Chem. 2023, 62, 715−729

(OtBu)$_3$]$_4$: Selective Epoxidation Catalysts. *Chem. Mater.* **2000**, *12*, 122−131.
(48) Abe, Y.; Kijima, I. Alkoxysilanes. IV. Preparation of Alkoxysiloxy Derivatives of Titanium. *Bull. Jpn. J. Chem.* **1970**, *43*, 466−469.
(49) Gunji, T.; Kasahara, T.; Abe, Y. Crystallization Behavior of SiO_2−TiO_2 Ceramics derived from Titanosiloxanes on Pyrolysis. *J. Sol-Gel Sci. Technol.* **1998**, *13*, 975−979.
(50) Brutchey, R. L.; Mork, B. V.; Sirbuly, D. J.; Yang, P.; Tilley, T. D. A dimeric molecular precursor [(*t*BuO)$_2$Ti{μ-O$_2$Si[OSi(OtBu)$_3$]$_2$}]$_2$ to Ti(IV)/SiO_2 catalysts fro selective cyclohexene epoxidation. *J. Mol. Catal. A: Chem.* **2005**, *238*, 1−12.
(51) Boyle, T. J.; Sewell, R. M.; Ottley, L. A. M.; Pratt, H. D., III; Quintana, C. J.; Bunge, S. D. Controlled Synthesis of a Structurally Characterized Family of Sterically Constrained Heterocyclic Alkoxy-Modified Titanium Alkoxides. *Inorg. Chem.* **2007**, *46*, 1825−1835.
(52) Dhayal, V.; Atal, M. K.; Choudhary, B. L.; Nagar, M.; Bohra, R. Glycol modified titanosiloxane as molecular precursor for homogeneous titania-silica material: synthesis and characterization. *J. Sol-Gel Sci. Technol.* **2009**, *52*, 97−108.
(53) Dhayal, V.; Chaudhary, A.; Choudhary, B. L.; Nagar, M.; Bohra, R.; Mobin, S. M.; Mathur, P. Molecular precursors for the preparation of homogeneous zirconia-silica materials by hydrolytic sol-gel process in organic media. Crystal structures of [Zr{OSi(OtBu)$_3$}$_4$(H$_2$O)$_2$]-x2H$_2$O and [Ti(OtBu){OSi(OtBu)$_3$}$_3$]. *Dalton Trans.* **2012**, *41*, 9439−9450.
(54) Quadri, C. C.; Lalrempuia, R.; Hessevik, J.; Törnroos, K. W.; Le Roux, E. Structural Characterization of Tridentate N-Heterocyclic Carbene Titanium(IV) Benzyloxide, Silyloxide, Acetate, and Azide Complexes and Assessment of Their Efficacies for Catalyzing the Copolymerization of Cyclohexene Oxide with CO_2. *Organometallics* **2017**, *36*, 4477−4489.
(55) Boyle, T. J.; Alam, T. M.; Mechenbier, E. R.; Scott, B. L.; Ziller, J. W. Titanium(IV) Neopentoxides. X-ray Structures of Ti$_3$(μ_3-O)(μ_3-Cl)(μ-OCH$_2$CMe$_3$)$_3$(OCH$_2$CMe$_3$)$_6$ and [Ti(μ-OCH$_2$CMe$_3$)-(OCH$_2$CMe$_3$)$_3$]$_2$. *Inorg. Chem.* **1997**, *36*, 3293−3300.
(56) Widenmeyer, M.; Grasser, S.; Köhler, K.; Anwander, R. TiO_x overlayers on MCM-48 silica by consecutive grafting. *Microporous Mesoporous Mater.* **2001**, *44-45*, 327−336.
(57) Jarupatrakorn, J.; Tilley, T. D. Silica-Supported, Single-Site Titanium Catalysts for Olefin Epoxidation. A Molecular Precursor Strategy for Control of Catalysts Structure. *J. Am. Chem. Soc.* **2002**, *124*, 8380−8388.
(58) Brutchey, R. L.; Ruddy, D. A.; Andersen, L. K.; Tilley, T. D. Influence of Surface Modification of Ti-SBA15 Catalysts on the Epoxidation Mechanism for Cyclohexene with Aqueous Hydrogen Peroxide. *Langmuir* **2005**, *21*, 9576−9583.
(59) Yoon, C. W.; Hirsekorn, K. F.; Neidig, M. L.; Yang, X.; Tilley, T. D. Mechanism of the Decomposition of Aqueous Hydrogen Peroxide over Heterogenous TiSBA1 and TS-1 Selective Oxidation Catalysts: Insights from Spectroscopic and Density Functional Theory Studies. *ACS Catal.* **2011**, *1*, 1665−1678.
(60) Noh, G.; Lam, E.; Alfke, J. L.; Larmier, K.; Wolf, P.; Coperét, C.; Searles, K. Selective Hydrogenation of CO_2 to CH_3OH on Supported Cu Nanoparticles Promoted by Isolated Ti^{IV} Surface Sites on SiO_2. *ChemSusChem* **2019**, *12*, 968−972.
(61) Basset, J. M.; Choplin, A. Surface organometallic chemistry: A new approach to heterogeneous Catalysis? *J. Mol. Catal.* **1983**, *21*, 95−108.
(62) Anwander, R. SOMC@PMS. Surface Organometallic Chemistry at Periodic Mesoporous Silica. *Chem. Mater.* **2001**, *13*, 4419−4438.
(63) Copéret, C.; Comas-Vives, A.; Conley, M. P.; Estes, D. P.; Fedorov, A.; Mougel, V.; Nagae, H.; Núñez-Zarur, F.; Zhizhko, P. A. Surface Organometallic and Coordination Chemistry toward Single-Site Heterogeneous Catalysts: Strategies, Methods, Structures, and Activities. *Chem. Rev.* **2016**, *116*, 323−421.
(64) Samantaray, M. K.; Pump, E.; Bendjeriou-Sedjerari, A.; D'Elia, V.; Pelletier, J. D. A.; Guidotti, M.; Psaro, R.; Basset, J.-M. Surface organometallic chemistry in heterogeneous catalysis. *Chem. Soc. Rev.* **2018**, *47*, 8403−8437.
(65) Anwander, R.; Nagl, I.; Widenmeyer, M.; Engelhardt, G.; Groeger, O.; Palm, C.; Röser, T. Surface Characterization and Functionalization of MCM-41 Silicas via Silazane Silylation. *J. Phys. Chem. B* **2000**, *104*, 3532−3544.
(66) Deschner, D.; Liang, Y.; Anwander, R. Silylation Efficiency of Chlorosilanes, Alkoxysilanes, and Monosilazanes on Periodic Mesopororous Silica. *J. Phys. Chem. C* **2010**, *114*, 22603−22609.
(67) Kim, K. S.; Barteau, M. A. Reactions of aliphatic alcohols on the {011}-facetted Ti0$_2$ (001) surface. *J. Mol. Catal.* **1990**, *63*, 103−117.
(68) Rocco, M. L. M.; Haeming, M.; Batchelor, D. R.; Fink, R.; Scholl, A.; Umbach, E. Electronic relaxation effects in condensed polyacenes: A high-resolution photoemission study. *J. Chem. Phys.* **2008**, *129*, 074702−8.
(69) Syres, K. L.; Thomas, A. G.; Flavell, W. R.; Spencer, B. F.; Bondino, F.; Malvestuto, M.; Preobrajenski, A.; Grätzel, M. Adsorbate-Induced Modification of Surface Electronic Structure: Pyrocatechol Adsorption on the Anatase TiO_2 (101) and Rutile TiO_2 (110) Surfaces. *J. Phys. Chem. C* **2012**, *116*, 23515−23525.
(70) Kerber, S. J.; Bruckner, J. J.; Wozniak, K.; Seal, S.; Hardcastle, S.; Barr, T. L. The nature of hydrogen in x-ray photoelectron spectroscopy: General patterns from hydroxides to hydrogen bonding. *J. Vac. Sci. Technol. A* **1996**, *14*, 1314−1320.
(71) Sanjinés, R.; Tang, H.; Berger, H.; Gozzo, F.; Margaritondo, G.; Lévy, F. Electronic structure of anatase TiO_2 oxide. *J. Appl. Phys.* **1994**, *75*, 2945−2951.
(72) Diebold, U.; Madey, T. E. TiO_2 by XPS. *Surf. Sci. Spectra* **1996**, *4*, 227−231.
(73) Stefanov, P.; Shipochka, M.; Stefchev, P.; Raicheva, Z.; Lazarova, V.; Spassov, L. XPS characterization of TiO_2 layers deposited on quartz plates. *J. Phys. Conf. Ser.* **2008**, *100*, 012039.
(74) Thompson, A.; Attwood, D.; Gullikson, E.; Howells, M.; Kim, K.-J.; Kirz, J.; Kortright, J.; Lindau, I.; Pianetta, P.; Robinson, A.; Scofield, J.; Underwodd, J.; Vaughan, D.; Williams, G.; Winick, H. *X-ray Data Booklet*; Center for X-ray Optics and Advanced Light Source, Lawrence Berkeley National Laboratory, University of California, 2011; https://xdb.lbl.gov/.
(75) Detweiler, Z. M.; Wulfsberg, S. M.; Frith, M. G.; Bocarsly, A. B.; Bernasek, S. L. The oxidation and surface speciation of indium and indium oxides exposed to atmospheric oxidants. *Surf. Sci.* **2016**, *648*, 188−195.
(76) Kerber, S. J. Bioreactivity of titanium implant alloys. *J. Vac. Sci. Technol. A* **1995**, *13*, 2619−2623.
(77) Greczynski, G.; Hultman, L. A step-by-step guide to perform x-ray photoelectron spectroscopy. *J. Appl. Phys.* **2022**, *132* (1), 011101.
(78) Sen, S. K.; Riga, J.; Verbist, J. 2s and 2p X-ray photoelectron spectra of Ti^{4+} ion in TiO_2. *Chem. Phys. Lett.* **1976**, *39*, 560−564.
(79) Kashiwaya, S.; Morasch, J.; Streibel, V.; Toupance, T.; Jaegermann, W.; Klein, A. The Work Function of TiO_2. *Surfaces* **2018**, *1*, 73−89.
(80) Yew, R.; Karuturi, S. K.; Liu, J.; Tan, H. H.; Wu, Y.; Jagadish, C. Exploiting defects in TiO_2 inverse opal for enhanced photoelectrochemical water splitting. *Opt. Express* **2019**, *27*, 761−773.
(81) Li, H.; Xie, C.; Liao, Y.; Liu, Y.; Zou, Z.; Wu, J. Characterization of Incidental Photon-to-electron Conversion Efficiency (IPCE) of porous TiO_2/SnO_2 composite film. *J. Alloys Compd.* **2013**, *569*, 88−94.
(82) Kumarasinghe, A. R.; Flavell, W. R.; Thomas, A. G.; Mallick, A. K.; Tsoutsou, D.; Chatwin, C.; Rayner, S.; Kirkham, P.; Warren, S.; Patel, S.; Christian, P.; O'Brien, P.; Grätzel, M.; Hengerer, R. Electronic properties of the interface between p-CuI and anatase-phase n-TiO_2 single crystal and nanoparticulate surfaces: A photoemission study. *J. Chem. Phys.* **2007**, *127*, 114703.
(83) Scanlon, D. O.; Dunnill, C. W.; Buckeridge, J.; Shevlin, S. A.; Logsdail, A. J.; Woodley, S. M.; Catlow, C. R. A.; Powell, M. J.; Palgrave, R. G.; Parkin, I. P.; Watson, G. W.; Keal, T. W.; Sherwood, P.; Walsh, A.; Sokol, A. A. Band alignment of rutile and anatase TiO_2. *Nat. Mater.* **2013**, *12*, 798−801.

https://doi.org/10.1021/acs.inorgchem.2c02838
Inorg. Chem. 2023, 62, 715−729

(84) Maheu, C.; Cardenas, L.; Puzenat, E.; Afanasiev, P.; Geantet, C. UPS and UV spectroscopies combined to position the energy levels of TiO_2 anatase and rutile nanopowders. *Phys. Chem. Chem. Phys.* **2018**, *20*, 25629−25637.
(85) Henningsson, A.; Rensmo, H.; Sandell, A.; Siegbahn, H.; Södergren, S.; Lindström, H.; Hagfeldt, A. Electronic structure of electrochemically Li-inserted TiO_2 studied with synchrotron radiation electron spectroscopies. *J. Chem. Phys.* **2003**, *118*, 5607−5612.
(86) Tang, H.; Berger, H.; Schmid, P. E.; Lévy, F. Optical properties of anatase (TiO_2). *Solid State Commun.* **1994**, *92*, 267−271.
(87) Duncan, W. R.; Prezhdo, O. V. Theoretical Studies of Photoinduced Electron Transfer in Dye-Sensitized TiO_2. *Annu. Rev. Phys. Chem.* **2007**, *58*, 143−184.
(88) Rajh, T.; Chen, L. X.; Lukas, K.; Liu, T.; Thurnauer, M. C.; Tiede, D. M. Surface Restructuring of Nanoparticles: An Efficient Route for Ligand-Metal Oxide Crosstalk. *J. Phys. Chem. B* **2002**, *106*, 10543−10552.
(89) Drochner, A.; Symalla, M.; Vogel, H. Diffuse-Reflexions-Infrarot-Fourier-Transformations-Spektroskopie (DRIFTS). *Bunsen-Magazin* **2008**, *10*, 10−24.
(90) *APEX3 and COSMO*, version 2012.10 0; Bruker AXS Inc.: Madison, WI, 2012.
(91) *APEX3 and SAINT*, version 8.37 A; Bruker AXS Inc.: Madison, WI, 2017.
(92) *SADABS*: Krause, L.; Herbst-Irmer, R.; Sheldrick, G. M.; Stalke, D. *J. Appl. Crystallogr.* **2015**, *48*.
(93) *SHELXL*: *ActaCrystallogr.* **2015**, *C71*, 3−8.
(94) *SHELXLE*: Hubschle, C. B.; Sheldrick, G. M.; Dittrich, B. *J. Appl. Crystallogr.*. **2011** *44*, 1281−1284.
(95) Sheldrick, G. M. *TWINABS: Bruker AXS Scaling for Twinned Crystals*, version 2007/3, and *SADABS*; Bruker AXS Inc.: Göttingen, Germany, 2007.
(96) Farrugia, L. J. *J. Appl. Crystallogr.* **1997**, *30*, 565.
(97) *POV-Ray*, version 3.6; Persistence of Vision Pty. Ltd.: Williamstown, Victoria, Australia, 2004; http://www.povray.org/.
(98) Brunauer, S.; Emmett, P. H.; Teller, E. Adsorption of Gases in Multimolecular Layers. *J. Am. Chem. Soc.* **1938**, *60*, 309−319.
(99) Barrett, E. P.; Joyner, L. G.; Halenda, P. P. The Determination of Pore Volume and Area Distributions in Porous Substances. I. Computations from Nitrogen Isotherms. *J. Am. Chem. Soc.* **1951**, *73*, 373−380.
(100) Beaudoin, M.; Scott, S. L. Spontaneous Evolution of Silica-Supported Ti Amide Fragments to Imine and Imido Complexes. *Organometallics* **2001**, *20*, 237−239.
(101) Barth, G.; Linder, R.; Bryson, C. Advances in charge neutralization for XPS measurements of nonconducting materials. *Surf. Interface Anal.* **1988**, *11*, 307−311.

https://doi.org/10.1021/acs.inorgchem.2c02838
Inorg. Chem. 2023, 62, 715−729

Supporting Information

Titanium(IV) Surface Complexes Bearing Chelating Catecholato Ligands for Enhanced Band-Gap Reduction

Andrea Sonström,[a] Barbara Boldrini,[b] Daniel Werner,[a] Cäcilia Maichle-Mössmer,[a] Karsten Rebner,[b] Maria Benedetta Casu,[c,*] and Reiner Anwander[a,*]

[a]Institut für Anorganische Chemie, Eberhard Karls Universität Tübingen, Auf der Morgenstelle 18, 72076 Tübingen, Germany

[b]Lehr- und Forschungszentrum "Process Analysis and Technology", Fakultät Angewandte Chemie, Hochschule Reutlingen, Alteburgstraße 150, 72762 Reutlingen, Germany

[c]Institut für Physikalische und Theoretische Chemie, Eberhard Karls Universität Tübingen, Auf der Morgenstelle 18, 72076 Tübingen, Germany

*E-Mail to R.A.: reiner.anwander@uni-tuebingen.de, benedetta.casu@uni-tuebingen.de

Table of Contents

Crystallographic Details

Table S1. Crystallographic Data for Complexes 1b, 1c, 2b, and 2c

	1b	**1c**[b]	**2b**	**2c**
CCDC	2165168	2165169	2165170	2165171
Formula	$C_{36}H_{66}N_2O_8Ti_2$	$C_{60}H_{116}O_{20}Si_4Ti_2$	$C_{28}H_{56}N_2O_4Ti$	$C_{42}H_{88}N_2O_{10}Si_2Ti$
M_w	750.70	1365.68	532.64	885.22
color/shape	Yellow/plates	Red/cubes	Red/plates	Red-brown/ plates
crystal dimensions [mm³]	0.112 0.053 0.043	0.298 0.219 0.132	0.246 0.154 0.094	0.269 0.246 0.114
crystal system	orthorhombic	monoclinic	orthorhombic	tetragonal
space group	P bca	C 2/c	P $mn2_1$	P $4_2/n$
a [Å]	14.6683(16)	24.533(2)	19.423(4)	28.271(2)
b [Å]	11.5028(12)	13.0369(13)	9.0809(18)	28.271(2)
c [Å]	24.685(3)	24.624(2)	9.0809(18)	26.0001(19)
α [°]	90	90	90	90
β [°]	90	101.959(2)	90	90
γ [°]	90	90	90	90
V [Å³]	4165.0(8)	7704.6(12)	1601.7(6)	20780(3)
Z	4	4	2	16
T [K]	100(2)	180(2)	100(2)	173(2)
ρ_{calcd} [gcm^{-3}]	1.197	1.177	1.104	1.132
μ [mm^{-1}]	0.430	0.331	0.298	0.260
F(000)	1616	2944	584	7744
θ range [°]	1.650/27.113	1.691/26.416	2.097/29.127	1.285/26.372
index ranges	-18 ≤ h ≤ 18 -14 ≤ k ≤ 14 -31 ≤ l ≤ 27	-30 ≤ h ≤ 30 -16 ≤ k ≤ 16 -30 ≤ l ≤ 30	-26 ≤ h ≤ 26 -12 ≤ k ≤ 12 -12 ≤ l ≤ 12	-35 ≤ h ≤ 35 -35 ≤ k ≤ 35 -32 ≤ l ≤ 32
total reflns	41674	52916	32520	293399
unique reflns / R_{int}	4595/0.0933	7917/0.0410	4641/0.0487	21243/0.1194]
observed reflns (I > 2σ)*	3387	6097	4144	13151
data/parameters/ restraints	4595/0/225	7917/756/582	4641/737/249	21243/0/1099
R1/wR2 (I > 2σ)[a]	0.0496/0.1144	0.0563/0.1445	0.0526/0.1178	0.0489/0.1175
R1/wR2 (all data)[a]	0.0757/0.1262	0.0757/0.1595	0.0627/0.1236	0.0960/0.1468
GOF[a]	1.026	1.035	1.099	1.018

[a] $R1 = \Sigma(||F_o|-|F_c||)/\Sigma|F_o|$, $F_o > 4\ \sigma(F_o)$. $wR2 = \{\Sigma[w(F_o^2-F_c^2)^2/\Sigma[w(F_o^2)^2]]\}^{1/2}$.

[b] The structure solution shows a highly disordered molecule and it was necessary to use strong restraints. This is caused by the bad crystal quality. There were no real single crystals, and separation of the reflections, belonging to different individuals, was not possible.

NMR Spectra

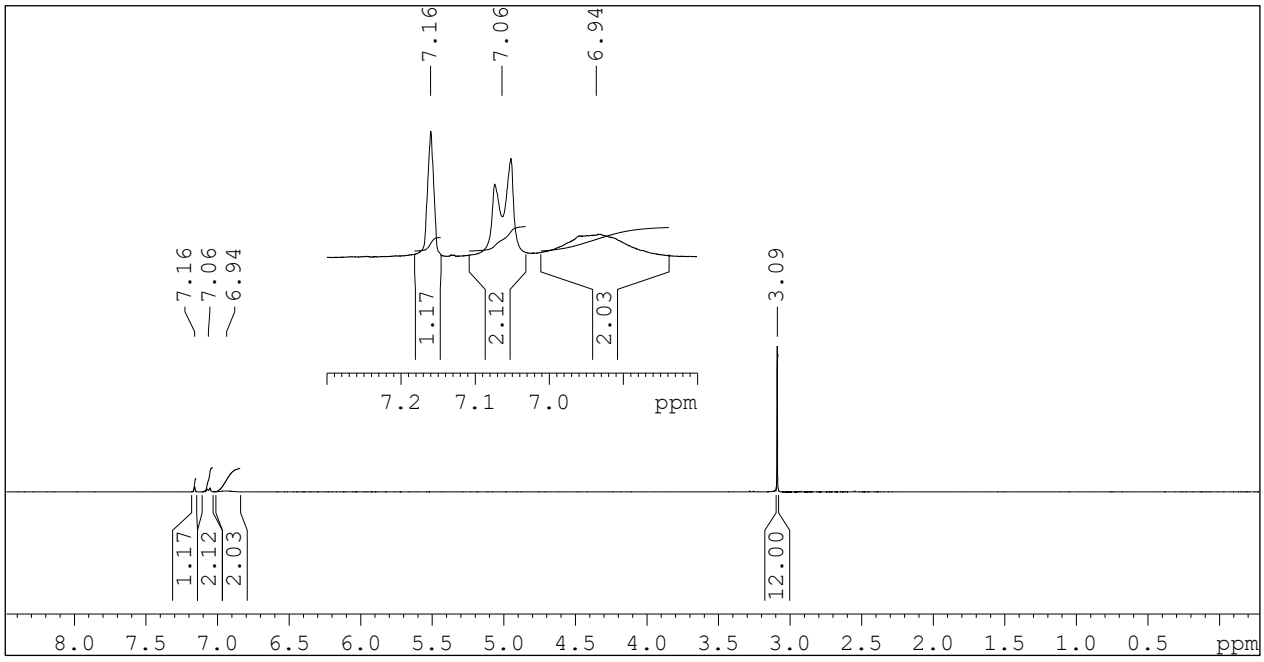

Figure S1. ^{1}H NMR spectrum (400 MHz, C_6D_6) of $[Ti(CAT)(NMe_2)_2]_2$ (**1a**) at 26 °C.

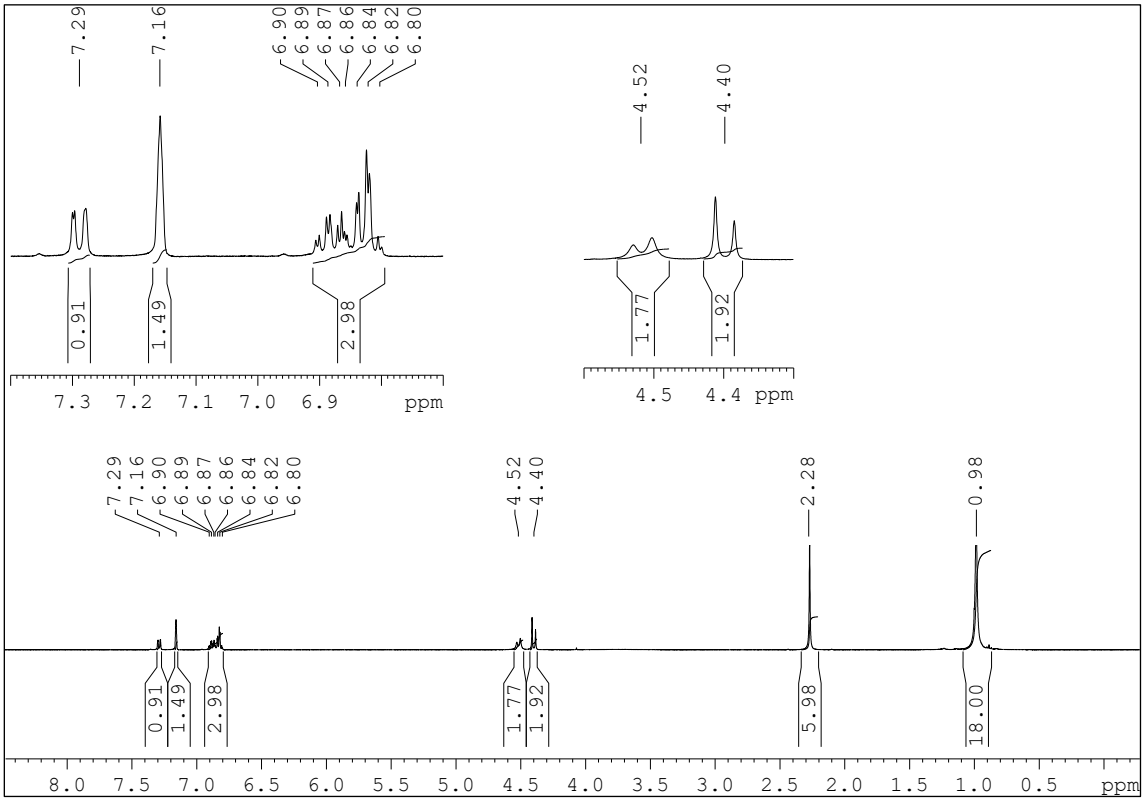

Figure S2. ^{1}H NMR spectrum (400 MHz, C_6D_6) of $[(Ti(CAT)(OCH_2tBu)_2)(HNMe_2)]_2$ (**1b**) at 26 °C.

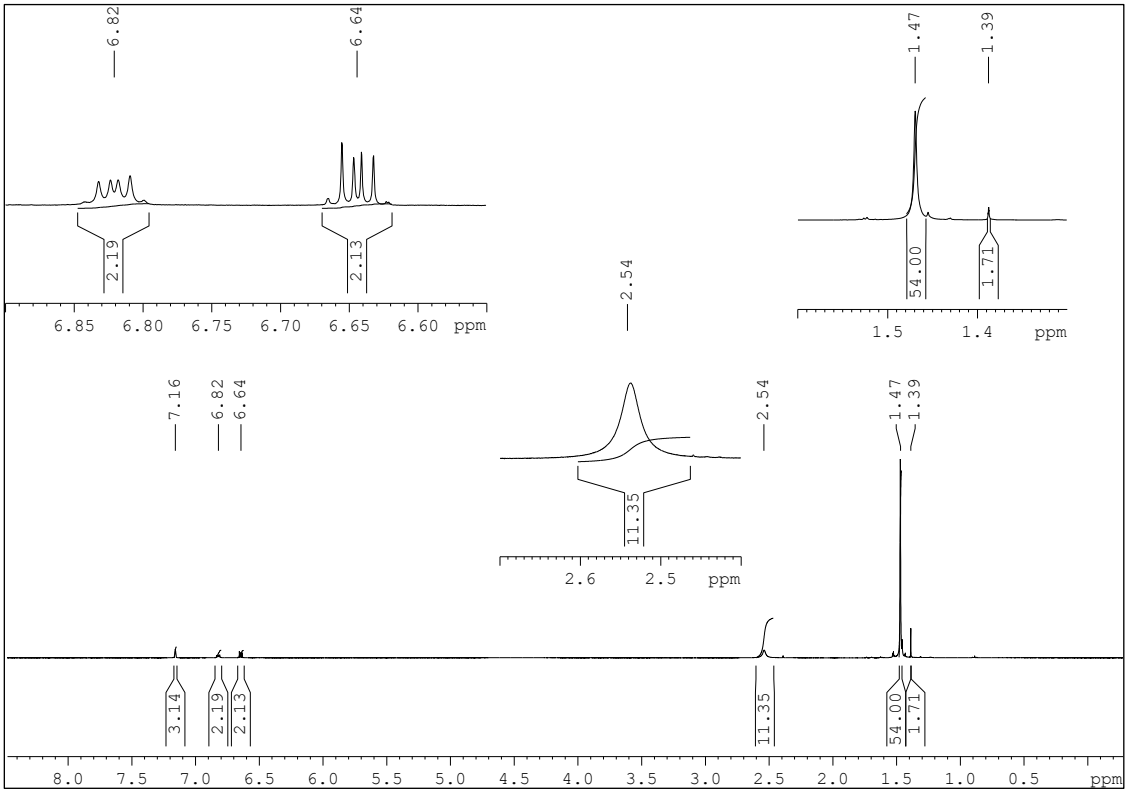

Figure S3. ^{1}H NMR spectrum (400 MHz, C_6D_6) of $[Ti(CAT)\{OSi(O\textit{t}Bu)_3\}_2(HNMe_2)_2]_2$ (**1c**) at 26 °C.

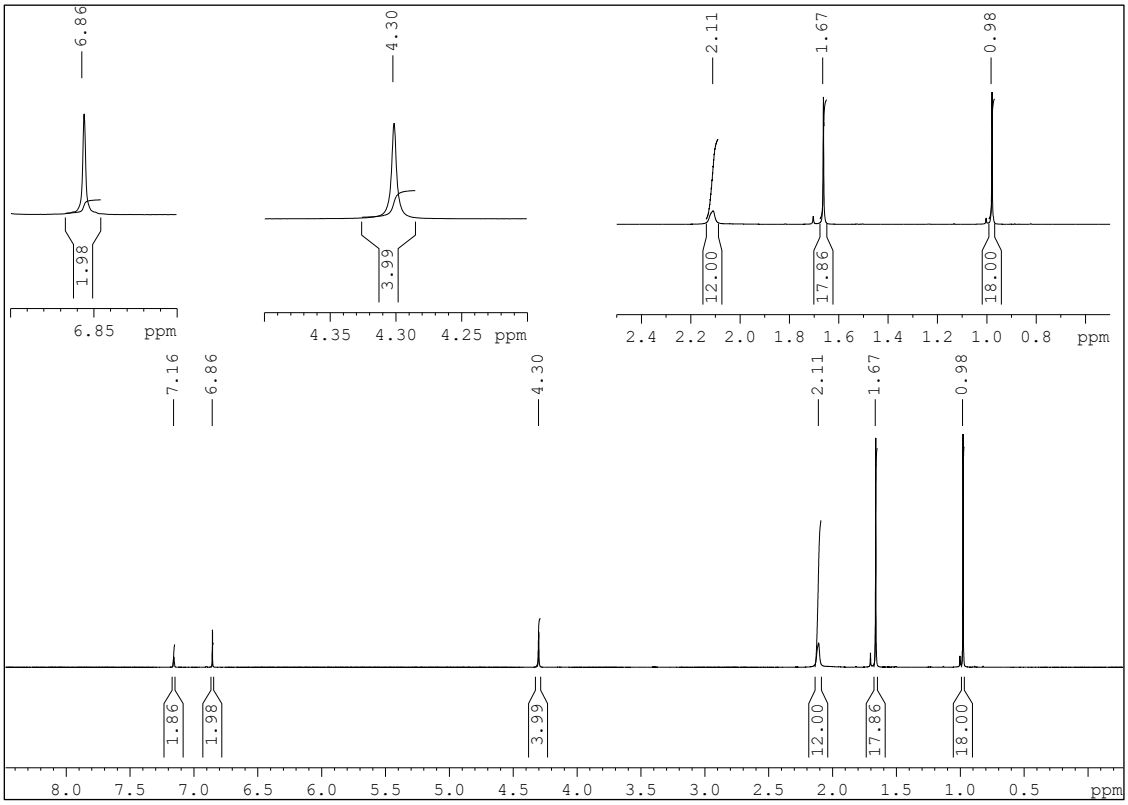

Figure S4. ^{1}H NMR spectrum (400 MHz, C_6D_6) of $[Ti(CAT\textit{t}Bu_2\text{-}3,6)(OCH_2\textit{t}Bu)_2(HNMe_2)_2]$ (**2b**) at 26 °C.

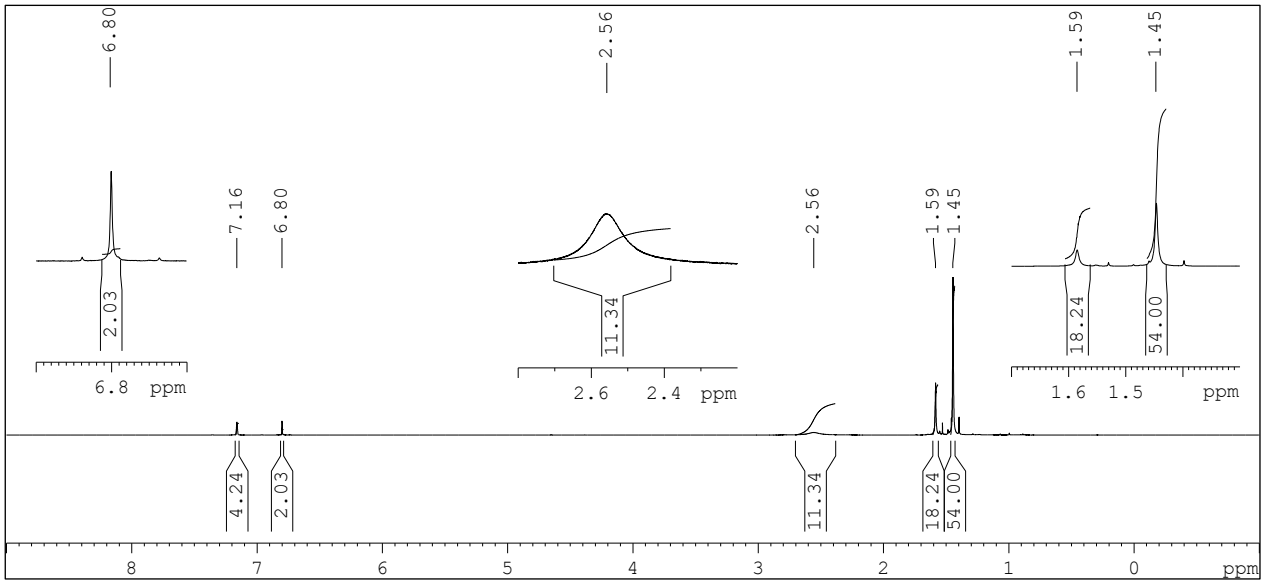

Figure S5. ^{1}H NMR spectrum (400 MHz, C_6D_6) of [Ti(CAT*t*Bu$_2$-3,6){OSi(O*t*Bu)$_3$}$_2$(HNMe$_2$)$_2$] (**2c**) at 26 °C.

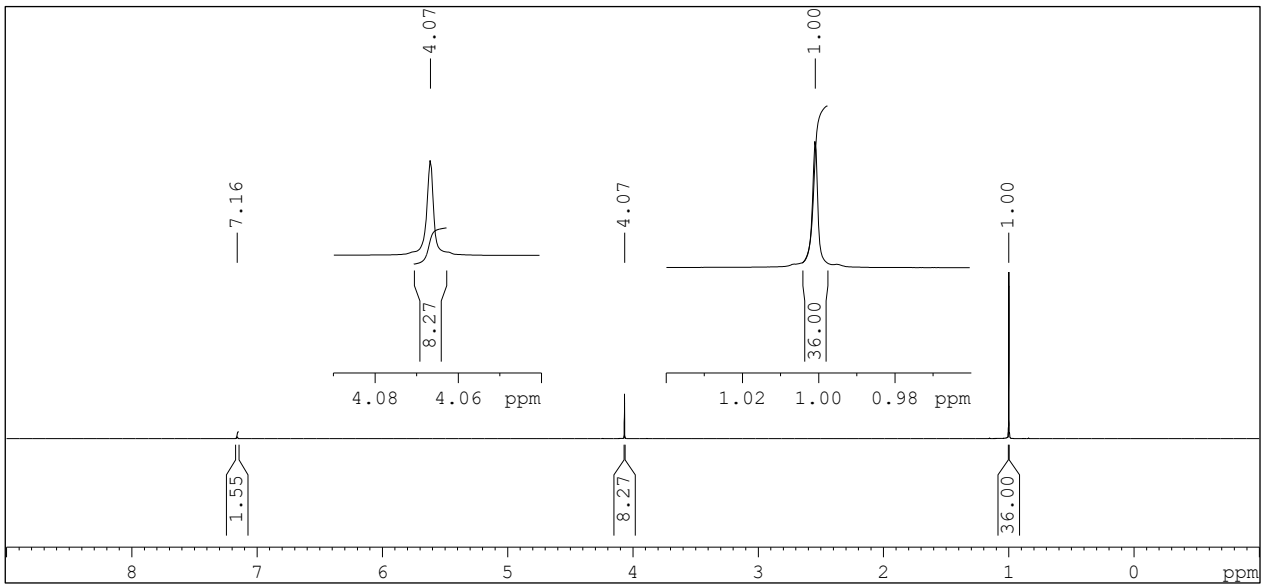

Figure S6. ^{1}H NMR spectrum (400 MHz, C_6D_6) of Ti(OCH$_2$*t*Bu)$_4$ (**3**) at 26 °C.

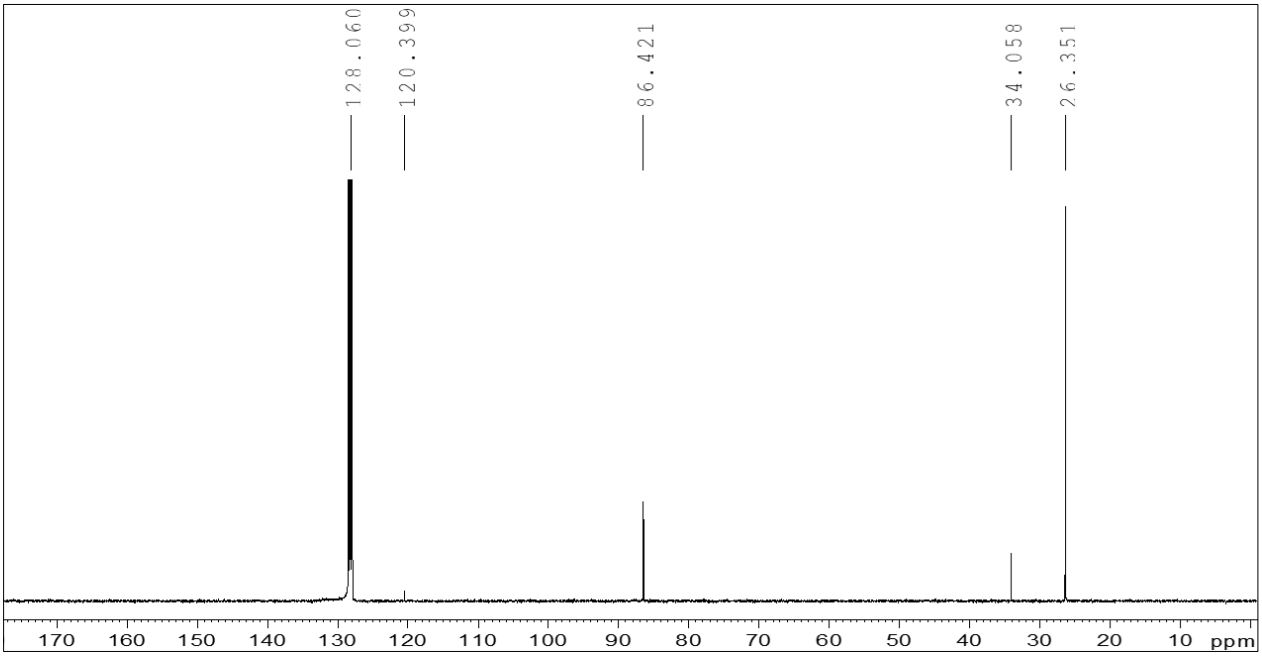

Figure S7. ^{13}C NMR spectrum (100 MHz, C_6D_6) of Ti(OCH$_2$*t*Bu)$_4$ (**3**) at 26 °C.

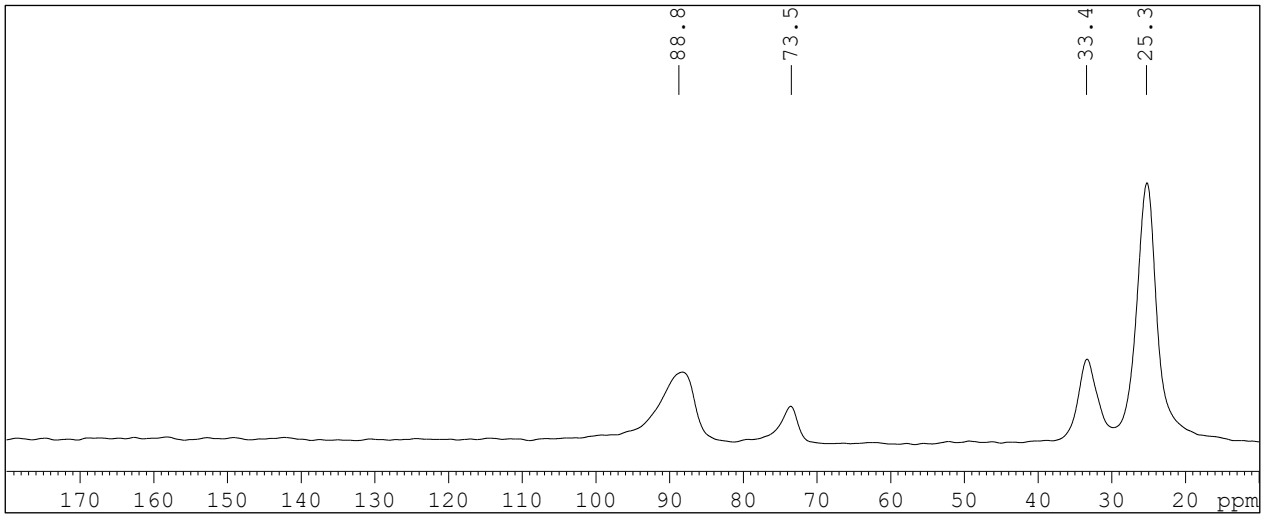

Figure S8. ^{13}C MAS NMR spectrum (75 MHz, CP/MAS, 10 kHz rotation) of Ti(OCH$_2$*t*Bu)$_4$@[KIT-6](**M1S1**) at 26 °C.

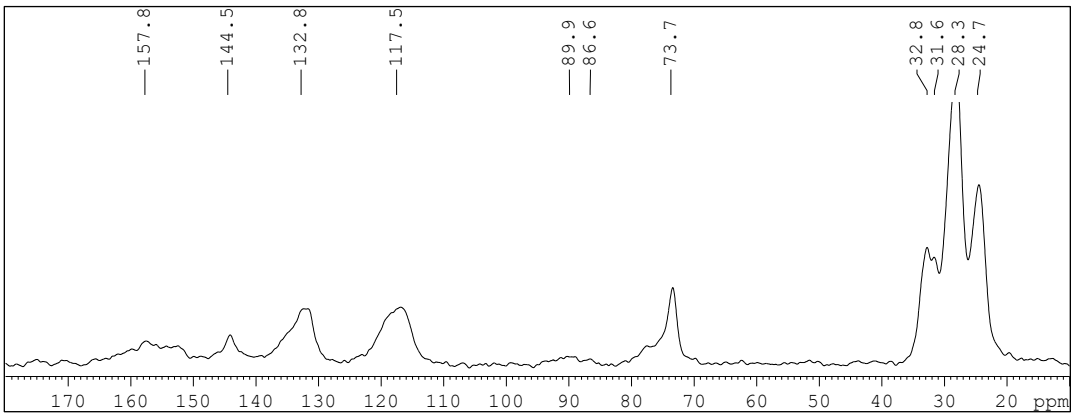

Figure S9. ^{13}C MASNMR spectrum (75 MHz, cp/MAS, 10 kHz rotation) of H_2CAT*t*Bu_2-3,6@Ti(OCH_2*t*Bu)$_4$@[KIT-6](**M1S2**) at 26 °C.

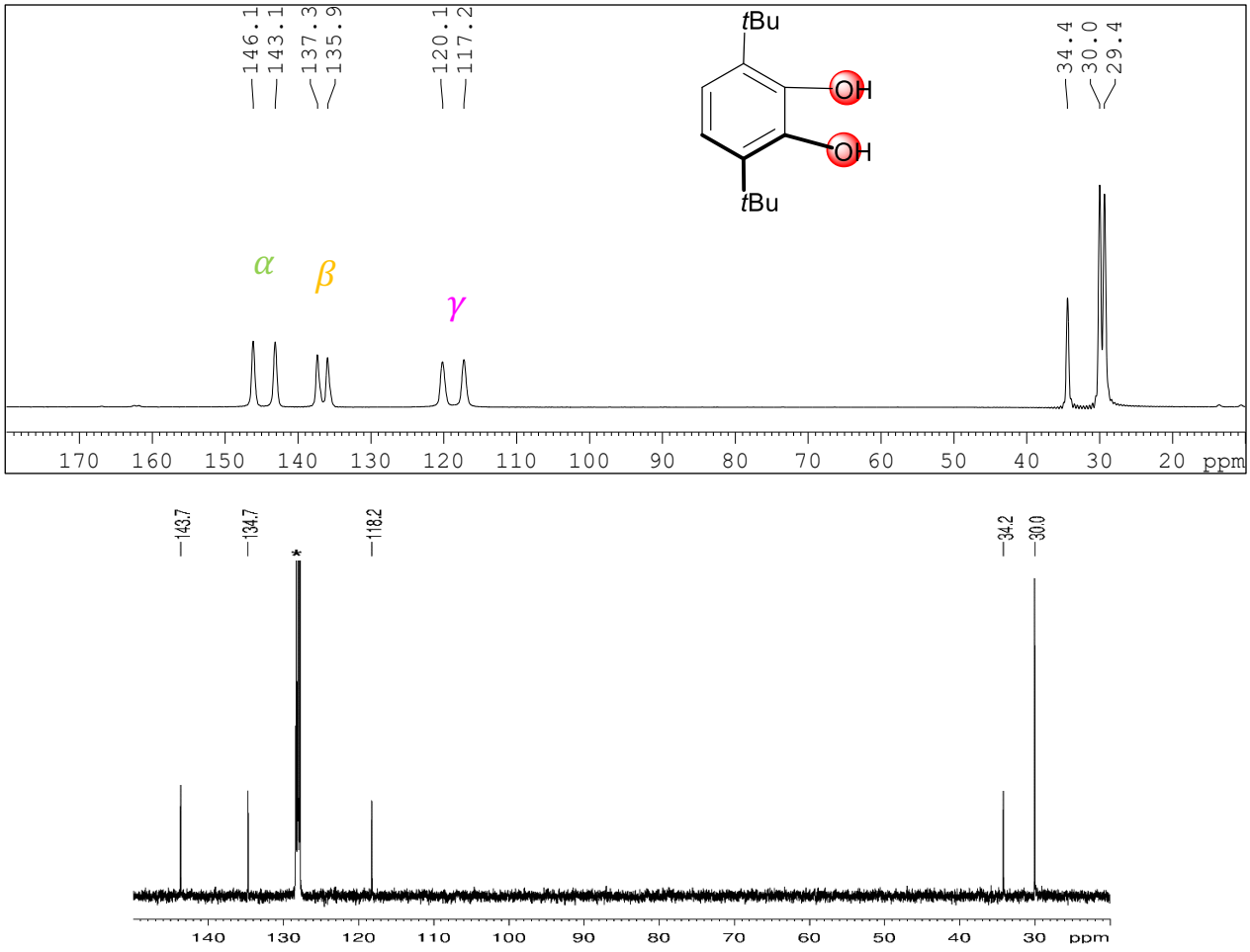

Figure S10. Top: ^{13}C MAS NMR spectrum (75 MHz, CP/MAS, 10 kHz rotation) of H_2CAT*t*Bu_2-3,6 at 26 °C. Bottom: ^{13}C NMR spectrum (100 MHz, C_6D_6) of H_2CAT*t*Bu_2-3,6 at 26 °C.

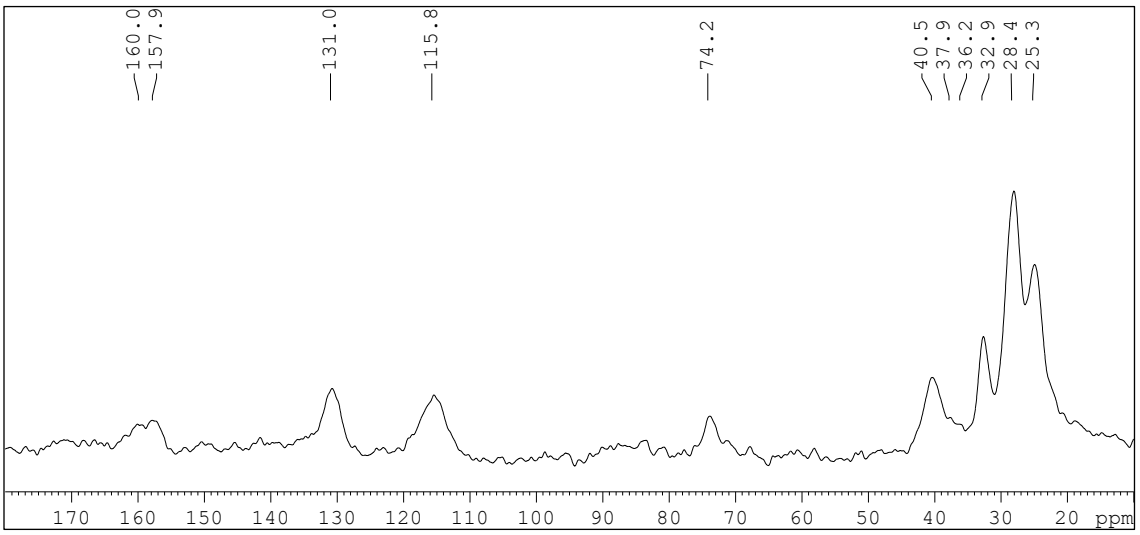

Figure S11. ^{13}C MAS NMR spectrum (75 MHz, CP/MAS, 10 kHz rotation) of [Ti(CAT*t*Bu$_2$-3,6)(OCH$_2$*t*Bu)$_2$(HNMe$_2$)$_2$] @[KIT-6](**M1C1**) at 26 °C.

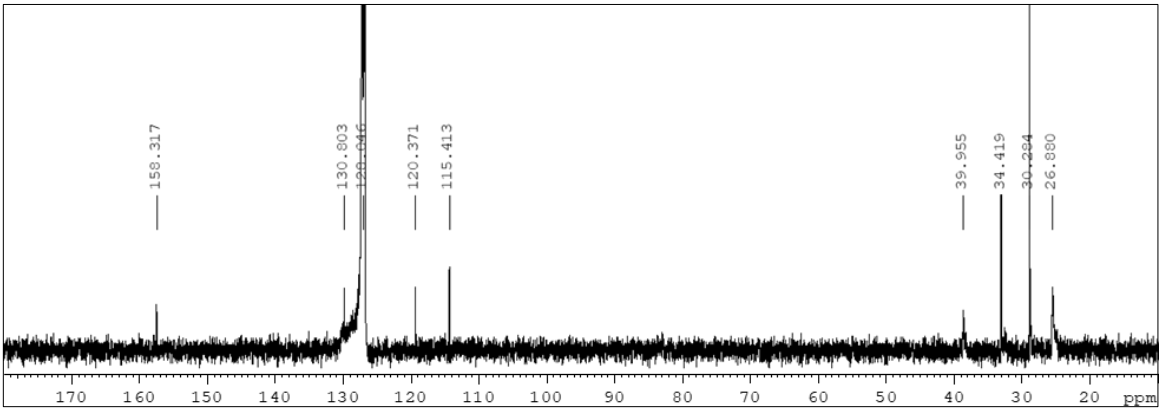

Figure S12. ^{13}C NMR spectrum (100 MHz, C_6D_6) of [Ti(CAT*t*Bu$_2$-3,6)(OCH$_2$*t*Bu)$_2$(HNMe$_2$)$_2$] (**2b**) at 26 °C.

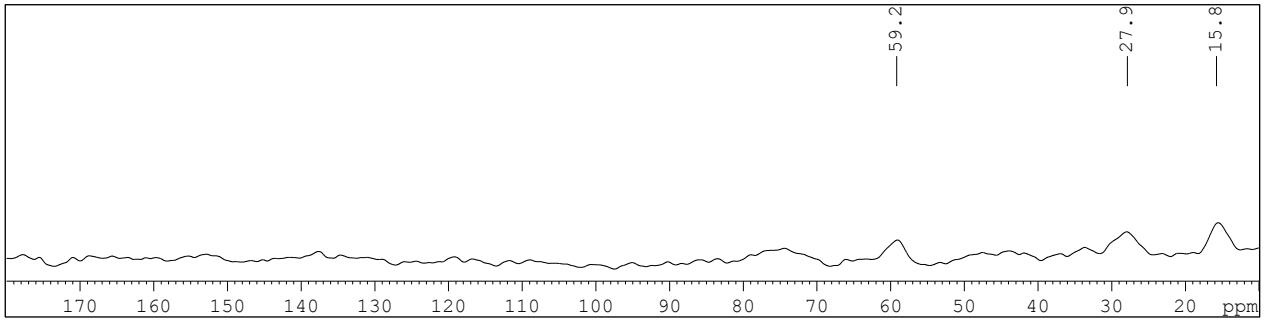

Figure S13. ^{13}C MAS NMR spectrum (75 MHz, cp/MAS, 10 kHz rotation) of H$_2$CAT*t*Bu$_2$-3,6@Ti(OH)$_x$@[KIT-6] (**M1A3**).

DRIFT Spectra

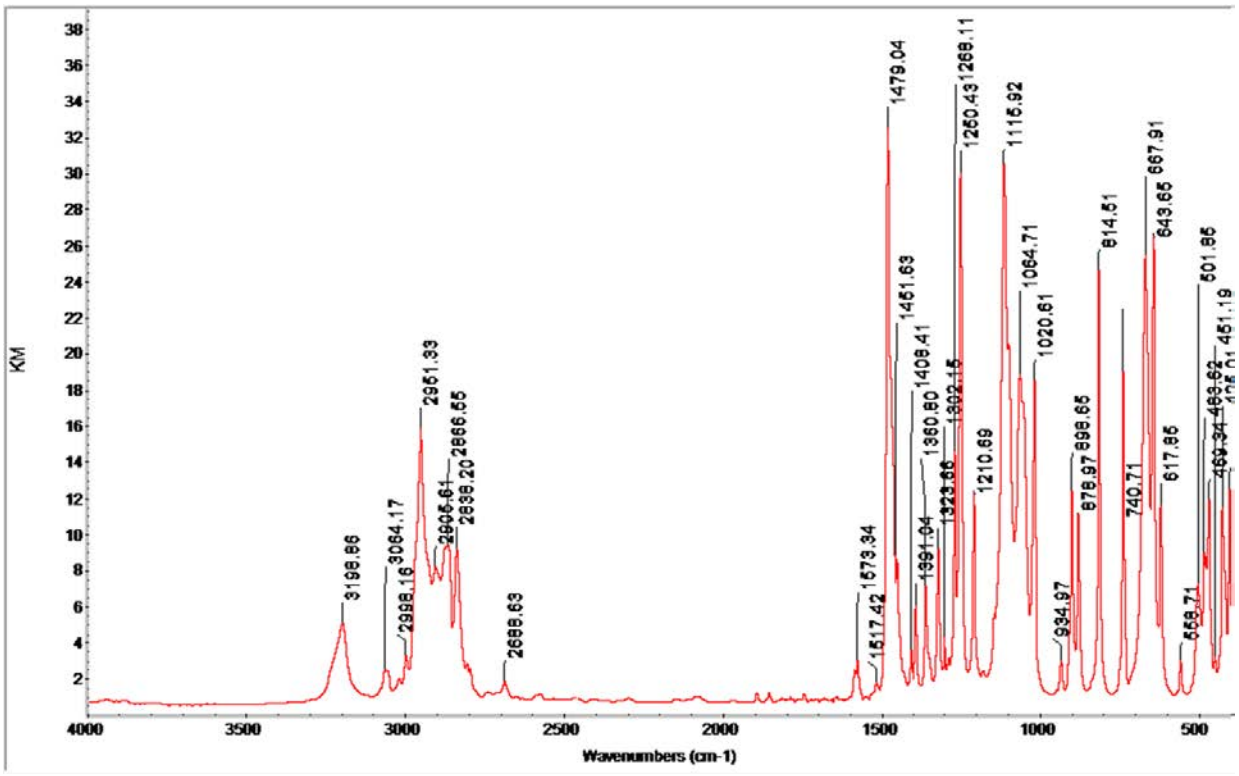

Figure S14. DRIFT spectrum (10 wt% in KBr powder) of $[(Ti(CAT)(OCH_2tBu)_2)(HNMe_2)]_2$ (**1b**).

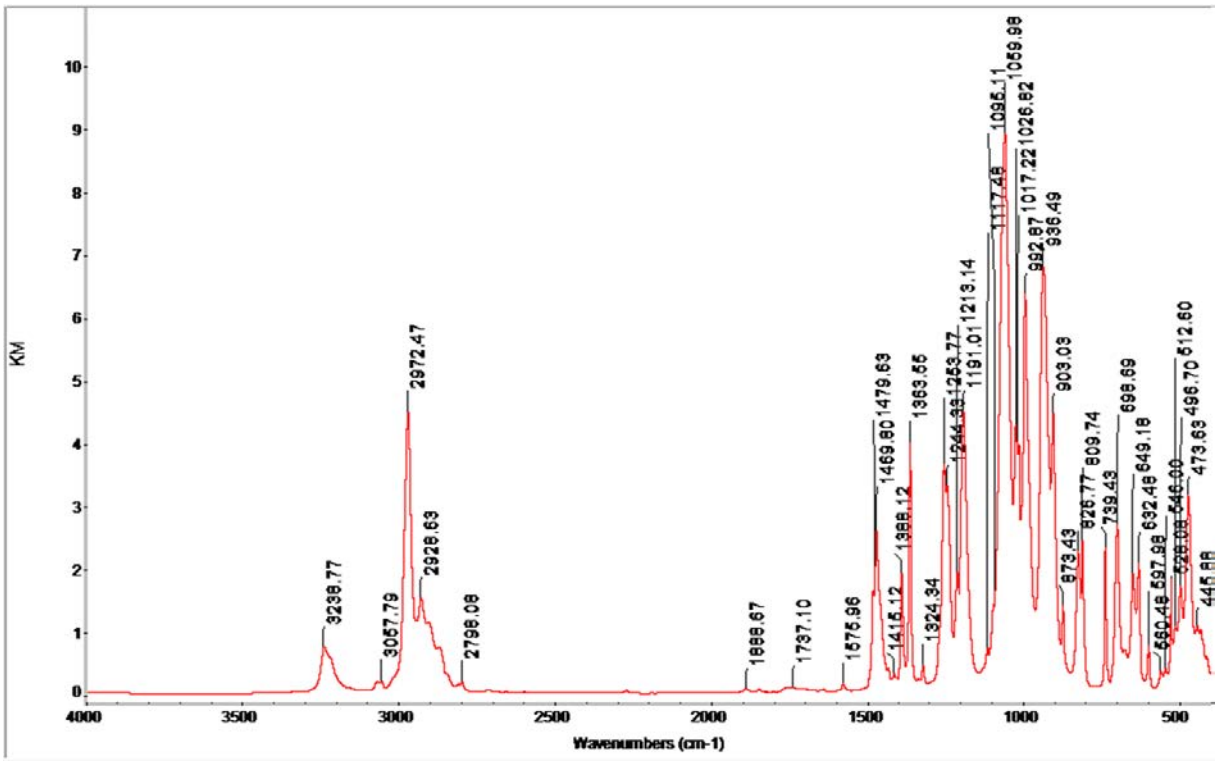

Figure S15. DRIFT spectrum (10 wt% in KBr powder) of $[Ti(CAT)\{OSi(OtBu)_3\}_2(HNMe_2)_2]_2$ (**1c**).

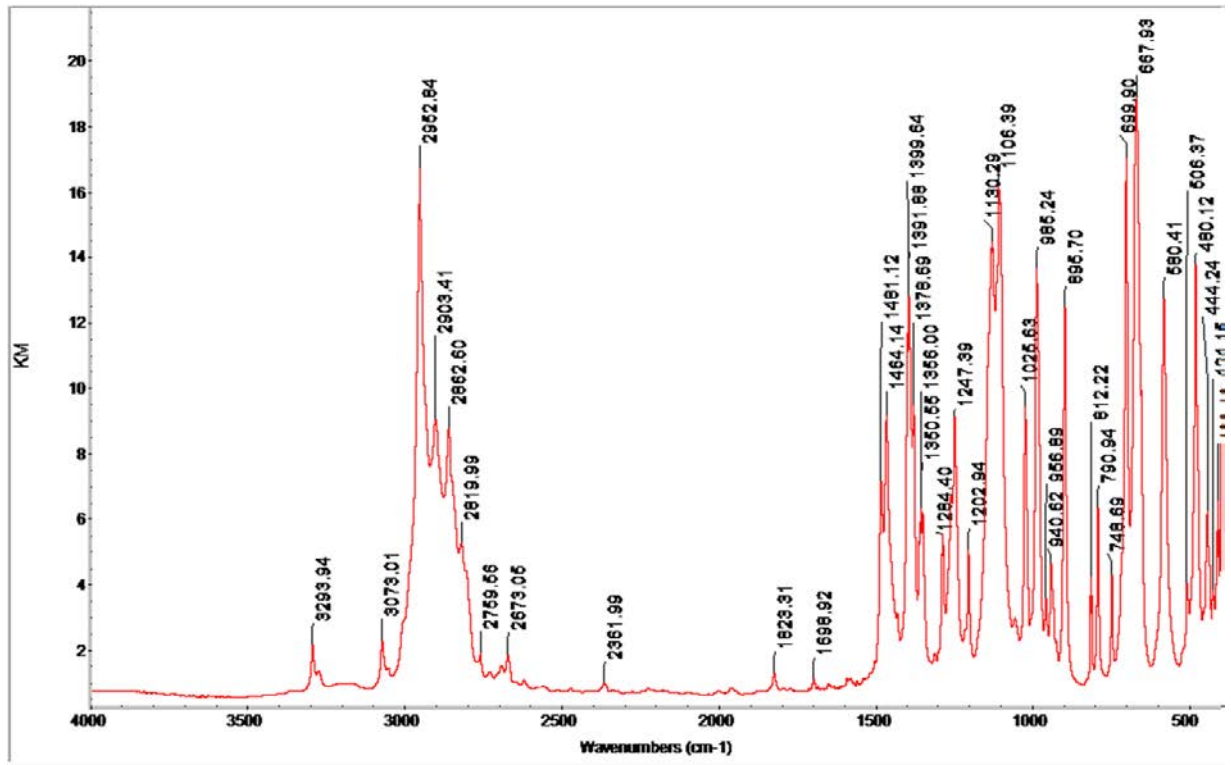

Figure S16. DRIFT spectrum (10 wt% in KBr powder) of Ti(CAT*t*Bu$_2$-3,6)(OCH$_2$*t*Bu)$_2$(HNMe$_2$)$_2$ (**2b**).

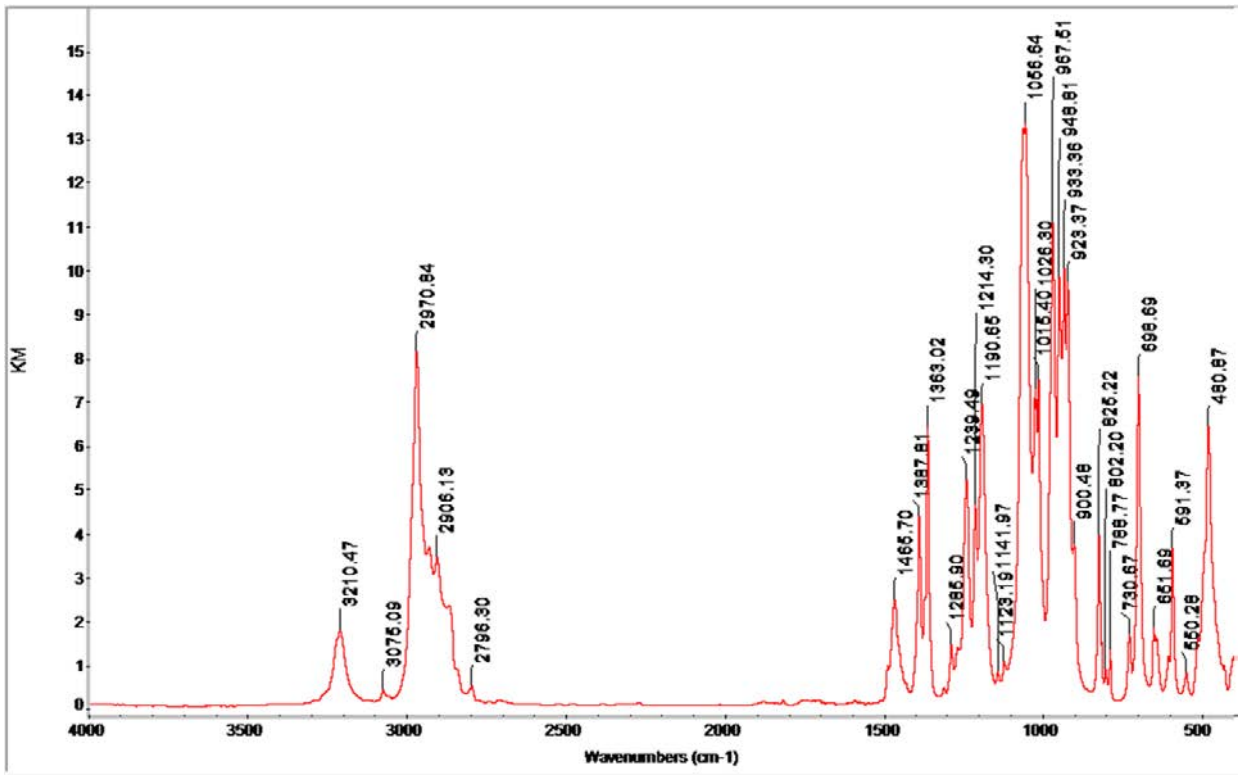

Figure S17. DRIFT spectrum (10 wt% in KBr powder) of Ti(CAT*t*Bu$_2$-3,6)[OSi(O*t*Bu)$_3$]$_2$(HNMe$_2$)$_2$ (**2c**).

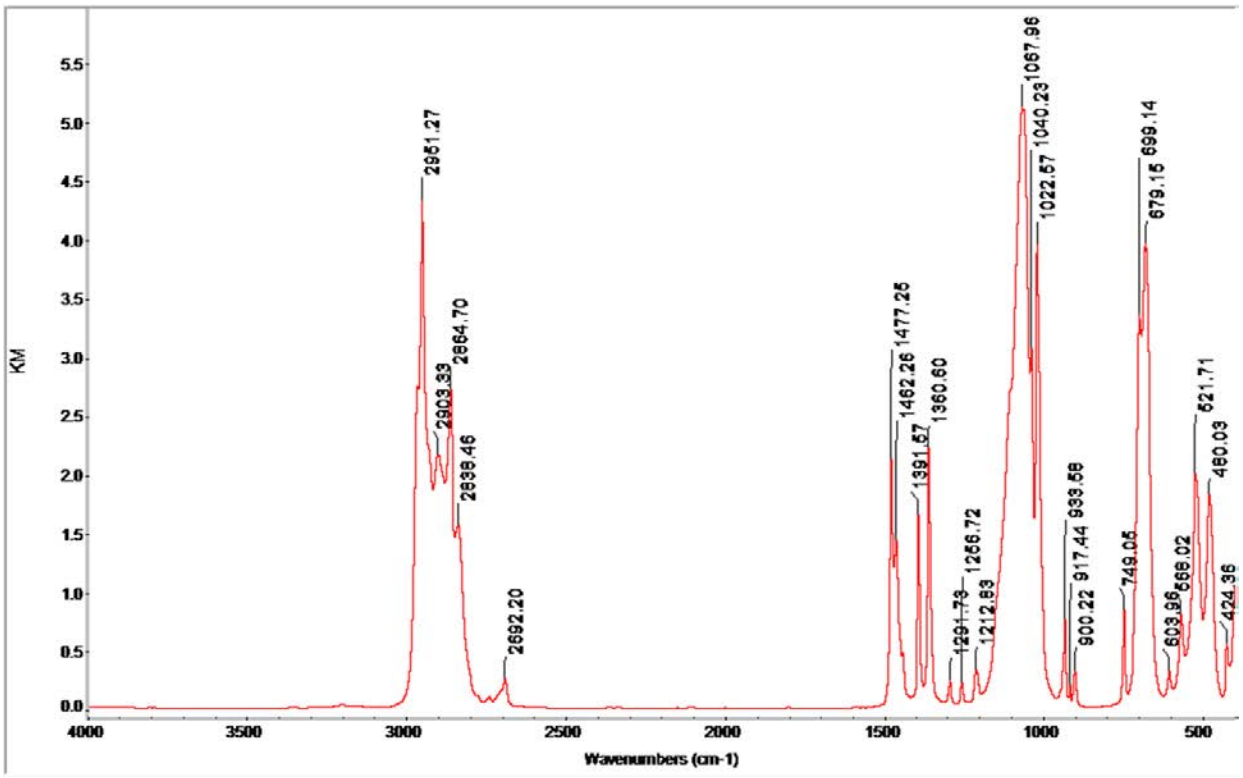

Figure S18. DRIFT spectrum (10 wt% in KBr powder) of $Ti(OCH_2tBu)_4$ (**3**).

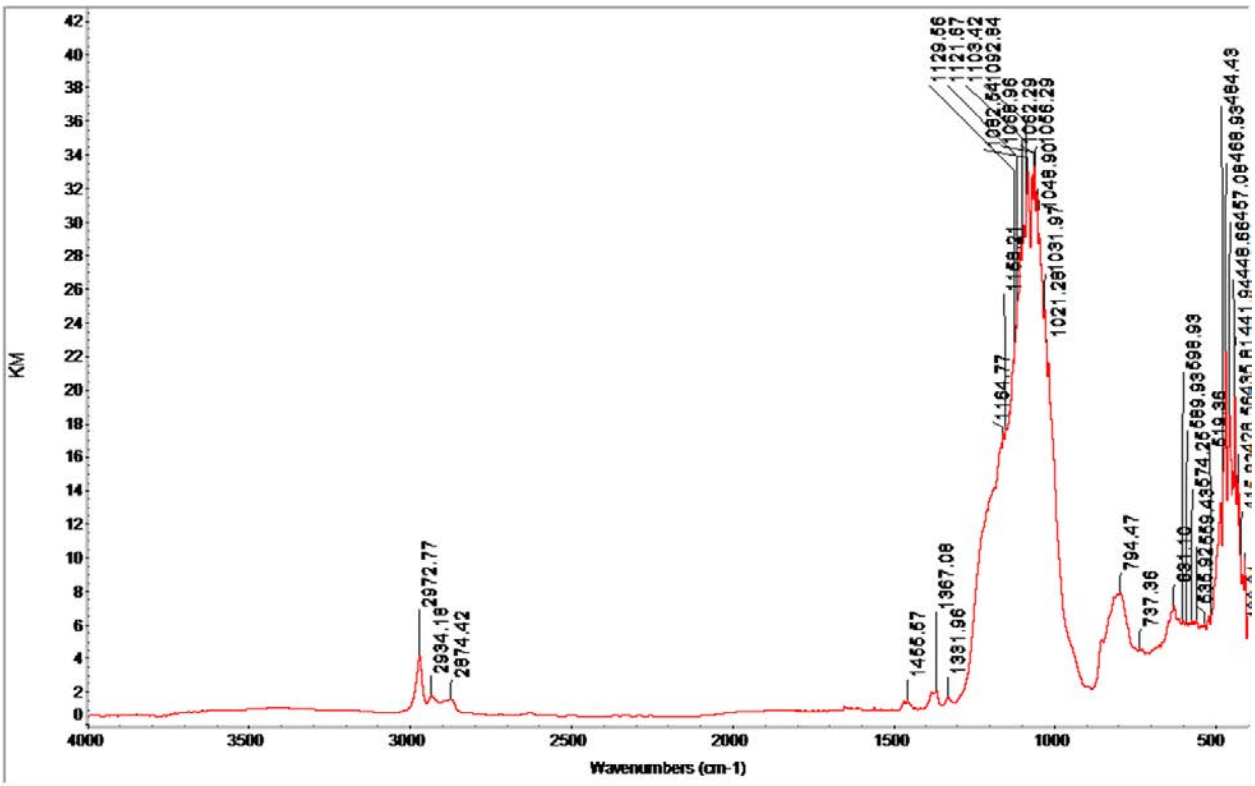

Figure S19. DRIFT spectrum (10 wt% in KBr powder) of $Ti(OiPr)_4$@[KIT-6] (**M1A1**).

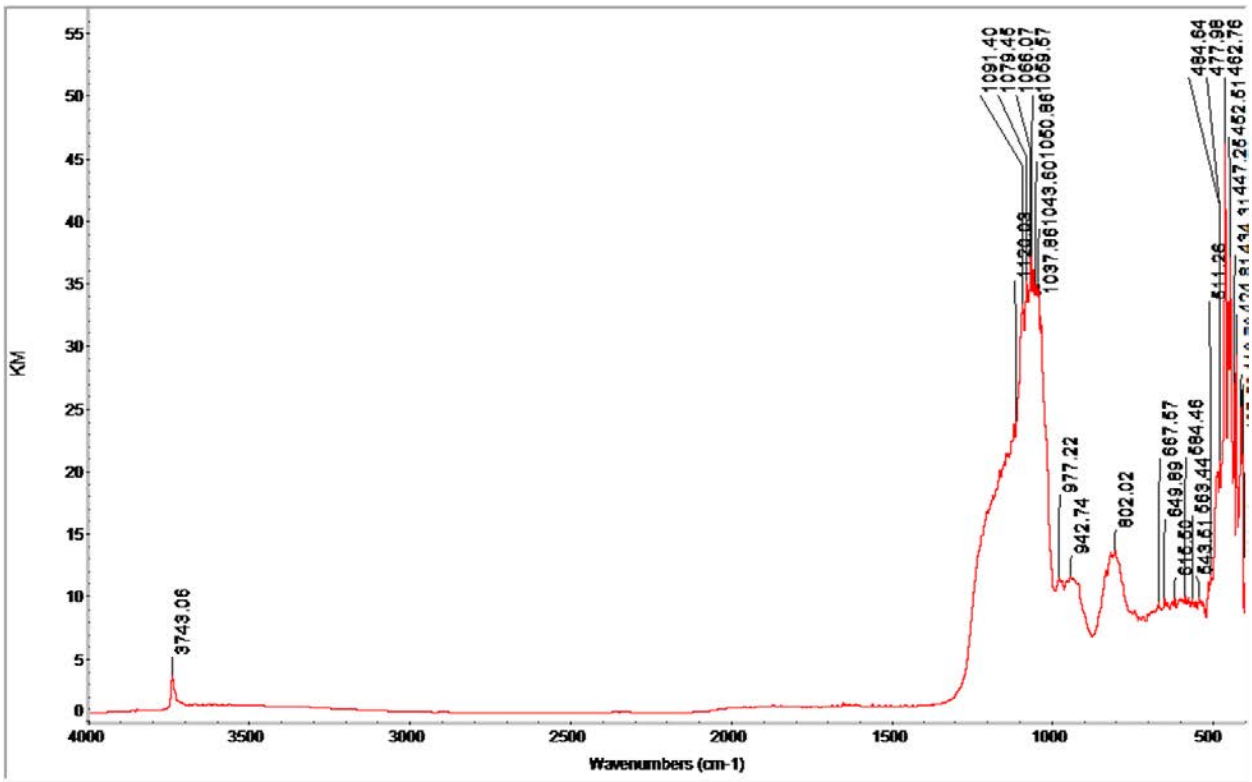

Figure S20. DRIFT spectrum (10 wt% in KBr powder) of $Ti(OH)_x$@[KIT-6] (**M1A2**).

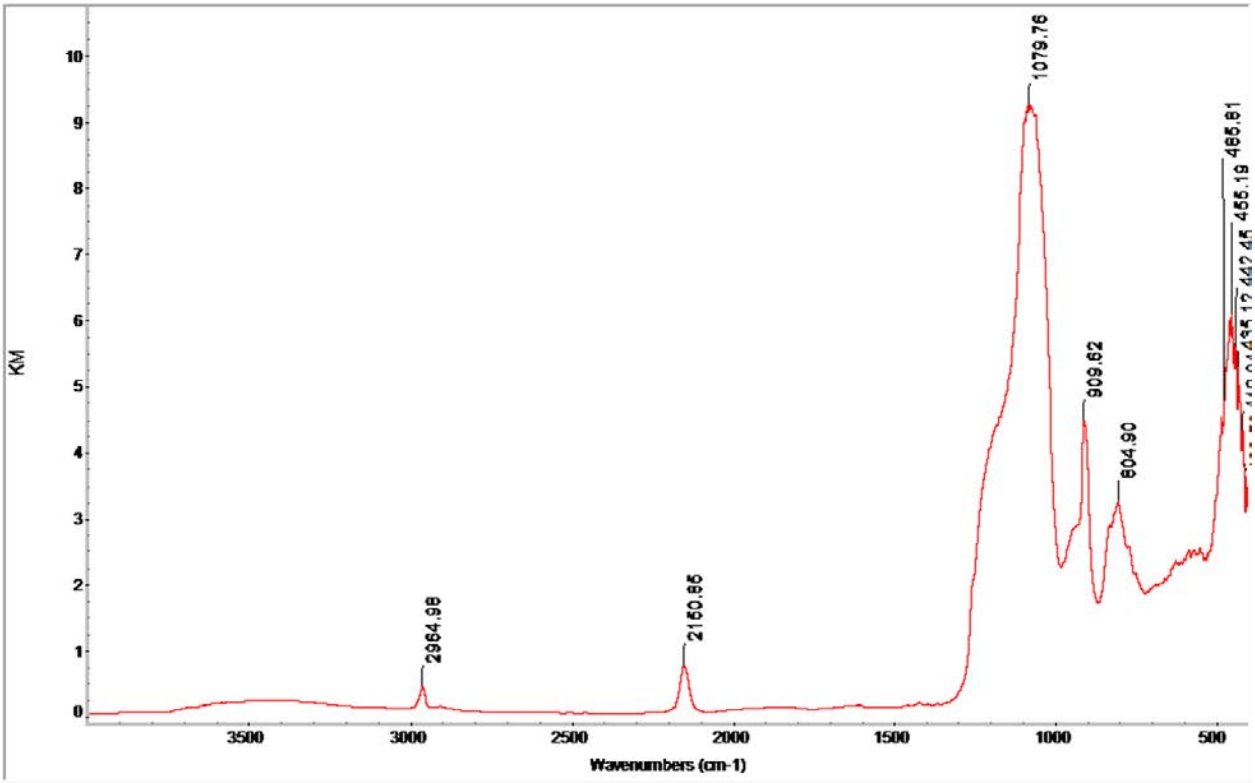

Figure S21. DRIFT spectrum (10 wt% in KBr powder) of $HN(SiHMe_2)_2$@$Ti(OH)_x$@[KIT-6] (**M1A2a**).

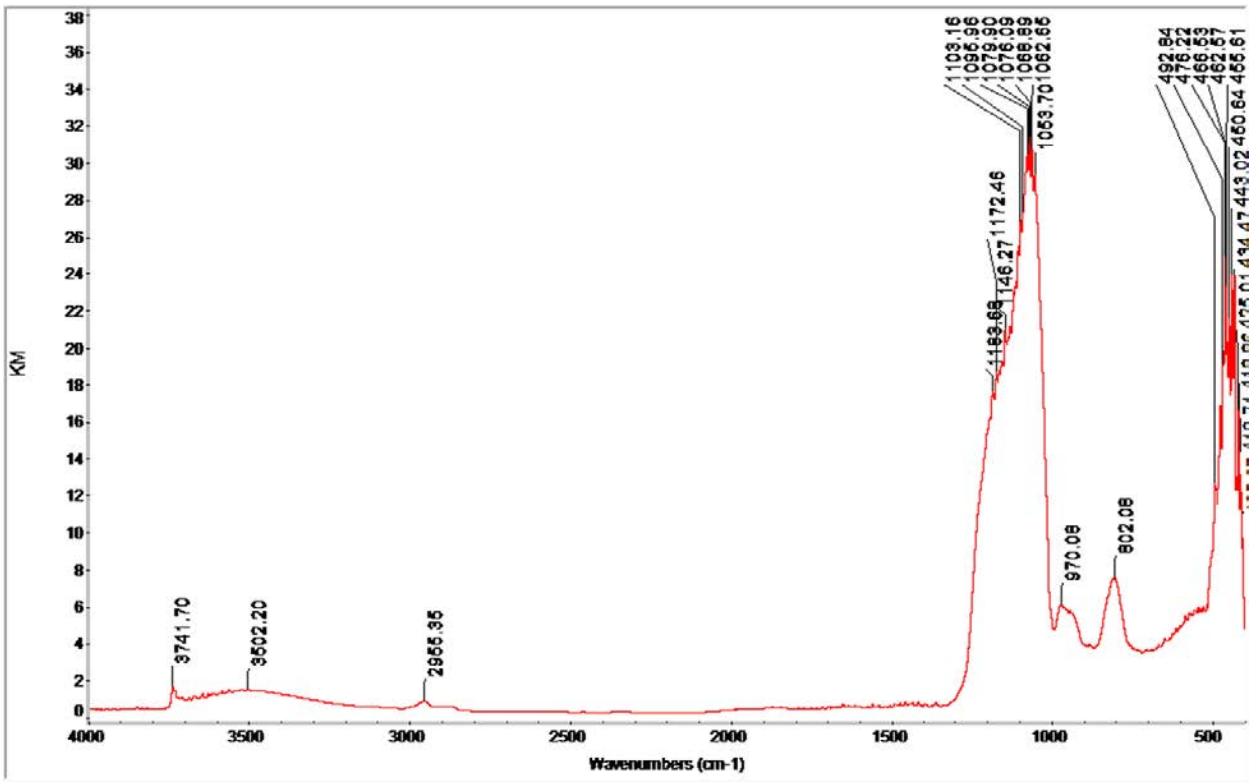

Figure S22. DRIFT spectrum (10 wt% in KBr powder) of $H_2CAT tBu_2$-3,6@$Ti(OH)_x$@[KIT-6] (**M1A3**).

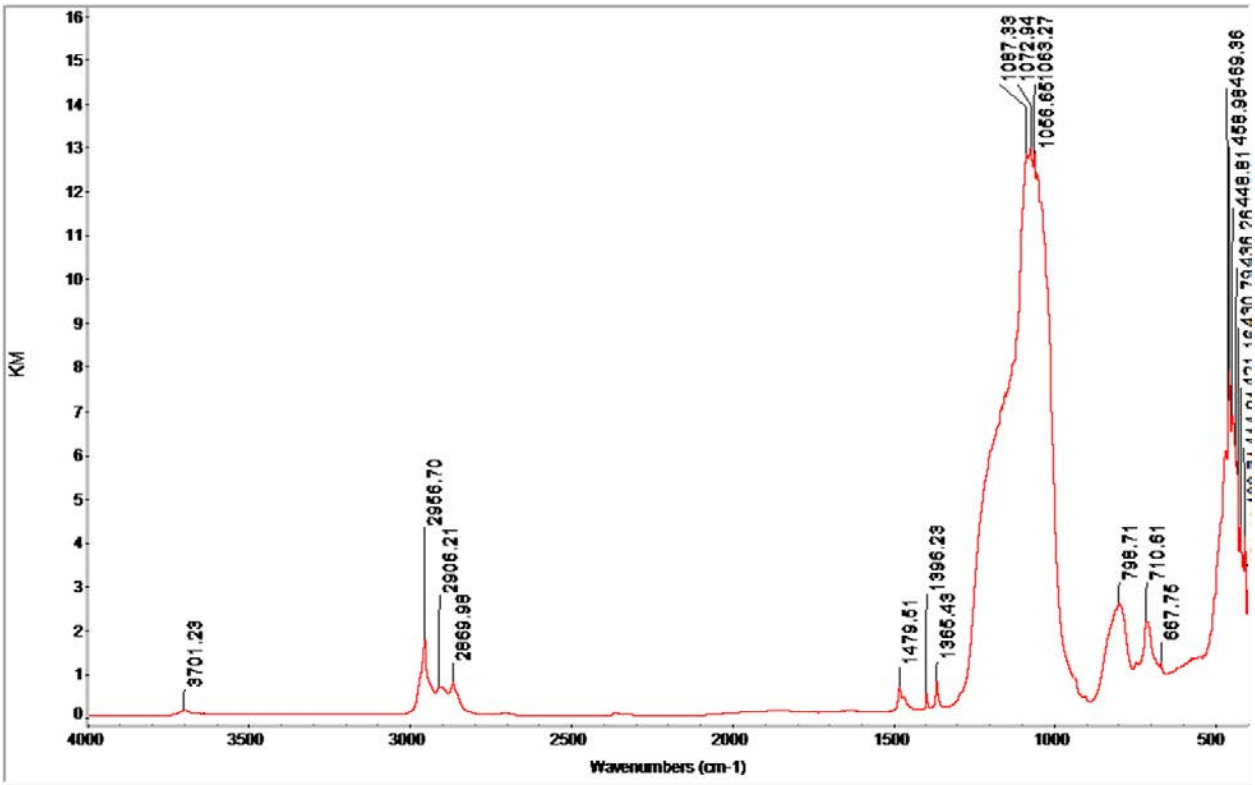

Figure S23. DRIFT spectrum (10 wt% in KBr powder) of $Ti(OCH_2tBu)_4$@[KIT-6](**M1S1**).

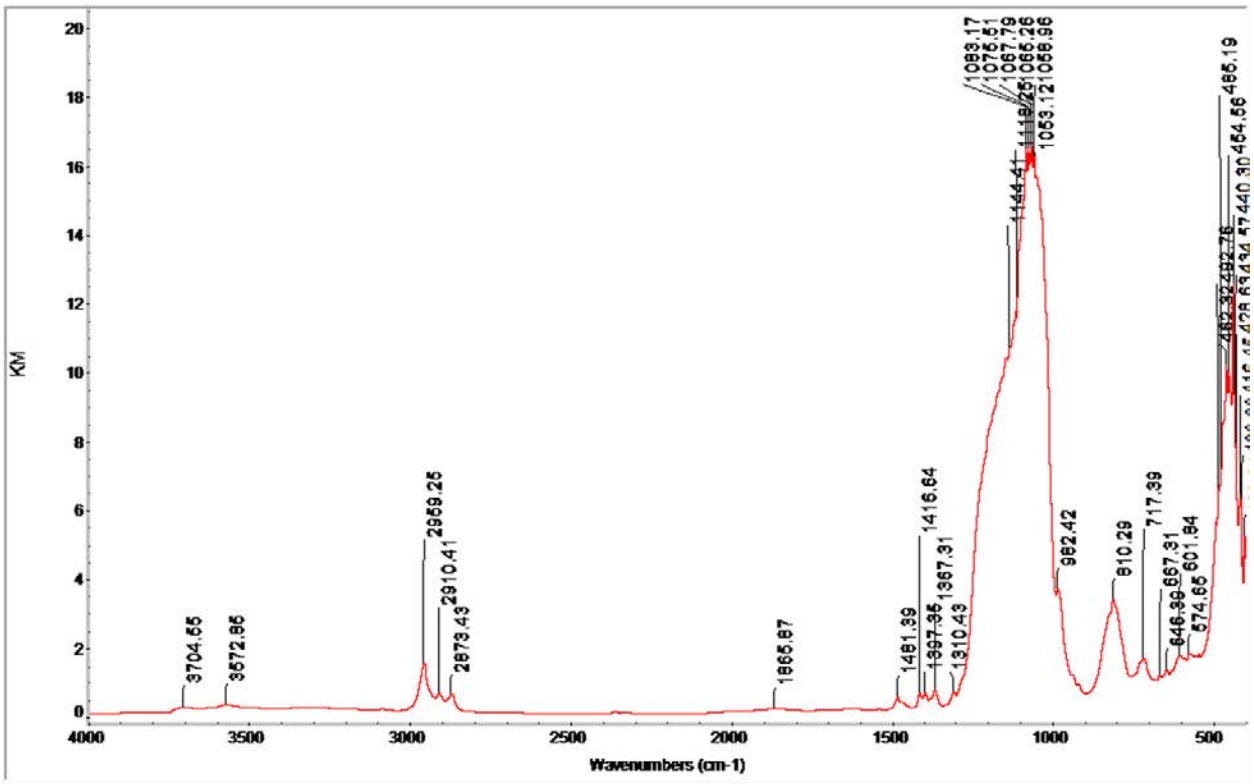

Figure S24. DRIFT spectrum (10 wt% in KBr powder) of H_2CAT*t*Bu_2-3,6@Ti(OCH_2*t*Bu)$_4$@[KIT-6](**M1S2**).

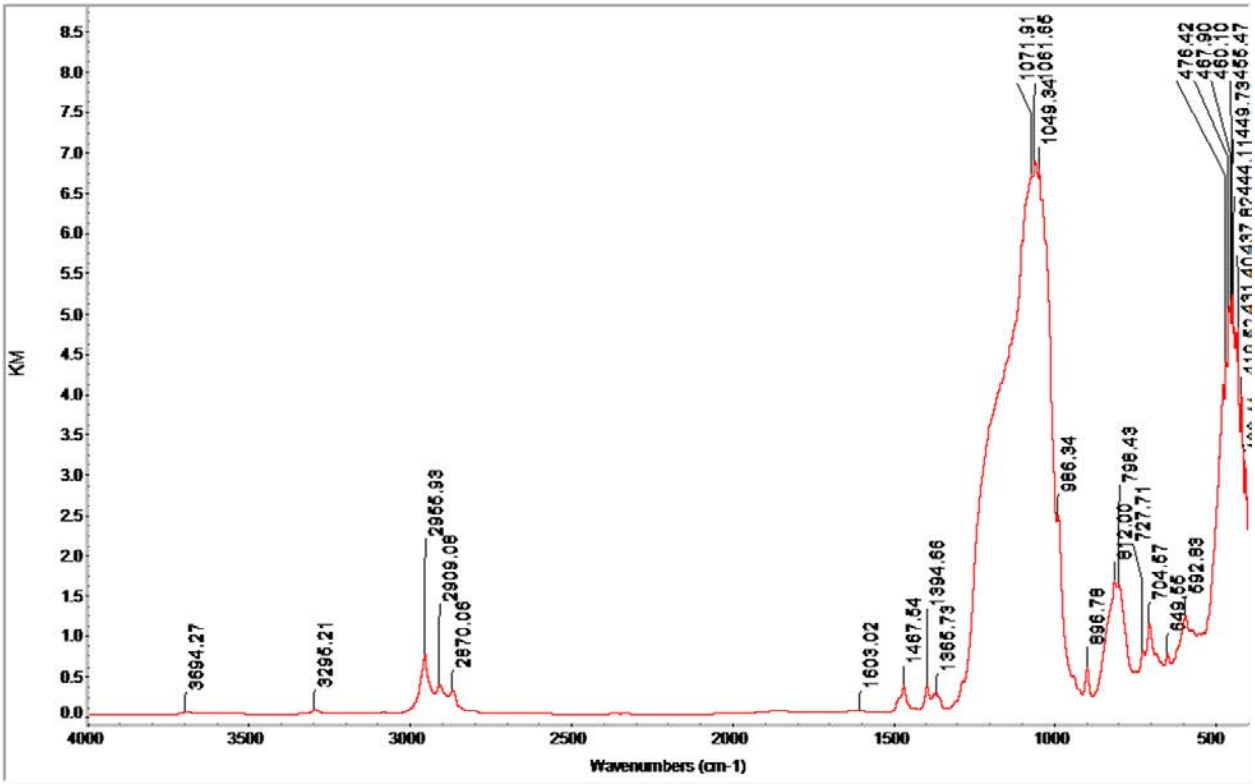

Figure S25. DRIFT spectrum (10 wt% in KBr powder) of [Ti(CAT*t*Bu_2-3,6)(OCH_2*t*Bu)$_2$($HNMe_2$)$_2$]@[KIT-6](**M1C1**).

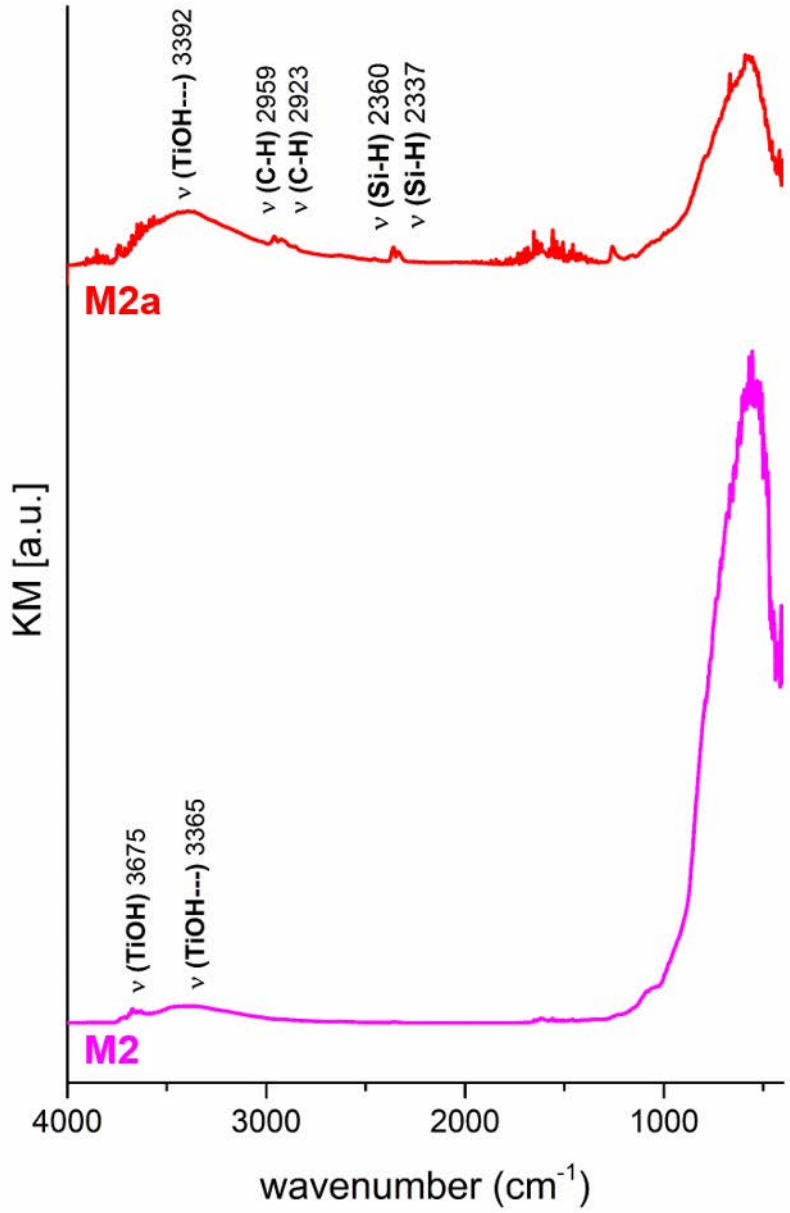

Figure S26. DRIFT spectra (10 wt% in KBr powder) of m-TiO_2 (**M2**) and $HN(SiHMe_2)_2$@[m-TiO_2] (**M2a**).

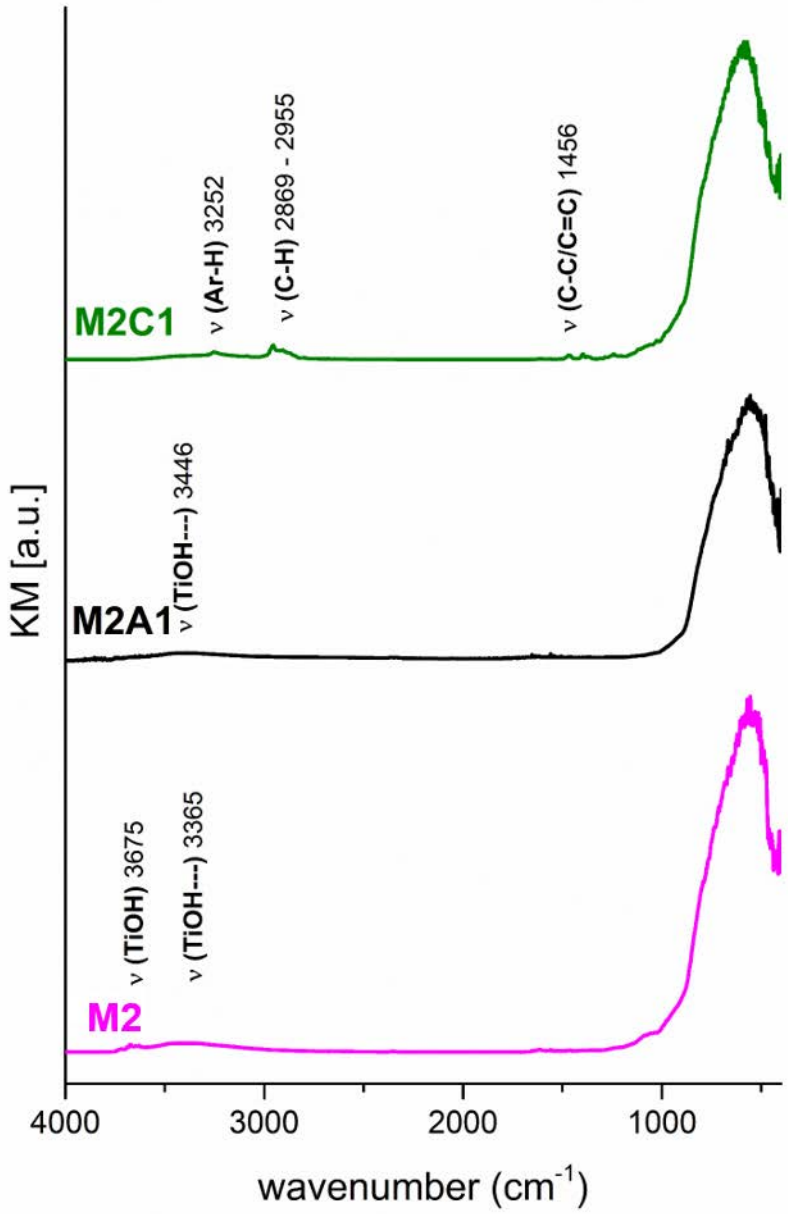

Figure S27. DRIFT spectra (10 wt% in KBr powder) of $H_2CAT^tBu_2$-3,6@[m-TiO_2] (**M2A1**) and [Ti(CAT^tBu_2-3,6)($OCH_2{}^tBu)_2(HNMe_2)_2$]@[m-TiO_2] (**M2C1**) compared to parent material m-TiO_2 (**M2**).

Nitrogen Physisorption

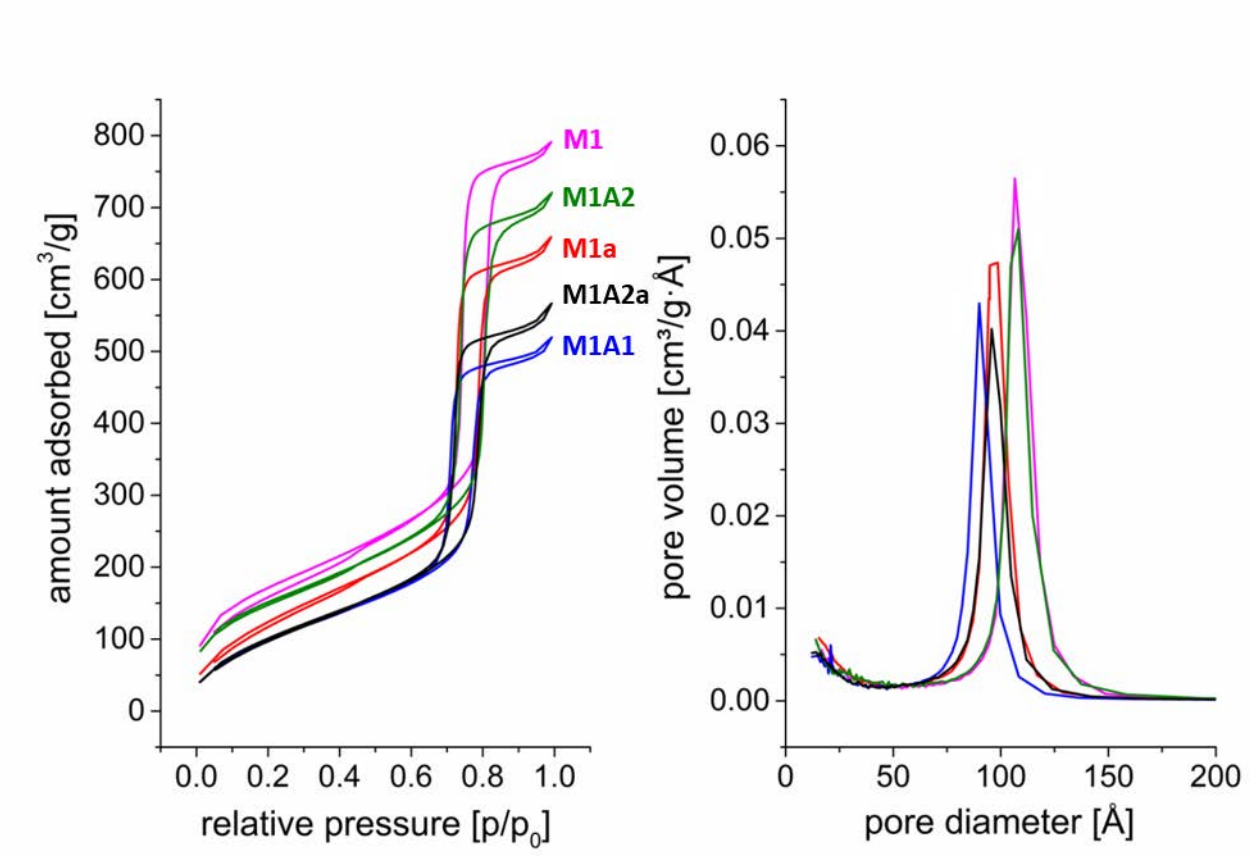

Figure S28. Nitrogen adsorption/desorption isotherms at 77.4K *(left)* and the corresponding BJH pore size distributions *(right),* derived from the respective isotherm adsorption branch, of KIT-6 (**M1**), $HN(SiHMe_2)_2$@[KIT-6] (**M1a**), $Ti(OiPr)_4$@[KIT-6] (**M1A1**), $Ti(OH)_x$@[KIT-6] (**M1A2**), and $HN(SiHMe_2)_2$@$Ti(OH)_x$@[KIT-6] (**M1A2a**).

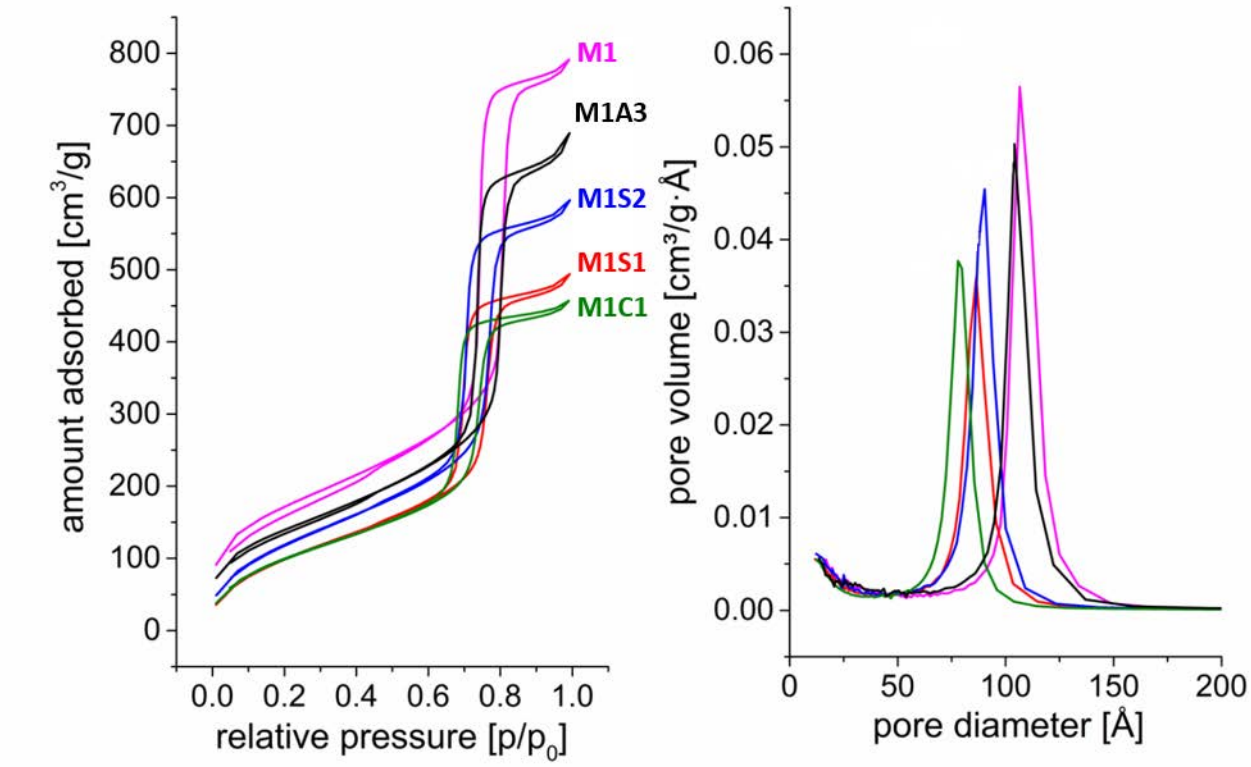

Figure S29. Nitrogen adsorption/desorption isotherms at 77.4K *(left)* and the corresponding BJH pore size distributions *(right)*, derived from the respective isotherm adsorption branch, of KIT-6 (**M1**), H_2CAT*t*Bu_2-3,6@$Ti(OH)_x$@[KIT-6] (**M1A3**), $Ti(OCH_2$*t*$Bu)_4$@[KIT-6](**M1S1**), H_2CAT*t*Bu_2-3,6@$Ti(OCH_2$*t*$Bu)_4$@[KIT-6](**M1S2**), and [$Ti(CAT$*t*Bu_2-3,6)$(OCH_2$*t*$Bu)_2(HNMe_2)_2$]@[KIT-6](**M1C1**).

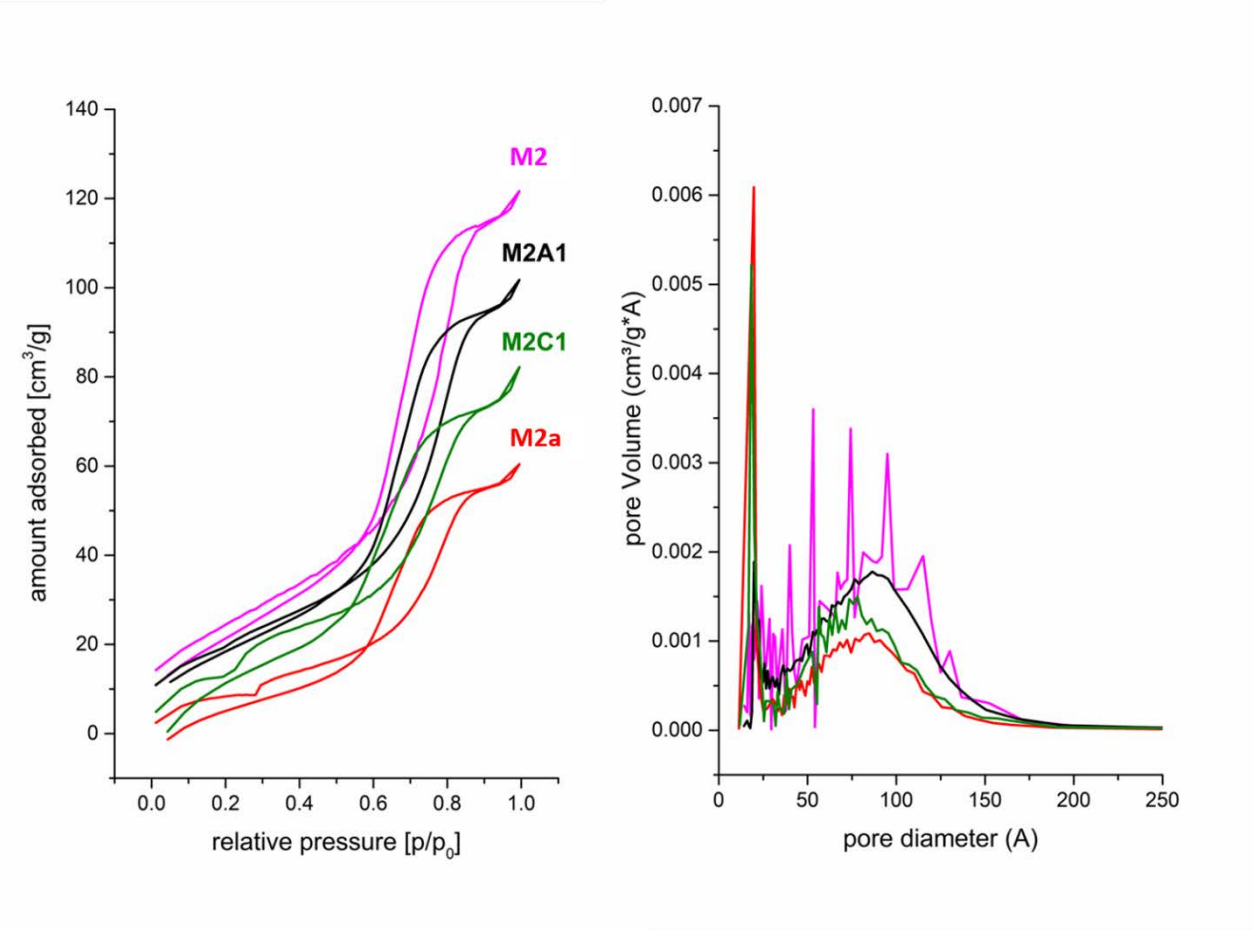

Figure S30. Nitrogen adsorptiom/desorption isotherms at 77.4K *(Left)* and the corresponding BJH pore size distributions *(Right),* derived from the respective isotherm adsorption branch, of m-TiO_2 (**M2**), $HN(SiHMe_2)_2$@[m-TiO_2] (**M2a**), $H_2CAT^tBu_2$-3,6@[m-TiO_2] (**M2A1**) and [$Ti(CAT^tBu_2$-3,6)$(OCH_2{}^tBu)_2(HNMe_2)_2$]@[m-$TiO_2$] (**M2C1**).

Elemental Analysis-based Calculations

Table S2. Elemental Analysis Data of Ti(O*i*Pr)$_4$@[KIT-6] (**M1A1**), H$_2$CAT*t*Bu$_2$-3,6@Ti(OH)$_x$@[KIT-6] (**M1A3**), Ti(OCH$_2$*t*Bu)$_4$@[KIT-6](**M1S1**), H$_2$CAT*t*Bu$_2$-3,6@Ti(OCH$_2$*t*Bu)$_4$@[KIT-6](**M1S2**), and [Ti(CAT*t*Bu$_2$-3,6)(OCH$_2$*t*Bu)$_2$(HNMe$_2$)$_2$]@[KIT-6](**M1C1**)

[a] … @KIT-6	[b] ω $_{Ti, EA}$ [wt%]	[c] ω $_{C, EA}$ [wt%]	[d] $\left[\frac{b_C}{b_{Ti}}\right]^{exp.}_{total}$
[a] **M1A1** Ti(O*i*Pr)$_4$	5.07*	9.76	7.7/1
[a] **M1A3** H$_2$CAT*t*Bu$_2$-3,6@Ti(OH)$_x$	3.53	4.92	5.6/1
[a] **M1S1** Ti(OCH$_2$*t*Bu)$_4$	3.74	12.66	14/1
[a] **M1S2** H$_2$CAT*t*Bu$_2$-3,6@Ti(OCH$_2$*t*Bu)$_4$	1.47	13.12	36/1
[a] **M1C1** [Ti(CAT*t*Bu$_2$-3,6)(OCH$_2$*t*Bu)$_2$(HNMe$_2$)$_2$]	2.82	15.77	22/1

[a] Compound grafted onto KIT-6.

[b] Weight percentage titanium obtained via ICP-OES.

[c] Weight percentage carbon obtained via CHNS elemental analysis.

[d] Ratio of corrected weight percentage values of carbon and titanium. Corrected weight percent values were calculated as follows[1,2] from experimentally obtained data: $\omega_i = \omega_{i,EA} / [(1\text{-}10^{-2})(\sum_i \omega_{i,EA})]$ Equation (S1).

* From hydrolyzed **M1A1** alias **M1A2** Ti(OH)$_x$@KIT-6.

Calculation based on elemental analysis and ICP-OES data

M1a – HN(SiHMe$_2$)$_2$@[KIT-6]:

$\omega_{i,EA}$ = C, 4.46; H, 0.50; N, 0.03 wt%.

2 SiO-H + HN[SiH(CH$_3$)$_2$]$_2$ → 2 SiO-SiH(CH$_3$)$_2$ + NH$_3$ Equation (S2)

For the parent KIT-6 material there is 1 hydrogen atom per surface SiOH group before-, and 1 silicon, 2 carbon and 7 hydrogen atoms after grafting. Thus: ΔSi = 1, ΔC = 2 and ΔH = 6.
These values are used to calculate the percentage contents %E of all these elements related to carbon, whereas the carbon content itself is used as received:

$$\%E = \frac{\Delta E * M_E}{\Delta C * M_C} \cdot \%C \qquad \text{Equation (S3)}$$

The obtained values are further used to calculate the relative carbon value, which tells the relative fraction of carbon-related to non-carbon-related species in wt%:

$$C_{Corr} = \frac{\%C}{100\% - \sum \%E_i} \qquad \text{Equation (S4)}$$

This can be taken to determine the amount of required surface sites for the postulated surface species and the given experimental results from elemental analyses:

$$\delta\ (SiOH) = \frac{\delta(C)}{\Delta C} = \frac{C_{corr}}{\Delta C * M_C} \qquad \text{Equation (S5)}$$

For the parent KIT-6 material the amount of surface silanol groups was δ(SiOH) =2.08 mmol g^{-1}.

^{13}C MAS NMR of material **M1S1** (Ti(OCH$_2$*t*Bu)$_4$@[KIT-6]) revealed the presence of a significant amount of neopentanol on the KIT-6 surface. The SiO-H stretching vibration in the corresponding DRIFT spectrum implies for non-consumed surface silanols, which are very likely to be blocked by neopentanol.

M1S1 – Ti(OCH$_2$*t*Bu)$_4$@[KIT-6]
δ_{OH}(KIT-6) = 2.08 mmol g^{-1}
$\omega_{i,EA}$ = C, 12.66; H, 2.36; Ti, 3.74 wt%.

Obtain correlated values:
The elemental contents $\omega_{i,EA}$, obtained *via* elemental analyses, are related to the overall system (grafted surface species onto silica top-layer and silica bulk). They need to be related only to the top-layer (silica substrate). Therefore, correlated values ω_i are calculated according to equation (S1).

The correlated elemental content ω_i related to 1 g material ($m_{\omega(i)} = \frac{\omega_i}{100}$ g) gives, divided by the respective atomic weight M_i, the molar surface coverage a_i with element i, (see Table S3).

Table S3. M1S1 – Ti(OCH$_2$*t*Bu)$_4$@[KIT-6]

i	ω_i [wt%]	$a_i = \frac{m_{\omega(i)}}{M_i} * 1000$ [mmol]	$b_i = \frac{a_i}{\text{smallest } a_i}$
C	15.58	13.0	13.5
H	2.90	28.8	30.0
Ti	4.60	0.961	1.00

Estimation of surface species type from titanium content:
The ratio of accessible surface hydroxyls to surface loading with titanium species is $\delta_{OH} : a_{Ti}$ = 2.08 : 0.961 ~ 2.2 : 1.0. For bipodal grafting a ratio of 2 : 1 is to be expected and for monopodal grafting the expected ratio would be 1 : 1. Therefore, the Ti(OCH$_2$*t*Bu)$_4$ is probably bipodally anchored at the KIT-6 surface.

In the case of H$_2$CAT*t*Bu$_2$-3,6@Ti(OCH$_2$*t*Bu)$_4$@[KIT-6] (**M1S2**), the calculations have been performed analogously:
M1S2 – H$_2$CAT*t*Bu$_2$-3,6@Ti(OCH$_2$*t*Bu)$_4$@[KIT-6]
δ_{OH}(KIT-6) = 2.08 mmol g^{-1}
$\omega_{i,EA}$ = C, 13.12; H, 2.04; Ti, 1.47 wt%.

Obtain correlated values:
The elemental contents $\omega_{i,EA}$, obtained *via* elemental analyses, are related to the overall system (grafted surface species onto silica top-layer and silica bulk). They need to be related only to the top-layer (silica substrate). Therefore, correlated values ω_i are calculated as follows according to equation (S1).

The correlated elemental content ω_i related to 1 g material ($m_{\omega(i)} = \frac{\omega_i}{100}$ g) gives, divided by the respective atomic weight M_i, the molar surface coverage a_i with element i, (see Table S4).

Table S4. M1S2 – H$_2$CAT*t*Bu$_2$-3,6@Ti(OCH$_2$*t*Bu)$_4$@[KIT-6]

i	ω_i [wt%]	$a_i = \frac{m_{\omega(i)}}{M_i} * 1000$ [mmol]	$b_i = \frac{a_i}{\text{smallest } a_i}$
C	15.74	13.1	35.6
H	2.45	24.3	66.0
Ti	1.76	0.368	1.00

Estimation of surface species type from titanium content:
The ratio of accessible surface hydroxyls to surface loading with titanium species is $\delta_{OH} : a_{Ti} = 2.08 : 0.368 \sim 5.7 : 1.0$. Thus, less titanium species are present at the surface of **M1S2** than at the one of **M1S1**. This implies for leaching of titanium species upon ligand exchange.

In the case of [Ti(CAT*t*Bu$_2$-3,6)(OCH$_2$*t*Bu)$_2$(HNMe$_2$)$_2$]@[KIT-6] (**M1C1**), the calculations have been performed analogously:

M1C1 – [Ti(CAT*t*Bu$_2$-3,6)(OCH$_2$*t*Bu)$_2$(HNMe$_2$)$_2$]@[KIT-6]
δ_{OH}(KIT-6) = 2.08 mmol g^{-1}
$\omega_{i,EA}$ = C, 15.77; H, 2.54; N, 1.59; Ti, 2.82 wt%.

Obtain correlated values:
The elemental contents $\omega_{i,EA}$, obtained *via* elemental analyses, are related to the overall system (grafted surface species onto silica top-layer and silica bulk). They need to be related only to the top-layer (silica substrate). Therefore, correlated values ω_i are calculated according to equation (S1).

The correlated elemental content ω_i related to 1 g material ($m_{\omega(i)} = \frac{\omega_i}{100}$ g) gives, divided by the respective atomic weight M_i, the molar surface coverage a_i with element i, (see Table S5).

Table S5. M1C1 – [Ti(CAT*t*Bu$_2$-3,6)(OCH$_2$*t*Bu)$_2$(HNMe$_2$)$_2$]@[KIT-6]

i	ω_i [wt%]	$a_i = \frac{m_{\omega(i)}}{M_i} * 1000$ [mmol]	$b_i = \frac{a_i}{\text{smallest } a_i}$
C	20.4	17.0	22.3
H	3.29	32.6	42.7
N	2.06	1.47	1.93
Ti	3.65	0.763	1.00

Estimation of surface species type from titanium content:
The ratio of accessible surface hydroxyls to surface loading with titanium species is $\delta_{OH} : a_{Ti} = 2.08 : 0.763 \sim 2.7 : 1.0$. As mentioned above, for bipodal grafting a ratio of 2 : 1 is to be expected and for monopodal grafting the expected ratio would be 1 : 1.
Therefore, Ti(CAT*t*Bu$_2$-3,6)(OCH$_2$*t*Bu)$_2$(HNMe$_2$)$_2$ is, like Ti(OCH$_2$*t*Bu)$_4$, probably bipodally anchored at the KIT-6 surface, too.

In the case of $H_2CAT\textit{t}Bu_2$-3,6@$Ti(OH)_x$@[KIT-6] (**M1A3**), the calculations have been performed analogously:

M1A3 – $H_2CAT\textit{t}Bu_2$-3,6@$Ti(OH)_x$@[KIT-6]
δ_{OH}(KIT-6) = 2.08 mmol g^{-1}
$\omega_{i,EA}$ = C, 4.92; H, 1.04; N, 0.16; Ti, 3.53 wt%.

Obtain correlated values:
The elemental contents $\omega_{i,EA}$, obtained *via* elemental analyses, are related to the overall system (grafted surface species onto silica top-layer and silica bulk). They need to be related only to the top-layer (silica substrate). Therefore, correlated values ω_i are calculated according to equation (S1).

The correlated elemental content ω_i related to 1 g material ($m_{\omega(i)} = \frac{\omega_i}{100}$ g) gives, divided by the respective atomic weight M_i, the molar surface coverage a_i with element i (see Table S6).

Table S6: M1A3 – $H_2CAT\textit{t}Bu_2$-3,6@$Ti(OH)_x$@[KIT-6]

i	ω_i [wt%]	$a_i = \frac{m_{\omega(i)}}{M_i} * 1000$ [mmol]	$b_i = \frac{a_i}{\text{smallest } a_i}$
C	5.44	4.53	5.56
H	1.15	11.4	14.0
Ti	3.90	0.815	1.00

Estimation of surface species type from titanium content:
The ratio of accessible surface hydroxyls to surface loading with titanium species is $\delta_{OH} : a_{Ti}$ = 2.08 : 0.815 ~ 2.6 : 1.0. As mentioned before, for bipodal grafting a ratio of 2 : 1 is to be expected and for monopodal grafting the expected ratio would be 1 : 1.
If only considering the titanium content, one might assume the titanium surface species to be a bipodal one at the KIT-6 surface upon immobilization of $H_2CAT\textit{t}Bu_2$-3,6 at $Ti(OH)_x$@[KIT-6]. Considering the very low carbon content, too, the surface coverage for **M1A3** in general is low.

M1A2a - $HN(SiHMe_2)_2$@$Ti(OH)_x$@[KIT-6]:
$\omega_{i,EA}$ = C, 4.03; H, 1.20; N, 0.24 wt%.
2 TiO-H + $HN[SiH(CH_3)_2]_2$ → 2 TiO-$SiH(CH_3)_2$ + NH_3 Equation (S6)

For the material $Ti(OH)_x$@[KIT-6] there is 1 hydrogen atom per surface TiOH group before, and 1 silicon, 2 carbon and 7 hydrogen atoms after grafting. Thus: ΔSi = 1, ΔC = 2 and ΔH = 6.
These values are used to calculate the percentage contents %E of all these elements related to carbon (Equation (S3)), whereas the carbon content itself is used as received.

The obtained values are further used to calculate the relative carbon value according to Equation (S4), which tells the relative fraction of carbon-related to non-carbon-related species in wt%

This can be taken to determine the amount of required surface sites for the postulated surface species and the given experimental results from elemental analyses (Equation (S5)).

For the material $Ti(OH)_x$@[KIT-6] the amount of surface TiOH-groups was δ(TiOH) = 1.86 mmol g^{-1}.

Powder X-Ray Diffraction

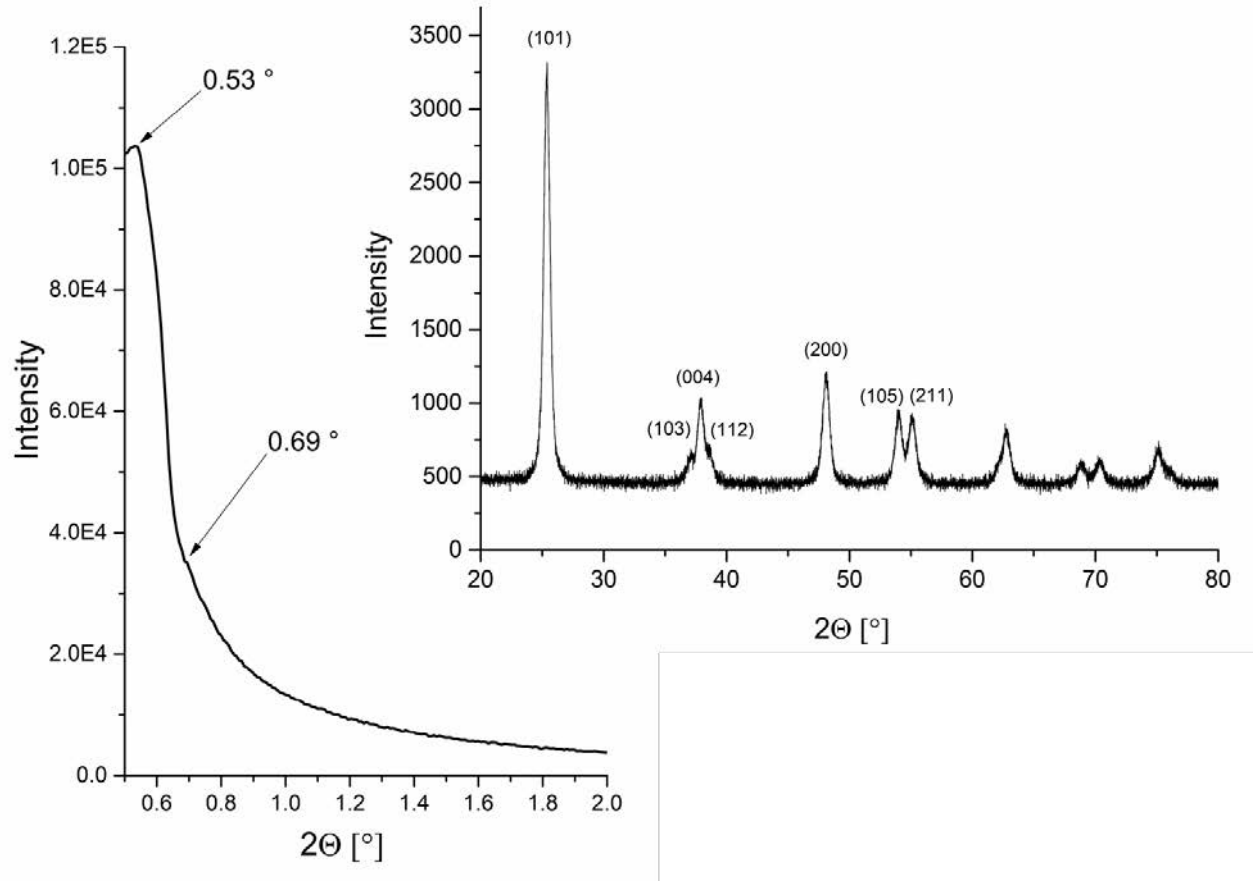

Figure S31. PXRDs of m-TiO_2 (**M2**). Small-angle (SA) PXRD: The d-spacings were calculated with Bragg´s law. But as the reflexes were not very sharp, no assignment was made *(left)*. Wide-angle (WA) PXRD: The planes belonging to the obtained reflex pattern indicate the m-TiO_2 to be anatase *(right)*.

X-Ray Photoelectron Survey Spectra

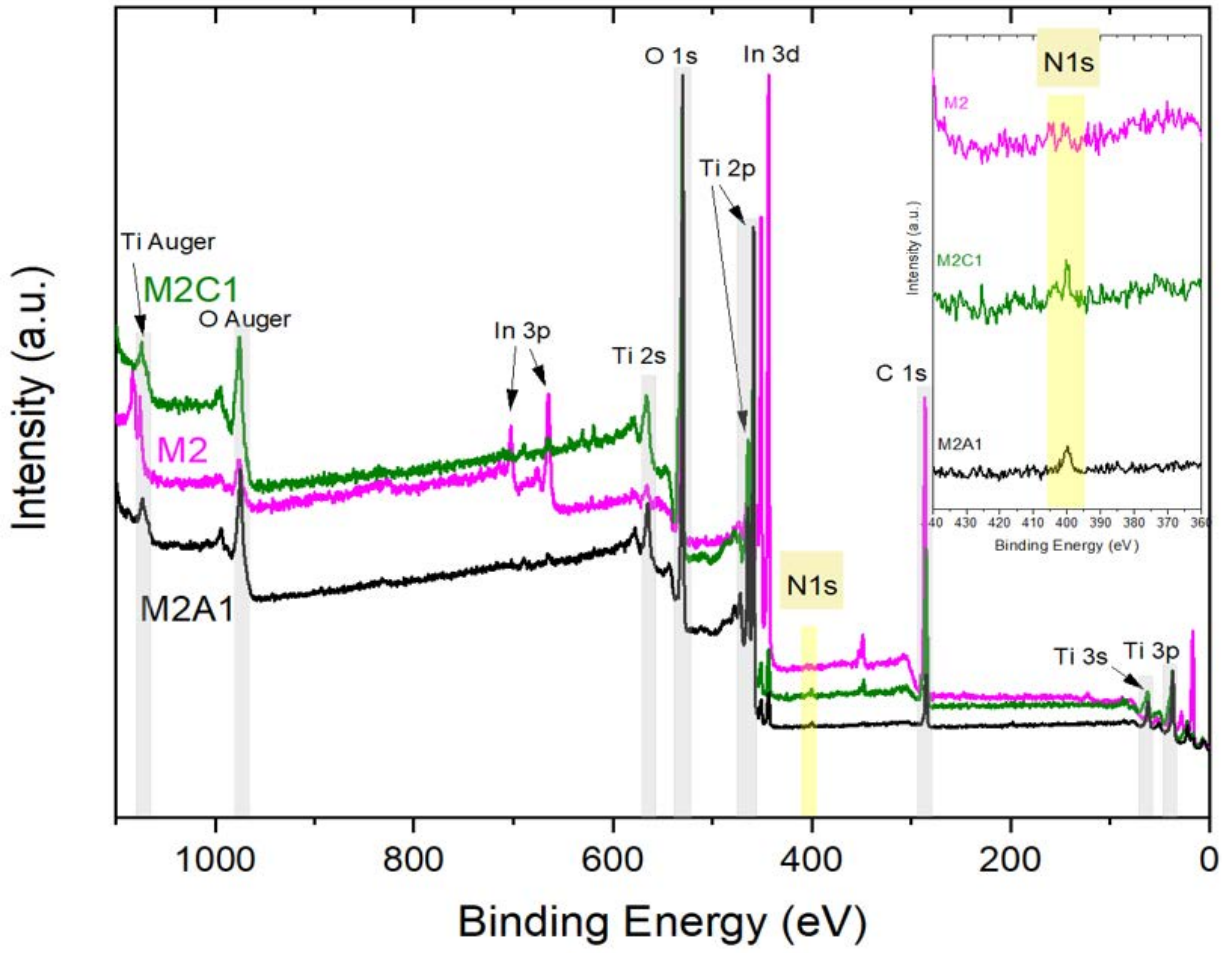

Figure S32. XP survey spectra of m-TiO_2 (**M2**), [Ti(CAT*t*Bu_2-3,6)(OCH_2*t*Bu)$_2$($HNMe_2$)$_2$]@[m-TiO_2] (**M2C1**) and H_2CAT*t*Bu_2-3,6@[m-TiO_2] (**M2A1**).

XPS surface sensitivity

The C 1s core-level spectrum of the m-TiO_2 (**M2**), shown in Figure 4a of the manuscript, displays a pronounced, symmetric peak at 286.2 eV. The elemental analysis results of the calcined material (see: Experimental section) gave a value for the carbon content of only 0.03 wt%, which is below the resolution limit (0.05 wt%) for C,H,N-elemental analysis (*EA*) with TPD columns. In the field of synthesis chemistry, the m-TiO2 (**M2**) is therefore defined as pure concerning residual compounds from the synthesis, as the carbon content is considered negligible. Since XPS has a much lower detection limit than elemental analysis (the sensitivity is three magnitudes higher in XPS than in elemental analysis), the peak at 286.2 eV in the C1s spectrum of **M2** shows traces of-impurities from the synthesis process, which are strongly coordinating to the m-TiO2 surface. The peak energy position suggests that the contaminants are alcohols.[3]

Solid-state UV/VIS Spectra

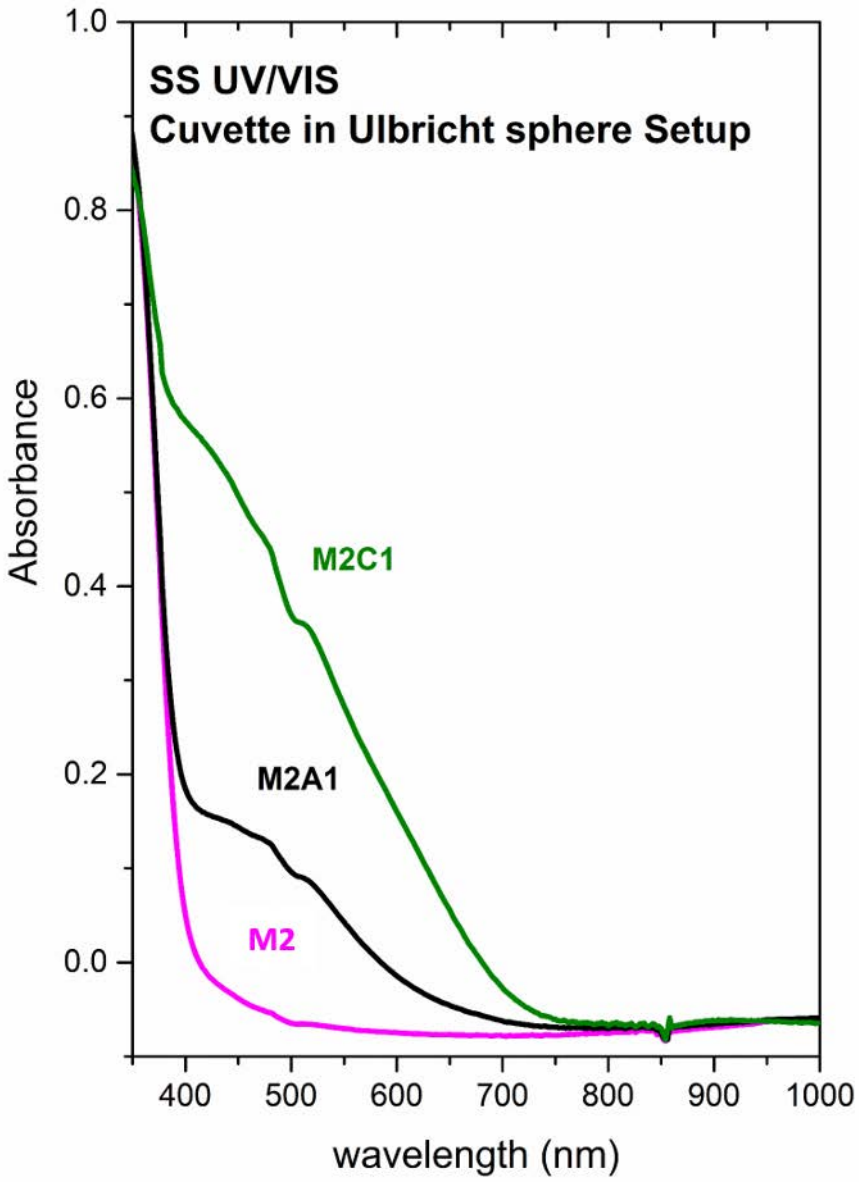

Figure S33. Solid-state UV/VIS spectra of m-TiO_2 (**M2**), [Ti(CAT*t*Bu_2-3,6)(OCH_2*t*Bu)$_2$($HNMe_2$)$_2$]@[m-TiO_2] (**M2C1**), and H_2CAT*t*Bu_2-3,6@[m-TiO_2] (**M2A1**). (Setup: Cuvette in Ulbricht sphere).

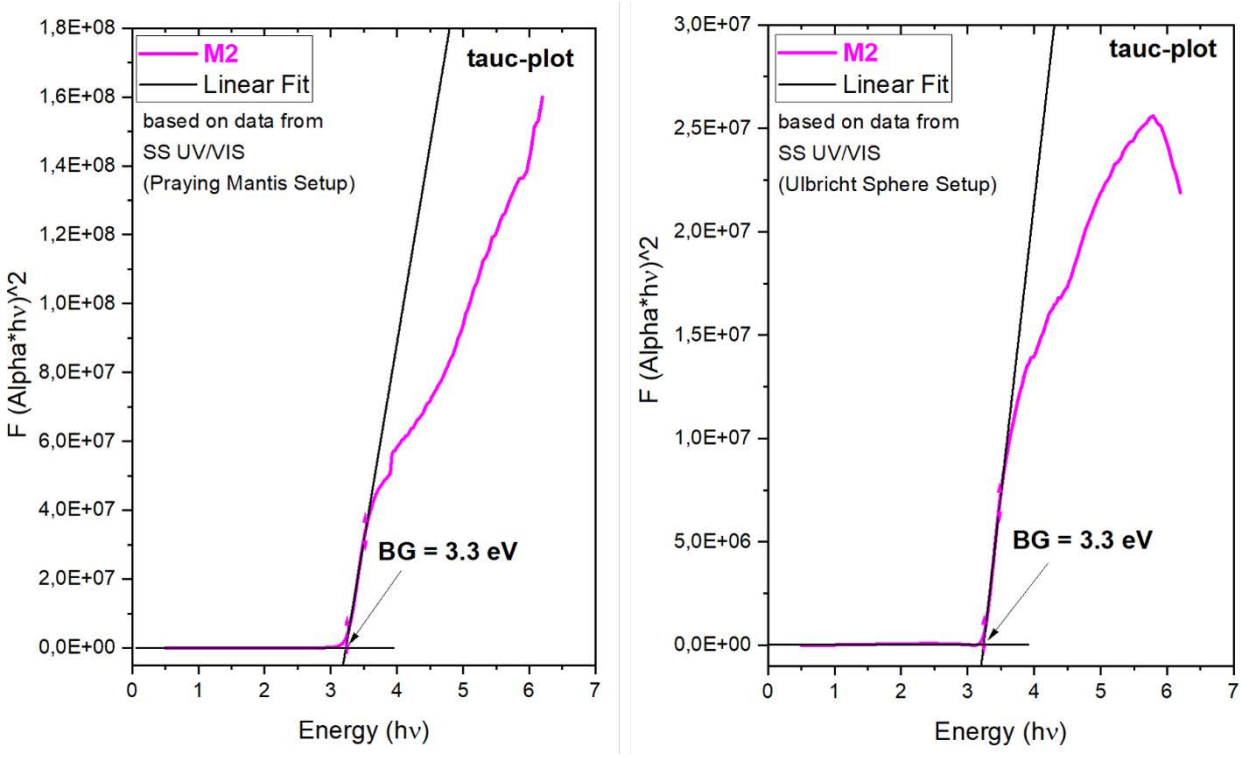

Figure S34. Tauc-plot analyses derived from **s**olid-state UV/VIS spectral data of m-TiO_2 (**M2**) obtained with two setups (*left:* Praying Mantis; *right:* cuvette in Ulbricht sphere).

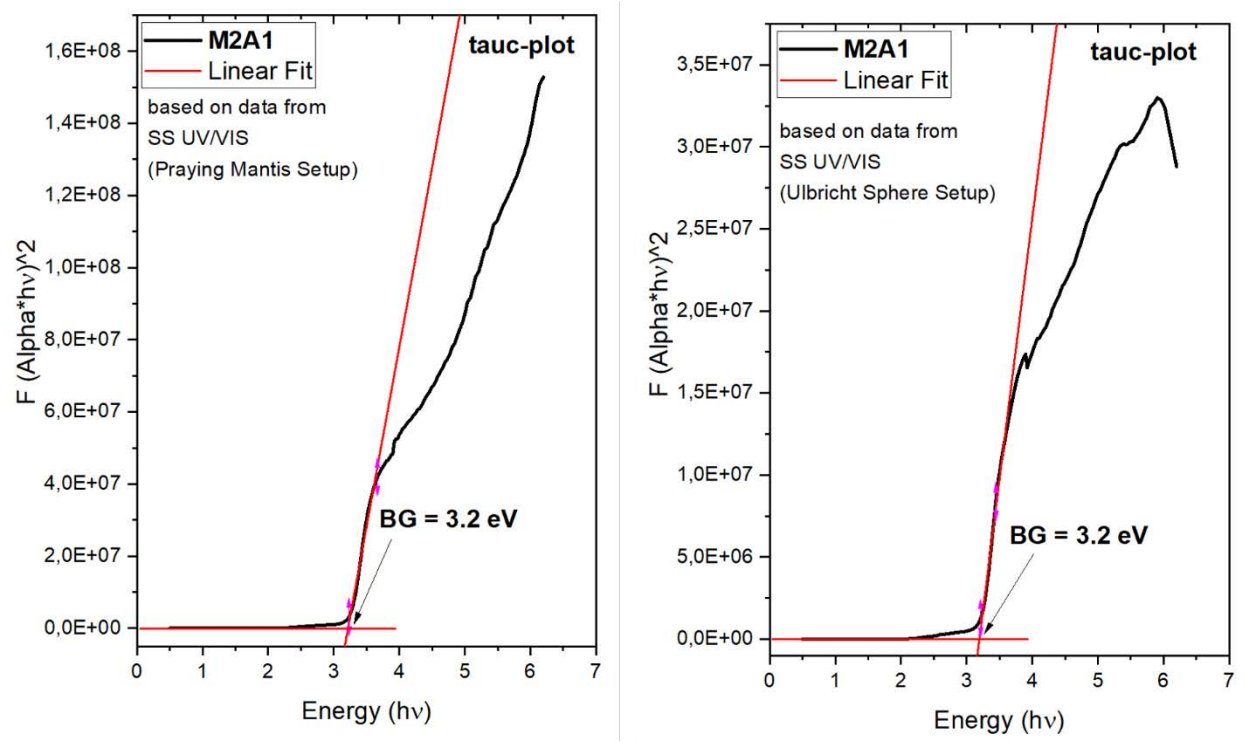

Figure S35. Tauc-plot analyses derived from **s**olid-state UV/VIS spectral data of H_2CAT*t*Bu_2-3,6@[m-TiO_2] (**M2A1**) obtained with two setups (*left:* Praying Mantis; *right:* cuvette in Ulbricht sphere).

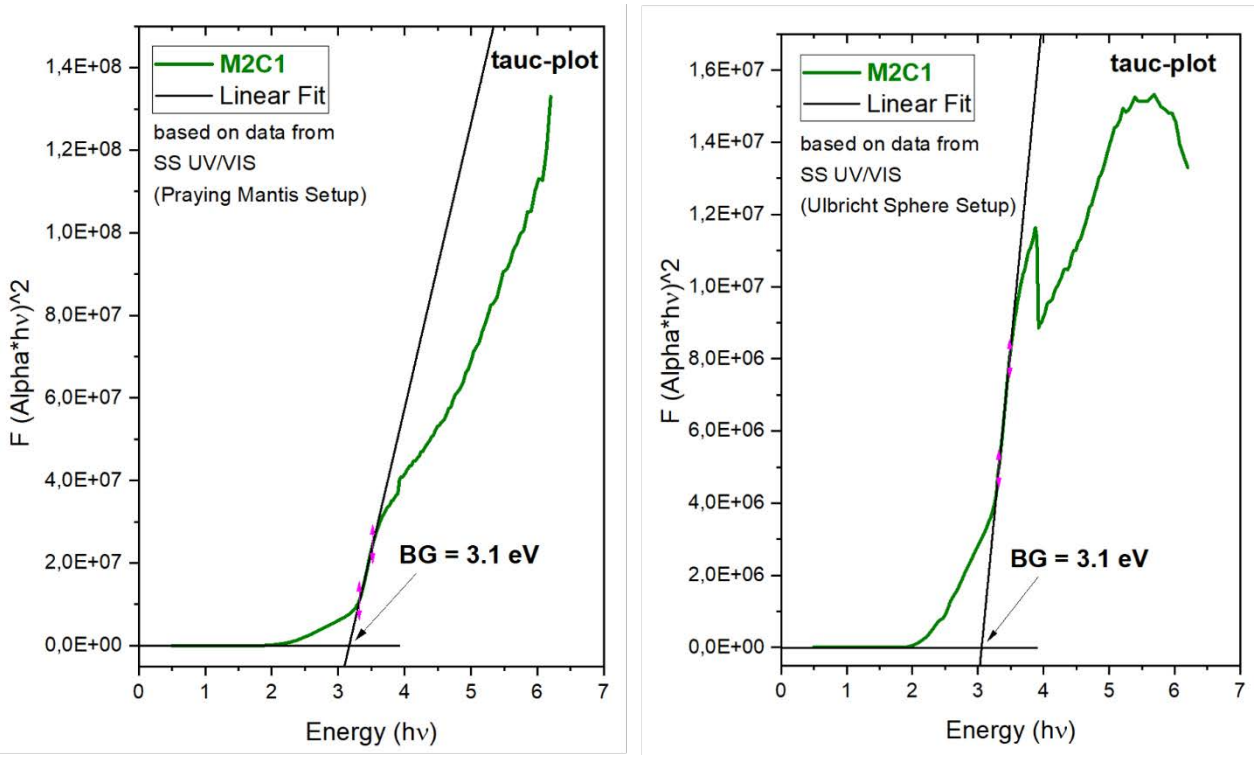

Figure S36. Tauc-plot analyses derived from **s**olid-state UV/VIS spectral data of [Ti(CAT*t*Bu$_2$-3,6)(OCH$_2$*t*Bu)$_2$(HNMe$_2$)$_2$]@[m-TiO$_2$] (**M2C1**) obtained with two setups (*left:* Praying Mantis; *right:* cuvette in Ulbricht sphere).

Ultraviolet Photoelectron Spectra and Calculations

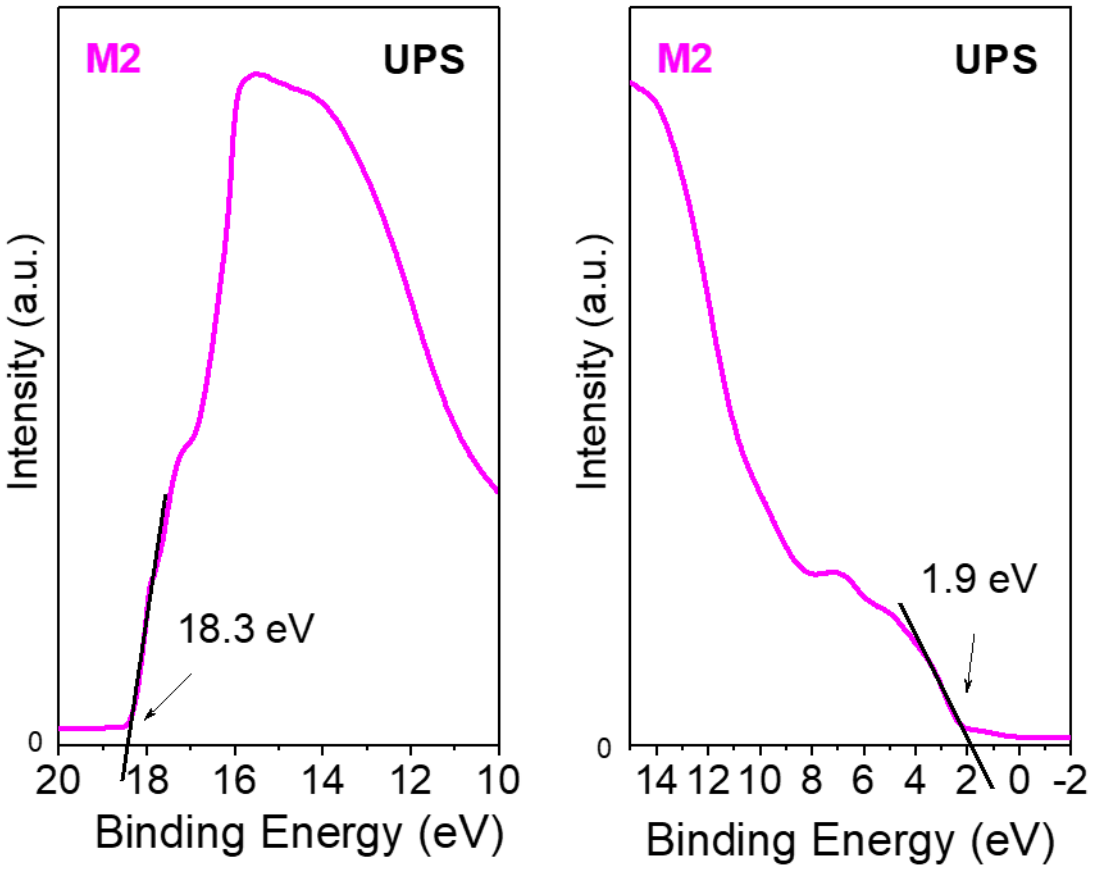

Figure S37. UP spectrum of m-TiO_2 (**M2**). (left) Secondary electron cut-off region. (right) Valence band region near the Fermi level (set to zero). The binding energy has been corrected taking the applied bias (-10 eV) into account.

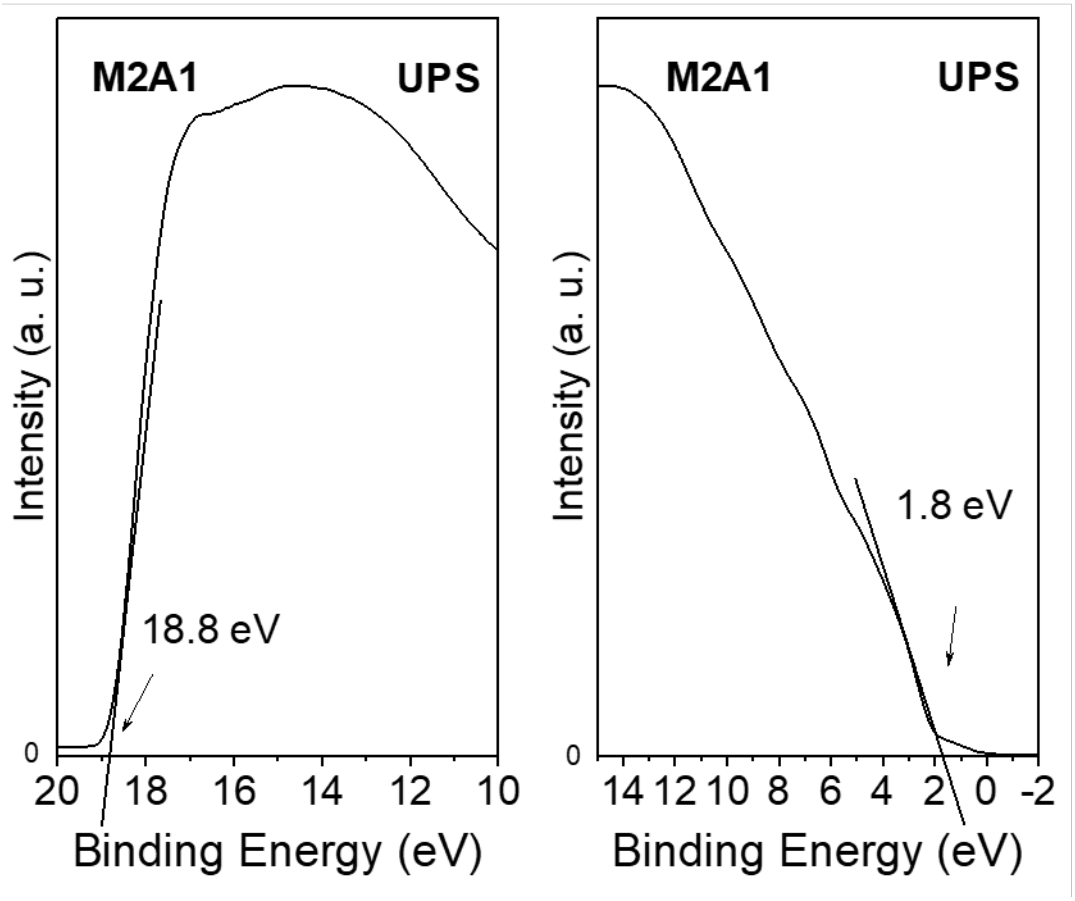

Figure S38. UP spectrum of $H_2CAT^tBu_2$-3,6@[m-TiO_2] (**M2A1**). (left) Secondary electron cut-off region. (right) Valence band region near the Fermi level (set to zero). The binding energy has been corrected taking the applied bias (-10 eV) into account.

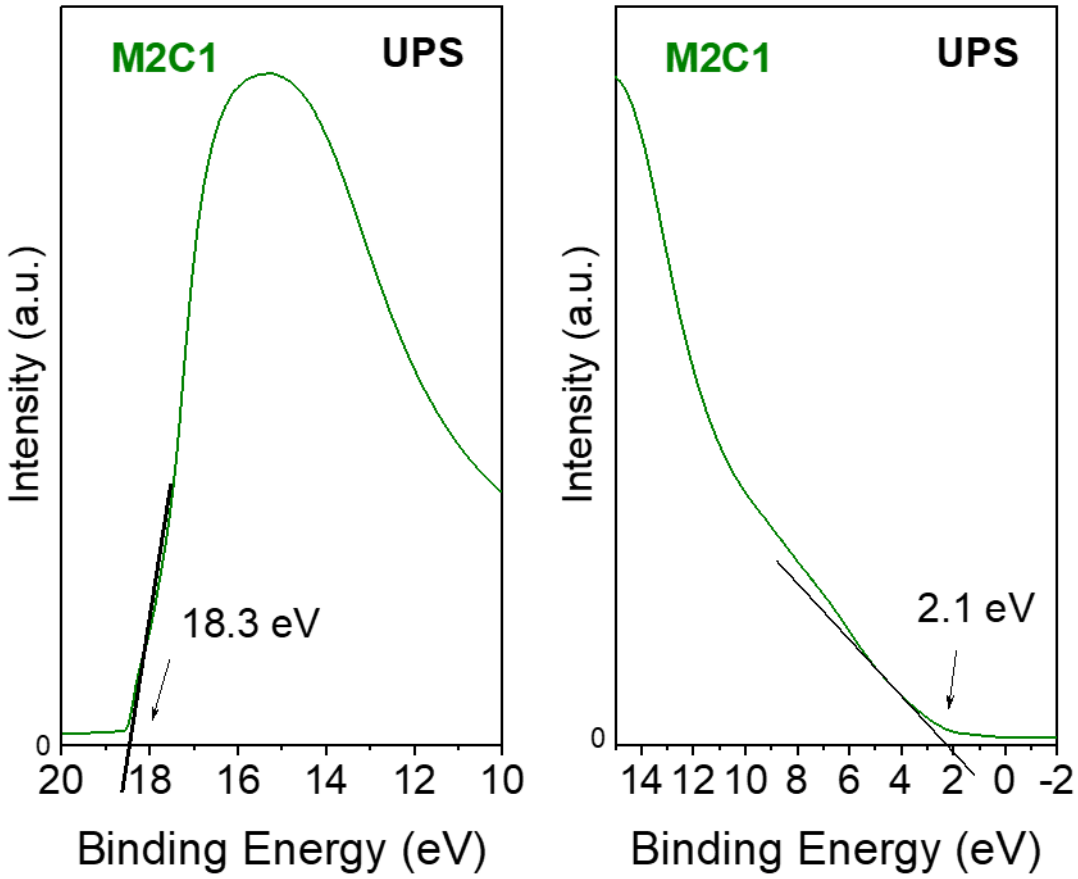

Figure S39. UP spectrum of [Ti(CAT*t*Bu$_2$-3,6)(OCH$_2$*t*Bu)$_2$(HNMe$_2$)$_2$]@[m-TiO$_2$] (**M2C1**). (left) Secondary electron cut-off region. (right) Valence band region near the Fermi level (set to zero). The binding energy has been corrected taking the applied bias (-10 eV) into account.

Table S7. Data obtained and calculated from UP spectra of m-TiO$_2$ (**M2**), [Ti(CAT*t*Bu$_2$-3,6)(OCH$_2$*t*Bu)$_2$(HNMe$_2$)$_2$]@[m-TiO$_2$] (**M2C1**) and H$_2$CAT*t*Bu$_2$-3,6@[m-TiO$_2$] (**M2A1**), (see: Figures S37-39)

Material	[a] E_{SECO} [eV]	[b] Spectrum width [eV]	[c] ϕ [eV]	[d] $Onset_{max}$ [eV]	[e] $\lvert E_{HOES}\rvert$ [eV]
M2	18.3	18.3	4.8	1.9	1.9
M2A1	18.8	18.8	4.2	1.8	1.8
M2C1	18.3	18.3	5.0	2.1	2.1

[a] Exact positions of E_F (is set to zero) and E_{SECO} determined by the intersection of low- and high-BE onsets with the baseline tangents of the respective UP-spectra.

[b] E_{SECO}-E_F.

[c] hν – spectrum width; hν = 21.2 eV (**He I**).

[d] Energies at the low-BE onset maxima in the respective UP-spectra.

[e] $Onset_{max}$ - E_F

Table S8. Processed values from Table S7, with E_F = 0 eV. and further data obtained and calculated from SS UV/VIS-spectra of m-TiO_2 (**M2**), [Ti(CAT*t*Bu_2-3,6)(OCH_2*t*Bu)$_2$($HNMe_2$)$_2$]@[m-TiO_2] (**M2C1**) and H_2CAT*t*Bu_2-3,6@[m-TiO_2] (**M2A1**), (see: Figures S34-36)

Material	[a] spectrum width [eV]	[b] ϕ [eV]	[c] E_{HOES} [eV]	[d] E_{BG} [eV]	[e] E_{LUES}* [eV]	[f] HIB [eV]	[g] IP [eV]	[h] EA* [eV]
M2	18.3	4.8	-1.9	3.3 / (3.3)	1.4	1.9	6.7	3.4
M2A1	18.8	4.2	-1.8	3.2 / (3.2)	1.6	1.8	6.0	2.8
M2C1	18.3	5.0	-2.1	3.1 / (3.1)	1.0	2.1	7.1	4.0

[a] E_{SECO}-E_F, as E_F is set zero, $|E_{SECO}|$ = spectrum width.

[b] hν – spectrum width; hν = 21.2 eV.

[c] As E_{HOES} is localized below E_F, it gets a negative algebraic sign.

[d] Value 1 / (Value 2) := from Praying Mantis Setup, used for further calculations* / (from Ulbricht sphere setup, only for comparison). These values were obtained (*via* tauc-plot analyses, see Figures S34-36) as follows:
The formula

$E = h\nu$ ($h = 6.626 \cdot 10^{-34}$ Js := Planck´s constant; ν := radiation frequency)

was extended to

$E = h\frac{c}{\lambda} = \frac{1.986 \cdot 10\text{^}-25\ J \cdot m}{\lambda\ [nm]}$ ($c = 2.998 \cdot 10^8 \frac{m}{s}$:= velocity of light),

considering 1 eV = $1.6022 \cdot 10^{-19}$ J

$E = \frac{1240\ eV}{|\lambda|}$

and was used to transform the wavelength scale into an energy scale giving values in units of eV.
The normalized absorbance values were divided by the layer thickness of the respective sample (which were $1.0 \cdot 10^{-3}$ m for the Praying Mantis setup and $0.5 \cdot 10^{-3}$ m for the Ulbricht sphere setup) to get the absorption coefficient Alpha.
Alpha-values were multiplied with the previously calculated energy values. The tauc-plot is then obtained by plotting (alpha · energy)^2 as a function of the energy. The visible x-intersection point of the elongation of the linear fit analysis of the first steep slope-range of the curve yields the bandgap value E_{BG} of the respective material – all values are shown in Table S8.

[e] E_{HOES}+E_{BG}.

[f] E_F-E_{HOES}.

[g] HIB+ϕ.

[h] IP-E_{BG}.

Onset- method applied to UP spectra

The Fermi level position E_F was determined by the intersection of the low-binding energy-onset (low-BE onset) with the baseline of the UP spectrum. The secondary electron cutoff E_{SECO} was analogously determined by the intersection of the high-BE onset with the baseline of the UP spectrum. The difference between these two points gave the spectrum width. The work function ϕ was calculated by subtracting the spectrum width from the energy of the incident He-I radiation hν = 21.2 eV. The position of the highest occupied electronic state(s) HOES was obtained from the low-BE onset maximum, and using the optical bandgap from solid-state UV/VIS enables the calculation of the energetic position of the lowest unoccupied electronic state(s) LUES. (Table 2 in the article). A ϕ-value around 5 eV for m-TiO_2 corresponds to typical values for anatase.[4-7] Thus, the energy-level scheme, shown in Scheme 3 (paper), is based on the values obtained from the onset-method applied to the UP spectra, and on the optical bandgaps calculated from the SS UV/VIS spectra *via* Tauc-plot analyses.

References

1. Widenmeyer, M.; Grasser, S.; Köhler, K.; Anwander, R., TiOx overlayers on MCM-48 silica by consecutive grafting. *Microporous Mesoporous Mater.* **2001,** *44*, 327-336.

2. Anwander, R.; Nagl, I.; Widenmeyer, M.; Engelhardt, G.; Groeger, O.; Palm, C.; Röser, T., Surface Characterization and Functionalization of MCM-41 Silicas via Silazane Silylation. *J. Phys. Chem. B* **2000,** *104*, 3532-3544.

3. Kim, K. S.; Barteau, M. A., Reactions of aliphatic alcohols on the {011}-facetted Ti02 (001) surface. *J. Mol. Catal.* **1990,** *63*, 103-117.

4. Kashiwaya, S.; Morasch, J.; Streibel, V.; Toupance, T.; Jaegermann, W.; Klein, A., The Work Function of TiO2. *Surfaces* **2018,** *1*, 73-89.

5. Yew, R.; Karuturi, S. K.; Liu, J.; Tan, H. H.; Wu, Y.; Jagadish, C., Exploiting defects in TiO2 inverse opal for enhanced photoelectrochemical water splitting. *Opt. Express* **2019,** *27*, 761-773.

6. Li, H.; Xie, C.; Liao, Y.; Liu, Y.; Zou, Z.; Wu, J., Characterization of Incidental Photon-to-electron Conversion Efficiency (IPCE) of porous TiO2/SnO2 composite film. *J. Alloys Compd.* **2013,** *569*, 88-94.

7. Kumarasinghe, A. R.; Flavell, W. R.; Thomas, A. G.; Mallick, A. K.; Tsoutsou, D.; Chatwin, C.; Rayner, S.; Kirkham, P.; Warren, S.; Patel, S.; Christian, P.; O'Brien, P.; Grätzel, M.; Hengerer, R., Electronic properties of the interface between p-CuI and anatase-phase n-TiO2 single crystal and nanoparticulate surfaces: A photoemission study. *J. Chem. Phys.* **2007,** *127*, 114703.